Fracture and fatigue crack propagation in a Ni-base metallic glass (Ni78Si10B12)

Thesis

FRACTURE AND FATIGUE CRACK PROPAGATION IN A Ni-BASE METALLIC GLASS ($Ni_{78}Si_{10}B_{12}$)

A THESIS SUBMITTED TO THE
MATERIALS SCIENCE DISCIPLINE OF
THE OPEN UNIVERSITY
FOR THE DEGREE OF
DOCTOR OF PHILOSOPHY

by
AHMET TUGRUL ALPAS
(BSc, MSc)

January 1987

Date of submission : 3 February 1987
Date of award : 10 March 1987

To Füsun

A.T. Alpas
The Open University

PhD Thesis
January, 1987

Fracture and Fatigue Crack Propagation in a Nickel Base Metallic Glass ($Ni_{78}Si_{10}B_{12}$)

Abstract

This work presents an investigation of fracture and fatigue in thin ribbons of a nickel base metallic glass: $Ni_{78}Si_{10}B_{12}$. The fracture and fatigue crack propagation behaviour of this high tensile strength (2100 MPa) and high toughness (67 MPa$\sqrt{m}$) amorphous alloy is of interest for two reasons: firstly, the alloy has no normal metallurgical microstructure, and secondly, the alloy shows an unusual form of plastic deformation which proceeds by nucleation and propagation of localized shear bands. On uniaxial tensile loading, failure of uniform ribbons occurs instantaneously at the yield stress by shear rupture through an intense shear band inclined at 45 degrees to the loading axis.

The development of a local plastic zone at the crack tip in single edge-notched specimens under monotonic tensile loading has been investigated by a replication technique. Under plane stress conditions, these plastic zones are dominated by elongated shear bands. Dugdale's 'strip yield' model offers a reasonable description of the zone size and displacement at the crack tip.

The propagation of shear cracks has also been studied by carrying out 'trouser leg' tear tests. The tear energy is found to depend strongly on specimen thickness and testing temperature. Three types of shear band are observed near the tip of the tear crack; one type is associated with the bending of the testpiece while the others are evidence of types II and III shear deformation. A model based on the geometry of these bands has been developed and used to obtain an estimate of the plastic work involved in tearing. Good agreement is found between the calculated and measured tear energies.

The relationship between fatigue crack growth per cycle, da/dN, and the alternating stress intensity factor, ΔK, has been determined as a function of R-ratio. For growth rates in the range 10^{-6} - 5×10^{-4} mm/cycle, the Paris Law (with an exponent $m \approx 2$) is obeyed independent of the R-ratio. The mechanisms of fatigue crack extension are shown to depend on the deformation microstructure of the alloy. At intermediate ΔK's, decohesion of 'parabolic' shear bands produces faceted fracture morphologies. At near threshold values of ΔK, growth rates deviate from the Paris Law, producing an extremely low ΔK_{TH}. This is accompanied by an unusual dependence on the R-ratio. As the R-ratio is raised, ΔK_{TH} increases and growth rates decrease. It is proposed that the applied mechanical factors modify the local crack driving force. This is confirmed by establishing a correlation between ΔK_{eff} and the crack tip opening displacements.

Preface

This thesis submitted for the degree of Doctor of Philosophy of the Open University is an account of research performed in the Materials Science Discipline under the supervision of Professor C.N. Reid between January 1984 and January 1987. The work reported is original and has been performed without collaboration. This thesis neither in part nor as a whole, is the same as any thesis submitted in this or any other university. Where the work of other authors has been included in the text, this has been acknowledged and its source given in an alphabetical list at the end of the thesis. Some parts of the work have been presented at these three conferences:

Rapid Solidification Conference, University of Oxford, 10-11 July, 1985.
Title of the paper: "Fracture and Tearing of a Ni-base Metallic Glass".

Metals and Materials '86, University of Manchester, UMIST, 21-23 April, 1986.
Title of the paper: "Fatigue Crack Growth in a Ni-base Metallic Glass".

1986 TMS Fall Meeting, Marriott's Orlando World Centre, 5-9 October, 1986.
Title of the paper: "Initiation and Propagation of Fatigue Cracks in Metallic Glasses".

The following paper will be published soon:

A.T. Alpas, L. Edwards, C.N.Reid, Shear Crack Propagation in a Ni-base Metallic Glass. To be published in Acta Metallurgica (accepted 17 July, 1986).

A.T. Alpas/ January 1987.

Acknowledgements

I would like to express my sincere gratitude to my supervisor Prof. C.N. Reid for his invaluable support at every stage of this research project. I am indebted to Dr. L. Edwards for his constant encouragement and for many inspiring discussions. I also wish to thank Dr. J.V. Wood for his interest and helpful comments.

I deeply appreciate the generous technical assistance supplied by all the members of the research laboratories and workshop at the Materials Science Discipline, in particular Mrs. N. Williams, Mr. R. Black and Mr. J. Moffat.

Many thanks to the research students of the Discipline, Mr. M. Igharo, Mr. V. Akdeniz and Mr. S. Gungor for their friendship and warm-hearted help.

The credit for the careful typing of the text goes to my wife, Fusun Alpas. It was her caring support that gave me the strength to overcome every difficulty I encountered over the past three years. I dedicate this thesis to her.

Table of Contents

List of Figures

Figure 2.13 Schematic representation of the monotonic and cyclic plastic zones (after Bathias and Pelloux).

Figure 2.14 Geometric model of fatigue crack growth by shear sliding (Laird-Smith-Neumann model). a) Initial configuration. b) Crack opened in tension with shear sliding on one slip plane above the crack plane.c) Followed by shear sliding on one slip plane below the crack plane.d) Crack unloaded with reversed shear sliding on slip plane of b. e) Followed by reversed shear sliding on slip plane of c; the crack has advanced. f) After a number of repetitions of the mechanism; note that fatigue striations have been formed (after Weertman, 1979).

Figure 2.15 Schematic representation of Tomkins and Biggs (1969) model of fatigue crack growth.

Figure 2.16 Three forms of crack closure. The residual displacement, δ_R, is the 'excess' material wedged between the crack flanks (after Fleck, 1984).

Figure 2.17 a) Influence of R-ratio (0.06-0.73) on fcg curves of medium C/Mn pearlitic steel tested in laboratory air (Beevers et al., 1975).

b) Experimentally-measured variation of threshold stress intensity with loadratio (R) in two 2.5 Cr-1Mo steels tested in laboratory air (Ritchie and Suresh, 1980).

Figure 3.1 Schematic representation of the two types of shear transformations observed in sheared bubble rafts:
a) a diffuse shear transtformation.
b) two stages of a concentrated shear transformation (after Argon, 1979).

Figure 4.1 A tensile specimen with a reduced gauge section.

Figure 4.2 A single edge notch tensile (SENT) specimen.

Figure 4.3 a) A trouser leg tear specimen.

b) Configuration of the specimen during the tests.

Figure 4.4 a) The test rig used for fatigue crack propagation tests.

b) Configuration of the SENT specimen during the fatigue tests.

Figure 4.5 Fatigue crack propagation curve at a constant stress amplitude

Figure 5.10 Morphology of the yielded region around the tear (the tear crack propagates to the top of the figure).

Figure 5.11 Interference micrograph of the steps produced by the shear bands on the surface of the specimen.

Figure 5.12 Nomarski contrast micrograph of the crack tip. The tear is directed towards the top (the mark at the top of the figure is a surface scratch).

Figure 5.13 Nomarski contrast micrograph of the region in the wake of the tear (tensile side of the ribbon).

Figure 5.14 SEM micrograph of the tear crack tip.

Figure 5.15 Crossection of the shear band ahead of the crack. The section was taken ~30 μm from the crack tip.

Figure 5.16 a) Fracture surface of a trouser leg tear specimen (crack propagation is from the right of the figure).

b) Displacements of the fragments of the material from the surface of the ribbon.

Figure 5.17 Schematic illustration of possible shear fracture modes in ribbon specimens loaded in tension;a) Shear crack propagation.
b) Plastic shear and fracture.

Figure 5.18 Tear specimen mounted in test configuration. The edges of the shadow correspond to the bending axes of the arms of the specimen.

Figure 5.19 Schematic diagram of the components of inhomogeneous deformation ahead of the tear crack tip. Numbers II and III represent mode II and III type of displacements respectively.n Shear bands due to bending are indicated by letter b.

Figure 5.20 a) Schematic diagram of the stress distribution in a ribbon bent into elastic-plastic regime. Due to the presence of superimposed tensile stresses, the neutral axis (AA') shifts from the geometric centre of the specimen.

b) Assumed surface morphology of bending shear bands.

Figure 6.1 S-N curve at R = 0.1.

Figure 6.2 Fatigue crack propagation curve at R = 0.1.

Figure 6.3 Fatigue fracture morphology at $\Delta K = 50$ MPa$\sqrt{m}$, $R = 0.1$.

Figure 6.4 Fatigue fracture morphology at $\Delta K = 60$ MPa$\sqrt{m}$, $R = 0.1$. Note the large mode III shear displacements and the vein pattern due to the static failure.

Figure 6.5 Fatigue fracture morphology at $\Delta K = 43$ MPa$\sqrt{m}$, $R = 0.1$.

Figure 6.6 A magnified section of figure 6.5 showing details of striations.

Figure 6.7 Fatigue fracture morphology at $\Delta K = 17$ MPa$\sqrt{m}$, $R = 0.1$.

Figure 6.8 Fatigue fracture morphology at $\Delta K = 13$ MPa$\sqrt{m}$, $R = 0.1$.

Figure 6.9 Fatigue fracture morphology at $\Delta K = 10$ MPa$\sqrt{m}$, $R = 0.1$.

Figure 6.10 Relationship between the spacing of periodic fracture markings and fatigue crack growth rate.

Figure 6.11 Fatigue fracture morphology at $\Delta K = 9$ MPa$\sqrt{m}$, $R = 0.1$.

Figure 6.12 Fatigue fracture morphology at $\Delta K = 5$ MPa$\sqrt{m}$, $R = 0.1$.

Figure 6.13 Fatigue fracture morphology at $\Delta K = 3$ MPa$\sqrt{m}$, $R = 0.1$.

Figure 6.14 Fatigue fracture morphology at $\Delta K = 2.1$ MPa$\sqrt{m}$ (area on the left) and $\Delta K = 1.65$ MPa$\sqrt{m}$, R =m 0.1.

Figure 6.15 Areal fraction of the paraboloidal facets (■) and the periodic fracture markings (□) as a function of ΔK.

Figure 6.16 Dependence of the length of the paraboidal facets to ΔK (the length of the facets werte measured in the crack growth direction).

Figure 6.17 Fatigue fracture morphology at $\Delta K = 0.7$ MPa$\sqrt{m}$, $R = 0.1$.

Figure 6.18 A high magnification detail from Figure 6.17.

Figure 6.19 Fatigue crack tip morphology at $\Delta K = 0.7$ MPa$\sqrt{m}$, $R = 0.1$.

Figure 6.20 Fatigue crack tip morphology at $\Delta K = 3$ MPa$\sqrt{m}$, R =0.1.

Figure 6.21 Fatigue crack tip morphology at $\Delta K = 5$ MPa$\sqrt{m}$, $R = 0.1$.

Figure 6.22 Fatigue crack tip morphology at $\Delta K = 16$ MPa$\sqrt{m}$, $R = 0.1$.

Figure 6.23 Sequential changes in the fatigue crack profile during a decrasing ΔK test.

Figure 6.24 Fatigue crack profile at $\Delta K = 9$ MPa$\sqrt{m}$, $R = 0.1$.

Figure 6.25 Effect of R-ratio on near-threshold and medium crack growth rates.

Figure 6.26 Variation of crack growth rates with R-ratio at a constant ΔK.

Figure 6.27 Fatigue fracture morphologies produced at $R = 0.1$ and $R = 0.5$ at $\Delta K = 3$ MPa$\sqrt{m}$.

Figure 6.28 Fatigue fracture morphologies produced at $R = 0.1$ and $R = 0.5$ at $\Delta K = 2$ MPa$\sqrt{m}$.

Figure 6.29 Fatigue fracture morphologies produced at $R = 0.1$ and $R = 0.5$ at $\Delta K = 5$ MPa$\sqrt{m}$.

Figure 6.30 Effect of R-ratio on crack growth rates in an AISI 316 austenitic stainless steel ($t = 50$ μm).

Figure 6.31 Variation of crack growth rates with R at a constant ΔK in a AISI 316 strainless steel.

Figure 6.32 a) Fracture surface of an AISI 316 stainless steel at $\Delta K = 13.3$ MPa$\sqrt{m}$, $R = 0.5$.

b) Fracture surface of an AISI 316 stainless steel at $\Delta K = 13.3$ MPa$\sqrt{m}$. $R = 0.1$.

Figure 6.33 a) Fatigue crack tip morphology of an AISI 316 stainless steel at $\Delta K = 13$ MPa$\sqrt{m}$, $R = 0.5$.

b) Fatigue crack tip morphology at an AISI 316 stainless steel at $\Delta K = 13$ MPa$\sqrt{m}$, $R = 0.1$.

Figure 6.34 Photographs of the crack tip during unloading half of fatigue cycling ($\Delta K = 5$ MPa$\sqrt{m}$, $R = 0.1$):
a) K_{max} b) $K_{min} + 20\,\% \Delta K$ c) K_{min}

Figure 6.35 Fatigue crack tip opening displacement as a function of the distance behind the crack tip:

a) $\Delta K = 5$ MPa$\sqrt{m}$, $R = 0.1$.

b) $\Delta K = 2.5$ MPa$\sqrt{m}$, $R = 0.1$.

Figure 6.36 Load versus crack tip opening displacement curves at $\Delta K = 2.5$ MPa$\sqrt{m}$ for $R = 0.1$ and $R = 0.5$.

Figure 6.37 Load versus crack tip opening displacement curves at $\Delta K = 5$ MPa$\sqrt{m}$ for $R = 0.1$ and $R = 0.5$.

Figure 6.38 Variation of the effective crack tip opening displacement range with R at $\Delta K = 5$ MPa$\sqrt{m}$ and $\Delta K = 2.5$ MPa$\sqrt{m}$.

Figure 6.39 Schematic illustration of the threshold crack growth mechanism.

Figure 6.40 Summary of the proposed fatigue crack propagation mechanisms and resulting fracture surfaces peculiar to amorphous $Ni_{78}Si_{10}B_{12}$ at medium and low ΔK levels.

CHAPTER ONE

INTRODUCTION

Metallic glasses are a new class of materials formed by quenching molten alloys so rapidly that crystallization is by-passed. These alloys came on the scene only a quarter of a century ago, through the pioneering studies of Duwez and co-workers (Klement, Willens and Duwez, 1960, Duwez and Willens, 1963). While investigating the limits of non-equilibrium crystallization, Duwez and co-workers discovered that the normal two phase mixture of equilibrium phases in a eutectic Au-Si alloy could be replaced by a non-crystalline phase if quenched with sufficient rapidity from the liquid state. Subsequently, several glass-forming metallic alloys have been discovered using alternative methods for achieving rapid solidification. Within a short period, a considerable amount of work has been accomplished on the structure and properties of these alloys and the results of this research effort have opened a new chapter in materials science. Developments in this field have become the subject of five international conferences (Grant and Giessen, 1976a, b, Cantor, 1978, Masumato, 1981, Grant, 1984) and numerous smaller conferences and symposia all over the world.

Metallic glasses can be obtained using various combinations of elements provided that the rate of cooling is sufficiently high ($\geq 10^6$ K/s). However, the cooling rates necessary to circumvent crystallization are lower for compositions near deep eutectics. These compositions include metal-metal pairs (e.g. $Cu_{40}Zr_{60}$) and transition metals containing ~20 atomic % metalloid as glass former (e.g. $Pd_{80}Si_{20}$). But perhaps the most important category of metallic glass contains ternaries or quarternaries of reasonably inexpensive metals like Fe, Ni and Co with additions of Si,B or P (e.g.$Ni_{40}Fe_{40}P_{14}B_6$). Most of these alloys possess an outstanding combination of electrical, magnetic, chemical and/or mechanical properties.

Interest in the properties of these alloys has been stimulated by the development of continuous casting techniques such as "jet-casting" or "melt-spinning" which provide the possibility of producing long wires and ribbons with uniform cross sections. In the melt-spinning process, a jet of molten metal is projected onto the surface of a rotating cylindrical chill-block. The metal is spread into a thin ribbon which is thrown off the substrate after solidification at a very high rate (~2 km/min). The production of ribbons in this way has several advantages when compared with conventional metallurgical processing. Being direct, it eliminates a number of forging, rolling, annealing and drawing steps. Since the metal is shaped in the liquid state, the process is opposed by a shear resistance much smaller than that of a solid. Moreover, the process is intrinsically fast. All these factors ensure economy of production. However, the requirement for rapid heat extraction imposes a constraint on the form of the metallic glass produced so that at least one dimension of the product must be small. Thus, metallic glass products are usually in the form of wires or ribbons. Typical ribbons are usually no more than ~0.05 mm thick.

Studies on the mechanical properties of these alloys started concurrently with the advent of continuous quenching techniques, mainly to evaluate the potential of metallic glass filaments as structural reinforcement elements. These studies soon revealed that these alloys, especially Ni and Fe based compositions, are distinguished by exceptionally high tensile strength levels. It is now well established that metallic glasses are not only among the strongest and hardest metallic materials but also ductile and tough in contrast to the oxide glasses. Although current trends indicate that the commercial applications of the metallic glass ribbons as structural elements will be limited because of their low fatigue limits and their restricted thermal stabilities (most of the metallic glasses devitrify at about 700 K and become brittle), scientific interest in their mechanical behaviour remains strong.

At ambient temperatures, plastic deformation of metallic glasses occurs by the nucleation and propagation of localized shear bands. These bands are capable

of undergoing large amounts of plastic flow with little or no work hardening. Extensive studies aiming to clarify the atomistic mechanisms of inhomogeneous deformation have resulted in considerable controversy. Part of the problem is associated with the absence of the conventional metallurgical microstructure of metallic glasses so that there are no models that can be 'borrowed' to interpret the deformation mechanisms in terms of their structure. In the absence of long range atomic periodicity, the concept of structural defects, such as vacancies and dislocations becomes questionable in contrast with the situation for crystalline alloys where the detail of dislocation behaviour is reasonably well established. In addition, the lack of experimental methods to identify the atomic structure of metallic glasses constitutes the other part of the problem. Shear bands are the basic deformation units which can be detected unambiguously with the present microscopical techniques but the atomic arrangements within these bands are not well characterized. The current approach in the studies of deformation processes at the atomic level is to build physical or computer-simulated models and to test these models against the known mechanical properties.

Although substantial effort is being expended to clarify the micromechanisms of flow, surprisingly little attention has been paid to the fracture and fatigue mechanisms occurring in these alloys. Only a few elementary reports exist on the crack propagation mechanisms and 'deformation microstructures' under monotonic and cyclic loads in terms of the concepts of fracture mechanics. In these situations, the formation of conspicuous shear bands at the tips of cracks facilitates the identification of local stress-strain distributions in contrast to crystalline alloys in which deformation proceeds more homogeneously.

The aim of the present work is to investigate the fracture and fatigue crack propagation behavour of a strong and tough nickel-base metallic glass ($Ni_{78}Si_{10}B_{12}$). The next chapter of the thesis first examines the macroscopic approach to the characterization of crack extension. The concepts of fracture mechanics which are applicable to thin specimens are underlined. The effect of crack tip plasticity and the continuum mechanics approach to the stress-strain

fields at the crack tips are considered next. The proposed models of the micromechanisms of crack extension in crystalline metals and alloys displaying localized deformation are summarized. The third chapter presents a review of the existing information on the plastic deformation, fracture and fatigue of metallic glasses. The metallic glass used, mechanical testing methods and the experimental techniques employed in this study are introduced in chapter four. The next two chapters present and discuss the results on the 'static' fracture and the fatigue crack propagation behaviour of the alloy studied. These results are summarized in the final chapter which also indicates directions that possible further work should follow.

CHAPTER TWO

MECHANICS AND MECHANISMS OF FRACTURE AND FATIGUE

Fracture implies the separation of a solid body into two or more pieces under the action of stresses (or strains). The nature of the fracture process varies from material to material and is often affected by the type of applied stresses, geometrical features of samples and conditions of temperature and strain rate. The differing types of fracture produced in "ductile" and "brittle" materials under monotonic or alternating stresses arise from the differences in the modes of crack nucleation and propagation. If a material contains an inherent flaw or crack, crack propagation becomes the first stage of the fracture process. In a brittle material, an essentially elastic crack may propagate with little energy absorbtion to give catastrophic failure. However, in ductile materials failure is characterized by large energy absorbtion which permits slow and stable crack propagation accompanied by local yielding around the crack tip.

At present, there exist two basic approaches to the fracture problem: the macroscopic approach treats materials as continuum solids and on the basis of linear elastic or elastic - plastic fracture mechanics, provides a quantitative treatment of crack propagation and failure in terms of large scale parameters. The second approach seeks to clarify the fracture behaviour of materials in terms of their microstructure. Since it is assumed that fracture occurs at a critical stress, strain or displacement at the crack tip, this approach requires sound knowledge of deformation fields in front of the cracks. A comprehensive treatment of basic concepts of fracture mechanics has been given in recent books by Knott (1973), Broek (1974) and Ewalds and Wanhill (1985).

This chapter presents an overview of the macro and local aspects of fracture, but it will be limited to the concepts applicable to metallic glasses.

2.1 Linear Elastic Fracture Mechanics (LEFM)

LEFM is concerned with the fracture of cracked bodies made from linear, elastic materials (i.e. homogeneous, isotropic and obeying Hooke's Law). Even though the concentration of stresses at or near the vicinity of a crack tip gives rise to some localized plasticity or non-linear effects in real materials, LEFM is still applicable to these materials provided that the extent of these non-linear effects is small. Fracture criteria for these materials can either be obtained using stress intensity factors at the crack tips or by considering the changes in the energetic state of the cracked bodies.

2.1.1 The Elastic Crack Tip Stress Field

All stress systems in the vicinity of a crack tip may be derived from the three modes of loading (opening, sliding, tearing) shown in Fig. 2.1. The superposition of these modes is sufficient to describe the three dimensional case of local crack tip stress and displacement fields. The standard method of finding stresses and displacements around the crack tip in an ideal Hookean solid involves searching for a suitable stress function which satisfies the requirements of: (i) equilibrium of stresses, (ii) compatibility of strains, (iii) the boundary conditions for the cracked body, (iv) the constitutive equations of the material. Analytical techniques along these lines have been developed by Westergaard (1939) and Muskelishvili (1953) for the special case of a sharp crack in a two dimensional infinite plate. The analyses have also been reviewed later by Irwin (1958), Paris and Sih (1965) and Broek (1974). The stress distribution at the tip of a sharp crack subjected to mode I type of loading can be given in terms of the coordinate system in Fig. 2.2 as

$$\begin{Bmatrix} \sigma_{xx} \\ \sigma_{yy} \\ \sigma_{xz} \end{Bmatrix} = \frac{K_I}{\sqrt{2\pi r}} \begin{Bmatrix} \cos(\theta/2)\,[1-\sin(\theta/2)\sin(3\theta/2)] \\ \cos(\theta/2)\,[1+\sin(\theta/2)\sin(3\theta/2)] \\ \sin(\theta/2)\cos(\theta/2)\cos(3\theta/2) \end{Bmatrix}$$

$$\begin{Bmatrix} \sigma_{rr} \\ \sigma_{\theta\theta} \\ \sigma_{r\theta} \end{Bmatrix} = \frac{K_I}{\sqrt{2\pi r}} \begin{Bmatrix} \cos(\theta/2)\,[1+\sin^2(\theta/2)] \\ \cos^3(\theta/2) \\ \sin(\theta/2)\cos^2(\theta/2) \end{Bmatrix} \qquad 2.1$$

$\sigma_{xz} = \sigma_{yz} = \sigma_{rz} = \sigma_{\theta z} = 0$, for plane stress

$\sigma_{zz} = \nu\ (\sigma_{xx} + \sigma_{yy}) = \nu(\sigma_{rr} + \sigma_{\theta\theta})$, for plane strain

These equations are valid only in a limited area around the crack tip as they represent the first terms in a truncated series and further away from the crack tip higher order terms would have to be considered. The term K_I is the stress intensity factor introduced to fracture mechanics by Irwin (1958). For mode I type of loading, the stress intensity factor K_I is expressed as

$$K_I = Y\ \sigma\sqrt{\pi a} \qquad 2.2$$

where σ is the nominal stress and a is either the length of edge crack or half the length of a central crack. Y is a dimensionless size correction factor that depends on the shape of the cracked body. For a sharp crack in an infinitely large plate, $Y = 1$. Other values of Y for a wide variety of crack and specimen configurations of engineering interest have been determined and catalogued (Paris and Sih, 1965,Rooke and Cartwright, 1976). Similarly, K_{II} and K_{III} represent stress intensity factors for mode II and mode III type loadings respectively. The general three dimensional form of Equation 2.1 in tensor notation can be written as (Rice, 1967)

$$\sigma_{ij} = \frac{1}{\sqrt{2\pi r}} \left[K_I f_{ij}^{I}(\theta) + K_{II} f_{ij}^{II}(\theta) + K_{III} f_{ij}^{III}(\theta) \right] \qquad 2.3$$

where dimensionless functions f^{I}_{ij}, f^{II}_{ij}, f^{III}_{ij} depend only on the angular position θ. Consequently, the whole stress field at the crack tip is known once the value of K is known.

Equations 2.1 and 2.3 are elastic solutions which do not prohibit stresses from becoming infinite at the crack tip. In real materials, this cannot occur: plastic deformation taking place at the crack tip keeps the stresses finite and causes the formation of a local plastic zone. Different approaches made to calculate the size and shape of plastic zones will be reviewed in section 2.2.1. When the plastic zone size is small compared to the crack size and that of the cracked body, the surrounding elastic field dominates the behaviour. It has been suggested that as a first order approximation the size of plastic zone should be at least $\approx$ 50 times smaller than the crack length and the specimen thickness to maintain the validity of LEFM (Knott 1981). This situation is called small scale yielding and it is expected that stresses and strains both within and outside of the plastic zone will be determined by K.

Crack extension occurs when the crack tip stresses and strains reach a critical value, i.e. when K becomes equal to a critical value K_c. The value of the critical stress intensity K_c at a particular temperature depends on specimen thickness and constraint. The variation of K_c with specimen thickness is schematically shown in Fig. 2.3. After an initial sharp increase with thickness for very thin sheets, K_c decreases to a limiting value which is generally attributed to the attainment of plane strain conditions along virtually the whole crack front. Beyond a certain thickness, the crack tip material is predominantly in a plane strain state and plasticity effects are minimal. In this region, the value of K_c tends to a limiting constant value K_{Ic} (for mode I type loading) called the plane strain fracture toughness which is a material property.

The fracture criterion involving the stress intensity factor is equivalent to the fracture criterion derived by considering the changes in the energies involved

during crack extension. This is considered in the next section.

2.1.2 The Energy Balance Criterion

Griffith (1920) reasoned that a crack in an elastic body should start to extend by a small increment da if the total energy U of the cracked body is decreased by the extension, i.e.

$$\frac{dU}{da} \leq 0 \qquad 2.4$$

Considering the case of a cracked plate under a load P, the total energy U of the system is composed of the elastic energy U_{el} contained in the plate, the energy absorbed by the fracture process U_γ and the work done by the external forces W. The Griffith condition for crack extension (Equation 2.4) can be rewritten as the condition of neutral equilibrium as

$$\frac{d}{da}(W-U_{el}) = \frac{dU_\gamma}{da} \qquad 2.5$$

The left hand side of Equation 2.5 represents the driving force or the energy available for crack extension. It is often referred as the strain energy release rate (per unit thickness) and denoted by G. The right hand side of the equation represents the energy opposing crack advance. It is the crack resistance, R. At the onset of crack growth

$$G = R \qquad 2.6$$

Griffith considered the particular problem of the fracture of brittle materials (glass) and used a stress analysis developed by Inglis (1913) to show that for

stress field in the vicinity of an edge crack in an infinite plate of unit thickness, the absolute value of U_{el} is given by

$$|U_{el}| = \frac{1}{2} \frac{\pi \sigma^2 a^2}{E} \qquad 2.7$$

Fracture in a truly brittle material occurs so suddenly that there is no time for external energy to be supplied during the process, thus the term (dW/da) = 0. Regarding the term, U_γ, for such a material the only resistance to crack extension is the surface energy γ_s of the material which can be expressed as $U_\gamma = 2a\gamma_s$. To a first approximation, it can be assumed that U_γ (due to the decohesion of atomic bonds) is the same for each increment da. Therefore R is a constant. This means that for the crack propagation to occur, G must exceed a certain critical value G_c. From Equations 2.5, 2.6 and 2.7, the threshold of instability for an edge crack of length a is

$$G_c = R = \frac{\pi \sigma_c^2 a}{E} = 2\gamma_s \qquad 2.8$$

The critical value G_c can be determined by measuring the stress σ_c required to fracture a plate containing an edge crack of known size a or a central crack of size 2a.

Irwin (1948) and Orowan (1949) independently suggested that the Griffith criterion for truly brittle materials could be modified and applied to materials which exhibit plastic deformation. This could be done by considering that the crack resistance R involves plastic work γ_p accompanying crack extension in addition to the surface energy γ_s. It can be shown that - for a constant displacement (fixed grip) or constant loading conditions where $G = |dU_{el}/da|$ -

Equation 2.8 can be changed to

$$G_c = \frac{\pi \sigma_c^2 a}{E} = (2\gamma_s + \gamma_p) = R \qquad 2.9$$

The plastic work γ_p required to produce a plastic zone at the tip of an advancing crack in metals is much larger than the surface energy γ_s, i.e. R consists mainly of the plastic work term γ_p and γ_s can be neglected. In this case, R need not be constant, therefore Equation 2.9 is a necessary but not a sufficient criterion for crack extension. It is no longer certain that instability will occur at a constant value G_c. In fact, R and hence G_c are constant only for the condition of plane strain. In this case, it is customary to write $R = G_{Ic}$. As Equation 2.9 needs to be multiplied by $(1-\nu^2)$ for plane strain conditions, the equilibrium condition for crack extension is given by

$$G_{Ic} = (1-\nu^2) \frac{\pi \sigma_c^2 a}{E} = R \qquad 2.10$$

This condition is represented graphically as in Fig. 2.4.

The relationship between stress intensity K, and strain energy release rate G can be obtained by substituting Equation 2.2 into Equation 2.9

$$G = \frac{K^2}{E} \qquad \text{for plane stress}$$

$$G = \frac{K^2}{E}(1-\nu^2) \qquad \text{for plane strain} \qquad 2.11$$

This direct relation between G and K means that under LEFM conditions the prediction of crack growth and fracture is equivalent for both energy balance and

stress intensity criteria.

2.1.2.1 Stable Crack Growth - Crack Resistance Curves

As mentioned in the previous section, a constant value of R is obtained only for the condition of plane strain. For specimens loaded in plane stress (or intermediate plane stress- plane strain conditions), R is no longer constant. A certain amount of slow stable crack growth precedes instability in tough materials. In terms of the strain energy release rate, this situation is depicted in Fig. 2.5. The crack resistance curve (R-curve) has a convex upwards shape which indicates that the energy required for crack growth R increases steadily with crack length a. During slow stable crack growth there is a continuous balance between the released and consumed energy. If there were no balance, then either crack growth would stop or become unstable. As shown in Fig. 2.5 crack extension begins at a stress σ_i but the situation remains stable because $G_{\sigma i}$ intersects the R-curve (G = R). Further crack growth cannot occur at σ_i because the crack driving force $G_{\sigma i}$ becomes less than R. The conditions for stable growth are maintained until σ_c and a_c are reached. At this point, the $G_{\sigma c}$ versus a curve becomes tangential to the R-curve and instability occurs. Therefore, the energy criterion for the fracture of thin plates of a tough material in the plane stress state requires two conditions to be fulfilled simultaneously

$$G = R$$

$$\frac{\partial G}{\partial a} = \frac{\partial R}{\partial a} \qquad 2.12$$

The critical value of G at the instability can be denoted as G_c which is not a material property but depends on the thickness of cracked specimens as well as on the nature of the material. Krafft et al. (1961) postulated that the R-curve has a constant shape for a given material of given thickness independent of initial

crack length a_0, i.e. an invariant R-curve may be placed anywhere along the horizontal axis of a (G,R) versus crack length diagram. Consequently, an R-curve at $a_{02} > a_{01}$ indicates that there will be a larger range of stable crack growth and a higher G_C. Therefore, the conditions for instability depend on the initial crack length. However, the hypothesis that the R-curve is invariant is not yet generally accepted.

On the other hand, there is also no definite analytical explanation as to why the R-curve has a rising shape. In sheet materials it has been observed that a gradual transition occurs in the orientation of the fracture surface plane from the standard starting crack (one inclined at 90° to the loading axis) to planes inclined at 45°. Accordingly, Krafft et al. (1961) proposed that this may account for the rising R-curve. They assumed that the energy required (per unit area) for square plane strain fracture is lower than that required for inclined plane stress fracture. Thus, as shear lips develop on the fracture surface with slow crack extension, there will be an increase in R and this increase will continue until the transition from the square to slant fracture is completed. However, this explanation is only valid for the R-curve behaviour under intermediate plane stress-plane strain conditions where such a transition takes place with increasing crack growth.

2.1.2.2 Tear Energy

Rivlin and Thomas (1953) applied the Griffith energy balance criterion to the case of tearing in rubber sheets. They devised a number of tests in which the energy balance in Equation 2.5 can be discussed in quantitative terms for an elastic material undergoing certain degrees of plastic deformation outside the limitations of the original theory, without the necessity of solving difficult boundary problems. However, these studies have been developed almost independently of those of metallic materials. This, together with some behaviourial differences, has led to the employment of different terminology. Thus, the process

of fracture in rubbers is traditionally called tearing and the energy required to propagate a crack is known as the tear (or tearing) energy Γ.

One of the tests introduced by Rivlin and Thomas has become known as the "trouser leg" tear test. In this test, a thin rectangular piece is cut centrally along its length so that two "legs" are formed. These are pulled in opposite directions out of the plane of the test piece by equal and opposite forces and the force at which the cut grows is measured. The tear energy can simply be estimated from this value of the force (e.g. Sawyers and Rivlin, 1974, Thomas, 1955). If the elastic energy stored in the legs is small compared with the work done by the applied force F (per unit length of tear), the elastic energy released during tearing from the legs of the specimen (dU_{el}/da) can be ignored (Anderton and Treloar, 1971). With this simplification the work done by the applied load to produce an increment in crack length da is 2F da. The energy to create the increment in the cracked area is $\Gamma dA = \Gamma dat$. Equating these gives

$$2Fda = \Gamma dat \qquad 2.13$$

where t is the thickness of the specimen. The expression for the tear energy, Γ (per unit area of tear) is then

$$\Gamma = \frac{2F}{t} \qquad 2.14$$

This simple result expresses the fact that since no significant energy is stored in the bulk of the specimen, the whole of the work performed by the force is consumed in the tearing process, i.e. in the deformation of the material in the vicinity of the crack tip, and in the formation of the new surfaces.

Greensmith and Thomas (1955) observed that in natural rubber sheets, tear fracture occurs under plane strain conditions, and there is no stable crack growth below a critical value, Γ_c. Therefore, in these materials Γ_c is a characteristic material property. Tear tests have subsequently been applied to thin sheets of

polymeric materials (Sims, 1975, Chiu et al., 1984) and various metals and alloys (Isherwood and Williams, 1978). It was observed that in these materials, where large amounts of local plastic deformation precede crack extension, tear energy involves the work performed in the formation of a new surface γ_s and the work performed by plastic deformation at the crack tip, γ_p so

$$\Gamma = \gamma_s + \gamma_p \qquad 2.15$$

In ductile materials, the tear energy was found to be strongly affected by variations in the specimen thickness. This thickness dependence has been attributed to the dependence of the volume of the plastically deformed material near the crack tip on the section thickness (Chiu et al., 1984).

2.2 Crack Tip Plasticity

According to Equation 2.3, as the distance ahead of the crack tip, r tends to zero, the local stresses become infinite. In practice such a stress singularity is not possible because real materials cannot sustain infinite, non-hydrostatic stresses. Either the fracture strength σ_F of the material will be reached and failure will occur or the yield strength σ_{Ys} will be exceeded and the material will be deformed plastically. Crack tip plasticity thus plays an essential role in the fracture process and the applicability of LEFM is limited by the extent of this plasticity which is manifested by the size of plastic zone formed. In this section, the theories developed to predict the size and shape of plastic zones will be reviewed. The implications of these theories were first used to produce correction factors to the crack length in LEFM calculations. However, the primary role of crack tip plasticity in the fracture process is to modify the stress and strain distribution within the plastic zone. Since fracture occurs when local stresses or strains (or combinations of both) exceed a critical value, accurate knowledge of the

stress-strain distributions in front of a stationary or propagating crack has substantial importance. The estimation of the magnitude and distribution of stress and strain has been made possible by the advent of analytical and numerical techniques. The next sections describe briefly the features of particularly relevant examples of mixed elastic-plastic stress analysis of cracked plates.

2.2.1 Plastic Zone Size Calculations

The simplest estimate of plastic zone size is based on the elastic solution for the stresses at the tip of a sharp crack. By substituting the value of the yield strength, σ_{Ys} for σ_{yy} into Equation 2.1 at $\theta = 0°$, the following expression for the plastic zone size r_p^* is obtained

$$r_p^* = \frac{1}{2\pi} \frac{K^2}{\sigma_{Ys}^2} \qquad 2.16$$

Assuming, as a first approximation, that the plastic zone has a circular shape with a diameter r_p^*, the distribution of σ_{yy} at the crack tip will be as shown in Fig. 2.6 (Rice, 1967).

Irwin (1960) pointed out that since the stress represented by the shadowed area in Fig. 2.6 has to be carried by the material ahead of the plastic zone, the actual plastic zone has to be larger than r_p^*. He proposed that the crack behaves as if it was longer than its actual size by an amount equal to r_p^*. The situation can be represented as in Fig. 2.7 where the "effective" crack extends to the centre of the plastic zone. This analysis was revised by Broek (1974) who noted that the plastic zone size is

$$r_p = 2r_p^* = \frac{1}{\pi} \frac{K^2}{\sigma_{Ys}^2} \qquad 2.17$$

It is also possible to associate an opening at the original crack tip with this effective crack as described in the following section.

2.2.1.1 Dugdale "Strip Yield" Model

A more accurate relationship between applied stress, crack length and the extent of plasticity in plane stress has been derived by Dugdale (1960). In Dugdale's "strip yield" model the deformation ahead of a crack loaded under plane stress conditions is assumed to occur in a narrow band ahead of the crack tip. This is often a realistic assumption since the concentration of plastic deformation into a shear band at the crack tip has been observed to occur in a number of sheet materials including metallic glasses (e.g. Waku and Masumato, 1981), glassy polymers (e.g. Kambour, 1964) as well as plain carbon steel plates (Hahn and Rosenfield, 1965). Dugdale considered that the internal crack of length 2c subjected to a tensile stress is allowed to extend elastically to a length 2a over a region which includes the narrow yielded regions |a-c| at each end, as shown in Fig. 2.8. It is assumed that the yielded zones are prevented from opening by internal restraining stresses equal to σ_{Ys}. By combining the internal stress field surrounding the plastic zones with the external stress field associated with the applied system, Dugdale demonstrated that

$$\frac{c}{a} = \cos\left(\frac{\pi}{2}\,\frac{\sigma}{\sigma_{Ys}}\right) \qquad 2.18$$

or since $a = c + R$

$$\frac{R}{c} = \sec\left(\frac{\pi}{2}\,\frac{\sigma}{\sigma_{Ys}}\right) - 1 \qquad 2.19$$

when the applied stress $\sigma << \sigma_{Ys}$, Equation 2.19 reduces to

$$R = \frac{\pi^2 \sigma^2 a}{8 \sigma_{Ys}^2} = \frac{\pi}{8} \frac{K^2}{\sigma_{Ys}^2} \qquad 2.20$$

Burdekin and Stone (1966) showed that the separation of the crack faces at the tip of a Dugdale crack is given by

$$COD = \frac{8}{\pi} \frac{\sigma_{Ys}}{E} a \ln\left[\sec\left(\frac{\pi\sigma}{2\sigma_{Ys}}\right)\right] \qquad 2.21$$

At $\sigma << \sigma_{YS}$, this may be simplified to give

$$COD = \frac{\sigma^2 \pi a}{E \sigma_{Ys}} = \frac{K^2}{\sigma_{Ys} E} \qquad 2.22$$

or using Equation 2.11

$$COD = \frac{G}{\sigma_{Ys}} \qquad 2.23$$

Thus, when LEFM conditions apply, the critical COD is equivalent to a critical G or K. It follows from Equations 2.20-2.22 that a given value of COD needs to be "accommodated" by a plastic zone. The relation between COD and R is

$$COD = \frac{8}{\pi} \frac{\sigma_{Ys}}{E} R \qquad 2.24$$

It is also possible to estimate the plastic zone size in mode III deformation using Equation 2.18, i.e.

$$\frac{a}{c} = \cos\left(\frac{\pi\,\tau}{2\,\tau_{Ys}}\right) \qquad 2.25$$

where τ and τ_{YS} are the appplied and yield stresses in shear. This result exactly agrees with the plastic zone size estimated by Bilby, Cottrell and Swinden (1963) who used a model of continuous screw dislocations to describe mode III displacements in a thin plate (BCS model). Similar agreements exist between Blarenblatt's (1962) model and Dugdale's model. Blarenblatt replaced the restraining yield stresses in the Dugdale model by molecular cohesive forces to eliminate the stress singularity at the crack tip.

2.2.1.2 The Shape of Plastic Zones

The Irwin and Dugdale models reviewed so far have been based on the assumption of a state of plane stress and they have considered a circular or linear plastic zone shape respectively along the x-axis ($\theta = 0$). The shape of the plastic zone at angles other than zero can be estimated by examining the yield criterion for angles $-\pi \le \theta \le \pi$ (Duffy, 1969, Broek, 1974). In doing so, the crack tip equations (Equation 2.1) need to be rewritten in terms of principal stresses and substituted into either the Tresca or Von Mises yield criterion. But, these analyses give only the boundaries where the material starts to yield and no account is taken of the fact that the original elastic stress distribution above σ_{YS} must be redistributed after yielding. Within these limitations, the extent of the plastic zone as a function of θ for plane stress and plane strain conditions is given by

$$r(\theta) = \frac{1}{4\pi}\frac{K^2}{\sigma_{Ys}^2}\left(1 + \frac{3}{2}\sin^2\theta + \cos\theta\right) \qquad \text{plane stress} \qquad 2.26a$$

$$r(\theta) = \frac{1}{4\pi}\frac{K^2}{\sigma_{Ys}^2}\left(\frac{3}{2}\sin^2\theta + (1-2\nu)^2(1+\cos\theta)\right) \qquad \text{plane strain} \qquad 2.26b$$

These expressions are obtained using the Von Mises yield criterion and the shape of plastic zones are shown in Fig. 2.9a (Mc Clintock and Irwin, 1965). Along the x-axis ($\theta = 0^{\circ}$) Equation 2.26a gives the same plastic zone size as Equation 2.16 for plane stress conditions. However, assuming that $\nu = 0.33$ in Equation 2.26b, the plane strain value of $r(\theta)$ at $\theta = 0$ is $\approx$ nine times smaller than the plane stress plastic zone size.

Fig. 2.9b shows the three dimensional plastic zone through the thickness in a plate of intermediate thickness (Mc Clintock and Irwin, 1965). It is assumed that the plate is sufficiently thick to develop plane strain conditions in the centre. At the outer surfaces, $\sigma_{zz} = 0$, so that there is a biaxial condition of plane stress. Proceeding inwards the stress state changes over to one of plane strain. Because $\varepsilon_{zz} = 0$, the material develops large stresses in the z direction due to the constraint of the surrounding elastic material. This leads to the development of a triaxial stress state in the middle of the plate. This increases the effective yield strength of the material and leads to a smaller plastically deformed zone compared to that at the surfaces. Mc Clintock and Irwin argued that it would be unlikely that sufficient constraint will be generated inside the material to produce a plane strain plastic zone that is nine times smaller than the plane stress plastic zone. By allowing the material to relax outside the elastic-plastic boundary predicted by Equation 2.26, they suggested that the plane strain plastic zone is about one third of the plane stress plastic zone, i.e.

$$r(\theta=0^{\circ}) = \frac{1}{6\pi}\frac{K^2}{\sigma_{Ys}^2} \qquad \text{plane strain} \qquad 2.27$$

More accurate analysis of elastic-plastic boundaries allowing the redistribution of stresses during plastic deformation (in non-hardening or hardening materials) have been performed using numerical methods and finite element analysis that satisfy compatibility conditions at the crack tip. Much of this work has been performed by Rice and co-workers (e.g. Levy et al., 1971, Rice

and Tracey, 1973). Levy et al. showed that in non-hardening materials the plane strain plastic zone is not symmetrical about the y-axis but it is rotated towards the positive x-axis so that maximum extent of the zone occurs at $\theta = 70°$. The plastic zone size is estimated to be

$$r_p(\theta=70°) = 0.175 \frac{K^2}{\sigma_{Ys}^2}$$

$$r_p(\theta=0°) = 0.032 \frac{K^2}{\sigma_{Ys}^2} \qquad 2.28$$

This is significantly larger than the plastic zone size derived using the Von Mises yield criterion. Rice (1967) suggested that a simple model of plane strain behaviour could be represented by a discrete slip line and Dugdale yield zone, acting at an angle of 70° to the crack advance. According to Hutchinson (1968a) and Rice and Rosengren (1968) the plastic zone size and shape are affected by the strain hardening rate. For a power law hardening material ($\sigma = k\varepsilon^N$, where N is the strain hardening exponent) the farthest boundary of the zone occurs at $\theta = 103°$. They also showed that for N = 0.05, the maximum dimension of the plastic zone is given as

$$r(\theta=103^\circ) = 0.29 \frac{K^2}{\sigma_{Ys}^2} \qquad 2.29$$

Parallel to the progress in analytical techniques, various experimental techniques have been developed to observe plastic zones in metals and alloys directly. Among these, one of the most effective techniques was the etching technique used by Hahn and Rosenfield (1965) to decorate dislocations and slip bands in a silicon iron. They observed that the plastic zone in thin sheets of this material consisted of two intersecting 45 degrees shear bands confined to a region

extending a distance from the crack nearly equal to sheet thickness. However, the etching technique is limited to a few ferrous materials only. Other experimental techniques include microhardness (Bathias and Pelloux, 1973, Saxena and Antolovich, 1975), SEM selected area channeling method (Davidson, 1976, Blind, 1983), and the double stage replication technique (Lankford and Barbee, 1974, Davidson and Lankford, 1976). Problems arise when analysing the outcome of these experiments because elastic and plastic strains cannot easily be distinguished. An extensive review of the experimental measurements on plastic zones has been given by Lankford et al. (1977). Although it was not always possible to compare directly the results obtained from different techniques, generally good agreement was found between the measured and theoretical values (i.e. numerical solutions) of plane stress and plane strain plastic zone sizes.

The amount of effort spent to calculate and observe plastic zone sizes goes beyond its value as a correction factor to LEFM stress intensity factors. The interest in the crack tip plastic zone reflects its importance in controlling the process of crack extension and fracture since the energy required for crack advance is expanded in this crack tip zone. However, to be able to relate the micromechanisms of fracture to the macroscopic LEFM parameters, it is also important to have sound knowledge of stress and strain distributions within the plastic zone.

2.2.2 Stress and Strain Distribution in the Plastic Zones

As mentioned in the previous section, plasticity is accompanied by redistribution of stresses and strains at the crack tip. For a thin plate in plane stress subjected to mode I loading, the stress in thickness direction is zero and yielding occurs on two intersecting sets of planes making 45 degrees to both the loading axis and the thickness direction. Using the Tresca yield criterion, it can readily be seen that the maximum stress σ_{yy} in the plane stress plastic zone is limited to the material's uniaxial yield stress σ_{Ys}. However, in plane strain, a

material loaded in mode I does develop large stresses in the thickness direction due to the constraint and a triaxial state of stress arises directly ahead of the crack tip.

Progress in understanding the elastic-plastic stress and strain fields under plane strain conditions started with the asymptotic analyses of the near crack tip field, (Hutchinson, 1968, Rice and Rosengren, 1968) which have recently been supplemented by accurate finite element numerical solutions (Levy et al., 1971, Tracey, 1976, Mc Meeking, 1977). On the other hand, the fully plastic cases have been analysed for many years on the basis of slip line field theory (Hill, 1950).

Rice and Johnson (1970) and Mc Clintock (1971) pointed out the relevance of the Prandtl slip line field in providing the stress distribution in the vicinity of a sharp crack in an isotropic, perfectly-plastic material loaded in tension (Fig. 2.10a). As illustrated, constant stress regions A and B result over 45° wedges ahead and behind the crack tip. The central fan C, joining these regions, has radial lines as principal shear directions and results in a steady increase in normal stress from A to B so that the maximum stress directly ahead of the crack tip (using the Von Mises yield criterion) is

$$\sigma_{YY} = (2+\pi)\ \tau_{Ys} \approx 3\,\sigma_{Ys} \qquad 2.30$$

Therefore, in a perfectly plastic material, the maximum stress at the crack tip is three times larger than the material's uniaxial yield stress. Levy et al. (1971) presented an elastic plastic finite element solution for the stress state at the tip of a sharp crack. Their results showed that for small scale yielding conditions, the theoretical value of σ_{yy} predicted by the Prandtl slip line analysis is only maintained at the crack tip. Stresses decrease rapidly within the plastic zone and become equal to $2\,\sigma_{Ys}$ where the elastic-plastic boundary cuts the line ahead of the crack tip and σ_{yy} reaches σ_{Ys} at a distance from the tip equal to the maximum extent of the plastic zone (i.e. at $r_{max}\,(\theta = 70^{\circ}) = 0.157\,(K^2/\sigma_{Ys}^2)$).

Rice and Johnson (1970) pointed out that no severe strain concentration exists directly ahead of the sharp crack tip. Intense shearing is concentrated above and below the crack tip. In this region the shear strain $\gamma_{r\theta}$ becomes infinite when the crack tip is approached through the fan C (Fig. 2.10a), i.e.

$$\gamma_{r\theta} = \gamma_0 \frac{R(\theta)}{r} \qquad 2.31$$

where γ_0 is the initial yield strain and the undetermined function $R(\theta)$ is a measure of the 'strength' of the strain singularity and may be interpreted as a distance over which the strain falls to a value comparable to γ_0. Levy et al. (1971), Devaux (1980) offered analytical expressions for $R(\theta)$ and used them to calculate the size of plastic zones (section 2.2.1).

When the Prandtl slip line field analysis is extended to the case of a blunt crack, a different picture of the stress-strain distribution ahead of the crack tip arises. Fig. 2.10b shows a blunted crack tip and the associated slip line field (Rice and Johnson, 1970). In this case, the fan C joining the constant stress regions A and B focuses intense strains into the region directly ahead of the crack tip. Exponential slip lines in this region intersect at a distance X_c, about two times larger than the crack tip opening displacement δ. Schwalbe (1977) proposed that the strain distribution ahead of the crack tip can be approximated by

$$\gamma(r,0) = 0.44 \frac{\delta}{X} - 0.23 \qquad 2.32$$

Since plastic strains become infinite at the blunted surface of the crack, triaxiality cannot be maintained there and the location of maximum stress σ_{yy} occurs some distance ahead of the crack tip.

The effect of strain hardening on the stress and strain distributions was

investigated by Hutchinson (1968) and Rice and Rosengren (1968). The effect of an increase in the strain hardening exponent is to increase the magnitude of the maximum tensile stress up to 5-6 times above σ_{YS} and to shift the position of the stress maxima closer to the crack tip.

2.2.3 Micromechanisms of Failure in Materials Displaying Localized Deformation

The stress and strain fields calculated by finite element analyses contributed largely to the development of models attempting to describe the micromechanisms of crack tip failure processes. Failure criteria based on achieving a critical stress or strain (or a combination of both) requires that crack tip deformation fields should be considered over a size scale which includes critical microstructural features. For example, the requirement in the cleavage fracture of mild steel is that the triaxial stress state (or maximum tensile stress) should exist over a suitable distance ahead of the crack tip (Ritchie, Knott and Rice, 1973). For this type of fracture it is necessary to have a nucleus to propagate, so the characteristic distances are thought to consist of one or two grain diameters because a nucleus is usually associated with a cracked grain boundary carbide. On the other hand, for ductile failure mechanisms involving microvoid formation at second phase particles, it is essential that the appropriate stress or strain criteria be considered over a volume sufficiently large which is physically and statistically capable of containing second phase particles (Hahn and Rosenfield, 1968, Rice and Johnson, 1970, Rawal and Gurland, 1976). In this section, the particular case of the micromechanisms of ductile failure in alloys with low work hardening capacity will be considered in conjunction with Rice and Johnson's slip line field analysis. These alloys tend to develop conspicuous shear bands during crack extension and their fracture behaviour is sometimes similar to that of the metallic glass investigated in the present study.

In metals, commonly observed microstructural stages in the initiation and

propagation of ductile fracture involve: i) the formation of a free surface at an internal discontinuity near the crack tip, ii) the growth of a void or a cavity around this discontinuity, iii) coalescence of the growing void with the crack tip. The final stage of the ductile fracture process in low strength alloys of high work hardening capacity usually occurs by the coalescence of the holes with the crack tip when ligaments between the holes neck to zero thickness (e.g. Mc Clintock, 1968). This internal necking process results in a "fibrous" fracture appearance. However, when materials lose their capacity for continued work hardening, flow begins to localize, eventually producing shear fracture along localized shear bands.

Green and Knott (1976) observed such a transition in a low alloy steel (HY80). In highly prestrained specimens, shear bands emerged from the crack tip and propagated to holes around inclusions. Since in non-prestrained specimens of the same alloy crack extension occurred by an internal necking process, crack growth along the shear bands has been attributed to the exhaustion of the specimen's work hardening capacity. Other examples of this process have been observed in quenched and tempered steels (Knott, 1980) and in age-hardened aluminium alloys (Hahn and Rosenfield, 1975) where the work hardening capacity is low and stress-strain curves approach that for rigid - perfectly plastic material. These can be interpreted in terms of the slip line field analysis around the crack tip and Rice and Johnson model of ductile fracture of rigid plastic materials. Rice and Johnson (1970) predicted that the critical strain for void nucleation ahead of a blunt crack tip must be achieved over a characteristic distance X_0 which is a function of the crack opening displacement, i.e. fracture in a non-hardening material initiates at a ratio of $(\delta/X_0) = 0.5$. They suggested that X_0 is the mean spacing of the second phase particles (Fig. 2.11a).

Clayton and Knott (1976) showed that in a material of high hardening capacity, flow is not localized until the crack tip has blunted significantly. In an annealed low alloy steel (HY80), void nucleation at the crack tip started at a ratio of $0.7 < (\delta / X_0) < 2.5$. Once a void at an inclusion ahead of the crack tip is "enveloped" by the slip lines, the process continues by the internal necking of the

ligament between the void and the crack tip (Fig. 2.11b).

However, in prestrained material with low hardening capacity, void nucleation begins at a lower crack tip displacement: $(\delta/X_0) \approx 0.5$. In this case, the crack tip slip line field is composed of logarithmic spirals as shown in Fig. 2.10b. Clayton and Knott (1976) suggested that shear strains localize into the spiral slip lines between the crack tip and the void and the crack extension proceeds by the decohesion of shear bands at a critical strain. This mechanism shown in Fig. 2.11c produces an "alternating spiral" crack profile on the specimen surface.

In high strength materials, such as marageing steels, shear localization does not produce a spiral crack profile but results in a "zig-zag' fracture path (Beecham and Yoder, 1973). Clayton and Knott (1977) suggested that in this case, fracture starts at the tip of a sharp crack. $(\delta << X_0)$ and the stress-strain distribution approximates to that shown by the Prandtl slip line field (Fig. 2.11d). Thus, strains are concentrated above and below the crack tip and the maximum extent of the plasticity occurs at 70° (Levy et al., 1971) in agreement with the angle that the zig-zag shear bands make with the crack tip.

2.3 Fatigue Crack Growth

In a material subjected to cyclic loads, failure by fatigue occurs after a number of cycles of alternating stress or strain whose peak amplitudes are much less than the tensile strength of the material. If the material is free of internal flows or cracks, its total fatigue life comprises both the crack initiation and propagation stages.

The role of slip bands on fatigue crack initiation is well known since the early works of Ewing and Humphrey (1903) and Thompson et al. (1956). Slip bands may be solely responsible for initiating the crack or they may interact with geometric or microstructural defects to nucleate microcracks. Microcracks usually initiate at singularities such as notches, sharp scratches, pores or inclusions, on or just below the surface of the materials. They act as stress raisers and facilitate slip band formation by increasing the local stress amplitudes. When the surfaces of materials are highly polished and defect free, fatigue cracks may still form. If the stress amplitude is high enough, plastic deformation takes place leading to slip steps on the surface which may increase in size under continued cycling until they initiate one or more microcracks. When the process is stopped and polished surfaces are examined before the initiation of the cracks, many slip bands can be observed. While most of these are easily removable by electropolishing, some require extensive electropolishing for removal and when the specimen is retested, slip bands form again in the same places: these are "persistant slip bands". The term was first introduced by Thompson et al. (1956). Forsyth and Stubbington (1957) observed intrusion-extrusion pairs associated with persistent slip bands in an Al-Cu alloy. Studies of Lukas et al. (1968), Finney and Laird (1975), Kim et al. (1978) clarified the relationship between the intrusion-extrusion pairs and microcrack initiation. The literature on fatigue crack initiation has been reviewed by Forsyth (1969), Frost et al. (1974), Fine and Ritchie (1979).

The transition of persistant slip bands to cracks has been studied by Forsyth (1969) and Brown (1977). Forsyth proposed that once nucleated on the surface,

microcracks propagate towards the interior along the slip bands on the planes of maximum shear stress (Stage I). After the crack reaches a certain size, the propagation continues on a plane perpendicular to the maximum principal stress (Stage II).

Division between micro and macrocrack growth periods is of basic importance in the context of fracture mechanics. In LEFM terms, the growth of a macrocrack can be described solely by the stress intensity factor without any microstructural restriction.

2.3.1 Application of LEFM to Fatigue Crack Growth

LEFM provides an empirical basis for the description of the propagation of fatigue macrocracks. Provided that small scale yielding conditions apply at the crack tip, the rate of fatigue crack propagation per cycle da/dN is governed by the alternating stress intensity factor ΔK

$$\frac{da}{dN} = f(\Delta K) = f(K_{max} - K_{min}) \qquad 2.33$$

where K_{max} and K_{min} are maximum and minimum stress intensities for each cycle. Fatigue crack growth data are usually presented in the form of log da/dN vs log ΔK plots. As shown in Figure 2.12, these curves exhibit a typical sigmoidal shape and three regions can be identified:

Region A: A low growth rate region where fatigue crack growth rates diminish rapidly with decreasing ΔK, ultimately reaching a threshold value ΔK_{TH} below which cracks remain dormant. In practice, ΔK_{TH} is defined in terms of highest ΔK at which no growth occurs within 10^7-10^8 cycles (Ritchie, 1977).

Region B: The middle region where fatigue crack growth occurs at intermediate ΔK's and the behaviour can be represented by a power law expression of the form

$$\frac{da}{dN} = C(\Delta K)^m \qquad 2.34$$

where C and m are experimentally determined constants and the value of m lies between 2 and 4. This empirical equation was originally proposed by Paris and Erdogan (1963) and often referred to as the Paris-Erdogan Law.

Region C: A high growth rate region where the fatigue crack growth rate rises rapidly as the maximum stress intensity K_{max} approaches the critical stress intensity factor K_c.

Recent studies have shown that a sigmoidal variation of crack growth rate with ΔK is associated with the operation of different crack growth mechanisms and the shape of the curve is modified by changes in thickness (plane stress-plane strain conditions), mean stress and environmental effects. Before considering the micromechanisms of crack growth at each of the three regions, it is convenient to review the concepts of reversed plasticity and crack closure.

2.3.1.1 Reversed Plasticity

Rice (1967) postulated that the application of cyclic loading results in the formation of a reversed (or cyclic) plastic zone at a fatigue crack tip. When a fatigue crack is uploaded during the tensile stroke of a stress cycle, a monotonic plastic zone is expected to form at the crack tip. Material stretched to a permanent deformation in this zone is compressed by the surrounding elastic material during unloading and residual compressive stresses arise. When the magnitude of these compressive stresses exceeds the compressive yield strength of the material, a reversed plastic zone proportional to the extent of reversed plastic deformation develops. The size of reversed plastic zone (r_c) can be deduced by assuming that under reversed loading, the local stress is twice the monotonic tensile yield stress (or cyclic yield stress). Using Equation 2.16, Rice (1967)

found that

$$r_c = \frac{1}{2\pi} \frac{\Delta K^2}{(2\sigma_{Ys})^2} \qquad 2.35$$

Thus, the reversed plastic zone size is only a quarter of the monotonic plastic zone size. The stress distribution ahead of a propagating fatigue crack at the maximum and minimum loads of a fatigue cycle is shown in Figure 2.13 . Reversed plastic zones have also been observed experimentally (Hahn et al., 1972, Bathias and Pelloux, 1973). The results of several experimental measurements on the cyclic plastic zone sizes were analysed by Lankford et al. (1977) who concluded that reversed plastic zones in metals are often 2-3 times smaller than predicted by Equation 2.35.

An estimation of the change in crack tip opening displacement (ΔCTOD) between the maximum and minimum loads of a fatigue cycle can be made using the above analysis. ΔCTOD can be obtained from Equation 2.22 as

$$\Delta CTOD = \frac{\Delta K^2}{2E\sigma_{Ys}} \qquad 2.36$$

2.3.1.2 Plasticity Induced Crack Closure

Based on compliance measurements of fatigue cracks at high ΔK levels, Elber (1970,1971) postulated that as a result of permanent tensile plastic deformation left in the wake of a propagating fatigue crack, premature contact between the crack faces can occur even during the tensile portion of the fatigue cycle. This modifies the stress state at the crack tip and will make more difficult the formation of reversed plasticity within the plastic zone. Thus, the consequence of

the crack closure is to decrease the actual alternating stress intensity factor from its nominal value of $\Delta K = K_{max} - K_{min}$ to a lesser value ΔK_{eff}, operating at the crack tip. The effective alternating stress intensity factor ΔK_{eff} may be defined as

$$\Delta K_{eff} = K_{max} - K_{cl} \qquad 2.37$$

where K_{cl} is the stress intensity factor at which the two fracture surfaces first come into contact during the unloading portion of the stress cycle. This closure mechanism is referred to as plasticity-induced crack closure or Elber closure (Fig. 2.16a). Elber (1971) also proposed that the fatigue crack propagation rate is governed by the effective value of stress intensity factor ΔK_{eff} such that

$$\frac{da}{dN} = C (\Delta K_{eff})^{m} \qquad 2.38$$

instead of by the Paris-Erdogan Equation. It is now widely accepted that plasticity-induced crack closure occurs in thin plates under plane strain conditions (Lindley and Richards, 1974, Mc Evily, 1977). There is strong evidence that it can also occur during mid-range fatigue crack growth in thick specimens (Fleck, 1984, Sehitoglu, 1985).

Recently, other closure mechanisms beside plasticity-induced closure have been detected. It has been observed that asperities on uneven crack surfaces (Halliday and Beevers, 1979) and oxide deposits formed at the crack tip (Suresh et al., 1982) may also cause premature closure. The effect of these closure mechanisms becomes prominent at near threshold crack growth and will be discussed within this context (Section 2.3.2.3).

2.3.2 Fatigue Crack Growth Mechanisms

The sigmoidal variation of crack growth rates with ΔK is characterized by different micromechanisms of fatigue crack growth. It is convenient to examine these mechanisms in terms of the three regions identified on the curve.

2.3.2.1 Intermediate Growth Rates -Striation Growth -

This region comprises fatigue crack growth rates between $\approx 10^{-5}$ - 10^{-3} mm/cycle where the experimental data show a good correlation with the Paris-Erdogan Equation. On a microscopic scale, cyclic growth of the cracks is usually associated with the formation of striations on fracture surfaces that represent successive positions of the crack front.

The presence of a pattern of striations on a fatigue fracture surface was first reported by Zappfe and Worden (1949) and programmed loading tests (Forsyth and Ryder, 1961) demonstrated that each striation is produced by one stress cycle although every cycle does not necessarily produce a striation. It is now well established that the process of crack extension during striation formation is controlled by reversed plasticity (e.g. Bathias and Pelloux, 1973, Pook, 1983), but the details of the exact mechanism leading to striation formation is not fully understood. Several crack growth models have been proposed to clarify the micromechanisms of striation formation. These models are reviewed by Tomkins (1975) and Weertman (1979) who pointed out that it is possible to collect crack growth models into two categories: models based on damage accumulation and models based on shear band activity.

Damage accumulation models consider that some sort of damage occurs in the plastic zone ahead of the crack tip and the material near the crack tip no longer holds together when this damage has increased to a critical value. Initially, this critical condition was taken to depend on a limiting fracture strength

being attained with cyclic loading (Head, 1953). The discovery of cyclic softening in some metals led Mc Clintock (1962) and Hahn et al. (1970) to consider damage as cyclic strain accumulation within the plastic zone. Other workers have examined the critical condition in terms of accumulated cyclic displacement or energy at the crack tip (Weertman, 1965, Rice, 1967, Yokobori, 1969). Credible expressions in the form of the Paris-Erdogan Equation with an exponent $m \approx 4$ have been obtained from these models. Ikeda et al. (1977) showed that the plastic work done in the region around the crack tip can be directly determined by experimental measurements and proposed an equation that gave again a ΔK^4 law for small scale yielding. However, damage accumulation models fail to explain why at some critical accumulated strain, displacement or energy, the material ahead of the crack tip fails and permits the crack tip to advance.

The second type of theory is based on progressive blunting and resharpening of the crack tip and proposes that crack propagation is controlled by plastic shear at the crack tip. Hence, they give a fuller picture of the fatigue fracture process itself.

Mc Clintock (1969) and Pelloux (1969) extended an early idea of Orowan (1949) who suggested that in a tensile specimen, crack growth at the tip of a flaw occurs by the help of two pairs of slip planes at 45° to the tensile axis, and independently postulated that under cyclic loads, alternating slip on these planes should lead to crack advance by striation formation. The first direct evidence on the formation of localized slip bands during fatigue was given by Tomkins and Biggs (1969) who reported that during high strain fatigue of pure aluminium specimens, plastic flow is concentrated in the maximum shear directions oriented at ±45° to the crack plane, leaving the material directly ahead of the crack tip relatively undeformed. Lankford and Kusenberg (1972) used a double stage replication method to show that similar shear bands are also formed in a stainless steel sample at about 70° to the crack plane during sharpening of the crack tip. Localized shear bands were also observed in a copper single crystal (Neumann,1974) and in an aluminium alloy (Lankford and Davidson, 1983). These

observations gave experimental support to the models based on plastic shear activity at the crack tip (Laird and Smith, 1962, Tomkins and Biggs, 1969, Neumann, 1974, Kanninen et al., 1976). Two alternative models of striation formation by shear sliding and shear band decohesion are illustrated in Figs. 2.14 and 2.15. Fig.2.14 shows a variant of the model originally proposed by Laird and Smith (1962) and it is due to Weertman (1979). In this model, the crack tip area, in a perfectly plastic and non hardening solid, is continually blunted during the loading part of the cycle and sharpened during the unloading part. This occurs by successive shear sliding on planes that make 70.5° with the crack plane followed by successive reversed shear sliding on parallel planes. Details of the process are explained in the caption of Fig. 2.15. In Tomkins model (Tomkins and Biggs, 1968), the crack is initially sharp under a small tensile load. On further tensile loading, shear bands start to nucleate and develop. When a critical strain is reached over a finite length of these bands, they decohere and the crack tip becomes blunted. This is followed by the tensile failure of the material at the centre of the blunt tip. Fig. 2.16 attempts to explain how a striation is formed by such a crack tip instability.

Neumann (1974) suggested that in the Laird-Smith model, the amount of shear sliding that causes striation formation is a function of the crack opening displacement. Similarly, Tomkins (1975) proposed that the strain required for shear band decohesion in his model depends on a critical value of the crack tip opening displacement. Fatigue crack growth rate may then be related to ΔCTOD as

$$\frac{da}{dN} = \alpha \, \Delta CTOD \qquad 2.39$$

where α is a constant related to the efficiency of blunting. Neumann (1974) and Mc Clintock (1967) suggested that $\alpha = 1/2$. If Equation 2.36 is used to calculate the value of ΔCTOD for a crack in a perfectly plastic solid, Equation 2.39 reduces to

$$\frac{da}{dN} = \alpha \frac{\Delta K^2}{2E\sigma_{Ys}} \qquad 2.40$$

leading to an exponent of two in the Paris-Erdogan Equation. Therefore, these shear sliding and shear band decohesion models as well as their variants (Lardner, 1968, Pelloux, 1970, Yokobori et al., 1977, Davidson, 1984) offer a plausible explanation to the crack growth by striation formation in materials that obey the Paris-Erdogan Law with an exponent $m \approx 2$. However, Donahue et al. (1972) extensively compiled fatigue crack growth data that fit a second power of Paris equation and pointed out that crack advance per cycle is only about 1% of ΔCTOD. This indicates that theories based on ΔCTOD must be further developed to explain why the crack propagation rate is such a small proportion of ΔCTOD. Davidson (1984) recently proposed a model in which the ΔCTOD was controlled by the number and the length of shear bands generated at a given ΔK and relating the slip characteristics to the number of dislocations nucleated at the crack tip, he found a good correlation between the predicted and experimentally measured ΔCTOD's.

Provided that static fracture modes do not interfere with the striation growth mechanism, for many alloys the effect of K_{max} (usually expressed in terms of the R-ratio (K_{min}/K_{max})) is minimal in mid-range fatigue growth rates (Heald et al., 1972, Ritchie and Knott, 1974, Ritchie, 1977). Nevertheless, in some aluminium sheets (Elber, 1970) as well as in some thick low strength steel specimens (Fleck, 1984) an increased R-ratio causes faster propagation rates when the crack advance occurs by striation formation. This has been explained in terms of plasticity induced crack closure (Elber, 1971, Schive,1979, Fleck, 1984).

2.3.2.2 High Growth Rates

In this region ($da/dN > 10^{-3}$mm/cycle), fatigue crack growth occurs under the combined effect of ΔK and K_{max} and the Paris-Erdogan Law seriously

underestimates the growth rates. The effect of K_{max} becomes especially dominant when the static fracture toughness of the material is approached. Crack growth rates are influenced by R-ratio, specimen geometry and microstructure. A transition from square to slant crack growth is often observed in thin sheets (Pook, 1983). This is associated with the change of stress state from plane strain to plane stress just below K_c. Shortly before the instability, fatigue crack growth in this situation occurs by a mixture of mode I and III displacements.

At a microscopic level, crack growth involves static failure mechanisms as well as striation formation. One of the common effects of the large monotonic plastic zone is to activate potential void nuclei at the crack tip. As the stress-strain distribution at high K_{max} values approximates to that of statically loaded crack tips, the void nucleation conditions stated by Rice and Johnson (1970) are applicable in this situation (Garret and Knott, 1975). However, there is evidence that voids link up to the crack tip by a true fatigue process and not simply by ductile tearing at the peak tensile load of the cycle (Griffiths et al., 1971). This is also confirmed by Tomkins (1980) who observed that void linkage occurs on the cyclic shear bands within the reversed plastic zone.

2.3.2.3 Threshold and Near Threshold Growth

At crack growth rates around 10^{-6}mm/cycle, extrapolation of the Paris-Erdogan Law provides an overestimate of crack growth rates and experimental plots decrease asympotically towards a zero rate at $\Delta K = \Delta K_{TH}$. It has been well documented that near the threshold, crack growth rates are strongly influenced by microstructural factors, environmental conditions and applied R-ratios (e.g. Davidson and Suresh, 1984).

In crystalline metals and alloys, the deviation from the linearity of fatigue crack growth curves is associated with the occurrence of microstructurally sensitive crack growth. This mode of growth leads to the formation of faceted

fracture morphologies. Beevers (1977) observed that the occurrence of such faceted morphologies is related to a grain size-crack tip plasticity interaction. When the size of the reversed plastic zone becomes comparable to the grain size, crack growth takes the form of planar transgranular or intergranular facets. Quantitative fractographic studies revealed that close to threshold, the proportion of these facets is very small increasing to a maximum as the plastic zone approaches the grain size and gradually diminishing again at higher ΔK values (Beevers,1977, Edwards, 1982). Priddle and Walker (1976) showed that transgranular facets are formed as a result of cyclic loads, but that they differ from the static cleavage facets due to monotonic loads. Both transgranular and intergranular facets are found to be randomly oriented on the fracture surfaces giving them a roughened appearance (Ward-Close and Beevers, 1980).

A third type of facet morphology is so called shear facets. These are observed in low carbon steels (Otsuka et al.,1975), in titanium alloys (Walker and Beevers, 1979), and in aluminium alloys (Minakawa and Mc Evily, 1981 and 1984). These authors accordingly suggested that near threshold crack growth takes place by mode II type displacements. Asaro et al. (1981) and Ritchie and Suresh (1982) pointed out that this type of crack growth occurs when the size of the reverse plastic zone becomes smaller than the grain size. In this situation, crack growth is expected to be confined to a single active slip system suitably oriented on one of the planes of maximum shear stress. The large mode II crack displacements accompanying such a crack advance have been confirmed experimentally using stereo imaging studies (Davidson, 1981). On the other hand, Louwaard (1977) and Minakawa and Mc Evily (1981) observed that mode II displacements lead to serrated or zig-zag crack trajectories that provide a mechanism of contact between crack surfaces behind the crack tip and cause premature closure of the crack faces before the minimum load of the stress cycle is reached. This phenomenon is called roughness-induced crack closure which reduces the applied ΔK to a lower value of ΔK_{eff}, thus leading to lower crack propagation rates (Fig. 2.16b).

Estimates of roughness-induced closure stress intensities (K_{cl}) were first reported by Purushothaman and Tien (1979). These authors suggested simply that K_{cl} could be calculated by equating the change in fracture surface height to the crack opening displacement. This model, however, does not consider the role of mode II displacements. Minakawa and Mc Evily (1981) have subsequently presented a model incorporating mode II and mode I displacements accompanying near threshold crack advance. This model qualitatively explains that a locally mixed mode of crack growth gives a lower K_{cl}/K_{max} ratio relative to mode I crack growth. Suresh and Ritchie (1982) modelled fatigue fracture surfaces as two intermeshing wavy asperities which match perfectly at the maximum load of the fatigue cycle. At lower loads, surfaces move normal to each other (mode I) and parallel to each other (mode II) until they come into contact. By assuming equal sized asperities, the non-dimensional closure stress intensity at the point of contact was derived to be

$$\frac{K_{cl}}{K_{max}} = \sqrt{\frac{2\gamma\, x}{1+2\gamma x}} \qquad 2.41$$

where the non-dimensional surface roughness parameter γ is the ratio of the height to the width of the asperities and x is the ratio of mode II to mode I displacements. Although the model ignores any contribution to roughness induced closure from residual plastic mode II displacements left in the wake of the crack, it shows that the roughness induced closure load is high when fracture surfaces are rough and mode II displacements at the crack tip are large.

A second type of crack closure mechanism leading to lower crack growth rates near ΔK_{TH} is due to oxide deposits formed on freshly exposed surfaces at the crack tip (Skelton and Haigh, 1978, Tu and Seth, 1978, Ritchie and Suresh, 1980). Moist atmospheres lead to the formation of oxide layers within the crack surfaces which are thickened by continual breaking and reforming of the oxide

scale behind the crack tip (Steward, 1980, Suresh and Ritchie, 1983). This process can be accelerated by repeated contact between fracture surfaces arising from mode II displacements and when the oxide layer reaches a thickness comparable to a crack tip displacement, the crack becomes effectively wedged closed at stress intensities above K_{min} (Fig. 2.16c). The role of oxide-induced crack closure on the threshold crack growth is described in detail by Suresh and Ritchie (1984) who offered a semi - empirical equation for K_{cl} in terms of the oxide thickness and its position with respect to the crack tip.

The plasticity-induced closure mechanism (Fig. 2.16a) was discovered before roughness-induced and oxide-induced closure mechanisms. Accordingly , the early tendency was to relate all experimentally observed crack closure effects to the residual compressive stresses occurring behind the crack tip. However, finite element studies of Newman (1976) and Ogura et al. (1977) showed that although at high crack growth rates a good correlation exists between ΔK_{eff} and residual compressive stresses, such a correlation deteriorates at near threshold growth rates. This is also confirmed by Fleck (1984) who demonstrated that the effects of oxide and roughness-induced closure outweigh the contribution from plasticity-induced closure as growth rates approach the threshold rate.

Another phenomenon that has been taken into account when interpreting near threshold fatigue crack growth data is the crack deflection, i.e. the deviation of the crack from a straight line path through the microstructure. Suresh (1983) considered the effect of this deviation on the magnitude of effective ΔK at the crack tip for the cases of both simple and multiple deflection (i.e. branching). It is shown that a crack deflection of 45° from the initial plane leads to a 20 pct reduction in the Mode I stress intensity factor and a 30 pct underestimate of the actual growth rate. However, when the branches are small (compared to the plastic zone size) the applicability of conventional fracture mechanics analysis leading to the above values may be questioned. Additional work on this topic is necessary.

One of the most striking characteristics of near threshold crack propagation is the strong dependence on the R-ratio. The effect of R-ratio on near threshold growth rates can be seen in Fig. 17a for a pearlitic steel (Beevers et al., 1975). The figure indicates that the value of ΔK_{TH} is markedly decreased and that propagation rates are increased as the load ratio is raised within the range of ~0.1 to 0.7. This is a typical result and it is in good agreement with a wide range of steels and nonferrous alloys tested at ambient temperatures (e.g. Cooke et al., 1975, Ritchie 1977, 1979). On the other hand, experimental data reported by Pook (1972), Weiss and Lal (1974), Beevers (1977) and Ritchie and Suresh (1980) show that the sensitivity of near threshold fatigue crack growth rates and ΔK_{TH} levels for many materials reduces at R-ratios $\geq$ 0.5 (Fig. 2.17b).

The effect of R-ratio on near threshold crack growth rates has been generally discussed in terms of the closure concept. Schmidt and Paris (1973) proposed such a model by assuming that the closure stress intensity K_{cl} is independent of R-ratio. The model predicts that below a critical R-ratio, $K_{cl}>K_{min}$. In this region, as ΔK_{eff} increases with R-ratio this results in an increase in crack growth rates and a decrease in ΔK_{TH}. Above the critical R-ratio where $K_{cl} < K_{min}$, the effect of closure disappears. ΔK_{TH} becomes insensitive to R-ratio and reaches a constant value controlled by the microstructure and flow characteristics of the material. Although this model is based on the plasticity-induced closure argument, it does not exclude other closure mechanisms. Suresh and Ritchie (1982) predicted a similar critical R-value in their roughness-induced closure model. Such a closure can only occur at low R-ratios where premature contact between mating surfaces during the crack tip shear displacements are predominant. When the crack tip opening displacement exceeds the scale of roughness at a given high R-ratio, the closure effect vanishes and the values of crack growth rate (and ΔK_{TH}) become independent of R-ratio.

The R-ratio dependence of fatigue thresholds is different from the behaviour predicted by the above models, in vacuum and in chemically aggressive

environments. In either case, the reduction in ΔK_{TH} with increase in R-ratio is far less marked than that in air (Cooke et al., 1975). Suresh and Ritchie (1984) interpreted this in terms of oxide-induced closure. In vacuum, the shallow dependence of ΔK_{TH} on R-ratio can be attributed to the fact that little or no corrosion deposits are formed at any R-ratio and unlike moist air the magnitude of oxide-induced closure does not vary with R-ratio. Very thick oxide layers form in aggressive environments at all R-ratios, and the extent of oxide-induced closure does not diminish with increasing R-ratio.

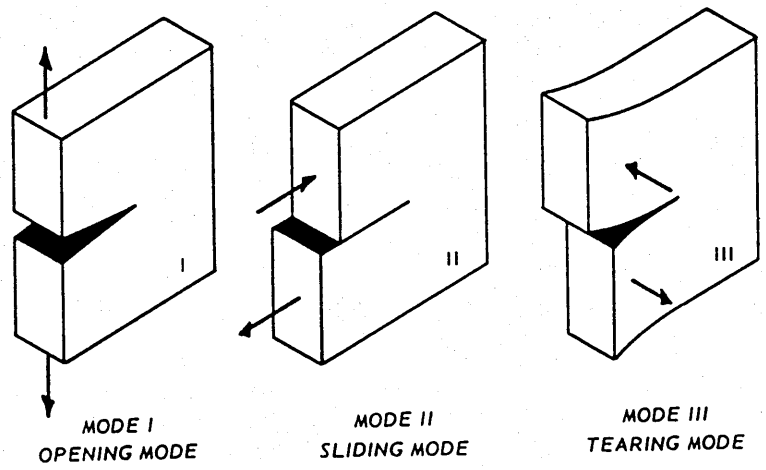

Figure 2.1 The three modes of crack loading.

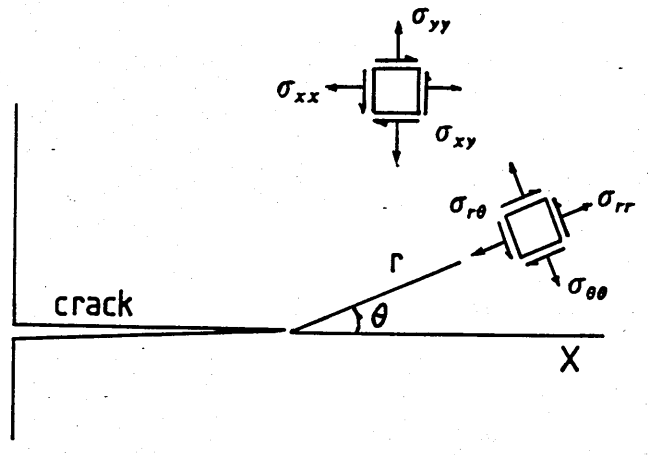

Figure 2.2 Components of stresses at the tip of an edge crack.

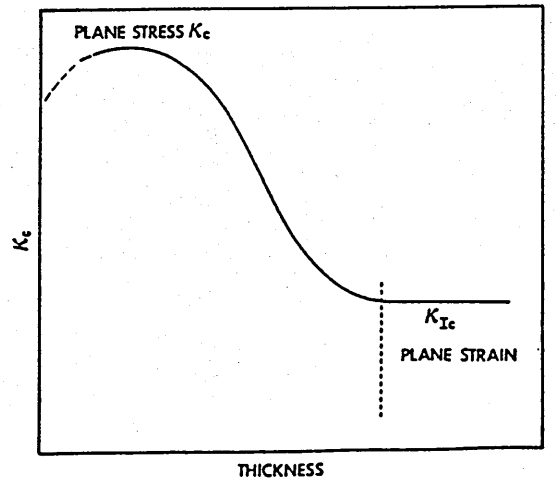

Figure 2.3 Variation in K_c with specimen thickness.

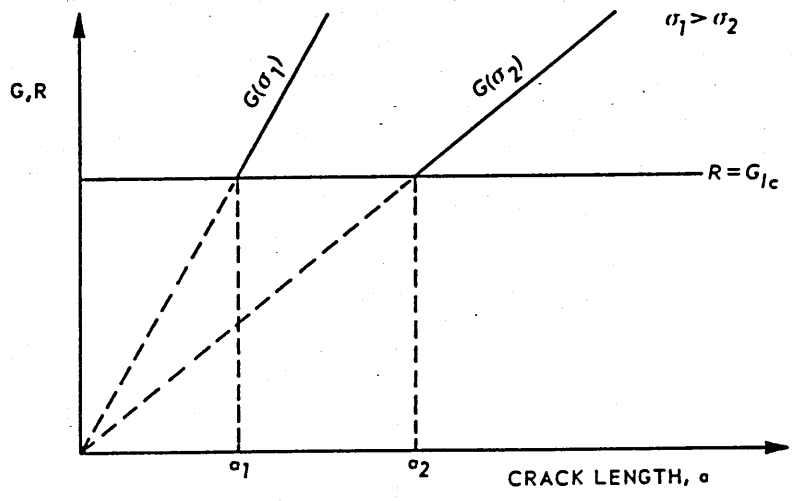

Figure 2.4 Graphical representation of the instability condition for plane strain (after Ewans and Wanhill, 1984).

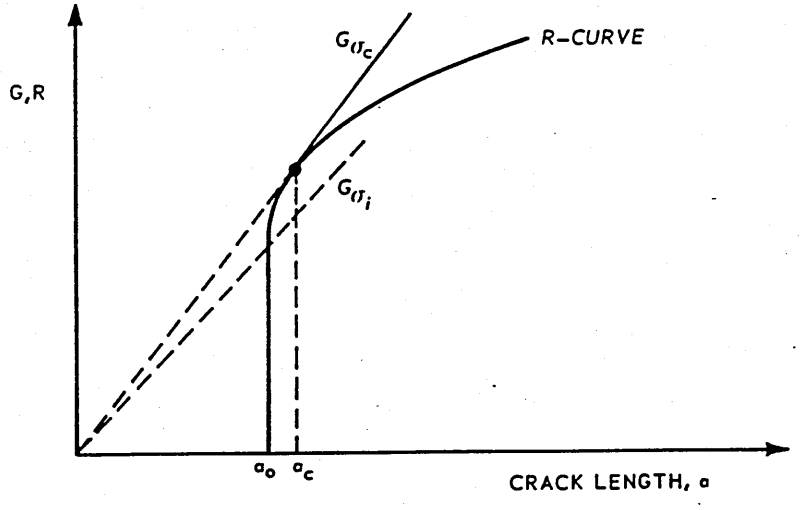

Figure 2.5 The rising R-curve (after Ewans and Wanhill, 1984).

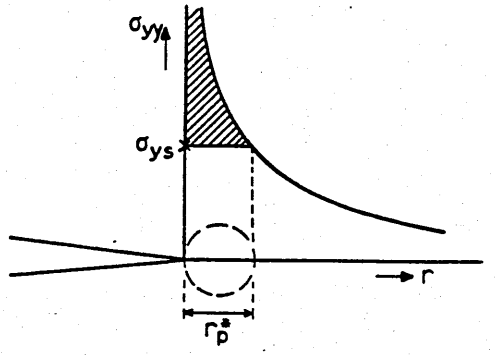

Figure 2.6 First estimate of plastic zone size (after Rice, 1967).

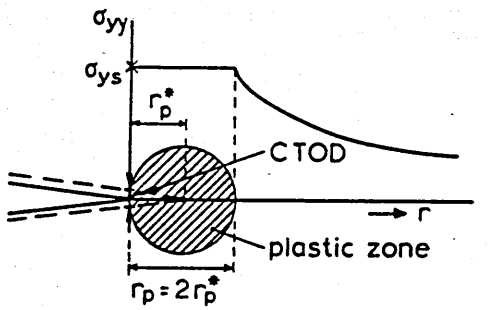

Figure 2.7 Irwin's plastic zone correction (after Broek, 1974).

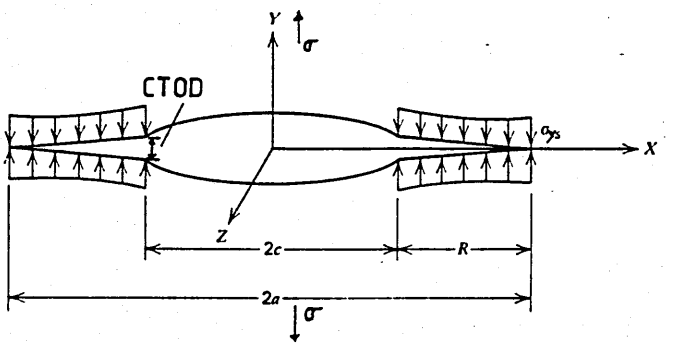

Figure 2.8 Dugdale plastic zone strip model for non strain hardening solids. Plastic zones R extend as thin strips from each end of the crack (after Hahn and Rosenfield, 1965).

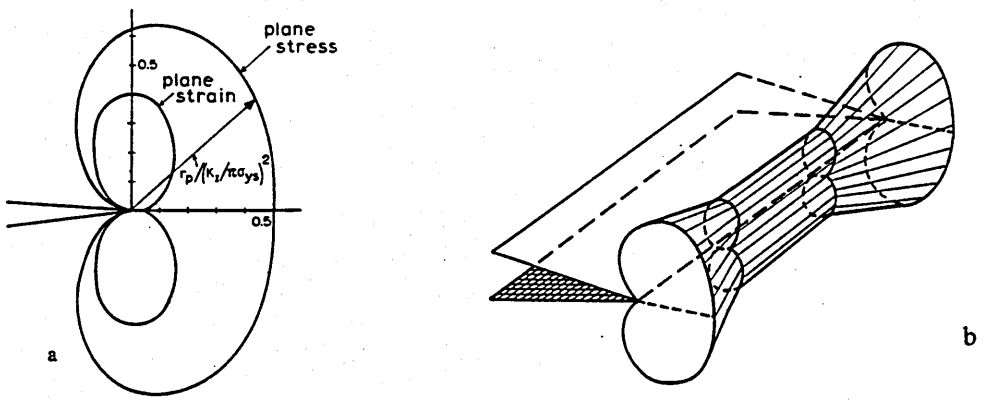

Figure 2.9a Plastic zone size according to Von Mises criterion (after Mc Clintock and Irwin, 1965).

b Three dimensional plastic zone (after Broek, 1974).

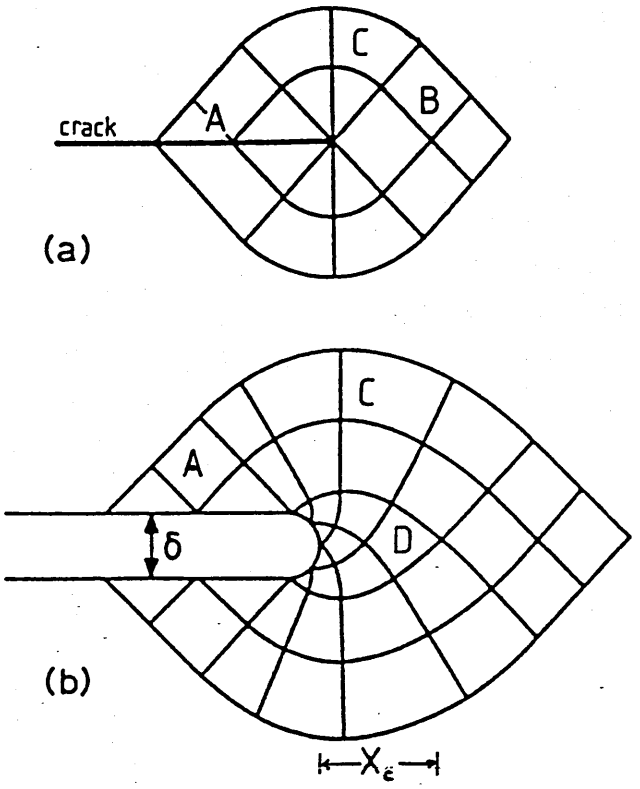

Figure 2.10a Prandtl slip line field near crack tip for plane strain yielding of a non-hardening material.

b Modification of slip line field in near crack tip due to progressive blunting with deformation (after Rice and Johnson, 1970).

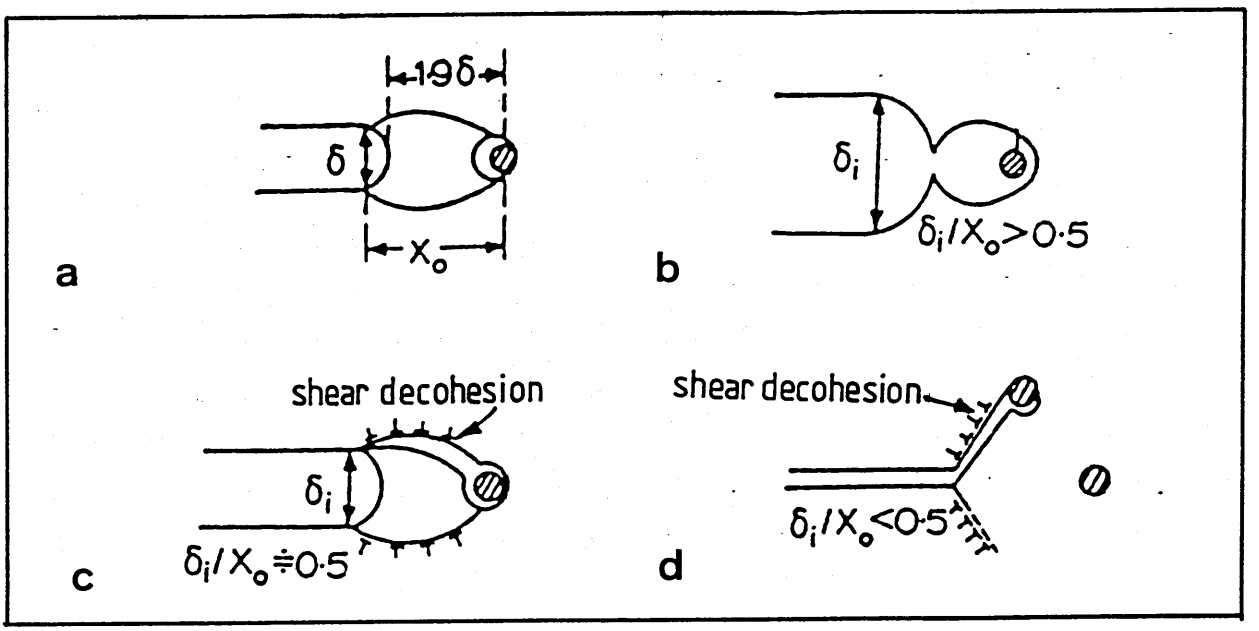

Figure 2.11 Schematic processes of crack growth: (after Clayton and Knott, 1976).

a Condition for void nucleation according to Rice and Johnson model.

b Void coalescence by internal necking in hardening matrix.

c Shear decohesion along the spiral lines.

d Shear decohesion at the tip of a sharp crack.

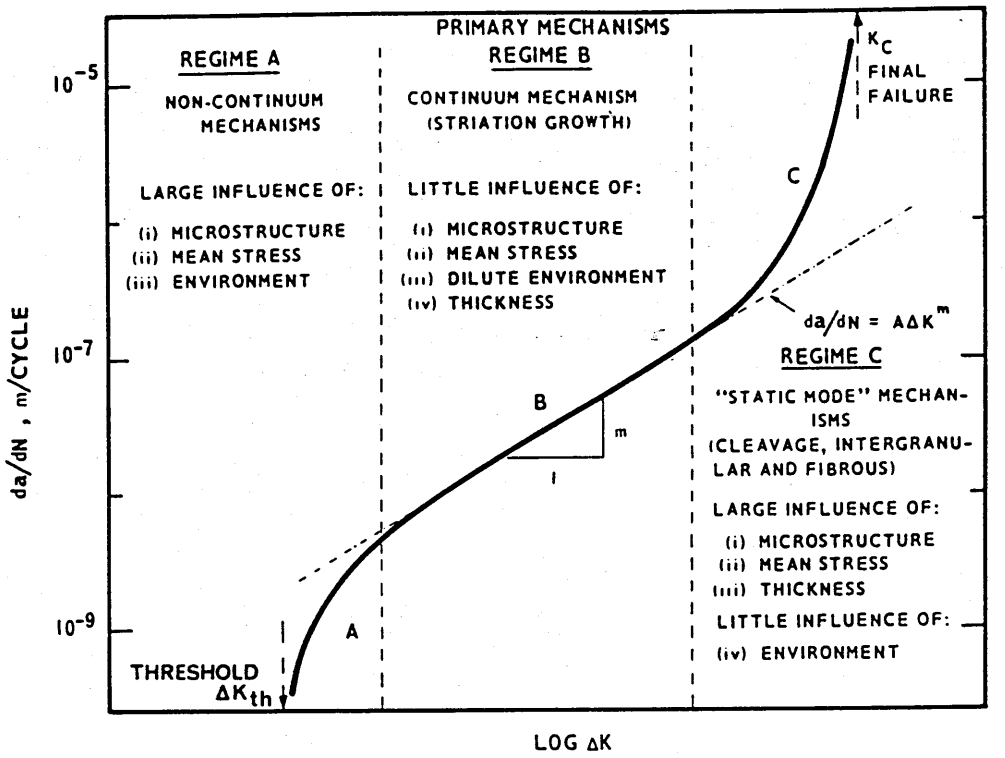

Figure 2.12 Sigmoidal variation of fatigue crack growth rate as a function of ΔK (after Lindley, Richards and Ritchie, 1976).

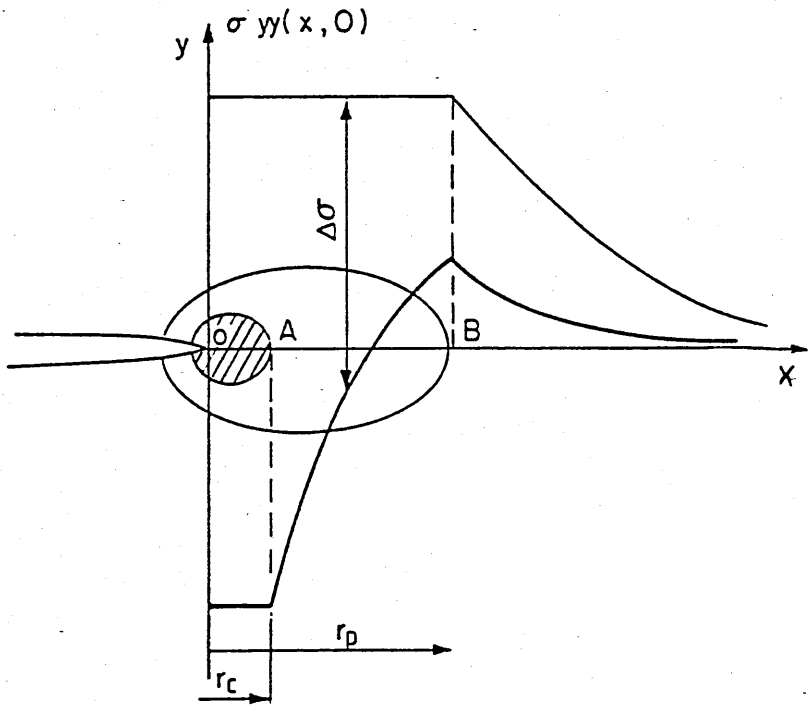

Figure 2.13 Schematic representation of the monotonic and cyclic plastic zones (after Bathias and Pelloux, 1973).

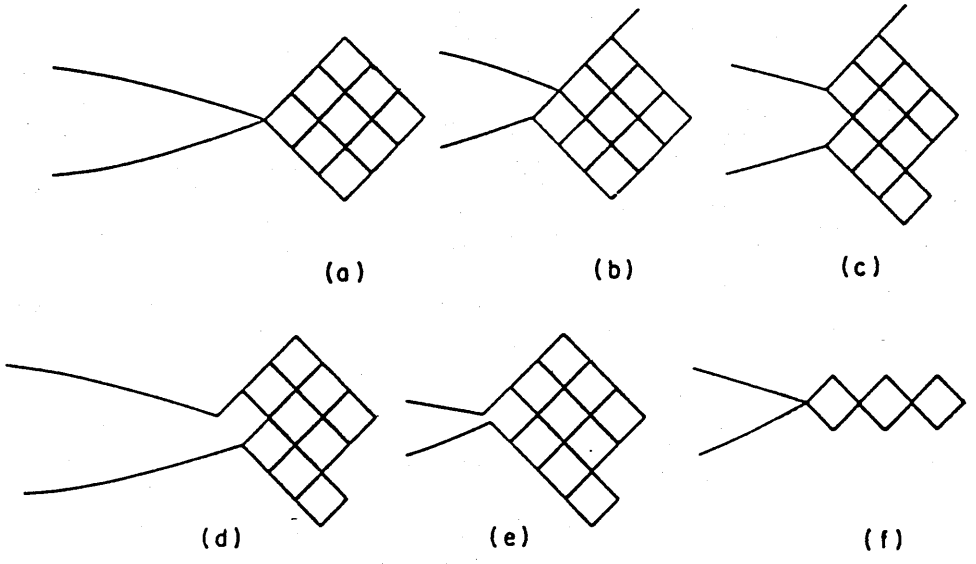

Figure 2.14 Geometric model of fatigue-crack growth by shear sliding (Laird-Smith-Neumann model). a) Initial configuration. b) Crack opened in tension with shear sliding on one slip plane above the crack plane. c) Followed by shear sliding on one slip plane below the crack plane. d) Crack unloaded with reversed shear sliding on slip plane of b. e) Followed by reversed shear sliding on slip plane of c; the crack has advanced. f) After a number of repetitions of the mechanism; note that fatigue striations have been formed. (after Weertman, 1979).

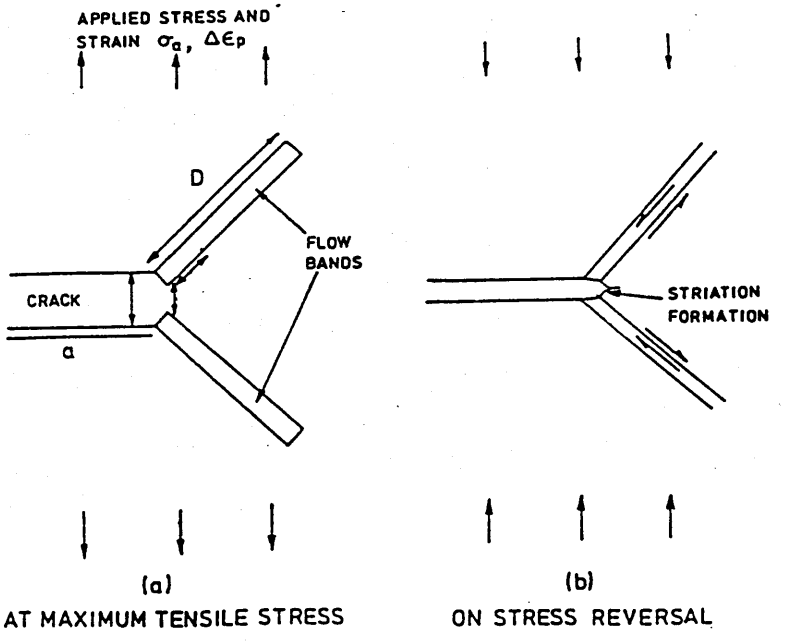

Figure 2.15 Schematic representation of Tomkins and Biggs (1969) model of fatigue crack growth.

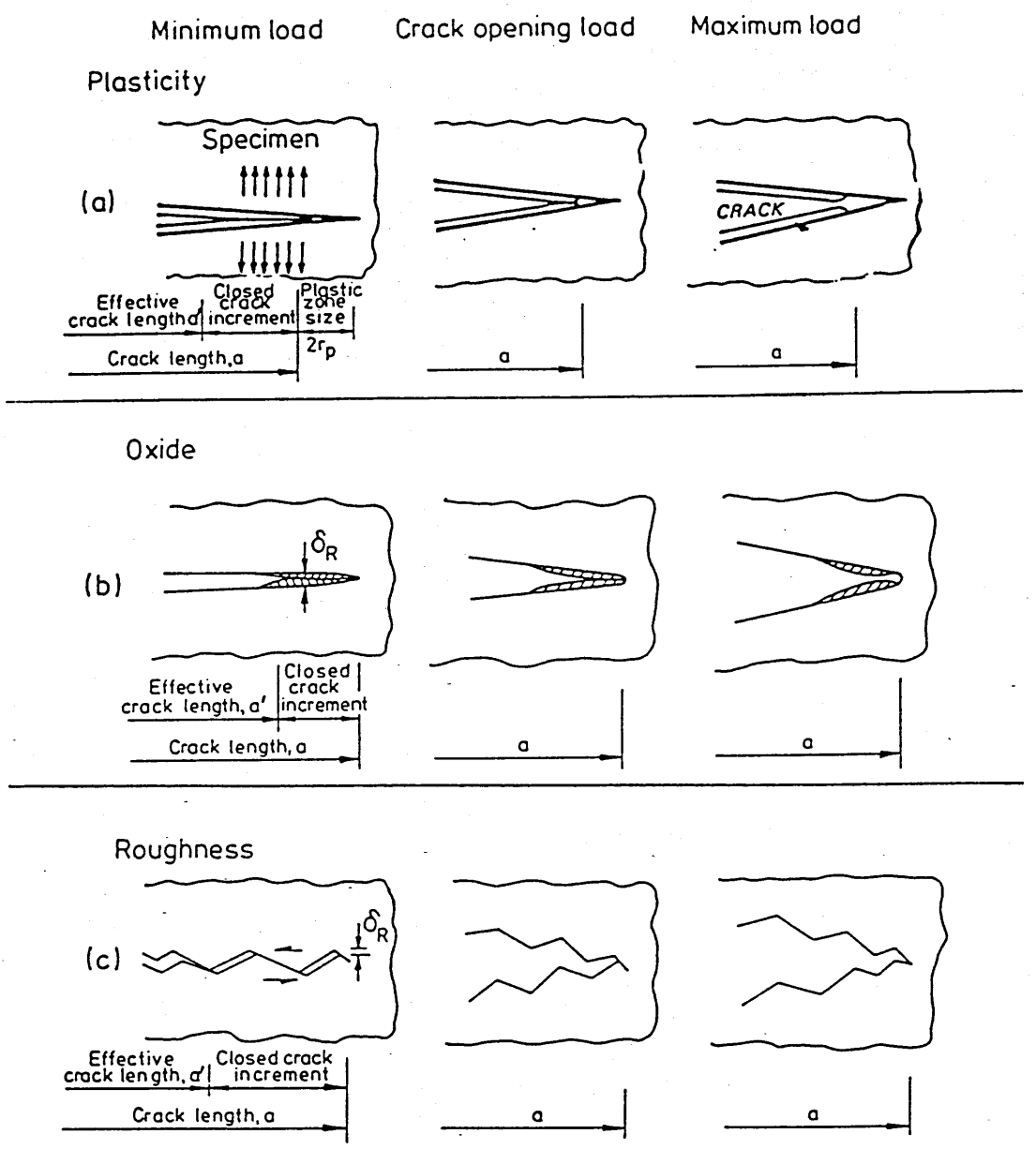

Figure 2.16 Three forms of crack closure. The residual displacement, δ_R, is the 'excess' material wedged between the crack flanks (after Fleck, 1984).

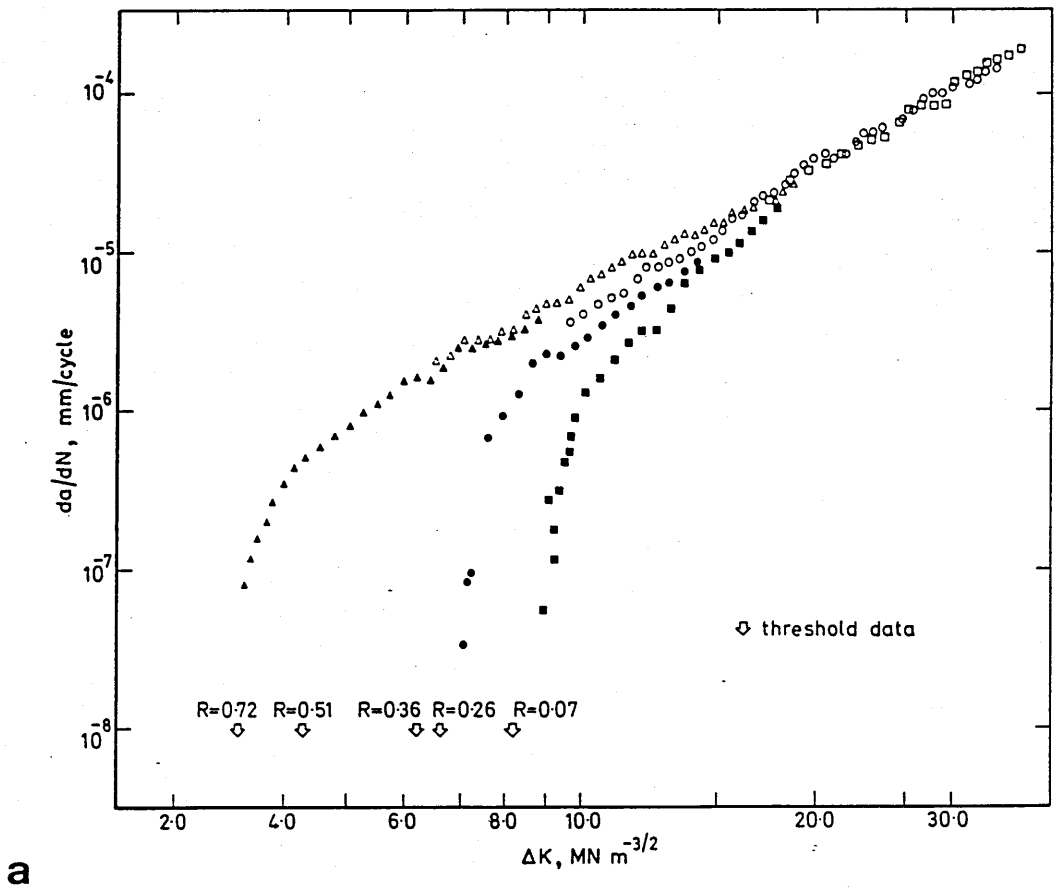

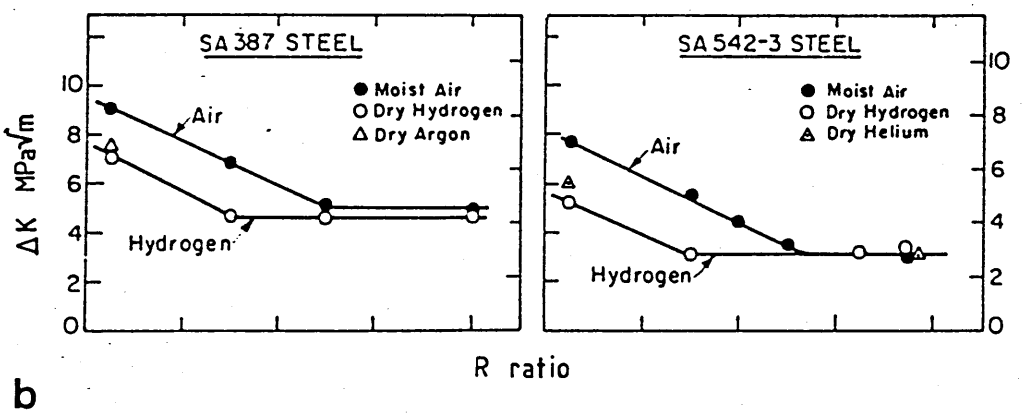

Figure 2.17a Influence of R-ratio (0.06-0.73) on fcg curves of medium-C/Mn pearlitic steel tested in laboratory air (Beevers et al., 1975).

b Experimentally-measured variation of threshold stress intensity ΔK_{TH} with load ratio (R) in two 2.5 Cr-1Mo steels tested in laboratory air (Ritchie and Suresh, 1980).

CHAPTER THREE

PLASTIC DEFORMATION, FRACTURE AND FATIGUE OF METALLIC GLASSES

Since their discovery by Duwez and co-workers (Duwez et al.,1960), structure and properties of metallic glasses have captured a worldwide attention. The interest in their mechanical properties started in 1970's with the development of rapid solidification techniques that produce sizeable specimens, uniform enough for these studies. As a result, metallic glasses attracted much scientific and technological interest because initial studies soon revealed their unique mechanical properties. It is now well established that metallic glass alloys are not only among the strongest and hardest metallic materials ever produced but also ductile and tough, in contrast to the oxide glasses. They also have a commercial potential since their production is less complicated and more economical than that of crystalline alloys having similar high levels of mechanical performance. Developments in the field of the mechanical behaviour of metallic glasses have been reviewed periodically (Pampillo, 1975, Masumato and Maddin,1975, Davis, 1978a, Li, 1982a).

The purpose of this chapter is to present a critical review of the existing information on the fracture and fatigue behaviour of metallic glasses. Since the static and cyclic fracture properties of these alloys have been generally discussed in terms of localized shear bands formed during room temperature deformation, it is appropriate to start the review by examining the deformation behaviour of metallic glasses.

3.1 Plastic Deformation

The observed plastic deformation modes in metallic glasses are classified relative to their glass transition temperatures, Tg. At temperatures between ~ 0.6-0.8 Tg, the deformation mode is termed "homogeneous" (Spaepen, 1977) and

occurs by a diffuse rearrangement of atoms (Argon, 1977). Deformation at ambient temperatures becomes inhomogeneous and takes place by the nucleation and propagation of discrete shear bands. This section is focussed on the inhomogeneous nature of plastic deformation in metallic glasses and reviews experimental studies of the properties of shear bands as well as the theoretical ideas proposed to interpret structural changes occurring during shear localization.

3.1.1 Inhomogeneous Plastic Flow and Strain Localization in Shear Bands

Shear bands were first observed by Masumato and Maddin (1971) in a $Pd_{80}Si_{20}$ alloy deformed by bending. On TEM examination of surface replicas taken from the tensile side of the sharply bent ribbons, it was found that shear bands about ~20 nm wide were formed parallel to the bending axis. The corresponding surface step heights measured using interference microscopy were as large as 200 nm. This shows that exceptionally high shear strains ~10 can be sustained by shear bands. Such enormous strains are indicative of intrinsic ductilities of metallic glasses and make a sharp contrast with the behaviour of oxide glasses which are brittle at ambient temperatures. This fundamental difference is explained by the predominantly metallic nature of bonds in metallic glasses (Pampillo, 1975, Argon, 1980).

In the same alloy, Leamy et al. (1972) also observed shear bands formed by bending. With increasing amounts of deformation, secondary shear bands nucleated at small angles to those initially formed parallel to the bending axis. These bands developed slip steps ~10 μm high without fracture. Similarly, secondary shear band formation was reported in a $Fe_{75}P_{16}C_9$ glass (Chen et al., 1973). However, in this alloy, cracks formed at the intersection of shear bands at low strains. Shear localization in a $Ni_{75}Si_8B_{17}$ alloy, which has a composition comparable to that used in the present study, was investigated by Zielinski and Ast (1983). In addition to the confirmation of the early observations, these

authors distinguished an initial homogeneous plastic deformation stage which preceded the nucleation of shear bands. Shear bands have been observed in a number of different metallic glass systems deformed by cold rolling (Takayama and Maddin, 1975, Pampillo, 1975), by wire-drawing (Takayama,1979), by hardness indentation (Koster and Hillenbrand, 1981) and by uniaxial compression (Pampillo, 1972, Pampillo and Chen, 1974).

While local displacements in single shear bands can be very large, the macroscopic ductility in tension remains very low, typically 0.1 % (Davis and Kavesh, 1975). Only a few isolated slip steps are found near the shear band on which failure took place. It appears that a tensile instability occurs at small macroscopic strains. On the other hand, in compression or rolling, the operation of multiple shear bands results in large macroscopic strains as well as local ductility. This was shown by Takayama and Maddin (1975a): in rolling of $Ni_{63}Pd_{17}P_{20}$ amorphous ribbons of 100 μm thick, substantial reductions in thickness up to 40 % could be achieved in spite of the very high flow stress of the alloy.

Once formed, shear bands persist and further plastic deformation occurs preferentially along these bands. In an early experiment performed by Pampillo and Chen (1974) a cylindrical specimen of $Pd_{77.5}Cu_6Si_{16.5}$ was deformed in compression and the surface shear bands were photographed. After unloading, the surface of the specimen was electropolished to eliminate any stress concentrators associated with the shear offsets. On subsequent reloading, it was found that only the previously formed shear bands were active. Similar observations were made by Pampillo (1975) and by Li (1981) in reverse bending experiments on $Pd_{83}Si_{17}$ and $Fe_{40}Ni_{40}P_{14}B_6$ alloys, respectively. Almost all the shear steps formed during forward bending operated in reverse when the direction of the applied force was reversed.

Several studies indicated that the structure of the material inside the shear bands differs from the matrix. Pampillo (1972) found that shear bands in a

deformed Pd-Si glass could be preferentially etched. In this experiment, the specimen surface was polished to remove the deformation bands and etched in a 25 pct nitric acid solution. The etching sensitivity of shear bands was later confirmed by Chen et al. (1973) and Li (1982b) who concluded that the chemical potential inside the bands is higher than that in the rest of material. Further information concerning the high energetic state of the deformed material was provided by the differential scanning calorimetric observations of cold rolled Pd-Cu-Si ribbons by Chen (1976). On heating of rolled ribbons, energy was released over a broader temperature range relative to undeformed material showing that deformation caused energy to be stored in the shear bands. More direct evidence for structural changes during deformation comes from X-ray diffraction studies of a wide range of metallic glasses including $Fe_{40}Ni_{40}P_{14}B_6$ (Walter et al.,1977), $Pd_{77}Si_{17}Cu_6$ (Waseda et al., 1979), and $Ni_{81}P_{19}$ (Waseda and Egami, 1979). With this method, a clear difference in the scattering behaviour of the diffracted beams from the shear bands and the surrounding material was obtained. However, it was not possible to interpret these differences to get a precise picture of the inhomogeneous structure.

As pointed out by Spaepen (1974) and Argon (1979), an important feature of the plastic deformation in metallic glasses is the dilatation of shear bands. Megusar et al. (1982) measured the length changes occurring due to crystallization in deformed and undeformed $Pd_{77.5}Si_{16.5}Cu_6$ cylinders and took this difference as a measure of the deformation induced dilatation of glass. By relating these measured dilatations to the number of shear bands and their average shear offset, they calculated residual dilatations as large as 20 % for compressive strains of the order of 70 %. Using a hydrostatic weighing method , Deng and Lu (1983) measured density changes occurring in the same alloy during cold drawing. Density reduction came to a steady state at a thickness reduction of 40 % and did not change with further reduction. However, at this deformation level, dilatations measured by Deng and Lu were about an order of magnitude smaller than those measured by Megusar et al.. Again for the same Pd-Si-Cu metallic glass, Cahn et al.

(1983) and Argon et al. (1985) reported density reductions due to dilatation of shear bands. Different measurement techniques were used by these investigators and large discrepancies exist between the published data.

There also exists some evidence for void formation inside the deforming shear bands. These were observed by Pampillo and Chen (1974) inside a 'pronounced' shear band in a compressed Pd-Cu-Si glass. Voids were also detected at the tip of a crack nucleated in a shear band during tensile loading of a $Ni_{55}Pd_{35}P_{10}$ amorphous alloy in an electron microscope (Takayama and Maddin, 1975b). During stable crack growth, the void and crack grew slowly and joined together. Finally, a large number of voids formed suddenly at the crack tip and the material failed by local necking of the ligaments in between the voids. Donovan and Stobbs (1981) examined the structure of shear bands in two metallic glasses, $Ni_{76}P_{24}$ and $Fe_{40}Ni_{40}B_{20}$, by means of TEM and observed a large number of voids inside the bands. According to these authors, voids were not nucleated during deformation but produced by relaxation when deformation stopped.

In summary, at ambient temperatures, plastic deformation in metallic glasses is inhomogeneous and occurs by the formation of localized shear bands which accommodate shear strains as large as 10, without cracking. The operation of multiple shear bands under the constraints of bending, compression and cold rolling results in large macroscopic strains as well as high local ductility. It appears that there is no mechanism in metallic glasses corresponding to work hardening in crystalline alloys. Several experimental results suggest that substantial structural changes occur within the shear bands: they are preferentially etched, they show different electron diffraction properties and they may dilate during deformation.

3.1.2 Micromechanisms of Inhomogeneous Plastic Deformation

The features of plastic deformation summarized in the previous section have been observed in a number of metallic glass systems, so they appear to be insensitive to the chemical composition of the alloys. This suggests that a deformation micromechanism common to all metallic glasses exists. For crystalline materials, the basic deformation mechanism is the movement of dislocations. However, in amorphous metals, the nature of the micromechanism responsible for the plastic deformation remains obscure. Direct experimental studies of atomic level deformation processes are very difficult in metallic glasses since the absence of long range order precludes the use of the conventional experimental techniques such as lattice imaging by an electron microscope. However, in recent years, several models of the micromechanisms in metallic glasses have been proposed and theories of inhomogeneous plastic deformation have been advanced.

To explain the inhomogeneous nature of plastic deformation, a purely phenomenological approach has been made by Masumato and Maddin (1971) who attributed deformation to an enhancement of viscous flow in regions of large macroscopic stress concentrations. Following this argument, Polk and Turnbull (1972) suggested the possibility that at temperatures below the glass transition temperature, plastic flow could destroy the compositional and structural short range order. The destruction of compositional short range order should lead to an increase in the number of metal-metal bonds across the sheared surface at the expense of stronger metal-metalloid bonds. The structural disorder created within the shear bands was assumed to be in the form of an increase in the average atomic volume (or dilatation) associated with plastic deformation. As a result of the destruction of compositional order and dilatation, deformation within the bands occurs at stresses lower than the surrounding matrix.

Leamy et al. (1972) suggested that strain localization could be due to the heating effect produced by plastic deformation, i.e. by adiabatic shear. The increase

in temperature within a deforming band was considered to be high enough to produce softening of the glass and promote further slip.

Spaepen and Turnbull (1974) proposed another phenomenological model based on the concepts of the Free Volume Theory (Cohen and Turnbull,1959, 1961, 1970). The free volume of an atom is defined as the part of its nearest neighbour cage in which the atom can move around without raising the energy of the system. The increase in the free volume in the regions of the matrix "dilated" by stress concentrators decreases the local shear viscosity sharply which results in the formation of a shear band. A quantitative development of this model has been advanced by Spaepen (1977) who assumed that local shear stress is produced by atomic jumps in the region of excess free volume. In the steady state, a dynamic equilibrium is maintained between stress driven nucleation and diffusional annihilation of free volume. At ambient temperatures where the diffusive decay of these dilatations is very slow, sheared regions retain a large non-equilibrium component of shear induced excess free volume. However, no atomistic details of these mechanisms have been developed. On the other hand, specific atomic level events during deformation were considered by Argon (1979) who ascribed the deformation as two different processes of localized shear tranformations. These transformations are a sharp shear translation which occurs in between two relatively close-packed layers of atoms and a diffuse rotational exchange of atoms. Both of the events were observed during an analogue experiment performed on soap bubble rafts (Argon and Kuo,1978). This model consisted of bubbles of two different radii deforming under controlled shear strain imposed by a frame. The sharp shear event was equivalent to the nucleation of a dislocation pair separated by ~ 5 atom diameters; the analogous event in three dimensions would be the nucleation of a dislocation loop (Fig.3.1). The diffuse shear event occurred where the local packing was somewhat looser. The shape of this region was circular again covering ~ 5 atoms. Argon's model predicts that the latter event is associated with large free volumes and dominates at high temperatures while the former is considered to be associated with small

free volumes and dominates at low temperatures. Once a dislocation loop nucleates at room temperature, plastic deformation proceeds by autocatalytic spreading out of free volume at the edges of a shear band.

A different approach was followed by Gilman (1975) who postulated the existence of dislocations with Burgers vectors which fluctuate along the dislocation lines and whose average magnitude is equal to the average nearest neighbour separation of atoms in the glass. Although Ashby and Logan (1973) showed that such dislocations are a possibility in tetragonally bonded network glasses, their existence as well defined defects is questionable in metallic glasses (Spaepen, 1978). A macro-dislocation description of plastic deformation in metallic glasses has been put forward by Li (1978) who described the stress and strain fields of shear bands terminating inside a sample as a "Somigliana" dislocation. The Burgers vectors of these dislocations vary in magnitude and direction and are much larger than nearest neighbour separation. Macro dislocations are considered to be formed by a series of excess volume elements and the deformation proceeds by repeated nucleation of excess free volume sites at the tip of a macro-dislocation (which is basically a shear band). In this sense , this model is similar to Argon's model.

Because of the limitations arising from the absence of the long range order in amorphous solids, direct experimental verification of these models is very difficult. However, such studies have been carried out using computer simulations. Results of some computer simulated models (Maeda and Takeuchi, 1977, Yamamoto et al., 1979) are in good agreement with the bubble raft model (Argon and Kuo, 1979) and show a correlation between local density fluctuations and shear band nucleation. Others (Kobayashi et al.,1981, Srolovitz et al.,1983) suggest that shear bands are nucleated from the regions of high shear stresses formed during deformation and act as stress concentrators to enhance local viscous flow.

3.2 Fracture

3.2.1 Strength and Tensile Fracture (of unnotched specimens)

Metallic glasses are extremely strong materials. For palladium based ternary alloys, tensile strengths of the order of 1.5 GPa were measured (Davis and Kavesh, 1975). Typical tensile strengths of Ni, Co or Fe based alloys vary between 2-4 GPa. For example, a simple $Fe_{80}B_{20}$ alloy discovered by Ray and Kavesh (1977) has a strength of 3.6 GPa. The highest tensile strength (4.5 GPa) was reported by Ray (1979) in a $Fe_{60}Cr_6Mo_6B_{28}$ metallic glass - which is probably the strongest metallic material known-. Studies on tensile strengths and fracture behaviour of metallic glasses have been surveyed by Pampillo (1975), Davis (1978) and Li (1982). The results are collected in Table 3.1 which indicates that beside their high tensile strength, these alloys are also very hard but have lower elastic moduli than crystalline alloys.

Thin metallic glass specimens, when tested in a conventional tensile testing machine, exhibit very little macroscopic ductility. Their stress-strain curves are almost linear up to failure. At room temperature, tensile plastic elongations (measured on stress-strain curves) have been reported to be between 0.1 and 0.5 % (Masumato and Maddin, 1971, Pampillo, 1975). However, this apparent brittleness is due to the fact that the energy required for inhomogeneous deformation and fracture is much smaller than the total elastic energy stored in the machine and the sample. Tests performed using a "hard" tensile testing machine with a very high stiffness designed by Murata et al. (1978) demonstrated that metallic glasses show extensive tensile ductility before failure. In this particular experiment, $Pd_{80}Si_{20}$ ribbons fractured by a perfect shear-off mechanism.

The yield stress of a metallic glass is only a few percent lower than its tensile strength. As soon as yielding begins, it becomes confined to a few shear bands. Further deformation and failure takes place in one of these bands. Among the early studies, Logan and Ashby (1974) found that in $Ni_{76}P_{24}$ wires, tensile

fracture occurred on a plane at 45 degrees to the wire axis. This is the expected sliding-off angle in rigid-plastic materials. Similarly, Leamy et al. (1971) and Davis (1975a) observed that in ribbons of rectangular section, fracture took place on a plane of maximum shear stress and zero width strain (i.e. on a plane at ~45 degrees to the loading axis and thickness direction). Measurements made by Megusar et al. (1978) and Kimura and Masumato (1983) indicated that the angle of the shear plane on which fracture took place was inclined at 55 ± 2 degrees to the tensile axis.

The ductile nature of the tensile failure is also manifested on the fracture surfaces. A detailed description of the fracture surfaces of amorphous $Pd_{77.5}Si_{16.5}Au_4$ alloys was given by Leamy et al. (1972) who observed two morphologically different zones. These were a smooth and featureless zone and a zone containing a vein pattern. The smooth zone formed during the initial localization of shear into the band. After a characteristic shear offset was achieved, final fracture occurred catastrophically leaving behind the vein pattern. Veins were protrusions on both fracture surfaces. Local necking at triple point junctions of the vein pattern showed pointed and curved filaments ~ 1 μm in height. Fracture surfaces containing similar features were also observed in $Ni_{60}Nb_{40}$ (Giessen et al.,1976), in various Fe base glasses (Davis, 1976), in $Ni_{55}Pd_{35}P_{10}$ (Takayama and Maddin, 1976b) in $Pd_{80}Si_{20}$ (Megusar et al., 1978).

Leamy et al. (1972) proposed that the vein pattern occurred as a result of adiabatic heating generated by localized deformation. Masumato and Maddin (1975) presented a series of simulation experiments in which two glass slides separated by a thin layer of fluid grease have been pulled apart. The separation started at the edges of glass slides and propagated in an unstable way by forming "fingers" which moved into the viscous medium. This mechanism is known as the Taylor meniscus instability (Taylor,1950). It occurs when an interface of a fluid is moved in the direction of its convex curvature by a suction gradient in the more viscous fluid. The interface between the two immiscible liquids becomes unstable and fingers from the less viscous fluid penetrate into the more viscous one. The

similarity between the vein pattern and the "fingers" seen in the simulation experiment led Masumato and Maddin (1975) and Pampillo and Reimschuessel (1974) to suggest that Taylor instability is responsible for the final failure of metallic glasses once a shear offset formed. This resemblance has also been considered as evidence of the formation of a fluid layer inside the "dilated" shear bands by Spaepen and Turnbull (1974) and by Spaepen (1977) who argued that the instability in the interface motion which produced the vein pattern is the fastest mode by which the two solid surfaces could be separated for a given viscosity of the fluid layer. A qualitative analysis of this situation was presented by Argon and Salama (1976). By combining a perturbation analysis of the flow of a fluid with the solution for strains and stresses in the tip region of shear offset (modelled as a blunt crack), they determined a relationship between critical crack opening displacement and the steady state wavelength for the formation of fingershaped interfaces.

It is worth noting that fracture by a Taylor instability mechanism has been observed in various metallic and polymeric materials, namely in the fibrillar break-up of adhesive tapes (Argon and Salama, 1976), in the intergranular fracture by diffusional flow at elevated temperatures in metals (Taplin and Wingrove, 1967) and in the production of crazes in glassy polymers (Argon, 1980).

3.2.2 Fracture Toughness

The fracture of metallic glass specimens containing cracks and notches has been studied in a few Ni-Fe and Pd based compositions. Fracture toughnesses of $Ni_{48}Fe_{29}P_{14}B_6Al_3$, $Ni_{39}Fe_{38}P_{14}B_6Al_3$ and $Ni_{49}Fe_{29}P_{14}B_6Si_2$ alloys were investigated by Davis (1975). Specimens were tested either in single edge notched tensile (SENT) or centre cracked tensile (CCT) configurations. The relative proportions of fatigue precrack and unstable fracture crack lengths were determined by SEM measurements. The average toughness values (K_C) for these alloys were 37, 19 and 9 MPa$\sqrt{m}$ respectively. They seemed to decrease with the

increase in the thickness of the specimens. The thicknesses, widths and the yield stresses of the specimens were such that plane strain conditions were probably met only for Ni_{49} glass. (It was assumed that the plastic zone size at the crack tip was equal to one third of the specimen thickness in this condition). The K_c value obtained for Ni_{49} glass was thus considered a valid plane strain toughness value K_{Ic}. Fracture surfaces of metallic glass ribbons failed under plane strain conditions exhibited an area of chevron pattern in the middle of the surfaces. On either side of it were shear lips 2-4 μm wide and oriented at about 45 degrees to the tensile axis.

Subsequent work (Davis, 1978) on a higher strength $Fe_{78}Mo_2B_{20}$ alloy gave K_c values ranging between 12-44 MPa$\sqrt{m}$ at a given specimen thickness. It was observed that 51 μm thick samples could fail either by 45 degrees shear rupture (high toughness) or by low energy square fracture associated with the chevron pattern. The specimens exhibiting low toughness had been subjected to lower cooling rates during solidification and thus had a higher susceptibility to crystallization (Davis, 1979).

Ast and Krenitsky (1976) measured the fracture toughness of $Ni_{40}Fe_{40}B_{14}B_6$ specimens after growing fatigue cracks from centrally located holes. A K_c value of 13 MPa$\sqrt{m}$ was calculated from the maximum cyclic load and fatigue crack length at failure. The size of the plastic zone at the crack tip determined from optical interference microscope images of surface replicas was 13 μm, i.e. 1/4 of the specimen thickness indicating that the measured K_c value approached the plane strain value K_{Ic}.

A more elaborate study to establish the relationship between the stress intensity factor K_c and crack tip parameters was presented by Waku and Masumato (1981). Fatigue cracks 0.3-2 mm long were grown at the notch tips of $Ni_{78}Si_{10}B_{12}$ amorphous ribbons. Specimens were loaded incrementally up to failure and the increase in the plastic zone size (r_p) and crack tip opening displacement (CTOD) were measured by an optical microscope. Specimens showed

a transition from plane strain to plane stress state in the early stage of plastic deformation (marked by the changes of the slopes of rp vs load curves) and a great part of plastic deformation and fracture occurred under plane stress conditions. The critical value of CTOD was 5.5 μm at the fracture which corresponded to $K_c = 45$ MPa$\sqrt{m}$.

Kimura and Masumato (1983) investigated fracture behaviour of notched $Pd_{78}Cu_6Si_6$ specimens. SENT specimens developed a local plane stress plastic zone at the notch root and failed following the propagation of mode III type cracks in a strong shear band within the plastic zone. Double edge notched specimens behaved differently. During tensile loading, they failed following the general yielding of the section in between the notches. Shear bands in the yielded zone formed patterns reminiscent of Prandtl slip line field patterns in elastic rigid plastic solids of the same geometry.

In thin metallic glass ribbons which fail in plane stress conditions, a certain amount of stable crack growth is expected to occur before the instability. Crack growth resistance curves (R-curves) of metallic glasses were recently studied by Henning et al. (1985). CCT specimens were prepared from a $Fe_{40}Ni_{40}B_{20}$ glass (12 mm wide, 40 μm thick), initially fatigued to different crack lengths and then loaded upto rupture. Stable crack extension Δa was determined by SEM. Crack resistance K_R vs Δa curves indicated that a stable crack extension up to 45 μm was achieved before the specimen failed at a stress intensity of about 50 MPa$\sqrt{m}$. Henning et al. also observed that the critical stress intensity factor K_c was a function of the initial crack length a_i. K_c vs a_i curves showed that the maximum K_c value of 60 MPa$\sqrt{m}$ occurred at $a_i = 0.4$ mm.

3.2.3 Tear Energy

A different approach to characterizing the toughness of metallic glasses was made by Kimura and Masumato (1975) who applied to these alloys "trouser leg"

tear tests originally developed to measure the fracture resistance of rubbers (section 2.1.2.2). The tear energies (Γ) of 1.5 mm wide, 30 μm thick amorphous $Fe_{80}P_{13}C_7$, $Pd_{80}Si_{20}$ and $Cu_{57}Zr_{43}$ specimens were obtained from the average tear forces using an expression proposed by Rivlin and Thomas ($\Gamma = 2F/t$, Equation 2.14). The tear energies for these alloys were 11, 4, 6 kJ/m^2 respectively. These were significantly higher than those of inorganic glasses and glassy polymers and comparable to those of crystalline metallic alloys in agreement with the observations of Davis (1975) made on the basis of critical stress intensity factors.

The tear energy contains essentially the work performed by plastic deformation at the crack tip, γ_p, and the work performed in the formation of new surfaces, γ_s. In their latter study, Kimura and Masumato (1981) reported that the visual appearance of the plastic zone in a $Pd_{80}Si_{20}$ alloy was a simple shear band extending ahead of the crack tip on the plane of maximum shear stress. Based on this observation, they concluded that the plastic work term, γ_p, in Equation 2.15 ($\Gamma = \gamma_s + \gamma_p$) is solely due to mode III type shear deformation. As the surface energy, γ_s, of common metallic glasses is of the order of $10^{-3} kJ/m^2$ Kimura and Masumato suggested that almost all of the tear energy was consumed in the formation of a mode III type shear band at the crack tip.

As a function of the speed of tearing , the tear energy of $Pd_{73}Si_{20}Fe_7$ glass increased from 4 kJ/m^2 at 0.01 mm/min to 7.6 kJ/m^2 at 10 mm/min and then, decreased to 6 kJ/m^2 at 100 mm/min. Similar behaviour was found at liquid nitrogen temperature. The corresponding values were 6.2, 9.6 and 6.5 kJ/m^2 respectively. The force-extension curves were also different. At low speeds such as 0.1 mm/min, the curve was smooth and showed a steady-state behaviour, but at high speeds such as 20 mm/min, the curve was serrated. As a function of temperature, the tear energy decreased with increasing temperature, similar to the behaviour observed in some polymers (Sims ,1975). Tear energy was also a function of ribbon thickness, decreasing linearly with the specimen thickness.

3.3 Fatigue

Fatigue properties are important features of metallic glasses proposed for practical use such as reinforcement fibres in rubber tyres and transmission belts. Furthermore, because of their relatively simple metallurgical microstructure - without any crystallographic features and complications like grain boundaries and second phase particles - they appear to be suitable materials for testing existing continuum theories on initiation and propagation of fatigue cracks. Surprisingly, however, the expected scientific and industrial interest in the subject has led to only a few elementary studies.

3.3.1 Fatigue Crack Initiation, S-N Characteristics

The first S-N curve of metallic glasses was obtained by Ogura et al. (1975a) who did fatigue tests (R = 0) on $Pd_{80}Si_{20}$ ribbons. The shape of the S-N curve was qualitatively similar to that of common crystalline and polymeric materials. The curve showed a fatigue limit (σ_∞) at σ_{max} = 220 MPa. This limit was only about 15 % of the tensile strength of the alloy. The value of the ratio of fatigue limit to the tensile strength (σ_F = 1500 MPa) of the amorphous alloy was lower than those of conventional high strength alloys. For example, the fatigue limit observed in a vacuum melted 4340 stainless steel (σ_F = 1300 MPa) is 690 MPa (Cummings et al., 1957). Thus, σ_∞/σ_F ratio in this alloy is 0.53, about three times larger than that of amorphous $Pd_{80}Si_{20}$. Later studies by Davis (1976) and by Frommeyer and Seifert (1981) on different Fe-Ni and Fe base alloys confirmed that such a low fatigue limit is not only peculiar to $Pd_{80}Si_{20}$ but is a common feature of metallic glasses. From Table 3.2 which summarizes some of the published aspects of S-N curves, it is seen that the σ_∞/σ_F ratios of metallic

glasses vary between 0.06 and 0.15. Koster and Hillenbrand (1980) attributed this behaviour to the lack of cyclic strain hardening in metallic glasses.

The influence of specimen and testing configurations on the fatigue lives of some Ni-Fe base metallic glasses was studied by Davis (1976). The fatigue lives of the alloys were found to be strongly influenced by the specimen geometries. The longest life-times were achieved by specimens with a reduced gauge section. The lives of specimens with centrally located holes were about two times shorter.

Ogura et al. (1975) observed that in a $Pd_{80}Si_{20}$ alloy, cracks initiated in the vicinity of an inclusion or a void. These were possibly casting defects generated during rapid solidification. The final fracture occurred on a 45 degree plane to this axis and exhibited a typical vein pattern. Fractographic observations made by Davis (1975) showed the existence of periodic striations in a $Ni_{39}Fe_{38}P_{14}B_6Al_3$ metallic glass. In this specimen,fatigue cracks were initiated near one of the narrow edges of the specimen and they were not associated with an internal defect. Outside the striated area, the morphology changed abruptly to a chevron pattern indicating typical unstable crack propagation in this low toughness alloy.

The formation of surface cracks in a $Fe_{78}Mo_2B_{20}$ glass was studied by Frommeyer and Seifert (1981). In this alloy, shear bands were formed at the edges of the ribbons after few cycles which then acted as crack initiators. These bands were at 45 degrees with the tensile axis suggesting that fatigue crack initiation in metallic glasses occurs by a mechanism similar to that proposed by Forsyth (1961) for ductile crystalline alloys. Once nucleated, cracks propagated on a plane perpendicular to the loading axis.

3.3.2 Fatigue Crack Propagation

Current knowledge on the fatigue crack propagation in metallic glasses is based largely on an early study of Ogura et al. (1975 b) on a $Pd_{80}Si_{20}$ alloy tested at different constant stress amplitude levels at $R = 0$. Crack growth in this alloy

occurred by the formation of striations which became coarser with the increase in the crack length. Ogura et al. observed the presence of a plastic zone extending from the tip of a growing crack. The plastic zone consisted of a large number of shear bands. It was apparent that the crack propagation on the specimen surface occurred along these bands. According to microinterferometric studies at high cyclic stresses, surface step heights of these bands could be as large as 0.5 μm. It was suggested that the fatigue crack growth rate (da/dN) was controlled by K_I and between the range $15 \leq K_I \leq 35$ MPa$\sqrt{m}$, it could be expressed as: ($da/dN = CK_I^m$, $m \approx 4$). Although the minimum crack growth rate determined in this study was about 5×10^{-6} mm/cycle, from the sigmoidal shape of da/dN vs K_I curves, there was evidence for a threshold stress intensity $K_{TH} \approx 5$-7 MPa$\sqrt{m}$.

The rate of fatigue crack propagation in glassy $Ni_{39}Fe_{38}P_{14}Al_3$ ribbons was determined by Davis (1975). Specimens in CCT configurations were tested at an R-ratio of 0.33. Measured crack growth rates were expressed as a function of cyclic stress intensity factor ΔK by a Paris-Erdogan Equation with an exponent m = 2.25 (Equation 2.34). A similar power law relationship was found between striation spacings and ΔK. However, striation spacing exceeded crack growth rate by a factor of ~6.

Crack propagation data for Ni and Fe-base metallic glass alloys have also been reported by Ast and Krenitsky (1976), Hillenbrand (1983) and Chaki and Li (1984) who showed that the cyclic stress intensity exponent, m (in the Paris-Erdogan Equation) for these alloys fall within a relatively narrow range of 2-4.

Recently, Chaki and Li (1984) studied the effect of overloading on two Co-Fe-Mo based commercial metallic glasses using CCT specimens 25 mm wide and 30 μm thick. An overload of x 2 was applied to the cracks propagating under constant stress conditions (R = 0.1). After 5 overload cycles, a sharp decrease in crack growth rate was observed and it took about 5×10^3 cycles to restore crack growth values to normal. This was due to the blunting of the crack front.

In summary, fatigue behaviour of metallic glasses bears many similarities to

that of ductile crystalline alloys as revealed by their growth by striation formation and by their crack tip plasticity. However, they have a much lower fatigue limit compared to the high strength conventional alloys and they have faster crack growth rates, probably as a consequence of the lack of work hardening inside the cyclic shear bands.

3.4 Summary

In metallic glasses, deformation at ambient temperatures occurs by the nucleation and propagation of localized shear bands. Individual bands can sustain extensive shear strains up to ~10. Shear bands undergo a substential structural change during deformation; for example, when shear bands exist in the material, further deformation occurs preferentially along these bands, they are preferentially etched and show different electron diffraction properties. It is not conclusively known whether these bands are dilated during deformation. However, current theories on the micromechanism of localized deformation suggest that the flow nucleates at free volume sites and propagates by autocatalytic spreading of excess free volume at the tip of a shear band which is sometimes modelled as a macrodislocation.

Although they are among the strongest materials known, the absence of work hardening leads to the mechanical instability of the metallic glass ribbons when loaded in uniaxial tension. Clear evidence of plastic flow in this case can only be seen in the vein pattern on the fracture surfaces. There is some evidence that vein patterns are formed by a Taylor meniscus instability.

Fracture toughness values of metallic glasses vary between 10-70 MPa$\sqrt{m}$ depending on the composition, purity and thickness of a particular specimen. During tensile loading of cracked specimens, plastic deformation concentrates in the plastic zone at the crack tip. Mode III type shear failure is the common fracture mode when a critical crack tip opening displacement or plastic zone size is reached. It has been suggested that the "trouser leg" tear test is a convenient

testing method to determine the toughness (fracture resistance) of metallic glasses.

S-N curves of metallic glasses show a distinct fatigue limit which is much lower than those of the high strength crystalline alloys. At high ΔK levels, fatigue crack growth occurs by the formation of ductile striations.

Table 3.1 Mechanical Properties of Metallic Glasses

	σ_F (GPa)	E(GPa)	E/σ_F	Hv	Ref.
$Pd_{80}Si_{20}$	1.34	88	65	490	Masumato &Maddin (1971),Davis(1976a)
$Pd_{77.5}Si_{16.5}Cu_6$	1.60	90.7	57	–	Pampillo &Chen (1974).
$Ni_{75}Si_8B_{17}$	2.7	105	39	860	Masumato (1977)
$Fe_{78}Si_{10}B_{12}$	3.4	128	38	910	Masumato (1977)
$Fe_{80}B_{20}$	3.63	166	46	1079	Davis &Hasegawa (1981)
$Ni_{36}Fe_{32}Cr_{14}P_{12}B_6$	2.73	141	52	863	Davis &Hasegawa (1981)

Table 3.2 S-N characteristics of metallic glasses

Alloy	σ_∞ MPa	σ_F MPa	σ_∞/σ_F	R	Ref.
$Pd_{80}Si_{20}$	400	1340	0.21	0.0	Ogura et al.,(1975)
$Pd_{77.5}Cu_6Si_{16.5}$	460	1470	0.31	0.33	Davis, (1976)
$Ni_{49}Fe_{29}P_{14}B_6Si_2$	417	2430	0.17	0.33	Davis, (1976)
$Fe_{41}Ni_{41}B_{18}$	600	2500	0.24	-	Hillenbrand,(1983)
$Fe_{80}B_{20}$	190	3450	0.06	0.1	Frommeyer & Seifert (1981)

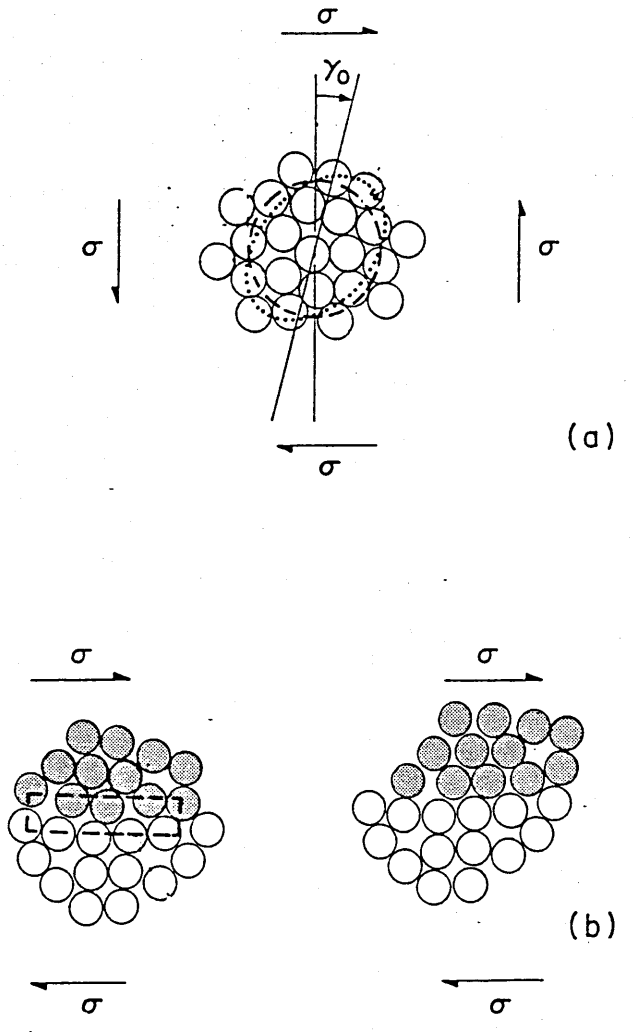

Figure 3.1 Schematic representation of the two types of shear transformations observed in sheared bubble rafts: a) a diffuse shear transformation b) two stages of a concentrated shear transformation (after Argon, 1979).

CHAPTER FOUR

MATERIAL AND EXPERIMENTAL PROCEDURES

4.1 The Material

The material selected for investigation was a nickel base metallic glass with the atomic composition: Ni 78 pct, Si 10 pct, B 12 pct ($Ni_{78}Si_{10}B_{12}$). This alloy was manufactured by Vaccumschmeltze under the trade name of VITROVAC 0080.

The alloy was supplied in the form of continuous ribbons of 30 m long, 20 mm wide and 0.057 mm thick.These ribbons were produced using a chill-block melt-spinning technique. In this method, the molten alloy was injected onto a cylindrical chill-block rotating below a crucible and the rapidly solidified ribbons were formed on the surface of the rotating wheel at a rate of ~20 m/s. (Hilsinger, 1984).

Ribbons of $Ni_{78}Si_{10}B_{12}$ alloy were one of the widest and thickest metallic glass ribbons available when the experimental programme started and provided a possibility of producing suitable test pieces for mechanical tests. The ribbons also had good dimensional stability: the fluctuations within the thickness and width were not larger than 5 pct.

All the results reported in this study were obtained from one single ribbon. Samples taken from the segments of the ribbon used for the preparation of mechanical test pieces were examined by X-ray and electron diffraction techniques. These investigations confirmed the "non crystalline" state of the alloy.

4.2 Mechanical Tests

4.2.1 Specimens and Test Fixtures

Mechanical tests, types of specimens and specifications of testing machines are summarized in Table 4.1. Unnotched specimens with a reduced gauge section were used for uniaxial tensile tests and for the determination of S-N curves.

Fracture toughness and fatigue crack growth tests were done on single edge-notched tensile (SENT) specimes. "Trouser-leg" specimens were utilized for the tear tests.

All the specimens were prepared from strips cut longitudinally from the as-cast ribbon. Unnotched specimens were given a reduced gauge section of 3.2 mm wide and 12 mm long (Fig. 4.1). The gauge sections were formed by removing extra material from the edges of rectangular strips, 40 mm long and 10 mm wide, using a spark erosion machine. The electrodes were made of 25 mm thick copper foils and the cutting current was kept at its minimum setting ($I \approx 0.1$ Amp.) to minimize the extent of the heat-affected zones. These zones were subsequently removed by polishing the edges of the specimens on a 4000 grit emery paper. Specimens prepared by spark erosion had closely controlled and reproducible dimensions.

Single edge-notched tensile (SENT) specimens were prepared in the form of rectangular pieces, 40 mm long and 20 mm wide. A notch of 1 to 4 mm depth - depending on the particular test - was put in the middle of one edge of the specimen using a pair of scissors. The notch was sharp enough to nucleate a fatigue crack. A SENT specimen is illustrated in Fig. 4.2.

"Trouser-leg" specimens for the tear tests were 40 mm long and 10 mm wide. They had a longitudinal slit of 25 mm cut from one end using a pair of scissors (Fig.4.3). The thickness of the specimens ahead of the slit were measured using a digital micrometer to confirm that the uniformity of the thickness met the requirements of ASTM standard D 1938-67 (ASTM, 1967).

To load the specimens, both ends were clamped between soft aluminium plates to prevent any premature failure within the grips. The ends were then compressed between steel grips which were pinned to clevices in the loading frame of the testing machine using lubricated pins. In all the mechanical tests, this arrangement permitted rotation and self alignment of the test pieces to occur during loading.

4.2.2 Tensile Tests

Uniaxial tensile tests were performed to determine the tensile strength and the elastic modulus of the alloy. Reduced gauge section specimens were loaded to fracture by a table model screw driven Instron testing machine. The load measurements were made using a 5 kN capacity load cell. Tensile strengths of the ribbons were measured at room temperature and at 77 K. A crosshead speed of 8.3×10^{-3} mm/s which corresponded to a strain rate of 8.3×10^{-4} was used. At least five specimens were tested at each temperature. Strengths were calculated after the cross-section of the fractured area of each specimen was measured in the SEM. Experiments at 77 K were performed in a polyethylene container filled with liquid nitrogen.

Strain measurements for the calculation of the elastic modulus were taken from two strain gauges positioned in the longitudinal and transverse directions on 40 x 10 mm size rectangular specimens. Each strain reading was taken after a load increment of about 10 pct of the average fracture load.

The hardness of the samples was measured using a Zeiss Vickers microhardness tester. Specimens were polished to 1 μm and mounted in epoxy resin. Measurements were made under an indenter load of 200 g. The use of this load ensured that specimen thickness to impression depth ratio was larger than 10:1. The average microhardness value (VHN) was obtained from at least ten valid measurements.

4.2.3 Tear Tests

Tear tests were performed on a screw driven Instron machine fitted with a load cell of 5 N capacity. The "legs" of the trouser specimens were pulled apart as shown in Fig.4.3b and the tear force versus extension curves were recorded.

The first measurement of load was made after the tear crack had reached a length of 2 mm to eliminate the effect of a relatively blunt scissor cut.

Subsequently, tear force readings were taken as the crack extended in length by up to 6.0 mm. Tests were concluded before the tear force became affected by the free end of the specimen.

Experiments were carried out at five temperatures between 77 K and 513 K in the Instron environmental chamber. The temperature inside the chamber was controlled within 1 K between 295 K and 513 K. Below room temperature, the required temperature was reached by pumping liquid nitrogen into the chamber. The fluctuations in temperature were then ~5 K. The rate of tear propagation (R) was studied over the range 8.5×10^{-4} to 2.0×10^{1} mm/s. At least three tests were done at each temperature and tear rate.

In order to evaluate the tear energy Γ, the value of the tear force F was required. This was obtained from the record of tear force versus extension using a random signal analysis method. The value of the force was determined at each turning point of the record. The average of these values was used to obtain the mean tear force. The standard deviation was computed in order to characterize the magnitude of tear force variations.

4.2.4 Fracture Toughness Tests

Fracture toughness tests were conducted on an Instron 8031 servo-hydrolic testing machine fitted with a 10 kN load cell. The machine was operated in closed loop configuration under load control. Tests were performed on precracked and fatigued SENT specimens shown in Fig. 4.2. The surfaces of these specimens were polished to 1 μm and a starter notch of ~ 4 mm depth was introduced. The fatigue precrack was grown at a ΔK within the range 10-12 MPa$\sqrt{m}$. As the desired crack length was approached, ΔK at the crack tip was reduced to ~ 8 MPa$\sqrt{m}$.

After the fatigue crack had grown to 6.5 mm (corresponding to (a/w)= 0.33), the specimen was loaded monotonically up to failure and the value of the load at fracture, P_Q, was noted. The load was applied at a rate of 0.01 mm/s and measured to a precision of 1 %. Before loading, an Instron clip gauge was fitted between the

knife edges of two steel arms mounted to the clevices of the machine. A plot of load vs clip gauge displacement was recorded on an X-Y plotter. Load-displacement records obtained with this method were linear up to failure. A total number of six specimens were tested in this way.

The provisional value of fracture toughness, K_Q, was calculated using an expression based on linear elastic stress analysis. For pin-loaded SENT specimens, this is given as (Rooke and Cartwright, 1976)

$$K_Q = \frac{P_q\sqrt{\pi a}}{wt}\left[1.12-0.23(a/w)+10.6(a/w)^2-21.7(a/w)^3+30.4(a/w)^4\right] \qquad 4.1$$

This equation is valid for $l/w \geq 1.0$ and $a/w \leq 0.6$ within an accuracy of 1 pct (where a is the size of the fatigue crack and l and w are the specimen length and width respectively).

The plastic zone sizes were measured by optical microscopy from the cellulose acetate replicas applied to the crack tip region during incremental loading of the specimens. Initially, the specimens were loaded to ~10 % of the expected fracture load, P_Q and replica tape was applied to the crack surface four minutes after the load was applied in order to allow the crack to stabilize. The loading / stopping / replication sequence was continued in increments of 5-10 % of the P_Q until fracture took place. The crack tip opening displacements (CTOD) were also measured from the replicas taken during incremental loading sequence.

4.2.5 Fatigue Crack Propagation Tests

Fatigue crack growth tests were performed on the model 8031 servohydrolic Instron machine fitted with a load cell of 500 N load capacity which could measure load amplitudes as low as 1.0 N with an accuracy of ± 2 %. The strain gauge output of the load cell was connected to the strain control input of the machine to

minimize the noise to signal ratio which enabled the above accuracy to be attained. The SENT specimens and test fixtures were similar to those used for fracture toughness tests with the exception of having shorter starting notches, about 1 mm in depth. The experimental configuration is shown in Fig. 4.4. Fatigue precracks were initiated from the tips of these notches and grown to a length about 30-40 % of the notch length. Crack growth data were collected after this length was attained. Crack measurements were done optically and without interrupting the tests. To increase its reflectivity, one of the specimen surfaces was polished to 0.25 μm. The measuring device was a low power travelling microscope (x 50) with a minimum graduation of 0.01 mm. Specimens were fatigued under positive R values using a sinusoidal waveform. All tests were carried out at room temperature (~ 21°C) and in laboratory air (~55 % humidity).

Two different experimental techniques were used to determine fatigue crack growth rates:

i) Constant load amplitude loading technique

ii) Constant stress intensity amplitude loading and load shedding technique

4.2.5.1 Constant Load Amplitude Loading Technique

In this method, a constant cyclic load amplitude, ΔP, was applied to the specimen and the crack length (a) was measured as a function of the number of cycles (N) using a frequency of 5 Hz. Crack length was determined at intervals of about 0.1mm. An example of the data obtained is shown in Fig. 4.5. Crack growth rates were calculated using a secant technique recommended by ASTM E647-81 (ASTM,1981). The technique involved calculating the slope of the straight line between two adjacent data points on the a versus N curve. This could be expressed as

$$\frac{da}{dN} = \frac{a_{i+1} - a_i}{N_{i+1} - N_i} \qquad 4.2$$

Cyclic stress intensity factors, ΔK, were calculated using the following expression (Rooke and Cartwright, 1976)

$$\Delta K = \frac{\Delta P\sqrt{\pi a}}{wt}\left[1.12-0.23(a/w)+10.6(a/w)^{2}-21.7(a/w)^{3}+30.4(a/w)^{4}\right] \quad 4.3$$

This equation is a variation of the equation 4.1 and is valid for SENT specimens under the conditions specified in Section 4.2.4.

As the da/dN computed by the secant method was an average rate over the $(a_{i+1}- a_i)$ increment, ΔK was calculated using the average crack length $[a = (a_{i+1} + a_i)/2]$.

The constant load technique was used with confidence to determine crack growth rates above 10^{-4}mm/cycle. However, the technique had two deficiencies which became significant when attempts were made to measure the threshold growth rates. Firstly, the crack growth rates calculated using the secant method varied with the choice of crack length measurement interval (Wei et al., 1979) and more sophisticated numerical analysis techniques such as the incremental polynomial method did not improve the accuracy of threshold crack growth data. Under constant load amplitude condition, the value of ΔK changes continuously as the crack grows leading to inaccuracy in the estimation of the value of ΔK. If, however, the crack tip loading is controlled so that the cyclic stress intensity remains virtually constant as the crack grows, the growth rate remains constant and is measurable with much greater accuracy. Thus, fatigue crack propagation tests below 10^{-4} mm/cycle were performed under conditions of constant ΔK.

4.2.5.2 Constant Alternating Stress Intensity Loading - Load Shedding Technique

The load shedding procedure consisted of a repeated sequence of load

shedding and subsequent crack growth at constant ΔK. To maintain ΔK constant at a given level, the crack length was measured using a travelling microscope, the new load required was computed from Equation 4.2 and the applied load amplitude was adjusted accordingly. Crack length measurements were made at intervals of about 0.05-0.10 mm. At a given ΔK level, about 10 measurements of crack length were made and the corresponding number of cycles was recorded. The crack growth rate (da/dN) was then obtained using a linear least mean squares fit. An example of a versus N data obtained by this method is shown in Fig. 4.6. It can be seen that there is little scatter in the data which results in a high correlation factor.

The collection of crack growth data was started at ΔK levels about 10 MPa$\sqrt{m}$. Once sufficient data were taken at a given ΔK, the applied load was decreased by 10-15 % to a new ΔK level. The systematic reduction of the applied loads following the measurement of crack rates under conditions of constant ΔK was continued until the threshold value of cyclic stress intensity (ΔK_{TH}) was reached. It was observed that load reduction in excess of 15 % were liable to give premature crack arrest due to residual plastic deformations. To prevent the retardation effects , the fatigue crack was grown to a distance about ten times larger than the plastic zone generated at the higher ΔK. The frequency was kept constant at 30 Hz except at higher ΔK levels where it was reduced to 15 Hz.

ΔK_{TH} is defined as the cyclic stress intensity range where no crack growth can be detected after 10^6 cycles. The minimum detectable crack growth increment was 0.02 mm giving a growth rate less than 2×10^{-8}mm/cycle at ΔK_{TH}. Upon establishing ΔK_{TH}, the test was resumed by increasing the load incrementally (15 %) and measuring crack growth rates under constant ΔK conditions until higher ΔK levels ($\Delta K \approx$ 25-30 MPa$\sqrt{m}$) were reached. The crack growth rates obtained at the same constant ΔK level by load shedding and load increasing were compared and averaged.

Fatigue crack propagation data were presented as plots of Log (da/dN) versus Log ΔK where crack growth rates were the average values calculated from several

tests. Fatigue crack propagation rate curves were composed of combined data collected using both constant load (high crack growth rates) and load shedding/increasing techniques (medium and threshold growth rates).

4.2.6. S-N Curve Determination

S-N curves were determined using the Instron 8031 servohydrolic machine with a 500 N load cell. Tests were performed under load control using a sinusoidal waveform at a frequency of 25 Hz. Reduced gauge section specimens (section 4.2.1) were tested at a constant stress ratio of R = 0.1. At least three specimens were tested to failure at a given applied mean stress level. 'Run out' was taken to occur at 10^7 cycles.

4.3. Metallography and Fractography

4.3.1 Double Stage Replication Technique

A replication technique was used to observe the changes in the crack tip morphologies of specimens during fracture toughness and fatigue crack growth tests. Cellulose acetate tapes applied to the specimen surfaces during the tests were subsequently examined by optical and/or electron microscopy to determine the crack tip displacements and the size of the plastic zones.

The following procedure (summarized in Fig. 4.8) was used to prepare the replicas for the examination by SEM:

A strip of cellulose acetate replicating tape (25 x 10 x 0.1 mm) was softened with a solution composed of 85 % by volume methylene chloride and 15 % methyl alcohol and laid against the surface of the specimen. Care was taken not to allow air bubbles to be trapped between the specimen and the plastic replica. After about ten minutes, the solvent evaporated and the acetate tape adopted the shape of the the crack profile. The tape was carefully peeled from the specimen with tweezers. This procedure was repeated at least three times to ensure that the crack tip was faithfully replicated. The resulting negative replica of the fatigue crack was stuck

down on a microscope slide (to prevent curling) and examined using a Nomarski contrast interference microscope.

A thin layer of gold (25 μm) was sputtered onto the surface of the replica in a vacuum sputtering unit. This was followed by copper plating of the replica in an electrolytic solution of copper sulphate. After the thickness of the electroplated copper layer reached about 0.3 mm, the copper replica was separated from the plastic replica and carefully washed in acetone.

The copper positive replica was resistant to the damage by the electron beam and thus ready to be examined by the scanning electron microscopy.

4.3.2. Optical Interference Microscopy

A Nomarski contrast interference technique was used to investigate the crack tip morphologies of the specimens. Quantitative analyses of shear bands were made using a two beam interference microscope.

A Zeiss optical microscope was converted to Nomarski contrast or two beam interference microscope by selecting the required objective and illumination. With Nomarski contrast technique (Nomarski and Weill, 1955), contrast was obtained from surface irregularities 20 to 50 nm high with a resolution limit of approximately 5 nm. The optical system required to obtain phase contrast in a Nomarski interference microscope included a double quartz wedge prism. The surface was illuminated with a polarized light.

The two beam interference microscope consisted of the reflection microscope fitted with a Watson 8 mm interference objective. Monochromatic sodium illumination of wavelength 590 nm was used. For the monochromatic sodium light, the fringe spacing was 295 nm so that a step height greater than 295 nm on the specimen surface produced a displacement of more than one fringe spacing.

4.3.3 Scanning Electron Microscopy

The fracture surfaces of the specimens and the positive copper replicas of the crack tips were examined by a Philips 501 scanning electron microscope. Specimens for fractographic examinations were cut 5 mm below their fracture surface and mounted vertically in slits cut into the specimen 'stubs'. To ensure good mechanical stability and electrical contact with the stubs, mounted specimens were glued with a conductive glue. An accelerating voltage of 7 or 15 kV was used to obtain secondary electron images. Specimens were examined at various angles of incidence (0 to 30 degrees) and magnifications (x 640 to x 10000). The measurement of crack tip displacements in fatigued samples was made at a magnification of x 5000. For qualitative measurements, the microscope was calibrated using standard latex balls of 100 nm diameter.

Table 4.1 Mechanical Tests, Specimens and Specifications of Testing Machines

Tests	Specimens	Testing Machines		
		Model		Load Cell (N)
Uniaxial Tensile	Unnotched	Screw Driven Instron	1180	5000
Tear	Trouser	Screw Driven Instron	1180	5
Fracture Toughness	SENT	Servohydrolic Instron	8031	10000
S-N Curve	Unnotched	Servohydrolic Instron	8031	500
Fatigue Crack propagation	SENT	Servohydrolic Instron	8031	500

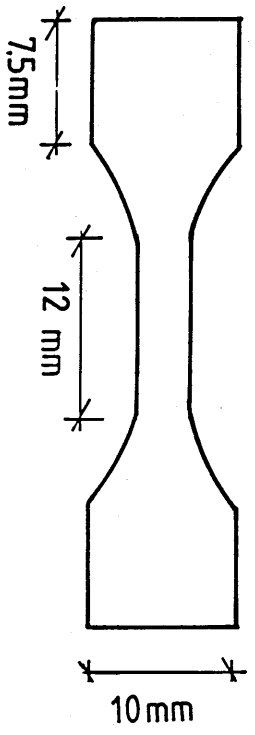

Figure 4.1 A tensile specimen with a reduced gauge section.

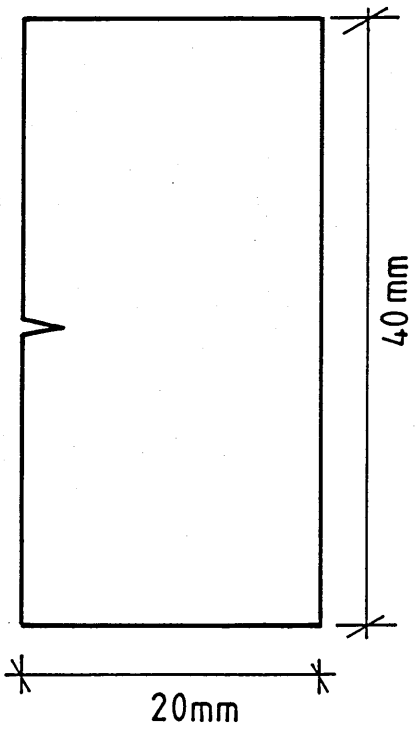

Figure 4.2 A single edge notch tensile (SENT) specimen.

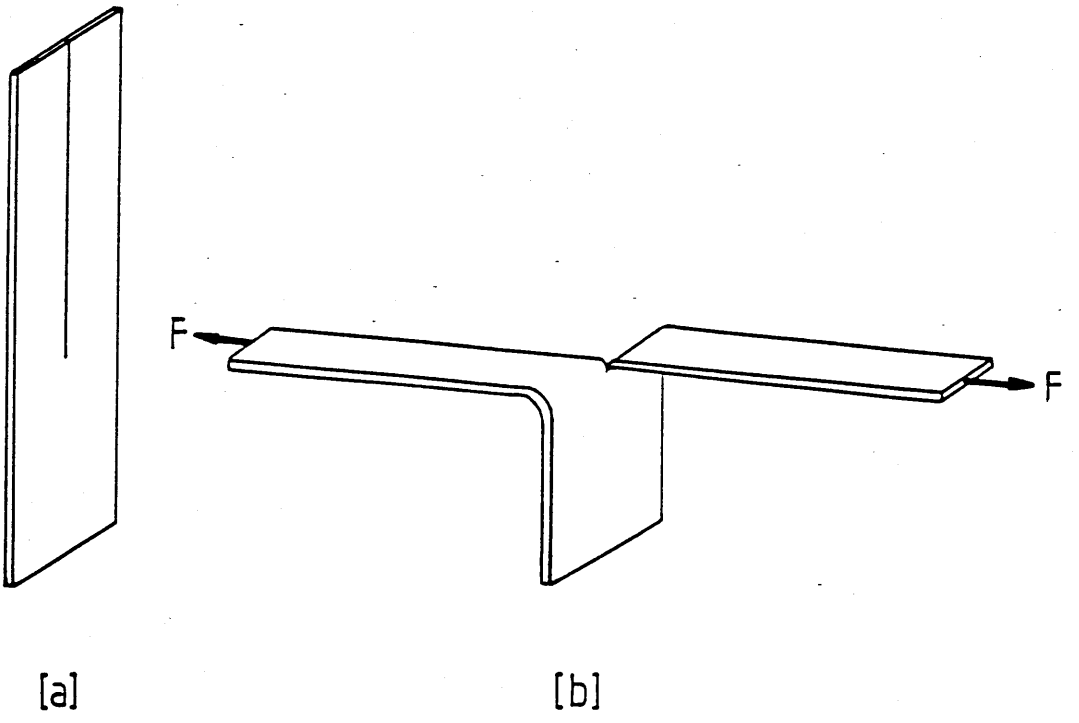

Figure 4.3a A trouser leg tear specimen.

b Configuration of the specimen during the test.

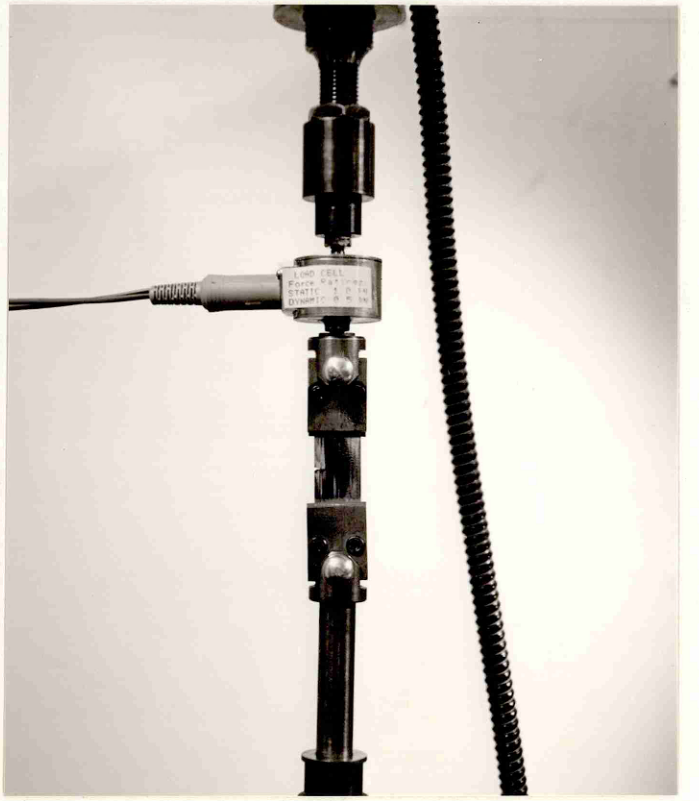

Figure 4.4a The test rig used for fatigue crack propagation tests.

b Configuration of the SENT specimen during the fatigue tests.

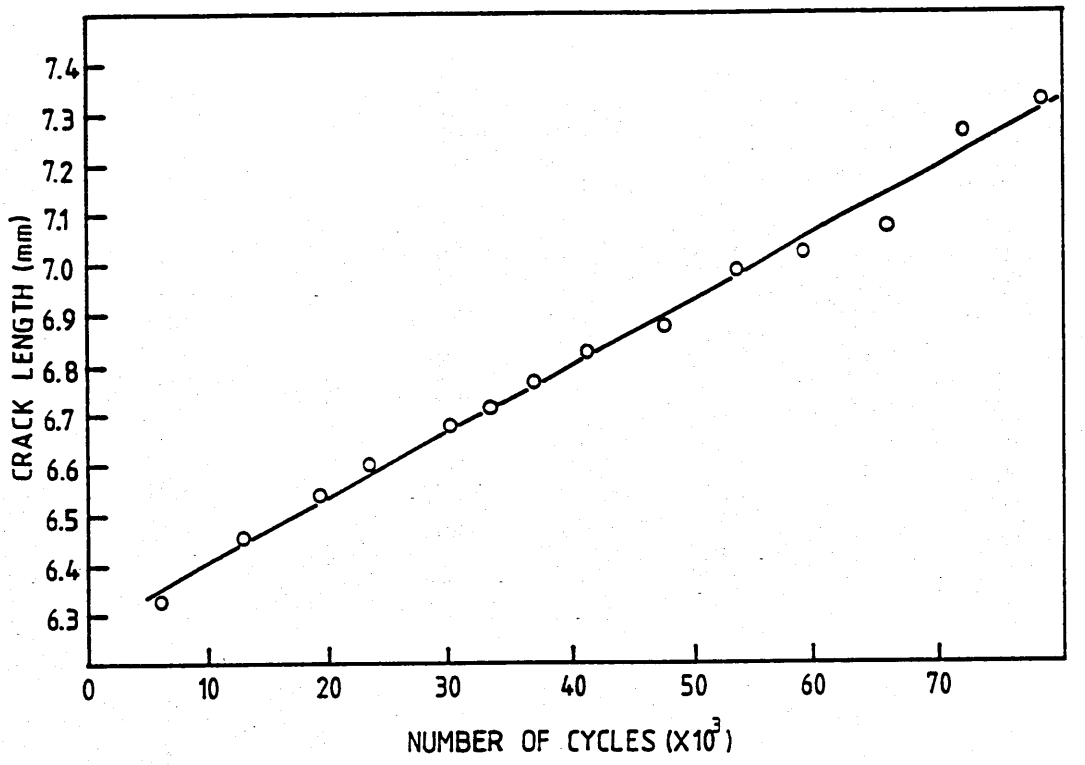

Figure 4.5 Fatigue crack propagation curve at a constant stress amplitude σ_a = 98 MPa and R = 0.1.

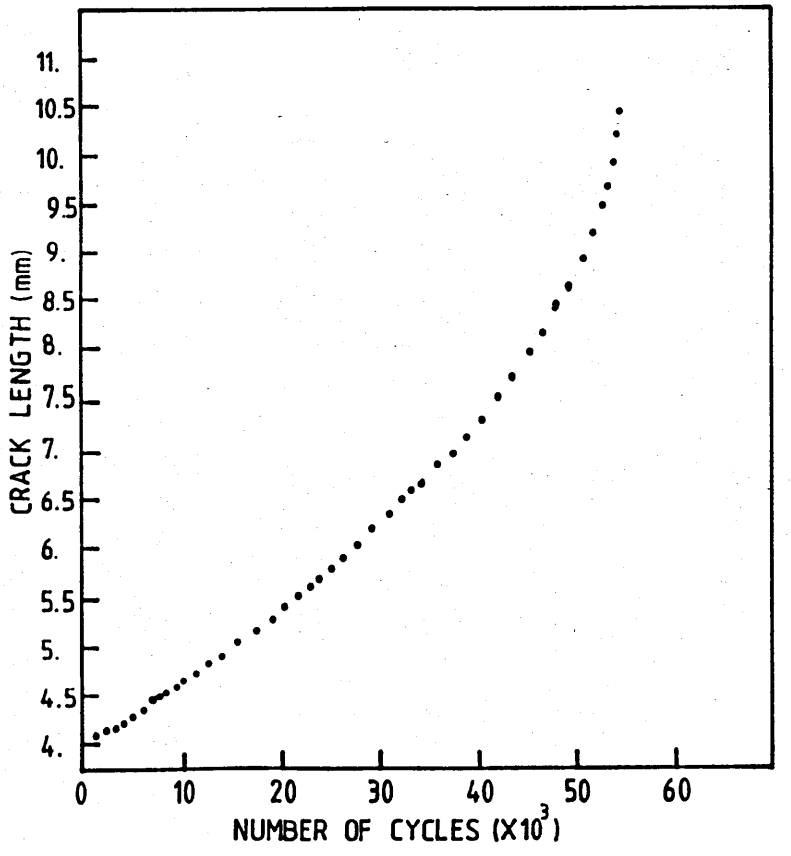

Figure 4.6 Fatigue crack propagation curve at a constant alternating stress intensity, ΔK = 7 MPa$\sqrt{m}$, and R = 0.1.

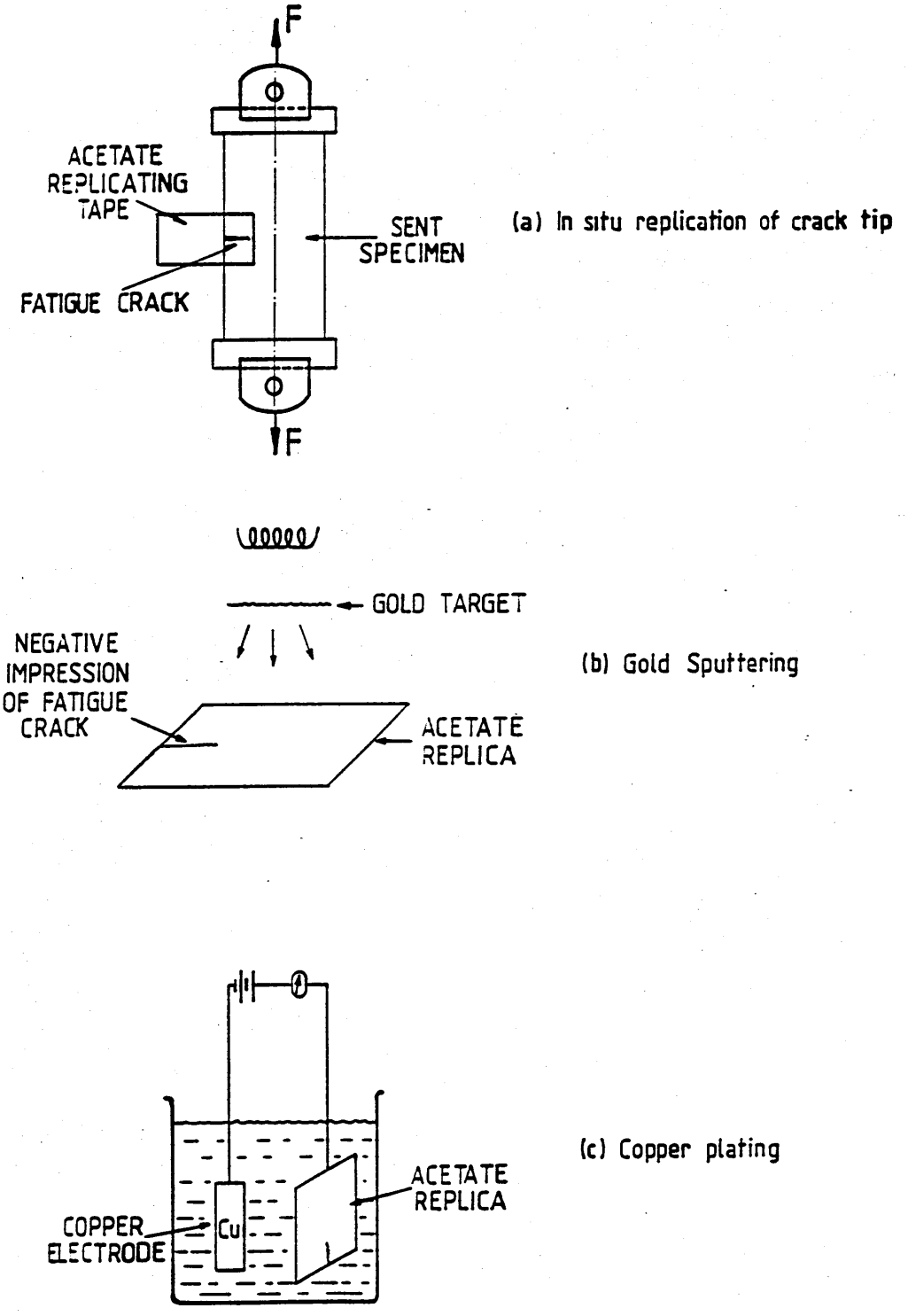

Figure 4.7 The double stage replication technique.

CHAPTER FIVE

DEFORMATION AND FRACTURE UNDER MONOTONIC LOADING

5.1 Results

5.1.1 Uniaxial Tensile Tests

The tensile strength (σ_{UTS}) and the Young's modulus (E) of the amorphous $Ni_{78}Si_{10}B_{12}$ specimens measured at room temperature are shown in Table 5.1. The diamond pyramid hardness number of the alloy is also given in this table.

Table 5.1 Mechanical Properties of amorphous $Ni_{78}Si_{10}B_{12}$

σ_{UTS} (MPa)	E(MPa)	σ_{UTS}/E	HV (Vickers)
2100	125000	59	930

Tensile load-elongation curves obtained using reduced gauge section specimens and a conventional screw driven testing machine were linear up to failure. They did not show any evidence of macroscopic ductility. Fracture occurred on planes inclined at ~45-50° to the tensile axis and the thickness direction. Fracture occasionally involved a series of transactions from one to another plane at ~45-50° to the tensile axis so that the macroscopic appearance of the fractured area of the specimens consisted of alternating slant planes ~0.5 mm long and perpendicular to each other. Sometimes a few localized shear bands

could be observed near the fracture on the specimen surfaces.

Fig. 5.1 shows a scanning electron micrograph of a typical tensile fracture surface of an unnotched specimen.The fracture surface exhibits two morphologically different regions: a smooth and almost featureless zone and a region characterized by a vein pattern. The veins are protrusions ~1 μm wide on both of the matching fracture surfaces. A local necking point at a junction of veins can be seen in Fig. 5.2.

5.1.2 Fracture Toughness Tests

The fracture toughness of the alloy was determined using prefatigued SENT specimens as described in section 4.2.4. By considering that the critical crack length at the moment of instability corresponded to the length of fatigue crack, the fracture toughness of amorphous $Ni_{78}Si_{10}B_{12}$ was found to be 67 ± 5 MPa$\sqrt{m}$ where the limits represent the standard deviation from the mean value of the specimens tested.

5.1.2.1 Crack Tip Deformation and Crack Opening Displacements

The size of the plastic zone at the crack tip and the crack tip opening displacements have been observed using a replication technique. Figs. 5.3a-f show the development of the plastic deformation at the crack tip of a SENT specimen accompanying an increase in the applied stress intensity K. The plastic zone on the surface of the specimen consisted of discrete shear bands. At low stress intensities, shear bands formed a fan in directions at roughly 70-80 degrees to the plane of the crack. With an increase in K, the size of the plastic zone increased in both the x and y directions simultaneously by the nucleation of new shear bands and by the growth of existing ones (Figs. 5.3a-c). At stress intensity levels above $K \approx 35$ MPa$\sqrt{m}$, the bands started to project forward vigorously with small increments in applied K. Consequently, the size of the plastic zone in the x direction, r_x, extended much faster than the corresponding increase in the y

direction (Fig. 5.3d). At above $K \approx 50$ MPa$\sqrt{m}$, the growth of only one of the shear bands in the plastic zone was favoured. Slow stable crack growth and final fracture followed the elongation of this band in the x direction (Figs. 5.3e,f).

Fig. 5.4 shows the variation of the plastic zone size, r_x and r_y in x and y directions respectively, as a function of the applied K. The solid line in this figure represents the size of the plastic zone calculated according to the Dugdale analysis using Equation 2.20. The increase in the CTOD with the applied K is shown in Fig. 5.5. The CTOD was measured perpendicular to the loading axis at a distance of 5 μm behind the crack tip. The measured CTOD is compared with the theoretical CTOD derived using Dugdale's model (Eq. 2.22).

5.1.2.2 Fractography

Fig. 5.6 shows the section of the fracture surface of a SENT specimen corresponding to the initial stage of the fracture process. The fatigue precrack on the left of the figure lies on a plane perpendicular to the loading axis and has a straight crack front. The beginning of static fracture is marked by a smooth region which exhibits fracture markings parallel to each other and extending across the thickness of the specimen. An important feature of this section is the existence of the pieces of material which have slipped from one edge of the specimen towards the middle of the fracture surface. A vein pattern started to develop at a distance ~150 μm from the fatigue crack front and the fraction of the area covered by veins, then increased almost linearly until at a distance ~ 500 μm from the fatigue crack where all the fracture surface became covered with the veins. It is difficult to visualize the angle that the fracture surface makes with the tensile axis from Fig. 5.6, but it was observed that the fracture surface was initially perpendicular to the loading axis, then became progressively slanted with an increase in distance from the fatigue crack. It appears that when the vein pattern covered all the section, fracture occurred on a plane inclined at ~45° to the loading axis.

5.1.3 Tear Tests

A typical load-extension record obtained from a "trouser leg" tear test at room temperature is shown in Fig. 5.7. Initially, there is a steep increase in the load and the curve then flattens and forms a serrated plateau. In the latter region, tearing undergoes irregular bursts but the average tear force remains constant throughout the process. The tear energy (Γ) of the alloy at room temperature calculated using Equation 2.14 ($\Gamma = 2F/t$) is 97.5 kJ/m^2 for a specimen 57 μm thick torn at a rate of 1.7×10^{-2} mm/s.

To determine the effect of the specimen thickness on the tear energy specimens smaller than 57 μm were prepared by grinding and polishing their surfaces. It was observed that the tear energy (Γ) depends strongly upon the thickness (t) of the specimen tested. The relationship between Γ and t is shown in Fig. 5.8 to be linear.

The effect of the temperature on the tear energy of amorphous $Ni_{78}Si_{10}B_{12}$ is shown in Fig. 5.9. The tear energy increases by about 50% when the temperature is reduced from 500 to 77 K. The tensile fracture strength of the alloy showed a similar proportional change with temperature over the range 77 K to 300 K, (i.e. 2100 MPa at room temperature and 2500 MPa at 77 K). It was observed that the testing temperature also affected the amplitude of the tear force oscillations (and the standard deviation of the tear energy). As shown in Fig. 5.9, the standard deviation increases as the temperature is reduced.

However, it was found that at 300 K, changes in tear rate over the range 8.5×10^{-4} to 20 mm/s caused no detectable changes in the mean and standard deviation of the tear force.

5.1.3.1 Crack Tip Deformation

Inspection of the tear crack revealed the presence of inhomogeneous shear bands within the crack tip plastic zone. In this region, three different types of

shear bands were identified.

The first type was composed of long, parallel bands that extended a distance L from each side of the tear crack (Fig. 5.10). For a 57 μm thick specimen tested at room temperature, L = 800-810 μm. Neither the density nor the orientation of these bands was symmetrical with respect to the crack surface. On the compression side of the crack tip (the concave surface of the ribbon during the test), shear bands made an angle (α) of 51° with the propagation direction of the crack, but this angle was 62° on the tensile side of the crack (the convex surface during the test). The density (n) of shear bands (i.e. the number of bands per mm of crack length) was significantly higher on the tensile side (n = 149) than on the compression side (n = 88.5). Fig. 5.11 is an interference micrograph of the shear bands. Any discontinuity of the interference fringes corresponds to a step on the surface produced by these bands. The height (h) of the step varies little over most of the length of the bands and is typically ~0.15 μm. The step height decreases abruptly just before the bands terminate inside the specimen.

Further examination of the crack tip revealed the presence of a second group of shear bands (Fig. 5.12). These bands lay approximately parallel to the crack propagation direction (towards the top of the micrograph) and they sheared the first group of shear bands. These features are also seen in Fig. 5.13 which shows the morphology of the region in the vicinity of the tear a few millimetres behind the crack tip. The width (w) of the region covered by the bands was about 105 and 160 μm on the tensile and compression sides of the tear respectively. Interference microscopy revealed that these bands left no measurable step on the specimen surface.

A third type of shear band was detected when the specimens were examined in the scanning electron microscope. This was a single band extending ahead of the tear crack (Fig. 5.14). Although it was difficult to distinguish the boundary between the crack tip and the shear band, its length was estimated to be 60-100 μm. Fig. 5.15 is the through-thickness section of the shear band ahead of the tear. The shear band (and the crack surface) is inclined at an angle of ~60-70° with the

surface of the sample.

The parameters describing the morphology of the shear bands are summarised in Table 5.2 for the amorphous alloy in two different thicknesses (t = 57 μm and 25 μm) at room temperature. These parameters were also measured on a sample 57 μm thick fractured at 77 K and the values are included in the table. No significant changes were observed in the parameters n, L, h, and w as a consequence of changes in the tear rate at 298 K over the range of rates studied (8.5×10^{-4} to 20 mm/s).

5.1.3.2 Fractography

Figs. 5.16a,b show the fracture surface of a specimen torn at room temperature. The surface is smooth and shows no indication of the vein pattern that was observed on the surfaces of notched or unnotched specimens failed in uniaxial tensile tests. The fracture surface contains curved transverse markings across the thickness of the specimen. At some locations, as shown in Fig. 5.16b, pieces of the material moved from the ribbon surface to the middle of the fracture surface following the traces of the curved markings.

5.2 Discussion

5.2.1 Tensile Failure of Unnotched Specimens

In amorphous $Ni_{78}Si_{10}B_{12}$, like other metallic glasses, deformation at room temperature is associated with the formation of inhomogeneous shear bands. Once nucleated, these bands persist and subsequent deformation proceeds by negligible strain hardening (Pampillo, 1974, Argon, 1978). In the alloy studied, these bands have been observed on the surface of bent ribbons, adjacent to hardness indentations as well as within the plastic zones at crack tips. However, during uniaxial tensile tests of uniform ribbons, as soon as shear becomes concentrated in a shear band, it is followed by the catastrophic failure of the section.

Examination of the specimen surfaces showed that only a small number of shear bands existed, apart from the one leading to fracture. This suggests that during static tensile loading, failure of unnotched specimens was coincident with general yielding. Thus, in amorphous $Ni_{78}Si_{10}B_{12}$ the yield strength σ_{YS} can be taken to be equal to the fracture strength σ_F so that $\sigma_{YS} = \sigma_F = \sigma_{UTS} = 2100$ MPa. As the shear deformation is restricted to a small region and the thickness is small, the displacement required to produce fracture by "sliding off" is small compared with the elastic displacement of the testing machine. Consequently, load-displacement curves obtained using conventional screw-driven machines such as the one used in this study do not show a well-defined yield point and an observable plastic strain. On the other hand, the true stress-strain curves of metallic glasses obtained using "hard" tensile testing machines (those with a large elastic stiffness) indicates a behaviour close to that of rigid-plastic (non-hardening) materials (Murata et al.,1978).

Accordingly, in agreement with most of the metallic glasses, the fracture surfaces of amorphous $Ni_{78}Si_{10}B_{12}$ are characterized geometrically by a slant fracture on a plane inclined at ~45-50° to the tensile axis and the thickness vector. This fracture plane is coincident with the plane of maximum shear stress.

The fracture surfaces of amorphous $Ni_{78}Si_{10}B_{12}$ are composed of two morphologically different regions, namely, a region with a vein pattern and a smooth and nearly featureless zone. It appears that the fracture process began by an initial shearing-off mechanism that produced large shear offsets such as the one seen in Fig. 5.1. After a characteristic offset is achieved, the process of separation is completed by a ductile rupture that results in a veined surface topology. The veins are always protrusions on matching halves of the fracture surfaces. The local necking point on a junction of veins seen in Fig. 5.2. should correspond to the last moment of the rupture event.

Regarding the relative positions of the featureless zone and veined region, it is concluded that these zones are not mirror images on the opposing fracture surfaces. Leamy et al. (1972) proposed two possible fracture modes leading to the

shear failure of thin metallic glass ribbons. These are illustrated in Fig. 5.17a,b. Of these mechanisms, it is concluded that the mechanism shown in Fig. 5.17b produces fracture surfaces which possess the features observed in this study.

5.2.2 Fracture Toughness and Crack Extension Under Mode I Loading

Amorphous $Ni_{78}Si_{10}B_{12}$ has a high fracture toughness ($K_c = 67 \pm 5$ MPa$\sqrt{m}$) for a material with a yield strength of $\sigma_{YS} = 2100$ MPa. However, to make a direct comparison between the fracture toughness of this alloy and high strength crystalline materials, it should be ensured that the measured value K_c corresponds to a standard plane strain fracture toughness value K_{Ic}. According to the recommendation of ASTM standard E399 (ASTM, 1981) for the determination of a valid K_{Ic} the specimen thickness t, the crack size a, and the length of the uncracked ligament (w-a) need to satisfy the following conditions

$$a, t \geq 2.5 \left(\frac{K_c}{\sigma_{Ys}}\right)^2$$

$$w \geq 5.0 \left(\frac{K_c}{\sigma_{Ys}}\right)^2 \qquad 5.1$$

For amorphous $Ni_{78}Si_{10}B_{12}$, the width (20 mm) and the crack size (~6 mm) of the specimens were above the minimum values specified by Equation 5.1 (w = 5.09 mm, a = 2.54 mm). However, their thicknesses were limited by the thickness of the melt spun ribbon (0.057 mm), i.e. ~ 45 times smaller than the recommended value. Thus, the critical stress intensity K_c at the instability does not correspond to a 'valid' K_{Ic}.

Examination of the replicas taken from the surface of the specimen showed

that the plastic zone at the crack tip is dominated by elongated shear bands (Figs. 5.3c-f). With the increase of the applied K, the growth of one of the shear bands is favoured and it appears that the fracture starts inside this well developed shear band. The existence of pieces of material that slipped from one edge of the specimen towards the middle of the fracture surface (Fig. 5.6) indicates that shear decohesion occurred by an antiplane strain or mode III mechanism.

The plastic zone defined by elongated shear bands resembles the plastic zone attending Dugdale's plane stress model (Dugdale, 1959). As mentioned in section 2.2.1, the Dugdale model of crack extension assumes that the plastic zone at the crack tip is in the shape of a thin strip whose length is given by Equation 2.20 as

$$R = \frac{\pi}{8} \frac{K^2}{\sigma_{Ys}^2} \qquad 2.20$$

The mathematical treatment of the Dugdale model offers a reasonable description of plastic zone size of amorphous $Ni_{78}Si_{10}B_{12}$ under monotonic tensile stresses. As shown in Fig. 5.4, the plastic zone size in this alloy, measured in the direction of crack advance, r_x, is in fairly good agreement with the predicted values of Equation 2.20. Similar agreement also exists between the measured and calculated values of crack tip opening displacements (Fig. 5.5).

At low K levels, the plastic zone is dominated by hinge components at the crack tip (Figs.5.3a,b) which are usually associated with plane strain conditions. At these K levels, the size of the plastic zone increases simultaneously in the x and y directions and assumes a circular shape until shear bands start to burst out in front of the crack plane at $K \approx 35$ MPa$\sqrt{m}$. At this stress intensity level, the size of the plastic zone is equal to the thickness of the specimen, i.e. $r_x = r_y \approx t \approx 0.06$ mm and it appears that a change of the stress and strain state starts to occur. Such a transition has also been observed in thin plain carbon steel sheets by Hahn and Rosenfield (1965). Although the hinge component represents a deviation

from the Dugdale plastic zone, the correlation between the measured and theoretical plastic zone sizes persists at low K values.

An important deviation is the fact that the plastic zone size r_x and crack opening displacement becomes larger than the calculated plastic zone size near the instability. This may be due to the occurrence of some slow stable crack growth before the final fracture but it was not possible to detect the growth rate of the crack into the shear band by surface examination. Stable crack growth would lead to an increase in the crack length to a value larger than the length of the fatigue crack which was used to calculate the stress intensity. Correction for this effect could be expected to move the points at the top of Figs. 5.4-5.5 to larger K values. Also, it is expected that the nominal value of K_c would increase as a result of stable crack growth.

5.2.3 Shear Crack Extension During Tearing

5.2.3.1 Shear Band Morphology

As mentioned in section 5.1.3.1, three types of shear bands have been identified in the vicinity of a tear crack. The significance of each type will now be considered.

Fig. 5.18 shows a tear specimen mounted in order to simulate its configuration during the test. The light source is positioned such that the edges of the shadow correspond approximately to the bending axes of the legs of the specimen. The angle that the shadow pattern makes with the tear crack is about 55° which is in good agreement with the angle that the first type of shear bands make with the crack (Figs. 5.10 and 5.11). It is proposed that these bands are associated with the bending of the legs of the specimen. Since there is a rapid increase in stress as the tip of the tear crack is approached, the radius of curvature of the bent material decreases towards the crack tip, causing the top of the trouser leg to be deformed into part of a roughly conical surface with the apex of the cone at the crack tip.

The second type of shear bands which are parallel to the crack propagation direction do not have any displacement perpendicular to the specimen surface. Thus, these should be mode II type shear bands which are formed by shearing on a plane approximately parallel to the propagation direction. The displacement within these bands is indicated by the steps they produced on the bending shear bands that they intersected (Fig. 5.12). It is proposed that these bands were formed to maintain compatibility between the tensile and compressive sides of the tear just ahead of the crack tip.

The single shear band extending ahead of the crack tip carries mode III type shear. This band can easily be differentiated from mode II displacements because it has a displacement component making an angle of about 70° to the surface of the sample (Fig. 5.15), and it leaves a step on the ribbon surface (Fig. 5.14). Also, mode III type displacements are indicated in Fig. 5.16b by the fragments of the material which moved from the ribbon surface towards the middle of the fracture surface.

The three components of plastic deformation ahead of a tear crack are depicted schematically in Fig. 5.19.

5.2.3.2 A Model of Tearing

In section 2.1.2.2, it was shown that for ductile materials, the tear energy Γ (per unit area of tear) is a measure of the plastic work γ_p for the production of a plastic zone at the tip of a crack and the energy required for the production of a new surface γ_s, i.e.

$$\Gamma = \gamma_s + \gamma_p \qquad 2.15$$

Breaking down the plastic work term in Equation 2.15 into three components, one for each of the identified modes of shear, we get

$$\Gamma = \gamma_s + (\Delta U_{bending} + \Delta U_{modeII} + \Delta U_{modeIII}) \qquad 5.2$$

where $\Delta U_{bending}$ is the plastic work due to bending of the legs of the specimen, $\Delta U_{mode\ II}$ and $\Delta U_{mode\ III}$ are the energies involved in mode II and mode III tearing, respectively.

i) Plastic work due to bending

Fig. 5.20a shows the stress and strain distribution in a linear elastic, perfectly plastic solid bent into a partially yielded state and it is assumed that this applies to the arms of a metallic glass specimen during the tear test. The plastic strain (ε_p) on the surface is given by

$$\varepsilon_p = nh \qquad 5.3$$

where h is the average step height of the shear bands and n is the number of bands per unit length (Fig. 5.20b). The elastic strain (ε_{Ys}) of the material at yield is

$$\varepsilon_{Ys} = \frac{\sigma_{Ys}}{E} \qquad 5.4$$

where E is Young's modulus and σ_{Ys} is the yield stress of the material. The total strain at the surface (ε_t) is the sum of these

$$\varepsilon_t = nh + \frac{\sigma_{Ys}}{E} \qquad 5,5$$

By assuming that the bending strain varies linearly with the distance from the neutral axis (which is taken to be at the centre of the section for simplicity), the

ratio of these strains can be written as

$$\frac{\varepsilon_{Ys}}{\varepsilon_t} = \frac{\frac{t}{2} - y_p}{\frac{t}{2}} \qquad 5.6$$

Combining Equations 5.4 -5.6 and rearranging gives the depth of the yielded region

$$y_p = \frac{tnh}{2\left(nh+\frac{\sigma_{Ys}}{E}\right)} \qquad 5.7$$

The plastic work due to bending may be expressed as

$$W_{bending} = \int \sigma_{Ys}\, \varepsilon_p \, dV \qquad 5.8$$

where dV is the volume of the element undergoing plastic deformation. Considering unit length of tear, the volume dV of the plastically deformed element of thickness d_y, situated at a distance y from the neutral axis is $(L\, d_y)$, where L is the width of the yielded zone. The plastic strain in this element is

$$\varepsilon_p = \frac{nh}{y_p}\left(y + y_p - \frac{t}{2}\right) \qquad 5.9$$

Combining Equations 5.7-5.9 and integrating over the depth of the plastic zone [from $y = (t/2 - y_p)$ to $y = t/2$] we get

$$W_{bending} = \frac{\sigma_{Ys} L (nh)^2 t}{4 (nh + \frac{\sigma_{Ys}}{E})} \qquad 5.10$$

the bending energy in each plastic zone per unit length of tear. There are four plastic zones adjoining the tear (one on each side of the tear, and one on each surface of the ribbon); two are in tension and the other two are in compression so the total bending energy per unit length of tear is the sum for the four zones. To get the energy per unit area of tear, this must be divided by the ribbon thickness t to give

$$\Delta U_{bending} = \frac{\sigma_{Ys} L_t (n_t h_t)^2}{2 (n_t h_t + \frac{\sigma_{Ys}}{E})} + \frac{\sigma_{Ys} L_c (n_c h_c)^2}{2 (n_c h_c + \frac{\sigma_{Ys}}{E})} \qquad 5.11$$

where the suffixes t and c refer to the tension and compression zones, respectively.

All the quantities on the right hand side of this expression have been determined experimentally. The values for a 57 μm thick specimen tested at room temperature are

$\sigma_Y = 2100 \times 10^6$ N/m^2

$E = 125 \times 10^9$ N/m^2

$L_t = 0.81 \times 10^{-3}$ m

$L_c = 0.80 \times 10^{-3}$ m

$n_t = 149 \times 10^3$ m^{-1}

$n_c = 88.5 \times 10^3$ m^{-1}

$h_c = h_t = 1.5 \times 10^{-7}$ m

Using these values gives $\Delta U_{bending} = 15.7$ kJ/m^2. This means that 16 % of the tear energy (97.5 kJ/m^2) is consumed in bending the legs of the trouser

specimens. The distribution of bending energy across the sides of the tear crack is not symmetrical. The plastic work expended on the convex side of the crack tip (that was subjected to a combination of direct tension and tensile bending) is 10.7 kJ/m^2, while the contribution of the concave side (subjected to direct tension and compressive bending) is only 5.0 kJ/m^2. This arises because the density of the bands is greater on the convex surfaces of the specimen. It is proposed that this difference between the convex and concave surfaces is due to the neutral axis being offset from the centre of the section when tensile and bending deformations are superimposed, as they are in each trouser leg in the vicinity of the tear tip.

ii) Plastic work involved in mode II deformation

The energy required for the formation of mode II type shear bands is

$$W_{modeII} = \tau_{Ys} \gamma \, dV \qquad 5.12$$

where τ_{YS} is the shear strength of the material (assuming that the Tresca criterion applies, $\tau_{YS} = \sigma_{YS}/2$), γ is the surface shear strain and dV is the volume of an element of material. For unit tear length, dV = wt where w is the width of the sheared region. Recalling the proposal that the purpose of these shear bands is to maintain compatibility between material on opposite sides of the tear, it follows that the shear strain in the bands varies linearly through the thickness and is zero at the centreline of the specimen, so the average shear strain in the volume element is taken to be only half that at the surface. The plastic work per unit area of tear mode II shear bands becomes

$$W_{modeII} = \frac{1}{2} \tau_{Ys} \gamma \, wt \qquad 5.13$$

The surface shear strain γ was estimated by measuring the change in the direction

of the bending shear bands caused by intersection with the mode II shear bands. Rewriting Equation 5.13 in terms of the values of γ and w on each surface of the ribbon, and dividing by the area of the tear (1 x t) gives

$$\Delta U_{modeII} = \frac{1}{2} \tau_{Ys}(\gamma_c w_c + \gamma_t w_t) \qquad 5.14$$

where suffixes t and c refer to the tension and compression zones respectively. Using the following data for a 57 μm thick specimen tested at room temperature

$\tau_{Ys} = 1050 \times 10^6$ MN/m^2

$\gamma_T = 0.26$

$\gamma_c = 0.36$

$w_t = 0.106 \times 10^{-3}$ m

$w_c = 0.163 \times 10^{-3}$m

the plastic work required for the mode II type shear bands is 45.3 kJ/m^2.

iii) Plastic work involved in mode III deformation

An expression for work done in mode III deformation (per unit area of tear) was derived by Kimura and Masumato (1981), and is

$$\Delta U_{modeIII} = \tau_{Ys} \frac{t}{2} \qquad 5.15$$

For a 57 μm thick ribbon tested at room temperature as $\tau_{Ys} = 1050$ MN/m^2 the expression gives a value for the plastic work of 30 kJ/m^2.

Kimura and Masumato (1981) assumed that the work done in mode III deformation accounted for all the tear energy of amorphous $Pd_{80}Si_{20}$. These

authors did not report detecting any other mode of deformation and indeed none is visible in their published micrograph. This is in sharp contrast to the results reported here which indicate that this mode of deformation contributes only 30-35% of the tear energy in amorphous $Ni_{78}Si_{10}B_{12}$. The two alloys have similar tear energies when compared at the same thickness, and the apparent absence of the bending and mode II bands near the crack tip in $Pd_{80}Si_{20}$ suggests that the deformation markings may have been obscured by surface roughness.

iv) The total plastic work

When the calculated values of plastic work due to bending and modes II and III shear are summed to give the total plastic energy (γ_p), a value of 91.0 kJ/m^2 is obtained which is in very good agreement with the measured value of tear energy (97.5 kJ/m^2). This estimate rests on the assumption that the shear band morphology observed after the test is characteristic of that which was obtained during the test. It is also assumed that no significant reversal of shear occurred during unloading. This estimate also depends on the assumption that the Tresca yield criterion holds for this alloy and that no work-hardening occurs. The criterion has been used to obtain a value for τ_{YS} from the observed value of the tensile yield stress, σ_{YS} (which was taken to coincide with the tensile fracture stress).

5.2.3.3 The Effect of Temperature on the Tear Energy

The components of tear energy (given by Equations 5.11, 5.14 and 5.15) at 77 K can be evaluated from the deformation parameters assembled in Table 5.2 and the results appear in Table 5.3. The estimated total tear energy at 77 K (124 kJ/m^2) is in good agreement with the measured value of 114 kJ/m^2. The increase in plastic work due to modes II and III which occurs over the temperature range

from 300 K to 77 K is about 15 %: this is due primarily to an increase in the shear strength τ_{YS} of 15 %. The increase in the plastic work due to bending is larger over this temperature range; the plastic work at 77 K is enhanced not only by an increase in the yield strength σ_{YS}, but also by an increase in the length of the shear bands on the tension surface, and to an increase in the average step height of these bands.

5.2.3.4 The Effect of Specimen Thickness on the Tear Energy

Published work has shown that the tear energy of brittle materials such as rubber is independent of thickness (Greensmith and Thomas, 1955), whereas that of plastically deforming materials shows a linear dependence on thickness (Sims, 1975, Isherwood and Williams, 1978). The amorphous $Ni_{78}Si_{10}B_{12}$ undergoes extensive plastic deformation during tearing, and accordingly, the tear energy has been found to be a linear function of the thickness of the sample over the thickness range studied (10-57 μm (Fig. 5.8)). A similar relationship between the tear energy and the specimen thickness was observed by Kimura and Masumato (1981) in amorphous $Pd_{80}Si_{20}$. These authors pointed out that this dependence is in accordance with Equation 5.15 in cases where the tear energy is dominated by mode III plastic work.

The present results indicate that the work associated with bending and mode II deformation is also thickness dependent. The dependence of tear energy upon thickness is directly related to the volume of the material yielded ahead of the crack tip. The width L of the region containing bending shear bands decreased from 800 μm to 350 μm and the width w of the mode II region decreased from 105 to 60 μm when the thickness of the specimen was decreased from 57 to 25 μm which means that there was approximately a five-fold decrease in the volume of the material deformed plastically (Table 5.2). Table 5.3 compares the plastic work calculated using equations 5.11, 5.14 and 5.15 with the experimentally determined tear energy (Fig. 5.8). The predicted 55 % decrease in plastic work when the

thickness is reduced from 57 to 25 μm is in agreement with the observed decrease in tear energy. A similar but less detailed explanation was advanced for ductile polymers by Chiu et al. (1984), and for a wide range of ductile metals and polymers by Isherwood and Williams (1978).

The three modes of plastic deformation described in this section are thought to be a general feature of tearing. They are manifested clearly in this alloy because deformation occurs by the formation of conspicuous shear bands. In crystalline alloys, slip bands are more diffuse but the same deformation geometry must apply.

5.2.4 Summary

Amorphous $Ni_{78}Si_{10}B_{12}$ is a tough and strong alloy. Plastic deformation at room temperature occurs by the nucleation and propagation of shear bands. In tensile tests, formation of localized shear bands leads to fracture before any large scale plastic deformation develops so that the clear evidence of plastic flow can only be seen in the vein pattern on the fracture surfaces parallel to the planes of maximum shear stress. A plastic zone forms ahead of the notch in specimens loaded in tension. Under plane-stress conditions, localized plastic zones are dominated by shear bands elongated in the direction of crack extension. These zones resemble the plastic zones attending Dugdale's plane-stress model of a crack in an elastic-plastic material. The mathematical treatment of the Dugdale model offers reasonable description of the sizes and displacements. In this case, fracture occurs by a mode III antiplane shear decohesion mechanism.

Trouser leg specimens loaded in mode III tension showed plastic zones with recognizable components of deformation. Three types of shear bands were observed near the tip of the tear crack; one type was associated with bending of the testpiece while the others were evidence of types II and III shear deformation. Based on these observations of the nature of plastic deformation, a model has been proposed from which an accurate estimate of the tear energy has been obtained. Among the

components of the tear energy, the contribution of mode III shear was only 30-35 %. The model accounts for the observed linear dependence of the tear energy with specimen thickness in terms of the volume of plastically deformed material. The increase in the tear energy with decreasing the test temperature is due mainly to the corresponding increase in the yield strength of the material.

Table 5.2 Influence of test temperature and specimen thickness on the morphology of shear bands (tear rate = 1.7×10^{-2} mm/s).

Temperature (K)	thickness (μm)	Bending Shear Bands						Mode II Shear Bands			
		n (mm^{-1})		L (μm)		h (μm)		w (μm)		γ	
		Tension	Compression	Tension	Compression	Tension	Compression	Tension	Compression	Tension	Compression
77	57	117.5	82.5	1100	860	0.25	0.25	82	201	0.30	0.30
298	57	149.0	88.0	800	810	0.15	0.15	106	163	0.26	0.36
298	25	270.0	170.0	350	325	0.07	0.07	60	65	0.30	0.32

Table 5.3 Calculated and observed tear energies

Temperature (K)	Thickness (μm)	Tear Energy (kJ/m^2)				
		Calculated				Measured
		ΔU_{bend}	ΔU_{II}	ΔU_{III}	ΔU_{pl}	
77	57	36.0	52.5	35.6	124.1	114.0
298	57	15.7	45.3	30.0	91.0	97.5
298	25	5.4	21.0	13.1	39.5	44.0

Figure 5.1 Tensile fracture surface of an unnotched specimen.

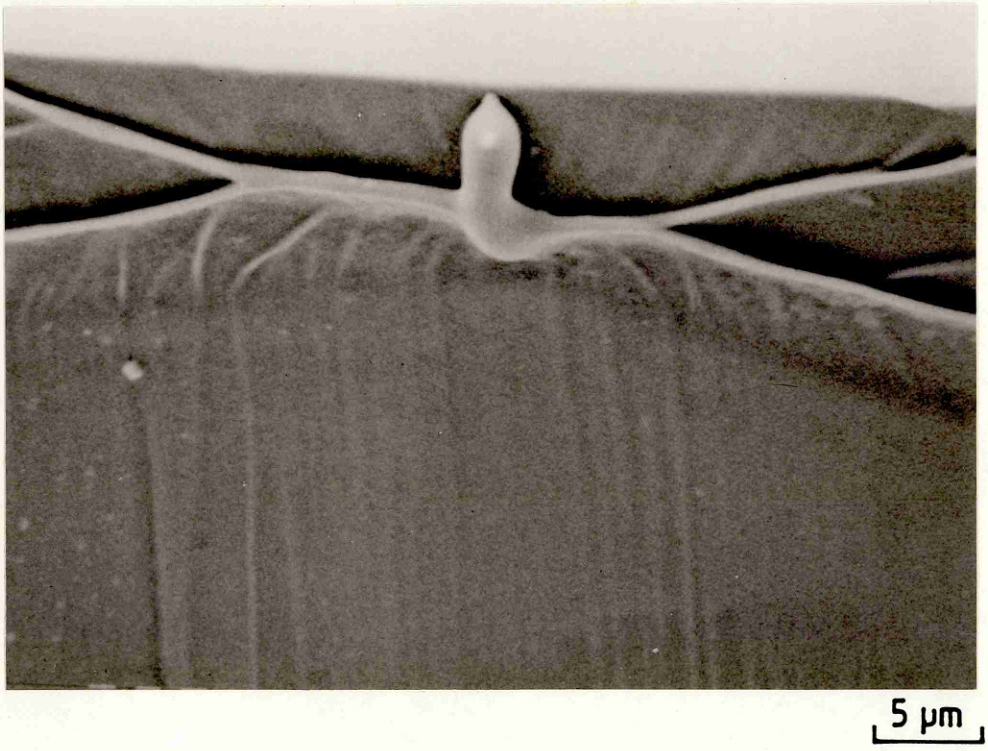

Figure 5.2 Local necking point at the junction of veins on the tensile fracture surface.

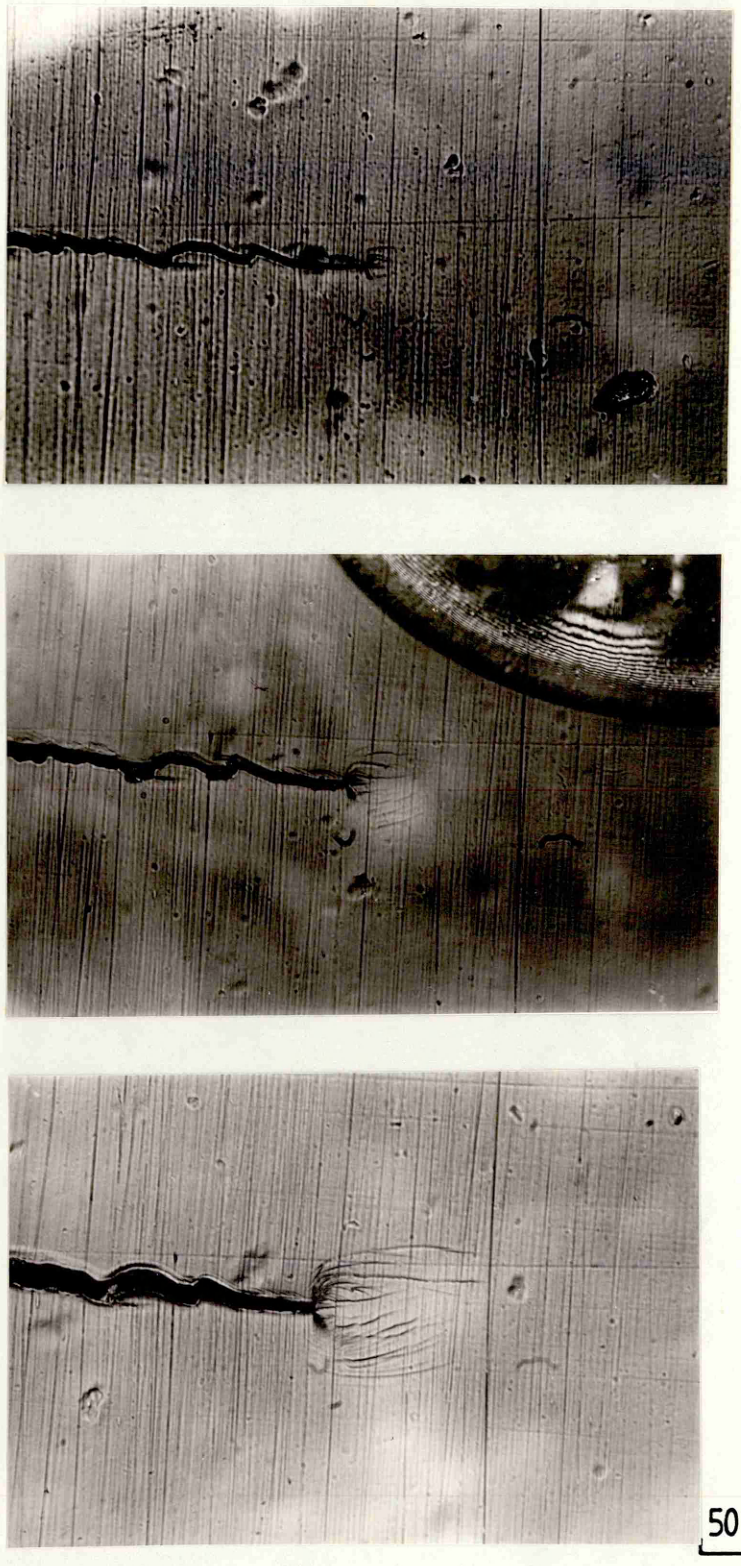

Figure 5.3 Development of the plastic zone at the crack tip of a SENT specimen with the applied stress intensity.

a $K = 11\ MPa\sqrt{m}$

b $K = 25\ MPa\sqrt{m}$

c $K = 36\ MPa\sqrt{m}$

d

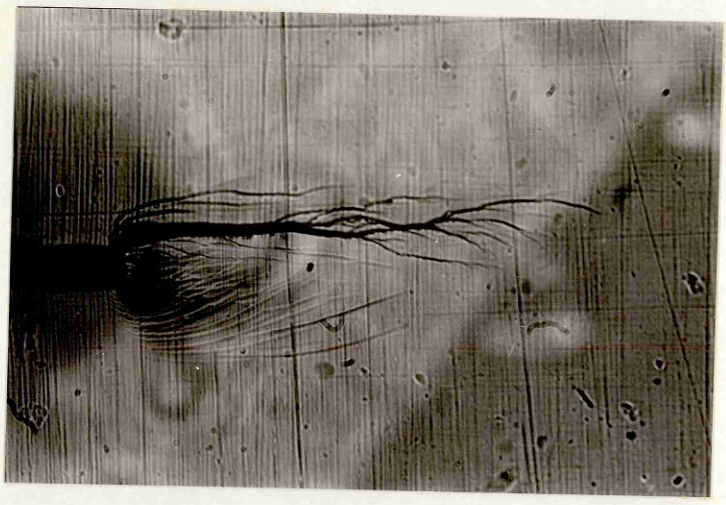

e

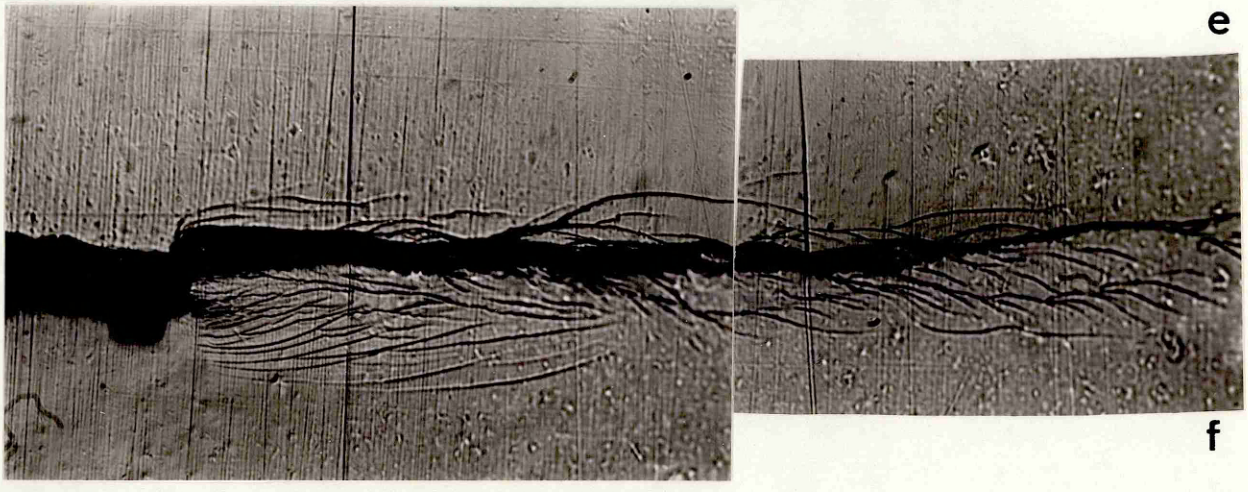

f

50 μm

Figure 5.3 (con'd) Development of the plastic zone at the crack tip of a SENT specimen with the applied stress intensity.

d $K = 42.5$ MPa$\sqrt{m}$

e $K = 52$ MPa$\sqrt{m}$

f $K = 65$ MPa$\sqrt{m}$

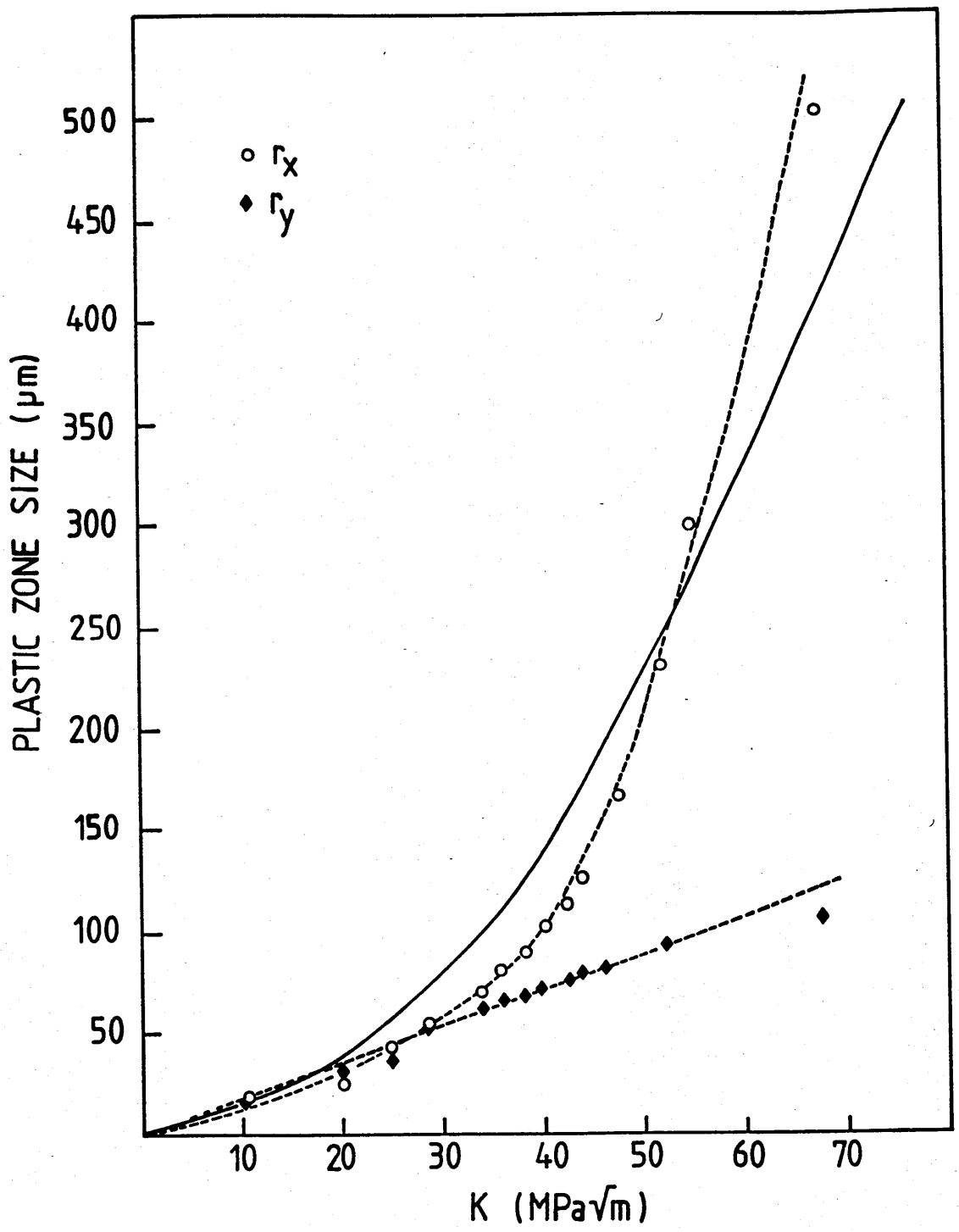

Figure 5.4 The size of plastic zone as a function of applied stress intensity (the solid line is the plastic zone size according to Dugdale model).

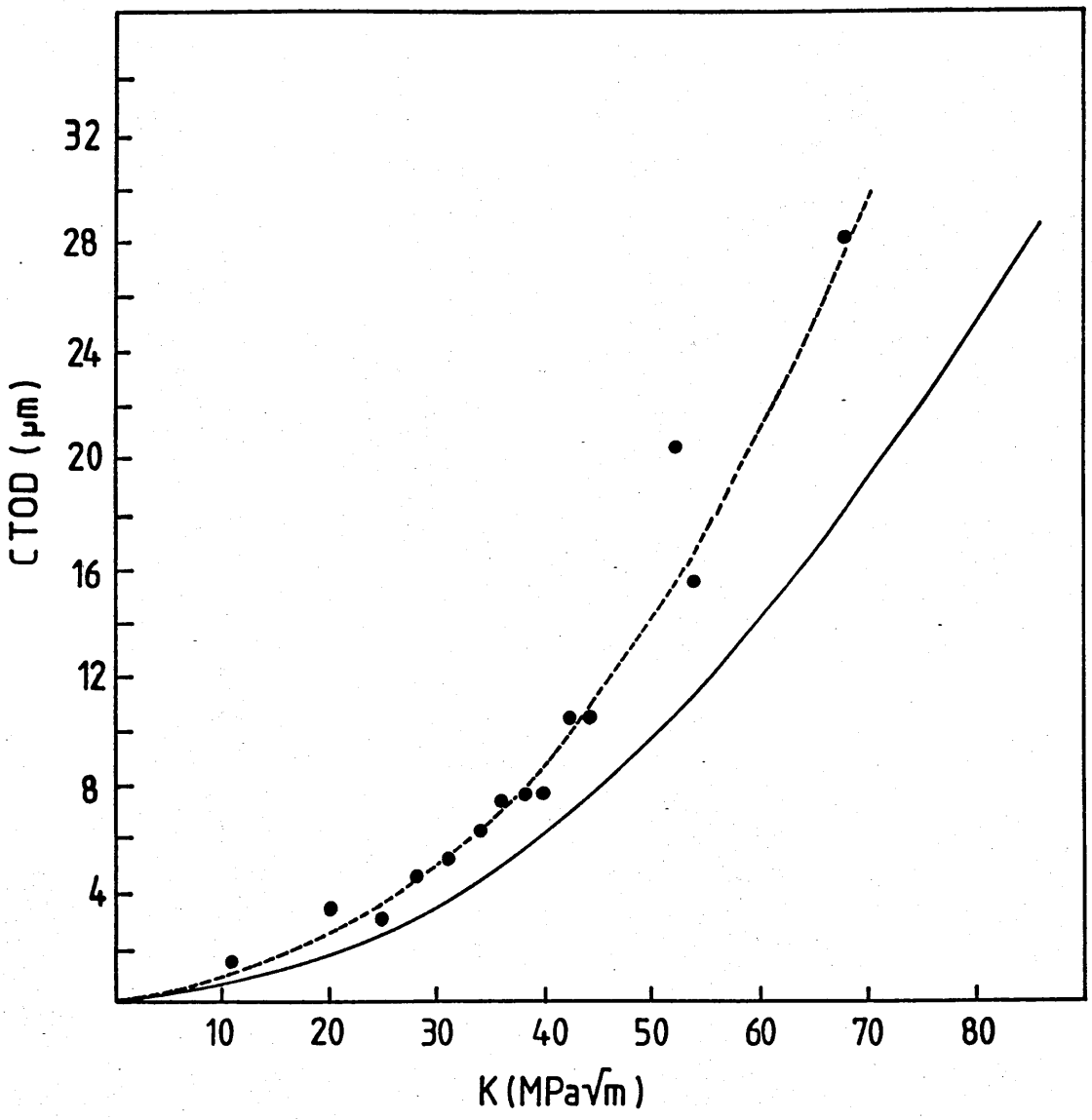

Figure 5.5 The crack tip opening displacement as a function of applied stress intensity (the solid line represents the crack tip opening displacement according to Dugdale model).

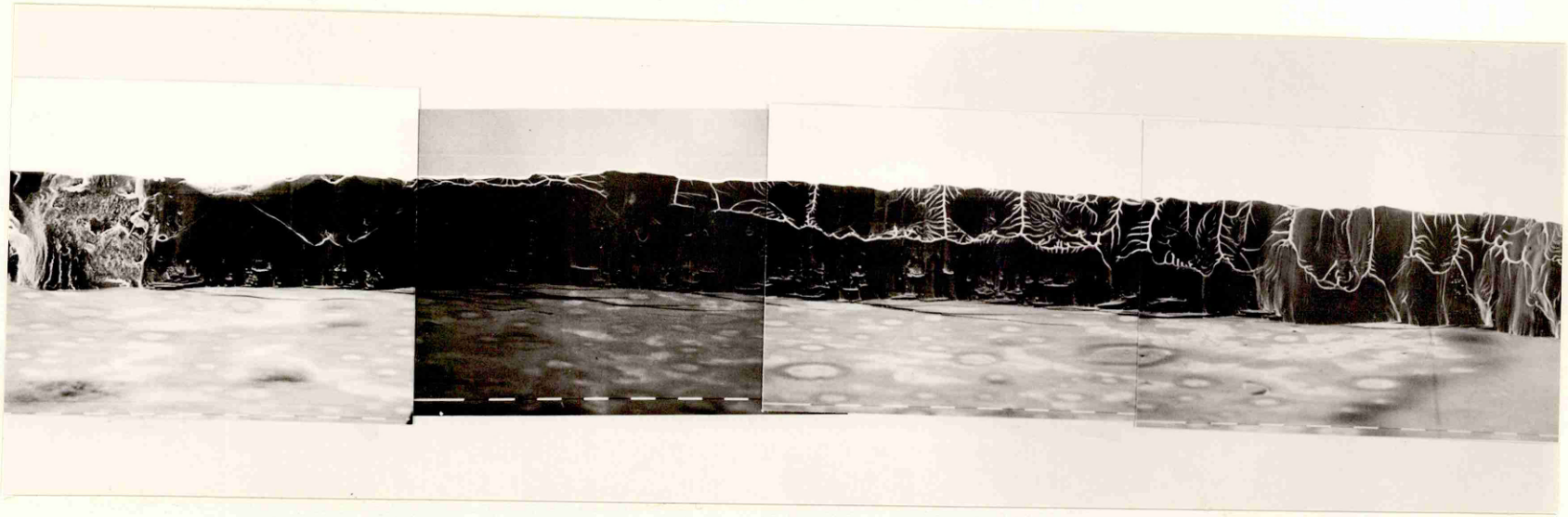

Figure 5.6 Fracture surface of a SENT specimen (K_c = 68 MPa√m).

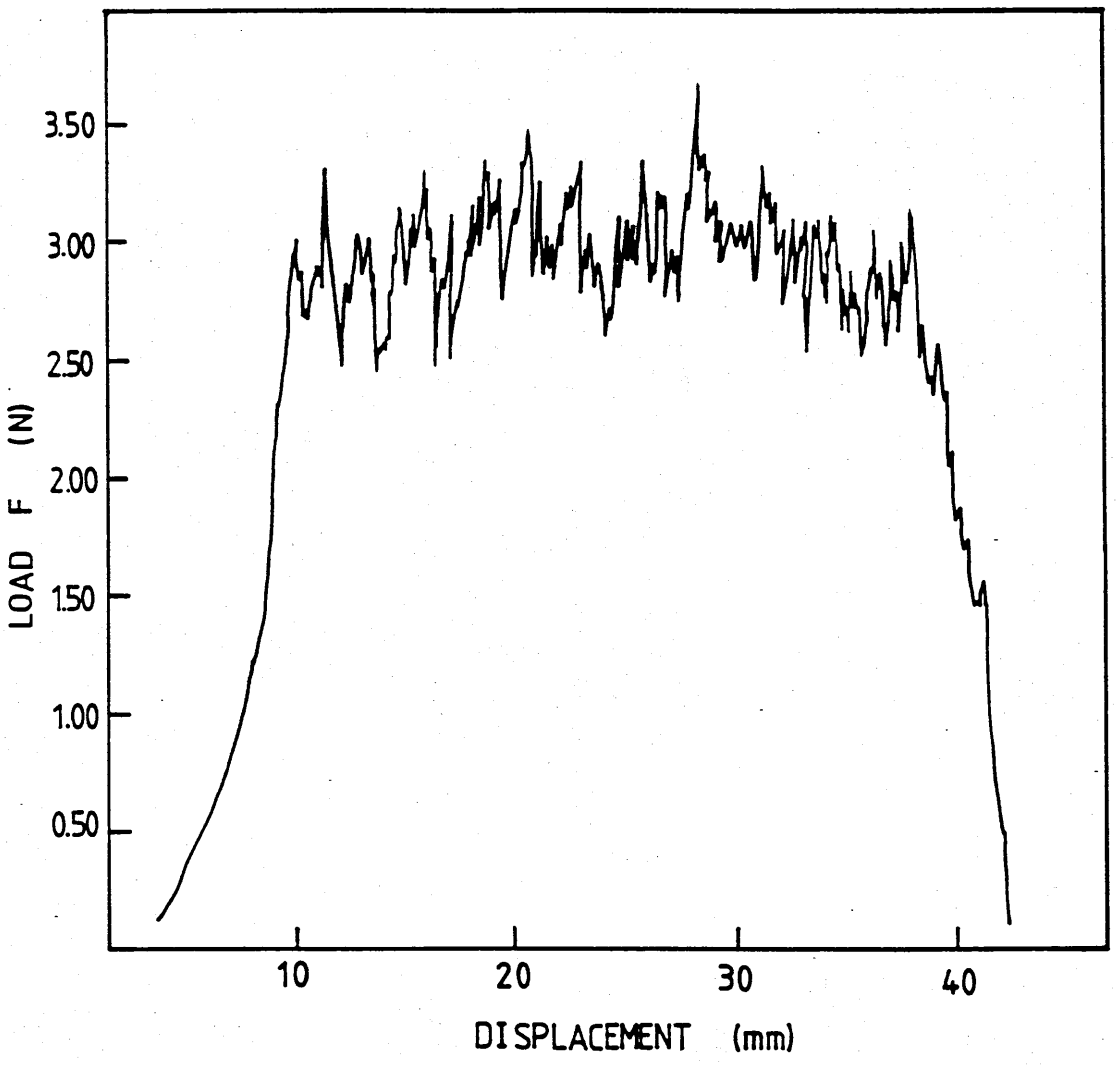

Figure 5.7 Tearing force F, versus extension curve for a 57 μm thick specimen ($R = 1.7 \times 10^{-7}$ mm/sec).

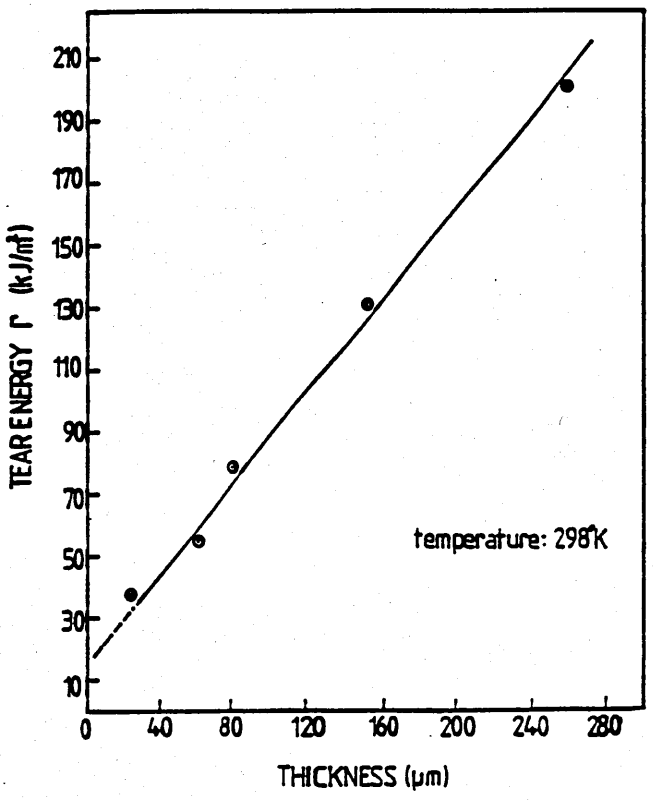

Figure 5.8 Dependence of tear energy, Γ, upon the thickness of the specimen.

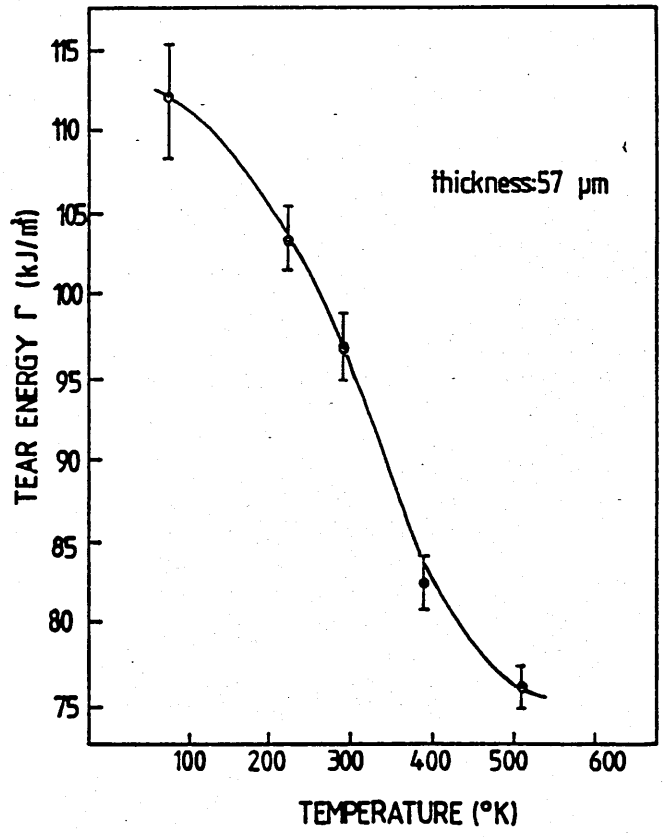

Figure 5.9 Dependence of tear energy, Γ, upon the test temperature (the bars represent the standard deviation).

Figure 5.10 Morphology of the yielded region around the tear. (the tear crack propagates to the top of the figure).

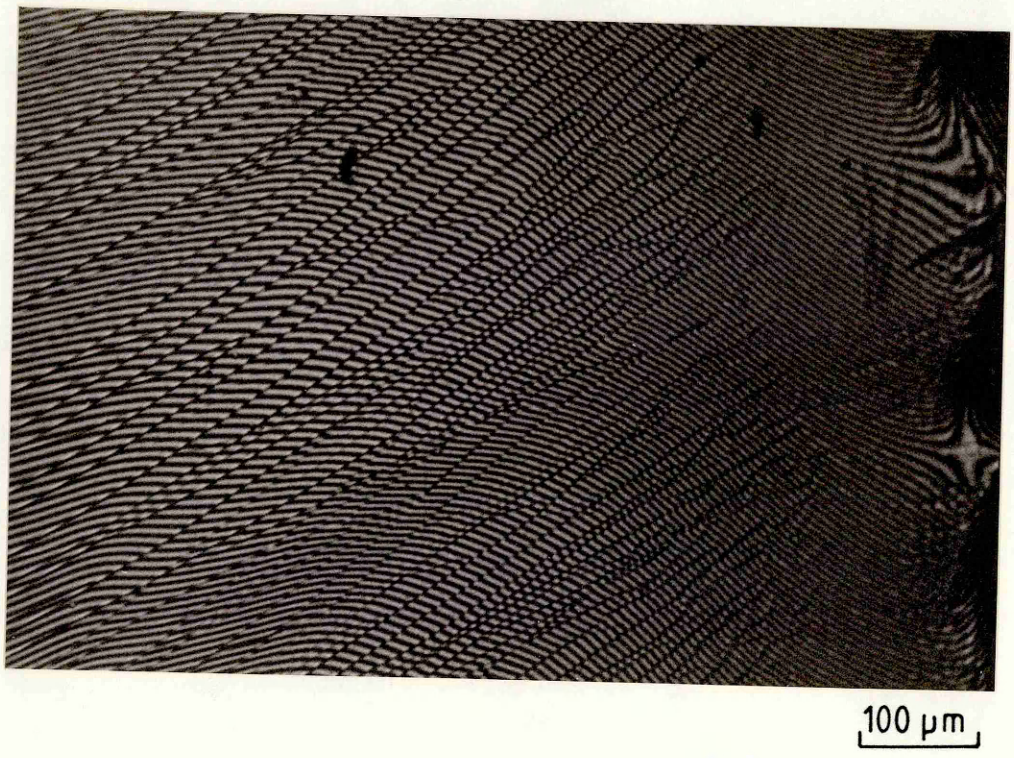

Figure 5.11 Interference micrograph of the steps produced by the shear bands on the surface of the specimen.

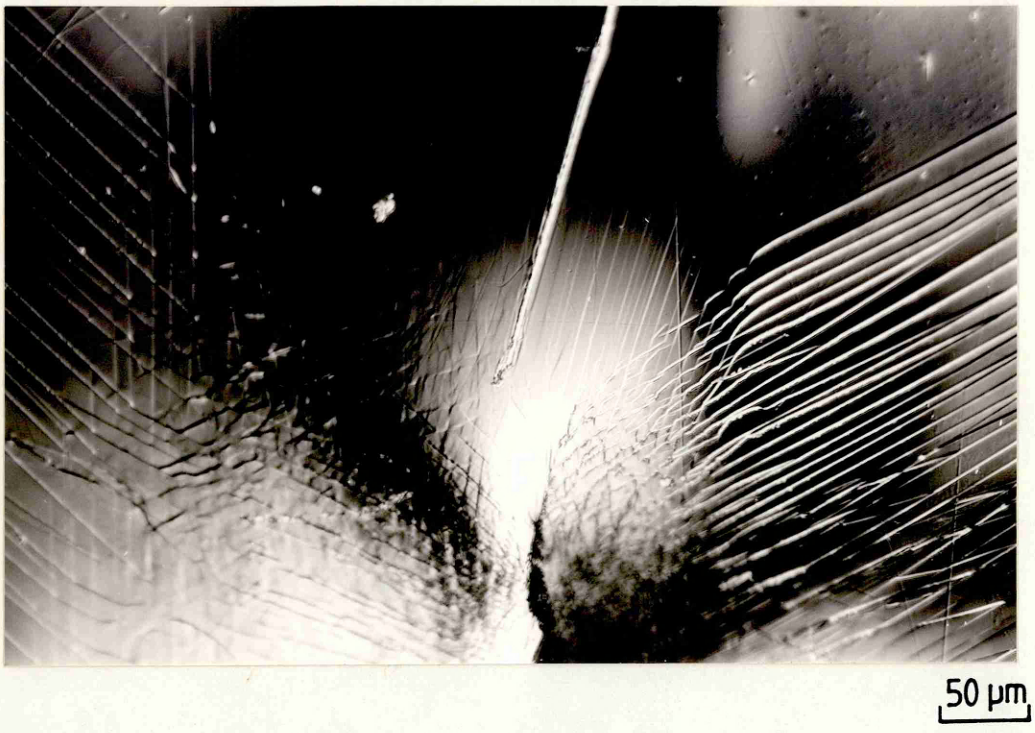

Figure 5.12 Nomarski contrast micrograph of the crack tip. The tear is directed towards the top (the mark at the top of the figure is a surface scratch).

Figure 5.13 Nomarski contrast micrograph of the region in the wake of the tear (tensile side of the ribbon).

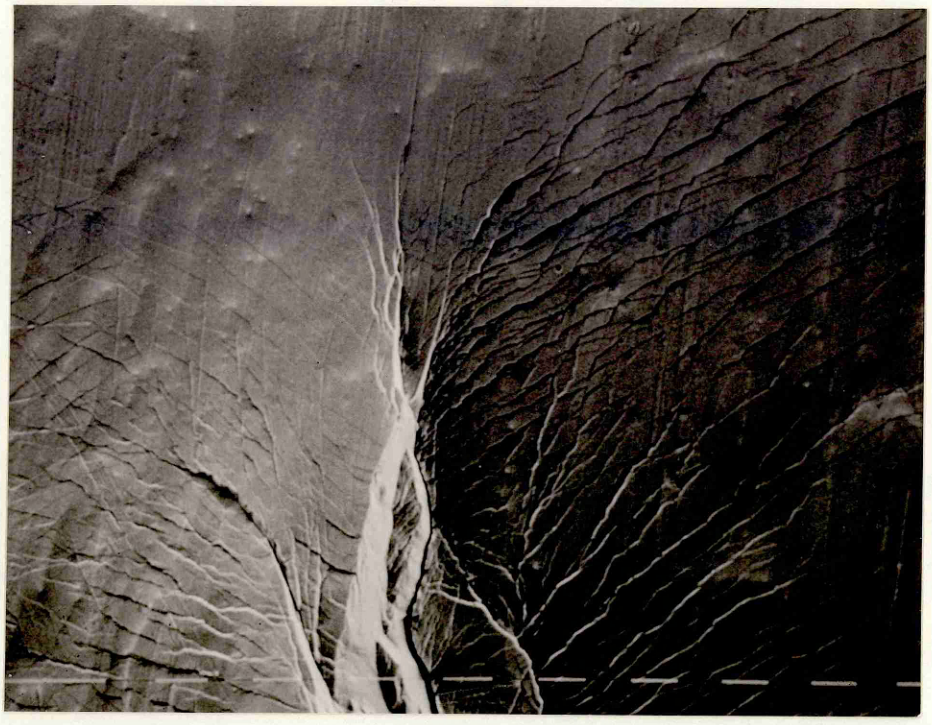

Figure 5.14 SEM micrograph of the tear crack tip.

Figure 5.15 Crossection of the shear band ahead of the crack tip. The section was taken ~30 µm from the crack tip.

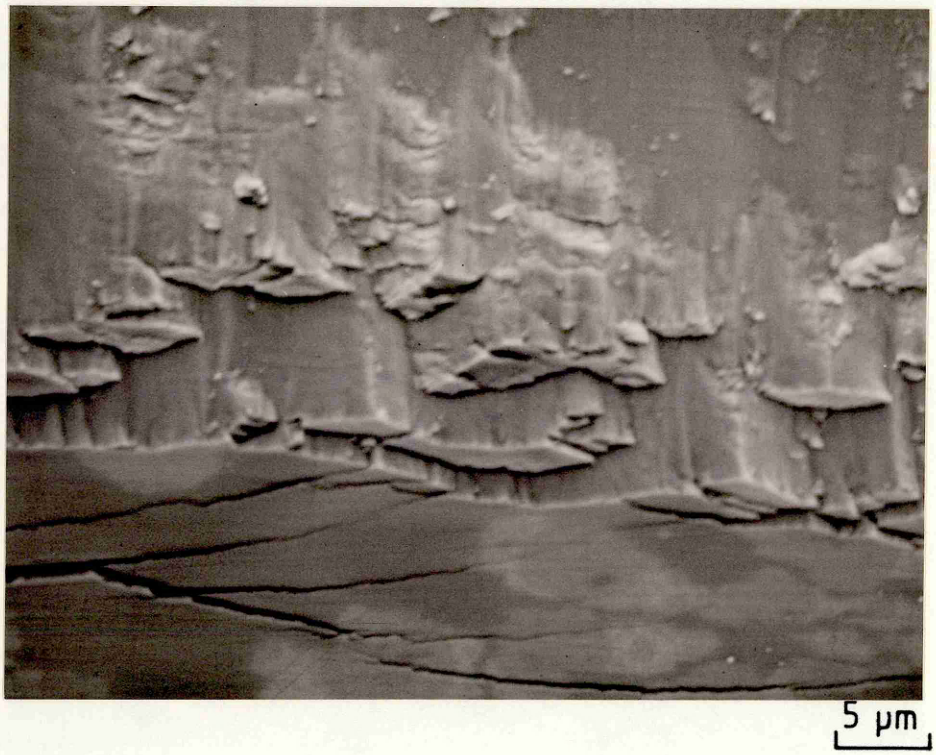

Figure 5.16a Fracture surface of a trouser leg tear specimen (crack propagation is from the right of the figure).

b Displacements of the fragments of the material from the surface of the ribbon.

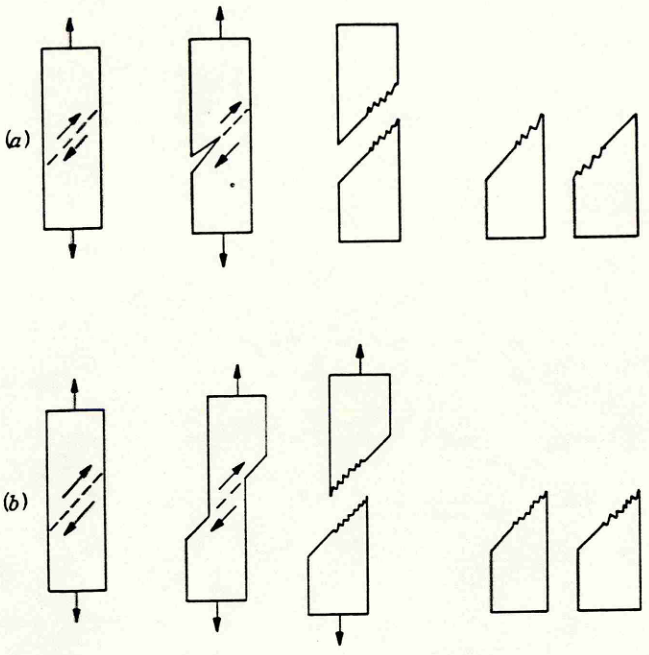

Figure 5.17 Schematic illustration of possible shear fracture modes in ribbon specimens loaded in tension; a) shear crack propagation b) plastic shear and fracture.

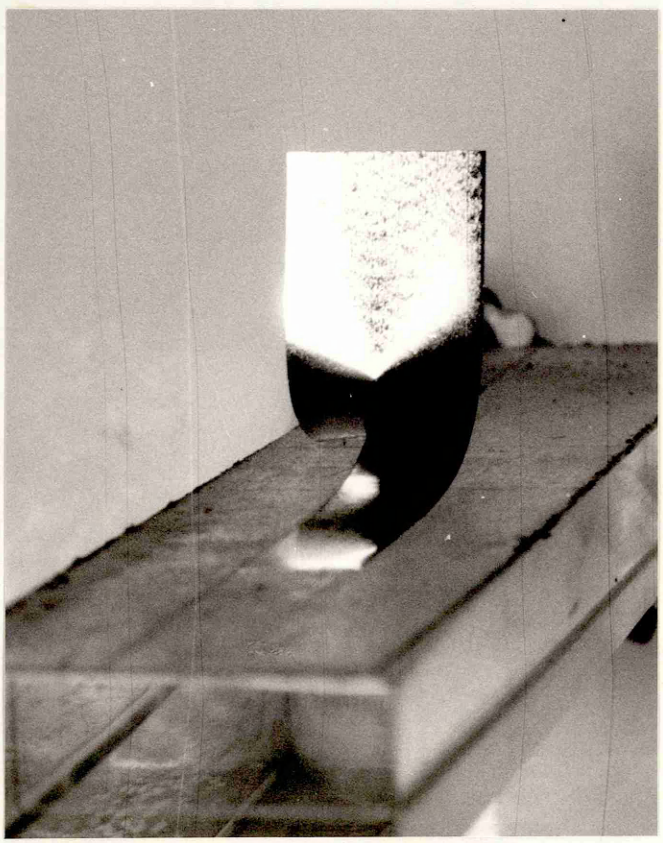

Figure 5.18 Tear specimen mounted in test configuration. The edges of the shadow correspond to the bending axes of the arms

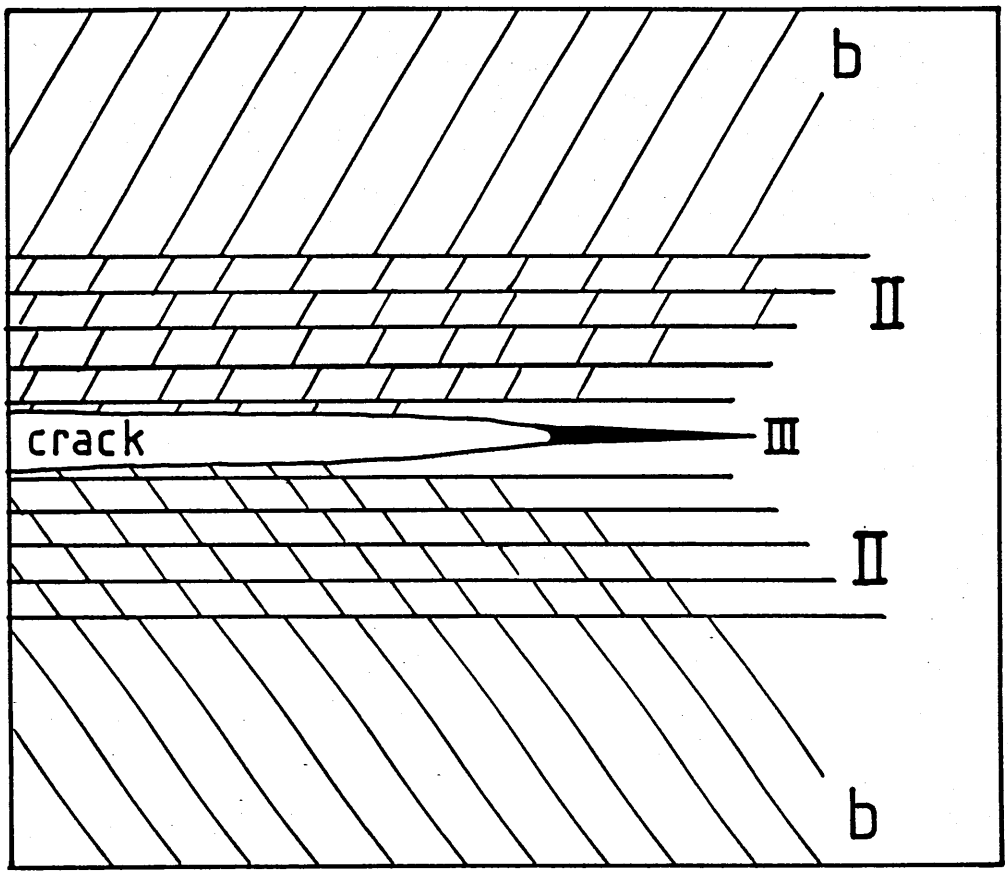

Figure 5.19 Schematic diagram of the components of inhomogeneous deformation ahead of the tear crack tip. Numbers II and III represent mode II and III type of displacements respectively. Shear bands due to bending are indicated by letter b.

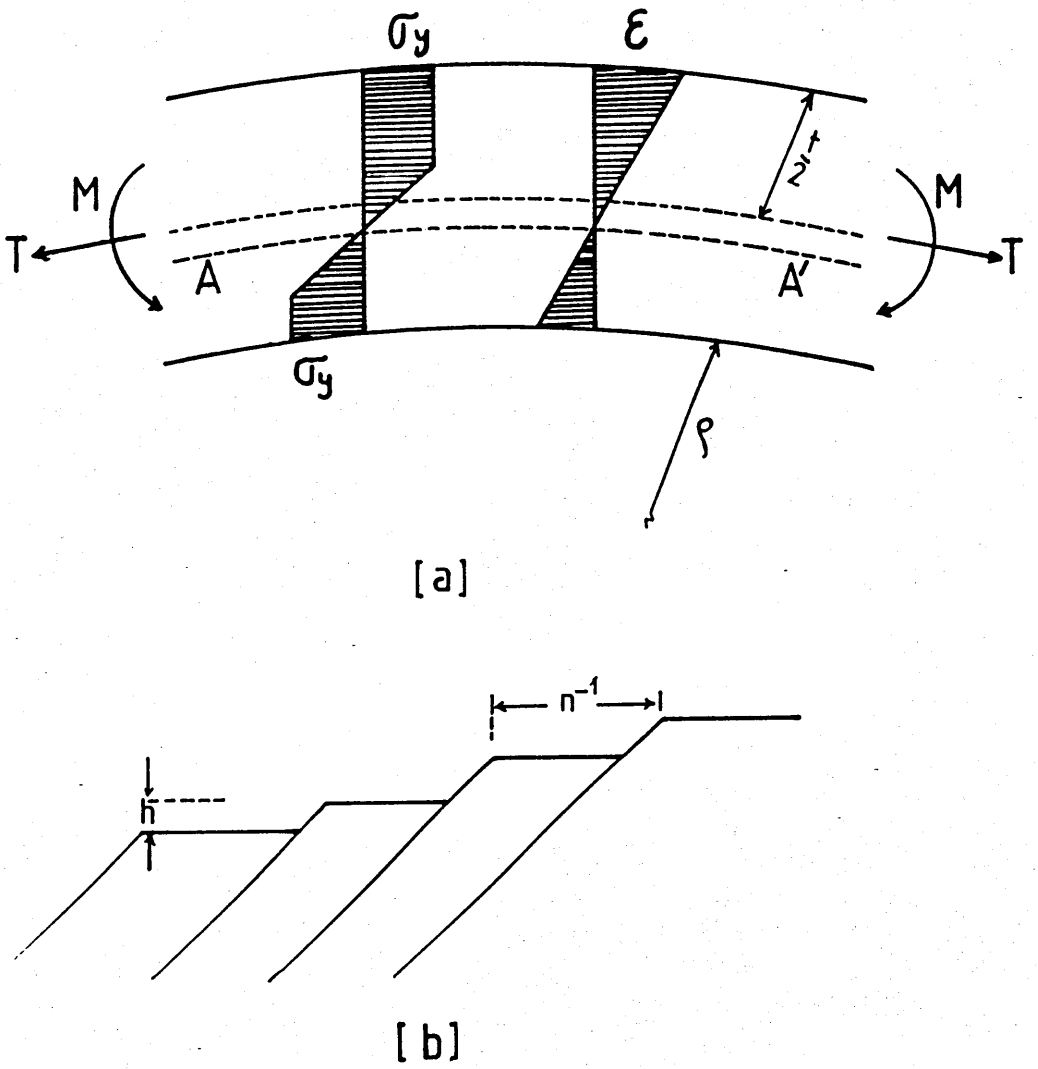

Figure 5.20a Schematic diagram of the stress distribution in a ribbon bent into elastic-plastic regime. Due to the presence of superimposed tensile stresses the neutral axis (AA') shifts from the geometric centre of the specimen.

b Assumed surface morphology of bending shear bands.

CHAPTER SIX

FATIGUE CRACK PROPAGATION

In this chapter, experimental results on the propagation of fatigue cracks in $Ni_{78}Si_{10}B_{12}$ are presented and discussed. Micromechanisms of crack extension and the effect of R-ratio on crack growth will be the two main subjects to be considered in detail.

6.1 Results

6.1.1 S-N Curve

The determination of the S-N curve was the first step of the experimental programme on the fatigue crack propagation behaviour of $Ni_{78}Si_{10}B_{12}$. Fatigue tests were carried out using specimens and procedures described in section 4. 2. 6. The S-N curve for the unnotched specimens tested at an R-ratio = 0.1 is presented in Fig. 6.1. The curve exhibits a distinct fatigue limit at $\sigma_{max} = \sigma_{\infty} = 510$ MPa.

At stress levels just above the fatigue limit, about 90 pct of the fatigue lives of the specimens was spent before the formation of identifiable fatigue cracks (~0.10 - 0.15 mm long) Cracks almost always initiated at or near the thin edges of the specimens. At high stress amplitudes, a number of well developed shear bands and arrested cracks were found at different locations. However, near the fatigue limit, no cracks could be detected other than the one that propagated to failure.

6.1.2 Fatigue Crack Propagation at R = 0.1

6.1.2.1 da/dN versus ΔK curve

Fatigue crack propagation tests were performed as described in section 4.2.5. The relation between the crack growth per cycle, da/dN, and the applied ΔK was

determined as follows: first, the mid-range growth rates were determined and then, the threshold ΔK_{TH} was approached using the manual load-shedding technique. High growth rate data was collected by the constant load technique. Each point on the curve represents an average of data from 3-8 different specimens. As seen in Fig. 6.2, the da/dN vs ΔK curve at $R = 0.1$ has a typical sigmoidal shape and three main regions can be identified according to the changes in the slope:

i) For mid-range growth rates $\sim 10^{-6} - 4 \times 10^{-4}$ mm/cycle, a linear relation exists between log da/dN and log ΔK. Although a slight deviation from linearity can be seen towards the lower growth rates in this region, the dependence of da/dN on ΔK can be expressed by the following Paris-Erdogan Equation

$$\frac{da}{dN} = (2.5 \times 10^{-7}) \Delta K^{2.2} \qquad 6.1$$

ii) At growth rates above $\sim 4 \times 10^{-4}$ mm/cycle, the slope of the curve increases drastically as the value of K_{max} approaches that of the critical stress intensity $K_c \approx 67$ MPa$\sqrt{m}$.

iii) At lower rates below 10^{-6} mm/cycle, the slope of the curve increases rapidly with decreasing ΔK to a threshold value of crack growth ΔK_{TH}. In this study, ΔK_{TH} is defined as the value of the stress intensity range corresponding to the situation in which no crack growth could be detected after 10^6 cycles. The value of ΔK_{TH} determined in this way was 0.5 MPa$\sqrt{m}$.

6.1.2.2 Fractography at R = 0.1

After the crack growth tests, fracture surfaces were examined by scanning electron microscopy. The observed variations in the fracture topologies correlate with the changes in the applied ΔK and the growth rate. These variations have been investigated with respect to the three regions of the da/dN vs ΔK curve.

Unless otherwise stated, the crack growth direction is towards the right of the figures.

i) High Growth Rates

Fig. 6.3 shows typical fractographic features of this region; the fracture surface is dominated by the "static" modes of failure. On the near edge of the specimen, the crack front has followed surface shear bands and divided the fracture surface into segments of different elevation. It can be seen that in each of these segments, striated areas have been formed. The featureless zone on the far edge of the specimen indicates the development of a shear crack. Macroscopically, the fracture surface is inclined at about 30-40 degrees to the loading axis. At a slightly higher value of ΔK, catastrophic failure of the specimen occurred with further development of the static shear cracks, as shown in Fig. 6.4.

ii) Intermediate Growth Rates

Along this region, a number of different fracture topographies are observed with decreasing ΔK. At high ΔK levels, fracture surfaces exhibited striations. An example of a striated area at $\Delta K = 43$ MPa$\sqrt{m}$ is shown in Fig. 6.5, and Fig. 6.6 illustrates a magnified view of the striated region. The average striation spacing in this area is ~0.3 μm. The striations do not form a continuous pattern. As the fracture surface corresponds to the high ΔK end of the linear growth law region, it still contains some features of the static modes of failure.

No striation pattern could be detected below $\Delta K \approx 30$ MPa$\sqrt{m}$. Figs. 6.7-6.9 show examples of fracture surfaces corresponding to ΔK values between $\Delta K = 17$ and 10 MPa$\sqrt{m}$. These surfaces are characterised by a series of curved, parallel lines extending in the thickness direction. The spacing between these lines decreases with ΔK as shown in Fig. 6.10, but the average spacings are about 20 times larger than the corresponding measured crack growth per cycle.

At ΔK's below 10 MPa$\sqrt{m}$, the fracture morphology changes once more. As seen in Fig. 6.11, at $\Delta K = 9$ MPa$\sqrt{m}$, the fracture surface exhibits large "paraboloidal" facets which cover about 50 pct of the fracture surface, while the remaining sections display periodic fracture markings. Figs. 6.12 and 6.13 show

the fracture surfaces at $\Delta K = 6$ and 3 MPa$\sqrt{m}$ respectively. These figures indicate that the paraboloidal facets are the only fractographic features at lower ΔK levels in the Paris region. The size of these facets progressively decreases with ΔK until below $\Delta K \approx 1.5$MPa$\sqrt{m}$, they tend to disappear (Fig. 6.14). Quantitative fractographic data presented in Fig. 6.15 shows the change in the relative proportions of the areas covered by coarse periodic fracture markings and paraboloidal facets as a function of ΔK. The variation in the average length of the paraboloidal facets (measured in the direction of crack advance) with ΔK is shown in Fig. 6.16.

iii) Near Threshold Growth

Fracture surfaces in this region become virtually flat and perpendicular to the loading axis. Figs. 6.17 and 6.18 show the fracture topology of the alloy at $\Delta K = 0.7$ MPa$\sqrt{m}$. These figures reveal that fracture surfaces near ΔK_{TH} exhibit fine elongated ridges extending in the direction of crack propagation, perpendicular to the crack front.

6.1.2.3 Crack Tip Morphology

A series of experiments was carried out to observe the crack profiles and the plastic zones at the crack tips at different ΔK levels: after growing the fatigue crack at the desired ΔK, the test was stopped and the crack tip was replicated using a cellulose acetate tape. These replicas were then processed as described in section 4.3.1 for examination by scanning electron microscopy and typical results are presented in Figs. 6.19-6.22. It can be seen that the plastic zones are characterized by localized deformation bands. The number, size, and distribution of these bands change according to the applied ΔK level.

The variation in the shape of the crack profile between $\Delta K = 9$ and 1 MPa$\sqrt{m}$ is shown in Fig. 6.23. The crack front follows a periodic spiral or a zig-zag path until $\Delta K \approx 3$ MPa$\sqrt{m}$. Below this value, it becomes straight and perpendicular to the loading axis. A high magnification picture of the crack profile at $\Delta K = 9$ MPa$\sqrt{m}$ is shown in Fig. 6.24.

6.1.3 Effect of R-ratio on Fatigue Crack Propagation

Fig. 6.25 is a plot of da/dN vs ΔK for the alloy at $R = 0.1$ and $R = 0.5$. To eliminate possible specimen to specimen variation, growth rates were determined at constant ΔK and by varying R-ratio on a single specimen. It was ensured that the increments over which measurements were taken represented distances 7-10 times larger than the maximum plastic zone size to avoid the retardation effects, especially after the measurements at $R = 0.5$ where K_{min} exceeds K_{max} at $R = 0.1$. The order of application of R-ratios has occasionally been reversed and it was observed that such a change did not affect the results. Each point shown in Fig. 6.25 represents an average of measurements taken from four different specimens. The data show a strong R-ratio dependence of threshold, with ΔK_{TH} increasing from 0.5 MPa$\sqrt{m}$ at $R = 0.1$ to about 1.1 MPa$\sqrt{m}$ at $R = 0.5$. It is also seen that near threshold crack growth rates at $R = 0.1$ are markedly faster than those at $R = 0.5$. For both conditions, the growth curves converge at about $\Delta K = 6$ MPa$\sqrt{m}$ and the crack growth rates become independent of R-ratio.

To obtain a more precise picture of the R-ratio dependence of crack growth rates, da/dN vs R-ratio plots have been determined at two constant ΔK levels, i.e. at $\Delta K = 2.5$ and 3.5 MPa$\sqrt{m}$ for R-ratios from 0.1 to 0.8. Results are presented in Fig.6.26 which shows that da/dN decreases as R-ratio is increased. A sharp decrease in growth rates occurs between $\approx 0.2 \leq R \leq 0.4$ but rates remain almost independent of further increases in R-ratio.

It was observed that the change in R-ratio has also a significant effect on the fracture surface morphology of the alloy. Fig. 6.27 shows the fracture morphology of the alloy at $\Delta K = 3$ MPa$\sqrt{m}$. Although the increase in R-ratio from 0.1 to 0.5 did not change the basic faceted appearance of the fracture surfaces, the size of the facets became smaller with the increase in R-ratio. Another example of the change in the size of facets as a function of R-ratio is given in Fig. 6.28 which also shows that the surface produced at $R = 0.5$ contains smaller facets than the

one obtained at R = 0.1 (for a constant $\Delta K = 2 MPa\sqrt{m}$). The fracture morphologies of the alloy at $\Delta K = 5 MPa\sqrt{m}$ are shown in Fig. 6.29 for R = 0.1 and 0.5. The change in R-ratio at this ΔK did not produce any significant change in the size of the facets.

6.1.3.1 Effect of R-ratio on Threshold Crack Growth in a Stainless Steel

In order to see whether such an R-ratio dependence of crack growth rates is peculiar to the metallic glass or is an aspect of very thin specimens, the fatigue crack propagation behaviour of stainless steel specimens (AISI 316) of 52 μm thickness has been studied as a function of R-ratio. AISI 316 is an austenitic stainless steel with the nominal composition (w/o) 0.08 % C, 0.03 % N(max), 18 % Cr, 12 % Ni, 2 % Mo, 1.5 % Mn (max). The alloy was supplied in the form of annealed sheets (grain size 15 μm) and has the following mechanical properties:

0.2% Proof Stress: 241 MPa

Tensile Strength: 541 MPa

Youngs modulus: 195 GPa

The R-ratio dependence of fatigue crack growth rates in the bulk specimens of this steel is well known (e.g. Pickard, 1975) and during the present study, da/dN vs ΔK tests have been carried out on SENT specimens with similar dimensions as those used for testing amorphous $Ni_{78}Si_{10}B_{12}$ (Fig. 4.2). As mentioned before, the latter specimens were only 5 μm thicker than the stainless steel.

The da/dN vs ΔK curves for AISI 316 at R = 0.1, 0.3 and 0.5 are shown in Fig. 6.30 (where each point is the average of measurements from three different specimens obtained following the same data collection procedure described for amorphous $Ni_{78}Si_{10}B_{12}$). Increasing the R-ratio from 0.1 to 0.5 increases near threshold crack growth rates and decreases ΔK_{TH} from $13 MPa\sqrt{m}$ at R = 0.1 to $7 MPa\sqrt{m}$ at R = 0.5. The curves converge with increasing ΔK and the effect of R-ratio diminishes.

Fig. 6.31 shows the change in da/dN with R-ratio at $\Delta K = 13.3 MPa\sqrt{m}$. As the

crack growth rates at R = 0.1 in this figure and in Fig. 6.26 (for $\Delta K = 2.5 MPa\sqrt{m}$) are similar (i.e. $da/dN \approx 1.5 \times 10^{-6}$ for AISI 316 and $\approx 2 \times 10^{-6}$ and amorphous $Ni_{78}Si_{10}B_{12}$ respectively), the effect of R-ratios can be compared on this basis. For AISI 316, on increasing R-ratio within the range 0.1-0.3, the crack growth rates increase by about an order of magnitude but then remain relatively unaffected by further increases in the value of the R-ratio.

Fractographic features of AISI 316 corresponding to crack growth rates at R = 0.5 and R = 0.1 are shown in Fig. 6.32a and b respectively (for $\Delta K = 13.3 MPa\sqrt{m}$). The fracture surfaces produced at low and high R-ratios show faceted, structure-sensitive features. A very similar fracture morphology is produced at both R = 0.1 and R = 0.5.

Fatigue crack tip morphologies of the stainless steel were examined by SEM after the tests. Fig. 6.33a and b show the profiles of the fatigue cracks on the specimen surface for R = 0.5 and R = 0.1 at $\Delta K = 13 MPa\sqrt{m}$. These figures reveal the transgranular nature of crack extension and indicate that the local plastic deformation pattern in the vicinity of the crack tip is considerably different from that of amorphous $Ni_{78}Si_{10}B_{12}$ (e.g. Fig. 6.21). In AISI 316, plastic deformation is more homogeneously distributed over a number of grains near the crack front and the slip bands are crystallographic.

6.1.3.2 Crack Opening and Closure

In amorphous $Ni_{78}Si_{10}B_{12}$, crack tip opening displacements (CTOD) at different stages of a fatigue cycle have been determined using a double stage replication technique. Crack opening measurements were made for R = 0.1 and R = 0.5 at two ΔK levels. The selected ΔK levels were $\Delta K = 5 MPa\sqrt{m}$, a level at which almost no effect of R-ratio on crack growth rates was observed and $\Delta K = 2.5 MPa\sqrt{m}$, a level at which crack growth rates decreased nearly 3 times with an increase of R from 0.1 to 0.5. Fig. 6.34 shows typical photographs of a crack at $\Delta K = 5 MPa\sqrt{m}$ and R = 0.1 during the unloading half of the fatigue cycle. Crack tip

opening displacements were determined over a distance of 15 μm at intervals of 1 μm from the crack tip . Figs. 6.35a and b show the variation of CTOD with the distance behind the crack tip for R = 0.1 at ΔK = 5 MPa$\sqrt{m}$ and ΔK = 2.5 MPa$\sqrt{m}$ respectively. The same behaviour was observed in both the loading and unloading halves of the fatigue cycle consistently.

At each load level, to eliminate the differences arising from the variations of CTOD with the distance from the crack tip, measurements were averaged over the distance of 15 μm from the crack tip and an average value CTOD was obtained. Fig. 6.36 shows the plot of the applied load vs average CTOD for R = 0.1 and R = 0.5 at ΔK = 2.5 MPa$\sqrt{m}$. Similarly, Fig. 6.37 shows the change of the average CTOD with the applied load for the same R-ratios at ΔK = 5 MPa$\sqrt{m}$.

6.2 Discussion

6.2.1 Fatigue Crack Initiation

The S-N curve of $Ni_{78}Si_{10}B_{12}$ under an R-ratio of 0.1 exhibits a distinct fatigue limit (σ_∞) at σ_{max} = 510 MPa or in terms of stress amplitude, at σ_a = 230MPa (Fig. 6.1). The fatigue limit can be expressed as a fraction of monotonic tensile strength of the alloy which gives a value of $\sigma_{max}/\sigma_{UTS}$ = 0.24 (σ_a/σ_{UTS} = 0.11). When this value is compared with the $\sigma_\infty/\sigma_{UTS}$ ratios of other metallic glasses shown in Table 3.2 (where σ_∞ is expressed in terms of σ_{max}), it is seen that this ratio is in good agreement with those of the glasses with comparable tensile strength.

For crystalline materials, the fatigue limit is also commonly expressed as a fraction of the ultimate tensile strength, σ_{UTS}. In steels, for example, the fatigue limit (expressed as the stress amplitude under an R-ratio of zero) for smooth specimens has long taken to be about 40 % of the tensile strength. On the other hand, the endurance limit (at 5×10^8 cycles) of some precipitation hardened

aluminium alloys has been determined to be about 25 % of σ_{UTS}.

In high-cycle fatigue approaching the fatigue limit, most of the life time of the specimens is spent in the crack initiation stage. In crystalline alloys , the role of slip bands in introducing a fatigue crack is well known (Fine and Ritchie, 1978). Accumulation of slip in a local region results in severe roughening of the surface of the material which in turn leads to the initiation of microcracks. Resistance to fatigue is thus expected to be lower in those materials in which plastic deformation is concentrated into deformation bands. Inhomogeneous slip produces large slip displacements ('extrusions' and 'intrusions') on the specimen surface which facilitates the nucleation of fatigue cracks. The effect of the slip distribution on the initiation of cracks has been studied widely in aluminium alloys and the observed low $\sigma_\infty/\sigma_{UTS}$ ratios in these alloys have been attributed to the localization of slip (Lu and Weismann, 1978, Graf and Hornbogen, 1978).

Since the localization of strain is an inherent aspect of deformation in metallic glasses, these arguments can be extended to explain the low fatigue limit seen in this alloy. As noted in section 6.1.1, the examination of the surface of the specimens during S-N tests revealed that near the fatigue limit, about 90 pct of the fatigue life of $Ni_{78}Si_{10}B_{12}$ specimens was spent in the formation of cracks of ~100-150 μm long. Thus, in smooth specimens crack nucleation is the critical stage of this process. Since it was ensured that the surfaces of the specimens were polished to 1 μm and that no inclusions or other defects could be detected in the region where cracks were nucleated, the fatigue limit may be identified with the stress required for the formation of a shear band. It is known that in metallic glasses, once the shear bands mucleate, they persist and subsequent deformation proceeds with very little work hardening in these bands (Pampillo, 1974) so that the onset of shear band formation may be regarded as synonymous with inception of microcracks. Therefore, it could be proposed that the fatigue limit in metallic glasses corresponds to the cyclic yield stress for shear band formation.

Verification of this hypothesis should be sought by determining the cyclic stress-strain curves of the alloy. However, as metallic glass specimens are in the

shape of thin ribbons, it is very difficult to determine these curves by either of techniques used for bulk specimens because they involve compressive loading. Thus, it is not surprising that no reports of the measurement of the cyclic stress-strain curves of metallic glasses could be traced in the literature.

6.2.2 Micromechanisms of Fatigue Crack Growth

Fractographic results presented in section 6.1.2 suggest that the formation of striations and the components of "static" fracture modes such as failure from 45 degrees shear bands are characteristic features of high crack growth rates. Over a large region of growth rates (between $\sim 10^{-6}$ - $\sim 4 \times 10^{-4}$mm/cycle) crack growth rates can be expressed by the Paris-Erdogan Law with an exponent $m \approx 2$. Striations have been observed only at high ΔK levels in this region. Fracture surfaces at lower ΔK's are first characterized by "coarse periodic structures" and then by "paraboloidal" facets. Near ΔK_{TH}, these facets are replaced by smooth fracture surfaces containing fine elongated ridges.

In crystalline alloys, the origin of the fracture morphologies have been interpreted in terms of the interaction between the crack tip plasticity and the microstructure. However, amorphous $Ni_{78}Si_{10}B_{12}$ has no specific metallurgical microstructure, i.e. no grain boundaries or second phase particles which can have important effects on fracture morphologies. But as we have seen, it has a distinct deformation structure. Thus, in this section, the micromechanisms of fatigue crack growth will be discussed by establishing possible correlations between the structure of the shear bands, the nature of fracture surfaces and the applied ΔK.

6.2.2.1 Threshold and Near Threshold Growth

Fatigue cracks in $Ni_{78}Si_{10}B_{12}$ can grow at remarkably low ΔK levels. At $R = 0.1$, the threshold stress intensity, ΔK_{TH}, has been found to be 0.5 MPa$\sqrt{m}$. The

measured ΔK_{TH} can be considered to consist of a component, ΔK_{TH}^{c}, over which the crack remains closed and a component related to the material's resistance to crack extension, ΔK_{TH}^{i}, over which the crack faces move apart. Thus, the ΔK_{TH} can be expressed as (eg. Suresh and Ritchie, 1984)

$$\Delta K_{TH} = \Delta K_{TH}^{c} + \Delta K_{TH}^{i} \qquad 6.2$$

ΔK_{TH}^{c} is the stress intensity range which must be exceeded to overcome the influence of roughness induced and/or oxide induced crack closure. ΔK_{TH}^{i} involves intrinsic material factors including the cyclic yield strength, the cyclic hardening exponent, the slip mode, the slip distribution and slip reversibility (Hornbogen, 1983, Gerberich, et al., 1984, Lankford, 1985).

Fig. 6.19 shows the morphology of the crack tip at the specimen surface at $\Delta K = 0.7$ MPa$\sqrt{m}$, just above ΔK_{TH}. The crack tip is attended by a plastic zone which consists of a single shear band about 0.5 μm long. Qualitatively, ΔK_{TH}^{i} in Equation 6.2 can be regarded as the minimum stress intensity range below which irreversible shear displacements cannot occur within this band. The low ΔK_{TH} observed in $Ni_{78}Si_{10}B_{12}$ is possibly due to the ease of the formation of such localized shear bands in metallic glasses.

The trace of the shear band on the specimen surface lies perpendicular to the loading axis, and it is of interest to consider how shear displacements can occur in such a shear band. The high magnification fractograph in Fig. 6.18 indicates the existence of elongated ridges on the fracture surface in the direction of crack growth. It is proposed that these are the decohered ligaments of the shear band and that the shear leading to the crack advance occurred on the slant faces of these bands. A simple model of crack advance by the shear decohesion on the faces of the band, idealized as prismatic facets, is shown in Fig. 6.39. The height of these bands is about 0.5 μm at ΔK=0.7 MPa$\sqrt{m}$ but increases to about 1.0 μm at ΔK=1.2 MPa$\sqrt{m}$.

6.2.2.2 Intermediate Growth Rates

At crack growth rates ~ 10^{-6} mm/cycle ($\Delta K \approx 2$ MPa$\sqrt{m}$), fracture morphologies start to change and the surfaces are characterized by "paraboloidal" facets. The size of the facets increases with ΔK until they disappear at growth rates ~ 10^{-5} mm/cycle (Figs. 6.11-6.14).

The origin of these facets can again be explained in terms of the morphology of the shear bands. A typical example of the crack tip morphology on the surface of the alloy at $\Delta K = 5$ MPa$\sqrt{m}$ is shown in Fig. 6.21. It is seen that the plastic zone is no longer a single shear band but comprises a number of bands that form a parabolic pattern. There exists a clear relation between the size and shape of the shear bands and the fracture path behind the crack tip. Thus, it is not difficult to predict that crack growth occurred by the advance of the crack front along one of the bands within the plastic zone. Alternating parabolic segments can be seen at the edge of the fracture surface at $\Delta K = 6$ MPa$\sqrt{m}$ (Fig. 6.12). It is suggested that in three dimensional form, crack growth along parabolic shear bands lead to the formation of paraboloidal facets across the specimen seen on this fractograph. The average length of these facets (measured in the direction of crack advance) is about 30 μm. This is in good agreement with the length of the region over which shear bands extend ahead of the crack tip at a similar ΔK (Fig. 6.21).

The distribution of shear bands in the plastic zone and shear stress-strain distribution pattern is close to that predicted by slip line field theory for isotropic plastic non-hardening materials. As noted by Rice and Johnson (1970), the theoretical stress distribution ahead of a sharp crack (under monotonic loading conditions) in rigid plastic materials can be represented by the Prandtl slip line field (Fig. 2.10). For small scale yielding conditions, the Prandtl slip line field analysis indicates that there is no shear strain concentration in the region ahead of the crack tip. The lack of focussing shear bands in this region in the metallic glass is consistent with this prediction. According to Rice and Johnson, shear

strains concentrate only in the regions above and below the crack tip, (i.e. in fan C in Fig. 2.10). Levy et al. (1971), on the other hand, calculated that shear strains should occur at an angle of 70 degrees to the crack plane in a non-hardening material (Equation 2.28). In $Ni_{78}Si_{10}B_{12}$, the measurement of the angle between the shear bands originating from the crack tip and the crack plane showed that this angle is about 75-80 degrees which is in good agreement with Levy's numerical analysis. However, it should be emphasized that analysis based on Prandtl slip line theory predicts stress-strain distributions for plane strain state and for monotonic loading conditions. The crack in $Ni_{78}Si_{10}B_{12}$ is under cyclic loading conditions and since the observed plastic zone lies on the surface of the specimen, it might represent a plane stress state. The size of the plastic zone at $\Delta K = 5$ MPa$\sqrt{m}$ (measured perpendicular to the crack plane between the two outlying shear bands) is ~ 20 μm. This can be compared with the plane stress plastic zone size predicted by Equation 2.16. When the monotonic yield strength of the alloy (σ_{YS}= 2100 MPa) is used, Equation 2.16 gives a plastic zone size $r_p = 0.99$ μm. However, if the cyclic yield stress $\sigma_{YS}^{c} = 510$ MPa (assumed to be equal to fatigue limit stress) is used instead, r_p is found to be 15.3 μm in good agreement with the measured value.

By increasing ΔK from 5 to 9 MPa$\sqrt{m}$, the size of the plastic zone increases from ~20 to ~45 μm and accordingly the length of the paraboloid facets enlarge from ~30 to ~50 μm (Figs. 6.23 and 6.11). Similarly, when ΔK is decreased to 3 MPa$\sqrt{m}$, the plastic zone size decreases to about 3 μm, leading to smaller fracture facets 5 μm long (Figs. 6.20 and 6.13).

Although it appears that the process is controlled by ΔK, the exact mechanism of shear band decohesion resulting in facet formation is not clear. However, fracture markings in the form of parallel lines observed on the surfaces of some paraboloidal facets suggest that fracture occurred by intermittent jumps of the crack front.

Faceted fracture morphologies have been widely observed in crystalline alloys. These facets, however, have been termed "microstructurally sensitive" and are strongly influenced by grain size/ plastic zone interactions (Beevers, 1977,

Ritchie, 1979, Minakawa and Mc Evily, 1981). Shear fracture along localized bands during fatigue appears to be unique to $Ni_{78}Si_{10}B_{12}$. Fracture morphologies of other metallic glasses at growth rates below 10^{-5} mm/cycle have not been studied in detail. But a fractograph of a $Pd_{80}Si_{20}$ alloy in a paper by Ogura et al. (1976) shows a feature referred to as a "large void" of 30 μm in diameter which resembles the facets observed in the present study.

Clayton and Knott (1976) showed that in high strength steels with low work hardening capacity, fracture under static loads occurred along localized shear bands (Fig. 2.11). It was observed that such a fracture resulted in an "alternating spiral" crack profile reminiscent of that seen in $Ni_{78}Si_{10}B_{12}$. Fracture surfaces of the specimens contained "rounded valleys". They attributed the formation of these valleys to the change in the direction of a shear band when it encountered an inclusion. However, as such microstructural obstacles are not present in $Ni_{78}Si_{10}B_{12}$, the effect might be attributed to the intersection of the shear bands.

At growth rates above ~10^{-5} mm/cycle ($\Delta K \approx 10$ MPa$\sqrt{m}$), the proportion of facets starts to decrease to the benefit of the areas covered by periodic fracture markings (Figs. 6.7-6.9). These markings which are in the form of curved lines parallel to the crack front are characteristic features of fracture surfaces between growth rates corresponding to $\Delta K \approx 11$- ~30 MPa$\sqrt{m}$. As shown in Fig. 6.10, there is a direct relation between the spacing of these fracture lines and growth rate. However, the average spacing between the lines exceeds the measured crack growth per cycle by approximately an order of magnitude. More specifically, at a given ΔK level, about 20 load cycles are required to advance the crack front between adjacent markings so that they do not correspond to striations in the classical sense. Fig. 6.22 shows the morphology of shear bands on the surface of a specimen tested at ΔK=16 MPa$\sqrt{m}$. It is seen that the plastic zone is composed of a much larger number of shear bands than those seen at lower ΔK's (e.g. Fig. 6.21). It is proposed that with the increase in shear band density, crack growth occurs by the decohesion of the ligaments between the shear bands. This is unlike at lower ΔK's

where crack extension occurs along one of the shear bands within the plastic zone.

Fine striations appear at even higher ΔK's in the Paris region (Fig. 6.6). By measuring the spacings between the striations, it is possible to calculate the microscopic growth rate and this can be compared with the macroscopic growth rate determined during the tests. This comparison is done at $\Delta K = 43$ MPa$\sqrt{m}$. At this ΔK, the average spacing between the striations is 0.3 μm. On the assumption that the striations are loci of the crack front on successive loading cycles, this corresponds to a microscopic growth rate = 3×10^{-4} mm/cycle. From the measured da/dN vs ΔK curve, the macroscopic growth rate at $\Delta K = 43$ MPa$\sqrt{m}$ is 1.4×10^{-4} mm/cycle. Thus, there exists reasonable correlation between the striation growth rate and the macroscopic growth rate, bearing in mind the possibility of small local variations in ΔK on the fracture surfaces.

6.2.2.3 High Growth Rates

The important aspect of the fracture surfaces at high growth rates is the transition from planar (90°) to slant (40-45°) crack growth. This is typical behaviour in thin sheets. It is possible to relate the onset of the transition to the occurrence of plane stress conditions. Above a critical ΔK ($\Delta K = 50$ MPa$\sqrt{m}$, i.e. $\Delta K \approx 0.75\ K_C$), featureless shear lips start to develop at the edges of the specimens. It was shown that shear lip development on 45° planes to the loading axis is associated with static loading. This suggests that crack growth is controlled by K_{max}. The development of shear lips is an instability effect and finally leads to the catastrophic failure of the specimen at $K_{max} = K_C$.

The mechanisms proposed to explain the fatigue crack extension near threshold and at medium growth rates are summarized in Fig. 6.40.

6.2.3 Effect of R-ratio on Threshold Crack Growth

Experimental results indicate that in amorphous $Ni_{78}Si_{10}B_{12}$, mid-range crack growth rates ($10^{-5} < da/dN < 5 \times 10^{-4}$ mm/cycle) are not affected by changes in R-ratio. However, below this range, crack growth rates show a strong R-ratio dependence: the growth rates at R = 0.5 fall below those at R = 0.1. The effect of R-ratio becomes more pronounced with a decrease in the applied ΔK and a two-fold increase in the value of ΔK_{TH} is observed when R is raised from 0.1 to 0.5. Examination of the variation of crack growth rates with R at constant ΔK values just above the threshold shows that the decrease in da/dN with increasing R occurs between R-ratios ~ 0.2-0.4. Crack growth rates then remain independent of further increases in R (Fig. 6.26).

An important aspect of near threshold fatigue crack growth in this alloy is the correlation between the crack growth rate and the fracture appearance. At a given crack growth rate which can be obtained by two different combinations of ΔK and R, fracture morphologies are similar, i.e. they contain facets of similar size. However, when R is raised from 0.1 to 0.5 at a constant applied ΔK level, the size of the facets becomes smaller while the crack growth rate decreases (Figs. 6.27-6.28). As discussed in the previous section, for a crack advance leading to a smaller facet size, both the size of the plastic zone and the length of the shear bands should become smaller. Therefore, a reduction in the facet size at a constant applied ΔK means that the effective driving force for crack extension (ΔK_{eff}) decreases when R is increased from 0.1 to 0.5. Consequently, the deceleration of crack growth rates with increasing R is associated with a reduction in ΔK_{eff}. It should be noted that at $\Delta K = 5$ MPa$\sqrt{m}$ where crack growth rates are almost independent of the value of R-ratio, no significant difference on the fracture morphologies produced at R = 0.1 and R = 0.5 can be observed (Fig. 6.29). Thus, at $\Delta K = 5$ MPa$\sqrt{m}$ and above (over the range studied) the driving force for crack extension remains virtually unaffected by R-ratio.

Strong dependences of threshold crack growth rates and ΔK_{TH} on the applied

R-ratio have been observed in steels (Ritchie, 1977) in aluminium (Bretz et al., 1983, Minakawa and Mc Evily, 1984), titanium (Walker and Beevers, 1979, Beevers, 1980) and nickel base alloys (Venables et al., 1983, Byrne and Duggan, 1982). However, contrary to the present case, an increase in the R-ratio in these alloys usually accelerates near threshold crack growth rates and decreases the value of ΔK_{TH}. On the other hand, it has been observed that the effect of R-ratio on mid-range crack growth rates is much smaller in agreement with the results reported for amorphous $Ni_{78}Si_{10}B_{12}$.

The effect of R-ratio on threshold crack growth rates has been generally ascribed to the crack closure which occurs at low ΔK levels. A detailed review of the closure mechanisms observed in this region and the models proposed to account for the effect of R-ratio on crack growth has been given in sections 2.3.1 and 2.3.4. The consequence of closure of the crack faces occurring during the load cycle is to decrease the effective stress intensity range from the nominal applied value ΔK to a lower value ΔK^c_{eff} (where superscript "c" refers to closure) defined as

$$\Delta K^{c}_{eff} = K_{max} - K_{cl} \qquad 6.3$$

where K_{cl} is the value of stress intensity at which the two surfaces come into contact during the unloading portion of stress cycle.

Using this concept of closure, a phenomenological explanation of the influence of R-ratio on near threshold crack growth rates and ΔK_{TH} was presented by Schmidt and Paris (1973). It was proposed that the onset of closure occurs at a fixed value of K_{cl}, independent of applied R-ratio. Thus, at low R values where $K_{cl} > K_{min}$, for a given value of applied ΔK, ΔK_{eff} increases with R-ratio resulting in an increase in crack growth rates (also in a decrease in ΔK_{TH}). Above a critical value of R where $K_{min} > K_{cl}$, the effect of closure disappears and crack growth rates (and ΔK_{TH}) become insensitive to further increases in R. The predicted nature of

the R-ratio dependences of near threshold growth rates and ΔK_{TH} has been found to be consistent with experimental results obtained for steels, aluminium, titanium and nickel base alloys (e.g. Davidson and Suresh, 1984). Two mechanisms have been proposed to account for the occurrence of crack closure in bulk specimens of crystalline materials at low values of ΔK. The first of these mechanisms, termed "oxide induced crack closure" arises from the fact that when oxide deposits formed on freshly exposed surfaces at the crack tip reach a thickness comparable to the crack tip opening displacement, the crack can become effectively wedged-closed at stress intensities above K_{min}. The second mechanism, "roughness induced crack closure" arises in situations where the size scale of the fracture roughness is comparable to the crack tip opening displacements (and when significant mode II displacements exists). In these closure mechanisms, the value of K_{cl} is determined by the thickness of the oxide layer and the asperity or facet size of the material respectively. Thus, the prediction of the Schmidt-Paris model that the stress intensity K_{cl} at which crack closes is independent of R is applicable to the cases where closure is oxide or roughness induced.

A third source of crack closure is due to the formation of plastically stretched material at the crack tip and flanks and its attendant residual stresses. In this case, the extent of the monotonic plastic zone which determines the severity of the compressive residual stresses - and thus the closure - may be assumed to depend on K_{max}. Consequently, the value of K_{cl} should be affected by an increase in K_{max}. In other words, K_{cl} should increase with the value of the applied R-ratio. Such plasticity induced closure is considered to be prevalent under essentially plane stress conditions, i.e. at ΔK's above the threshold region (Lindley and Richard, 1974, Fleck, 1986), but not at low ΔK's in bulk specimens where the size of the plastic zone is much smaller than the specimen thickness (Ritchie, 1979). It could be assumed that if the thickness of the specimen is very small, the ratio of plastic zone over thickness might become significantly larger than the thick specimens tested under the same ΔK conditions. Thus, at near threshold levels, plasticity induced crack closure might become a more effective mechanism

in thin materials, such as amorphous $Ni_{78}Si_{10}B_{12}$, than thick specimens. If this hypothesis was true, the value of K_{cl} might increase withR and if the rate of increase in K_{cl} exceeded that of K_{max}, ΔK_{eff} might decrease with R. With these assumptions it is possible to explain the inverse dependence of crack growth rates on R in thin $Ni_{78}Si_{10}B_{12}$ specimens.

The first step to check the suggested hypothesis is to establish whether the increase in near threshold growth rates with R-ratio is associated with the unusual thickness of the material (57 μm). (Amorphous $Ni_{78}Si_{10}B_{12}$ cannot be made in sections thicker than about 60 μm because a very high cooling rate is required for solidification). To clarify this point, the tests used to determine the effect of R-ratio on crack growth rates in amorphous $Ni_{78}Si_{10}B_{12}$ were repeated on stainless steel AISI 316 specimens of comparable thickness. The R-ratio dependence of crack growth rates of thick specimens of this alloy is known to follow the conventional pattern, i.e. da/dN decreases with increasing R-ratio at near threshold levels (Pickard et al., 1975). Results on 52 μm thick stainless steel specimens reported in section 6.1.3 clearly showed that the value of threshold stress intensity ΔK_{TH} decreased by a factor of two and near threshold crack growth rates increased significantly when the R-ratio was increased within the range of 0.1 to 0.5. These results are in good agreement with those reported for bulk specimens of the same alloy but they show a completely opposite trend to the R-ratio dependence of near threshold growth rates in 57 μm thick $Ni_{78}Si_{10}B_{12}$ specimens. It is concluded that the anomalous R-dependence of the amorphous alloy is not solely a consequence of its small thickness. Thus, the decrease in ΔK_{eff} at high R-ratios in $Ni_{78}Si_{10}B_{12}$ cannot simply be rationalized in terms of very small thickness of the specimens using plasticity induced crack closure arguments.

The R-ratio dependence of near threshold growth rates in thin stainless steel specimens can probably be interpreted on the basis of the roughness induced crack closure concepts previously proposed to explain the effect of R-ratio in

conventional bulk specimens (Minakawa and Mc Evily, 1981, Blom, 1984). Briefly, at a given ΔK, it can be assumed that K_{cl} is independent of R (because the scale of surface roughness is taken to depend only on the grain size of the material). Thus, according to the Schmidt and Paris model, the initial sharp increase in da/dN in Fig. 6.31 may be attributed to the increase in ΔK^c_{eff} with R. At the critical R-ratio ($R \approx 0.3$), the crack tip opening displacement may exceed the average size scale (amplitude) of the fracture surface roughness so that $K_{min} \geq K_{cl}$ and above this value, crack growth rates become virtually unaffected by further increases in R-ratio.

Clearly, it is not possible to explain the R-ratio dependence of low crack growth rates in amorphous $Ni_{78}Si_{10}B_{12}$ with this model. To assess the role of crack closure in modifying the effective driving force for crack extension, the change in crack tip opening displacement at various load levels of the fatigue cycle in this alloy has been determined for two values of ΔK and R ($\Delta K = 2.5$, 5.0 MPa$\sqrt{m}$, $R = 0.1$, 0.5). At $\Delta K = 2.5$ MPa$\sqrt{m}$ and $R = 0.1$, the slope of the load vs CTOD curve in Figure 6.36 decreases sharply above K_{min} which indicates that $K_{cl} > K_{min}$. The values of K_{cl} and ΔK^c_{eff} can be expressed as

$$K_{cl} = K_{min} + 0.25\,\Delta K$$

$$\Delta K^c_{eff} = 0.75\,\Delta K \approx 1.9\ \text{MPa}\sqrt{m}$$

However, for $\Delta K = 2.5$ MPa$\sqrt{m}$ and $R = 0.5$

$$K_{cl} \leq K_{min}$$

$$\Delta K^c_{eff} = \Delta K = 2.5\ \text{MPa}\sqrt{m}$$

Similarly at $\Delta K = 5$ MPa$\sqrt{m}$, where the R-ratio does not affect crack propagation rates and fracture morphologies, for $R = 0.1$

$$K_{cl} = K_{min} + 0.20\,\Delta K$$

$$\Delta K^c_{eff} = 0.80\ \Delta K = 4\ \text{MPa}\sqrt{m}$$

and for $R = 0.5$

$K_{cl} \leq K_{min}$

$\Delta K^{c}_{eff} = \Delta K = 5\ MPa\sqrt{m}$

The above analysis shows that crack closure occurs, and reduces the values of ΔK^{c}_{eff} at low R-ratios at $\Delta K = 2.5\ MPa\sqrt{m}$ (where crack growth rates are faster at high R-ratios) as well as at $\Delta K = 5\ MPa\sqrt{m}$ (where growth rates are not affected by R). These results disprove the hypothesis that K_{cl} increases with R-ratio to reduce ΔK^{c}_{eff} and therefore, this is not a tenable explanation of the inverse R-ratio dependence of crack growth rates around $\Delta K = 2.5\ MPa\sqrt{m}$. Closure is probably due to the premature contact of asperities on the fracture surfaces during the shear displacements required for crack extension by facet formation. However, the high value of ΔK_{eff} necessary for the formation of larger facets and higher growth rates imply that in this alloy there might be other factors that overcome the effect of crack closure and increase the local driving force for crack growth at low R-ratios. Pook (1985) suggested that the driving force for crack growth is controlled by local buckling at the crack tip. Although theoretical calculations have shown that buckling is a possibility at ΔK's where unusual R-dependence of crack growth rates have been observed, this point requires further investigation.

On the other hand, a good correlation has been found between ΔK_{eff} and the effective ΔCTOD defined as: [CTOD (at K_{max}) - CTOD (at K_{cl})]. Fig. 6.38 shows the change in the effective ΔCTOD with R-ratio at $\Delta K = 2.5$ and $5\ MPa\sqrt{m}$. At $\Delta K = 2.5\ MPa\sqrt{m}$, despite the closure occurring above K_{min}, the effective ΔCTOD obtained for $R = 0.1$ is two times larger than that for $R = 0.5$. As the value of ΔCTOD is an indication of ΔK_{eff}, when the effective ΔCTOD becomes smaller at high R, ΔK_{eff} decreases and this results in a three-fold decrease in da/dN. Consequently, the size of the facets on the fracture surfaces becomes smaller. In this way, a coherent picture of the effect of R-ratio on crack growth rates at $\Delta K = 2.5\ MPa\sqrt{m}$ can be obtained. At high ΔK's (i.e. at $\Delta K = 5\ MPa\sqrt{m}$), the value of the effective ΔCTOD is

almost the same at both R-ratios which means that ΔK_{eff} is not a function of R-ratio at $\Delta K = 5$ MPa$\sqrt{m}$. This is consistent with the observations that da/dN and the fractography of the specimens remain unaffected by the changes in R-ratio.

In summary, the fracture appearance in the alloy correlates with the crack growth rate, and it is possible to obtain the same fracture morphology by different combinations of ΔK and R which determine the effective driving force for crack growth. Near threshold, an increase in R-ratio at a constant ΔK causes a decrease in fatigue crack growth rates and smaller facet sizes. Such an unusual effect is attributed to the decrease of ΔK_{eff} with increasing R-ratio and this is confirmed by the smaller values of effective ΔCTOD at high R-ratios.

In crystalline alloys, near threshold crack growth rates are slower at low R-ratios. This has been interpreted in terms of the crack closure which decreases ΔK_{eff}. Crack closure is also observed in amorphous $Ni_{78}Si_{10}B_{12}$ at low loads but as crack growth rates seem to be faster at low R-ratios closure argument cannot be used to account for the high ΔK_{eff} at these R-ratios. Although it has been suggested that the observed effect could be due to the local buckling at the crack tip which might occur in thin ribbons, this point needs further clarification.

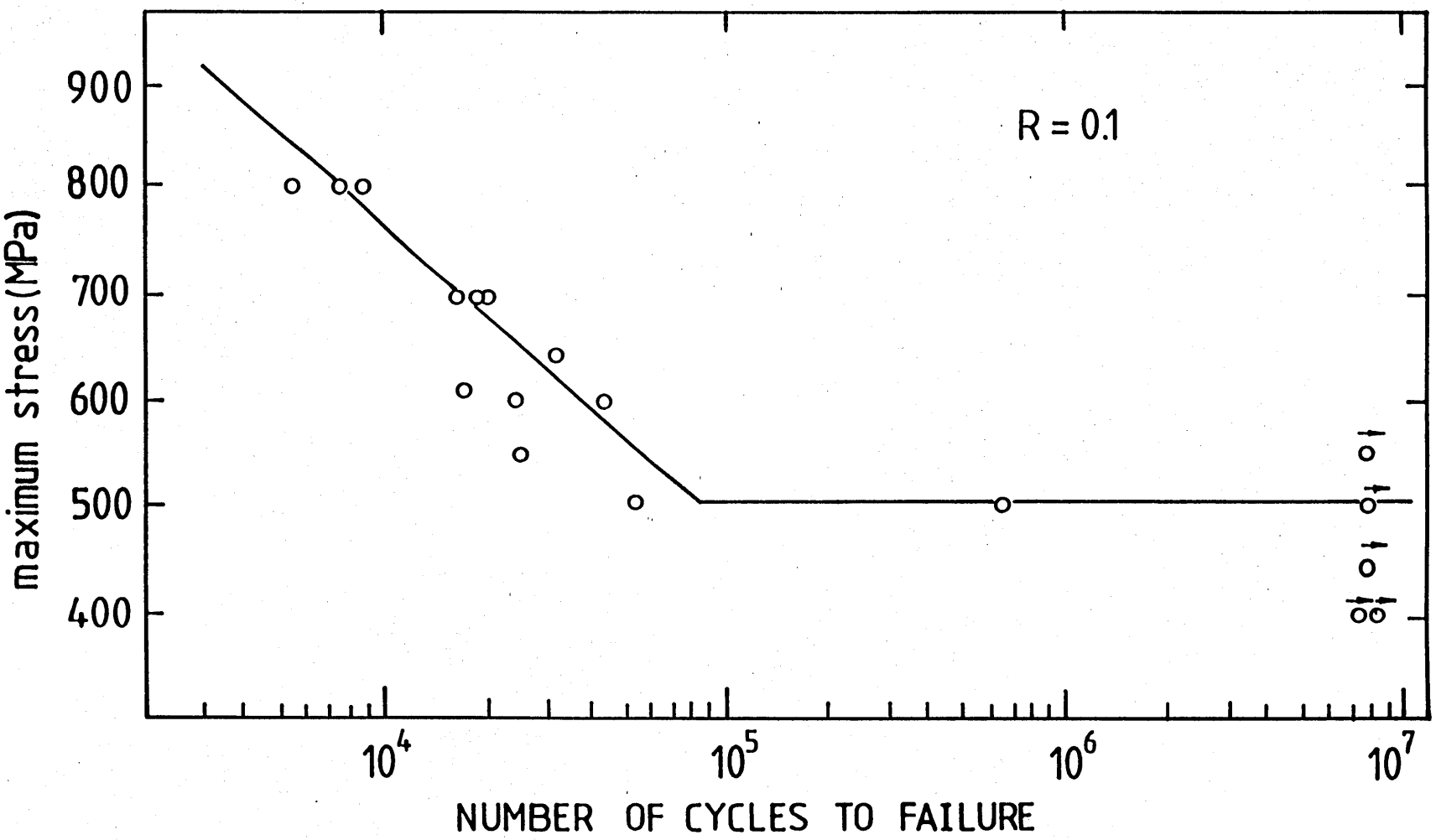

Figure 6.1 S-N curve at R = 0.1.

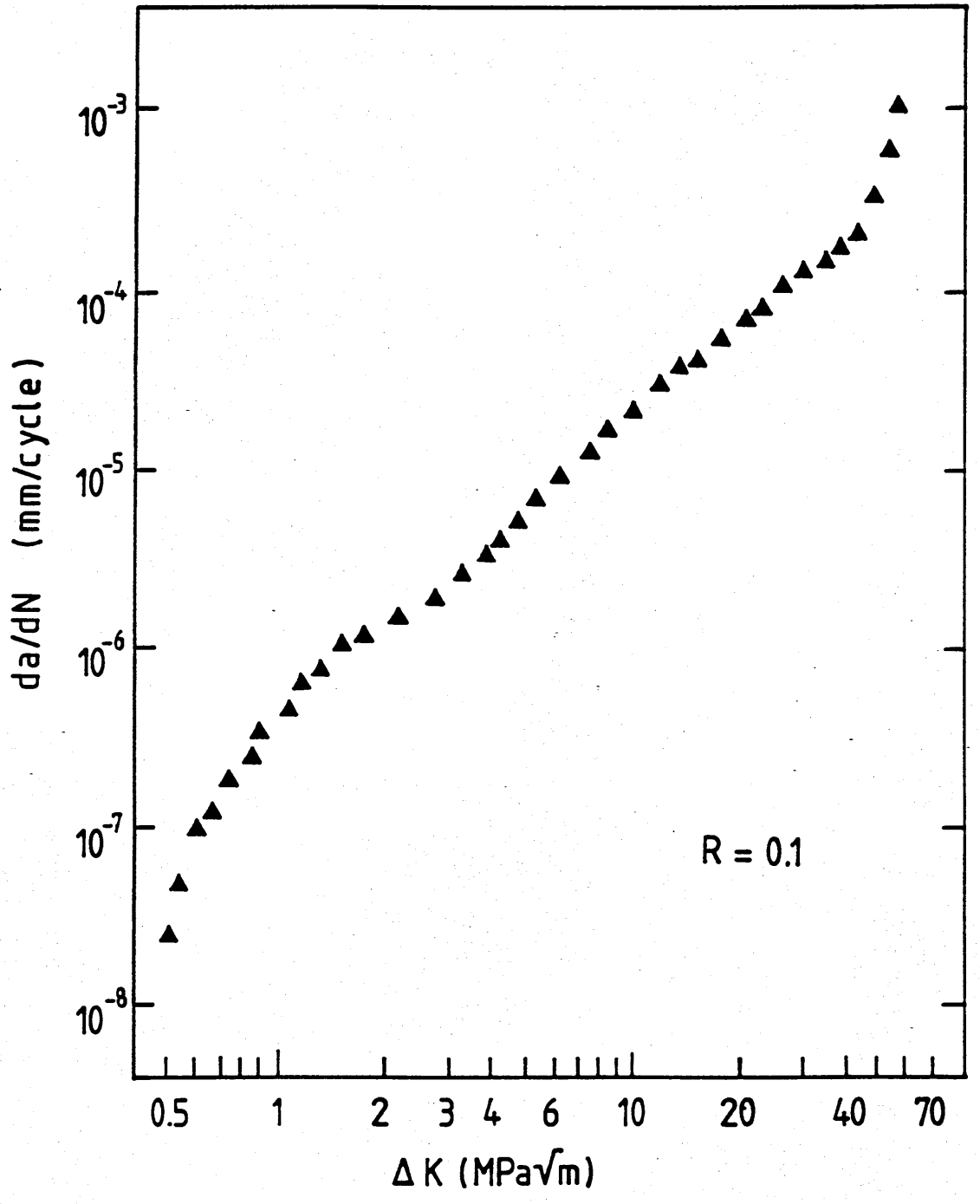

Figure 6.2 Fatigue Crack Propagation Curve at R = 0.1.

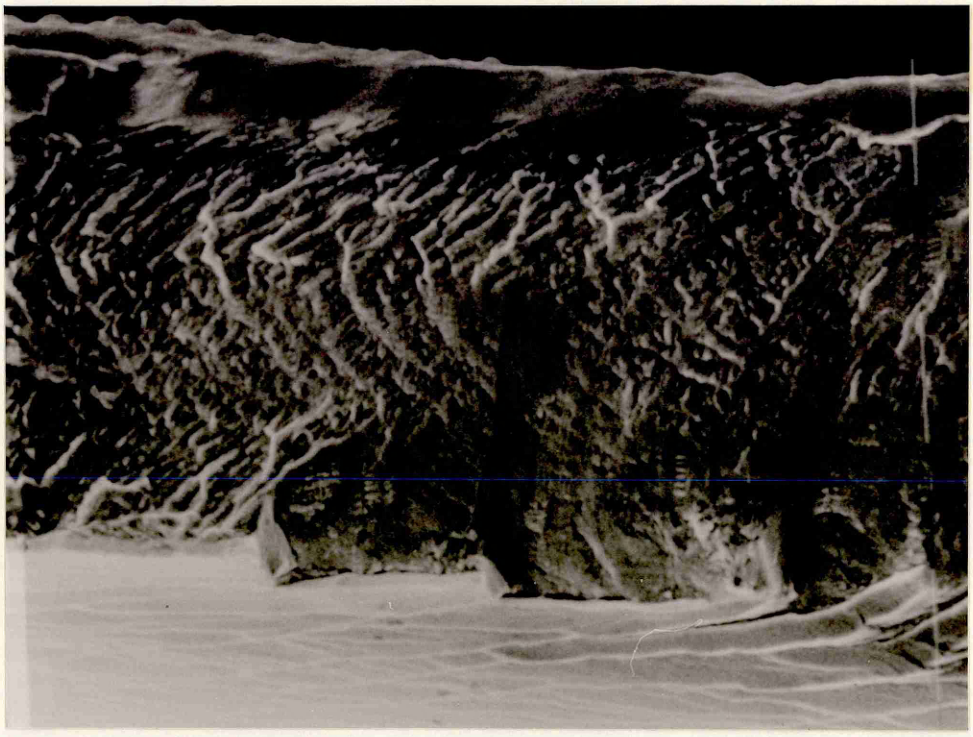

Figure 6.3 Fatigue fracture morphology at $\Delta K = 50$ MPa$\sqrt{m}$, R = 0.1.

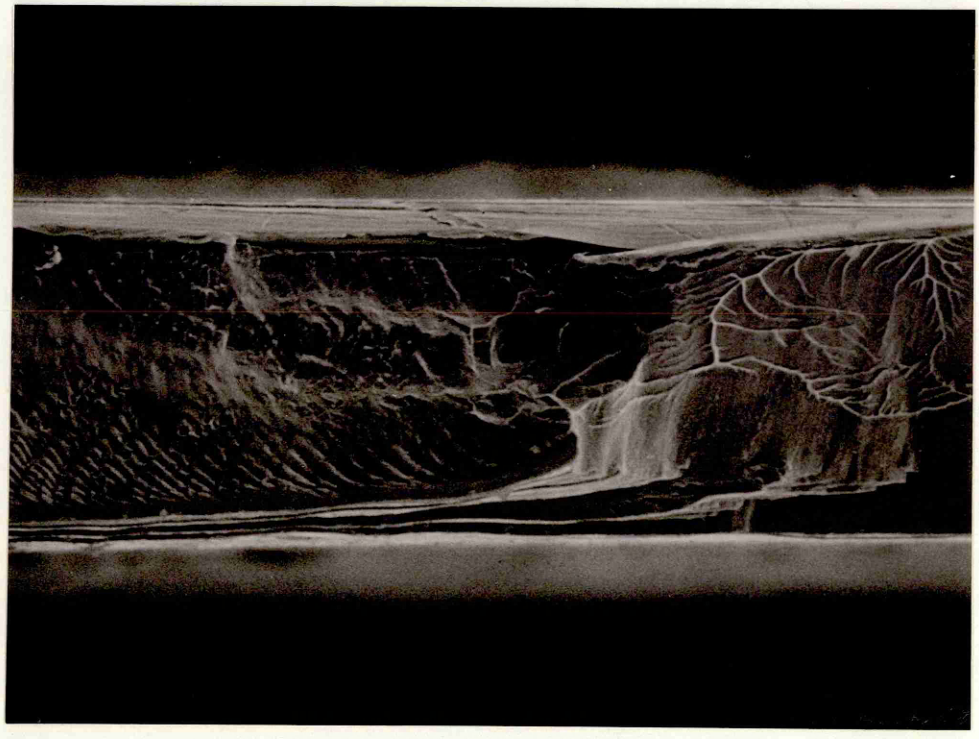

Figure 6.4 Fatigue fracture morphology at $\Delta K \approx 60$ MPA$\sqrt{m}$, R = 0.1. Note the large mode III shear displacements and the vein pattern due to the static failure.

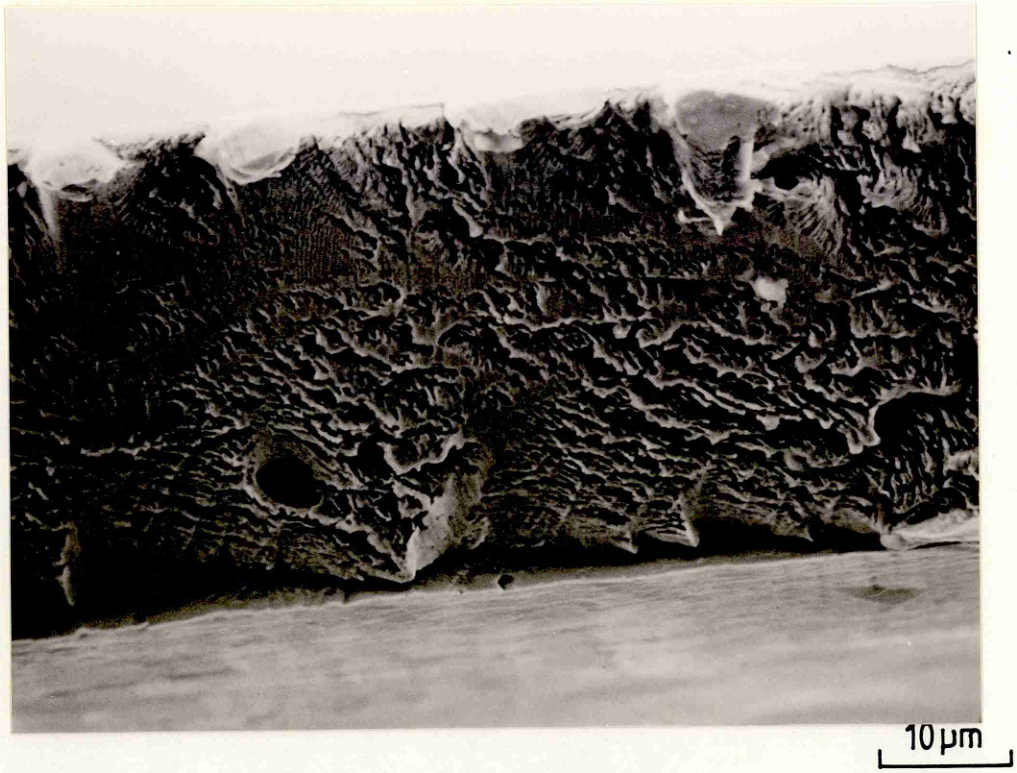

Figure 6.5 Fatigue fracture morphology at ΔK = 43 MPa$\sqrt{m}$, R = 0.1.

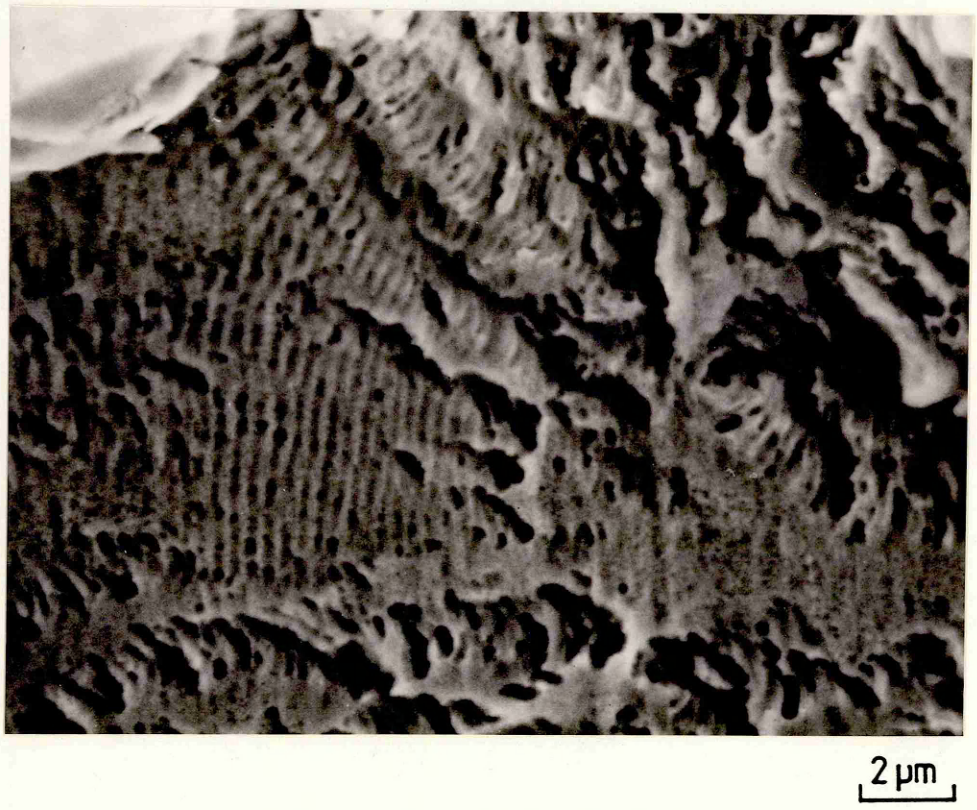

Figure 6.6 A magnified section of figure 6.5 showing details of striations.

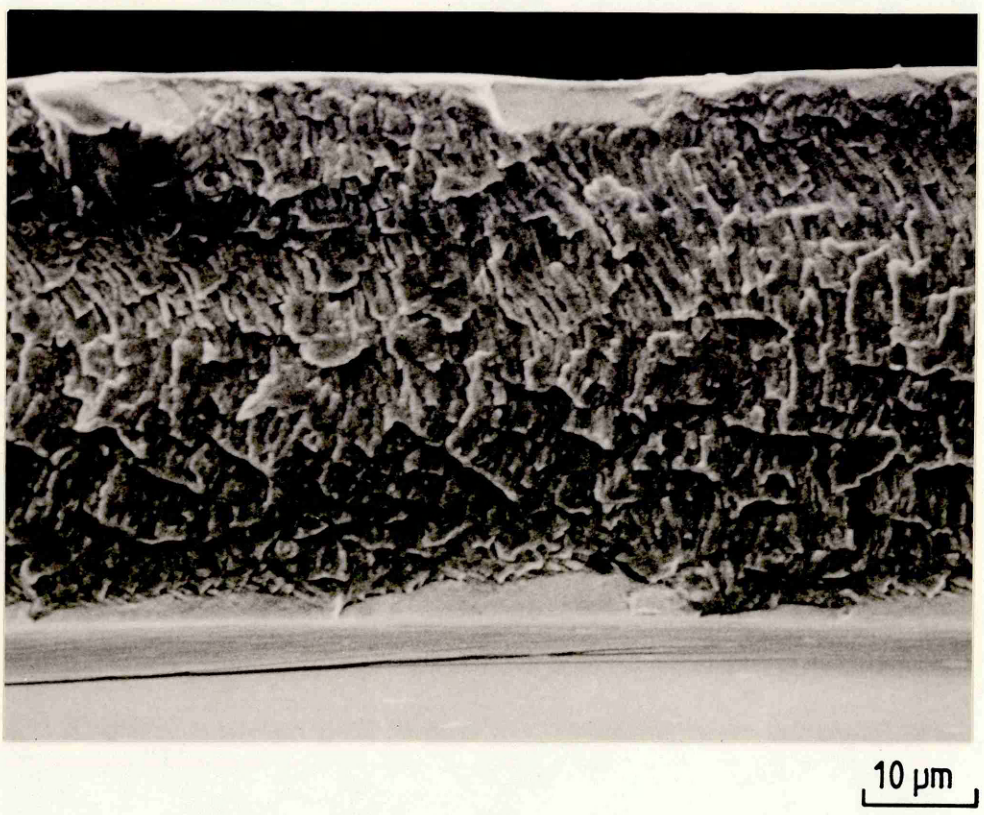

Figure 6.7 Fatigue fracture morphology at ΔK = 17 MPa$\sqrt{m}$, R = 0.1.

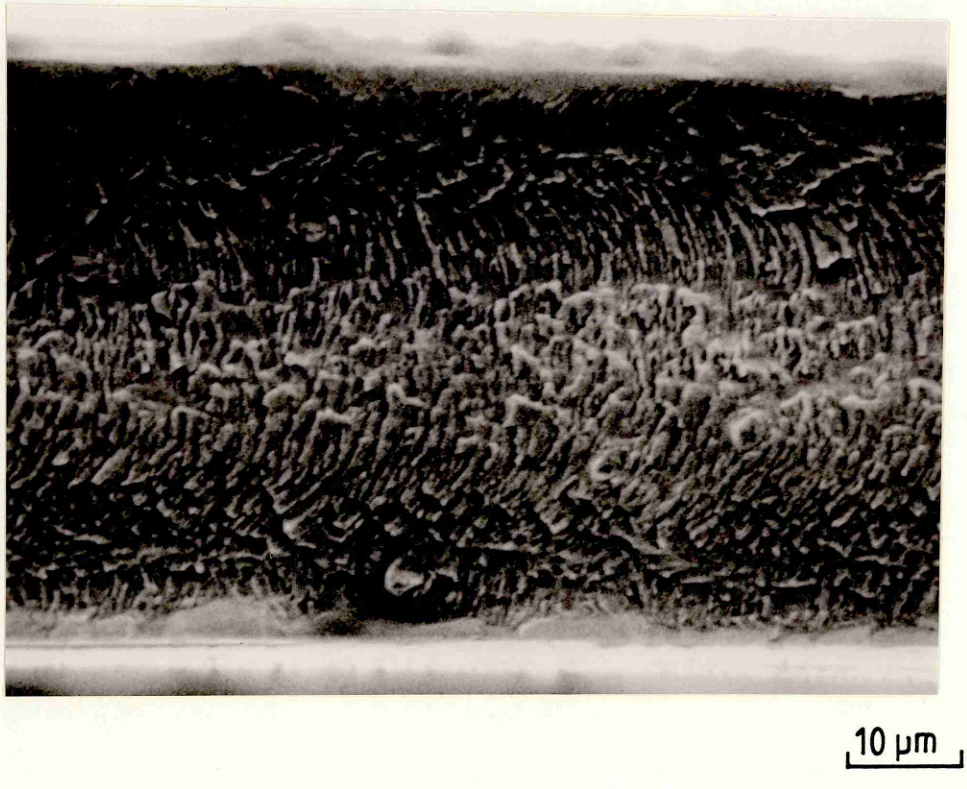

Figure 6.8 Fatigue fracture morphology at ΔK = 13 MPa$\sqrt{m}$, R = 0.1.

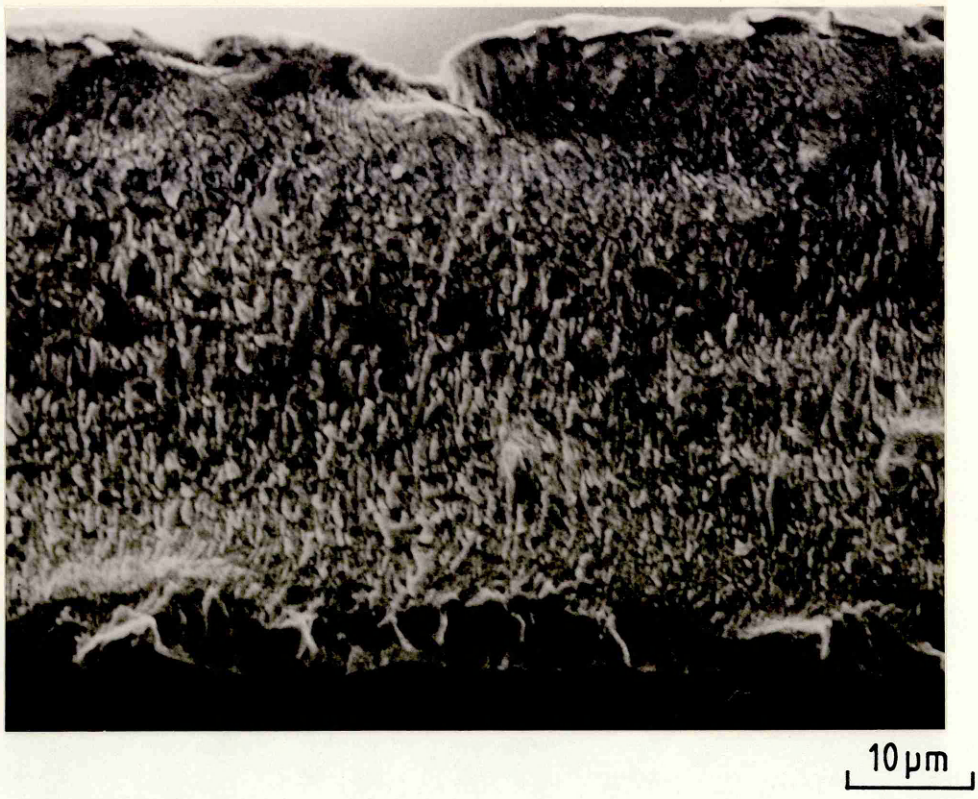

Figure 6.9 Fatigue fracture morphology at ΔK = 10 MPa$\sqrt{m}$, R = 0.1.

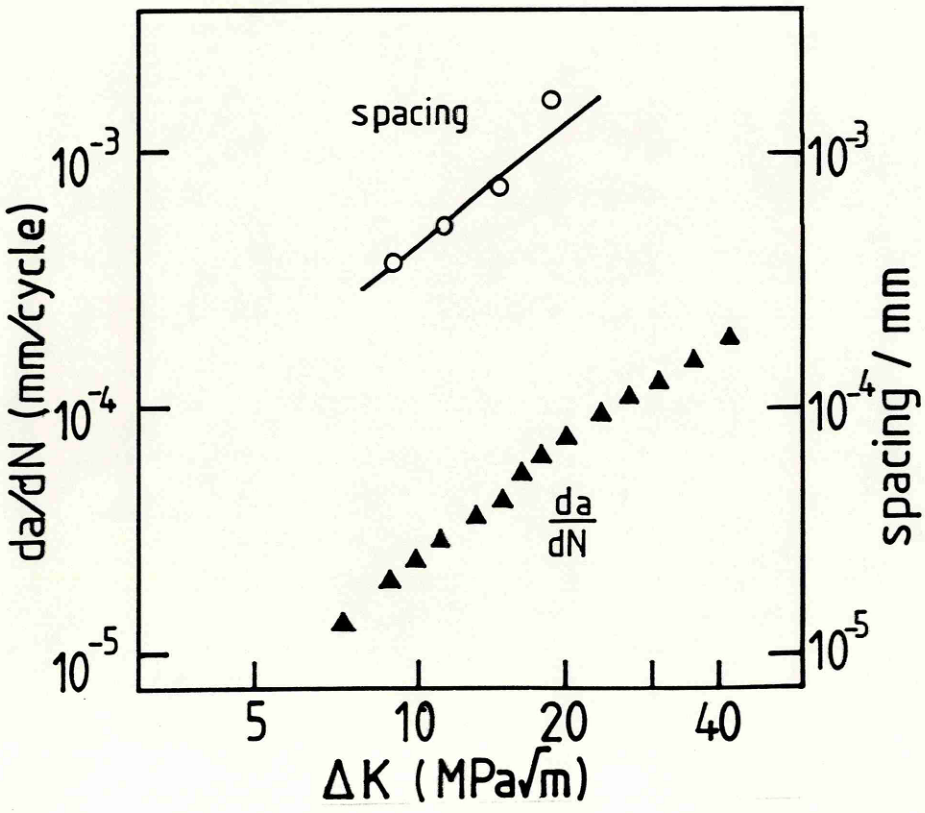

Figure 6.10 Relationship between the spacing of periodic fracture markings and fatigue crack growth rate.

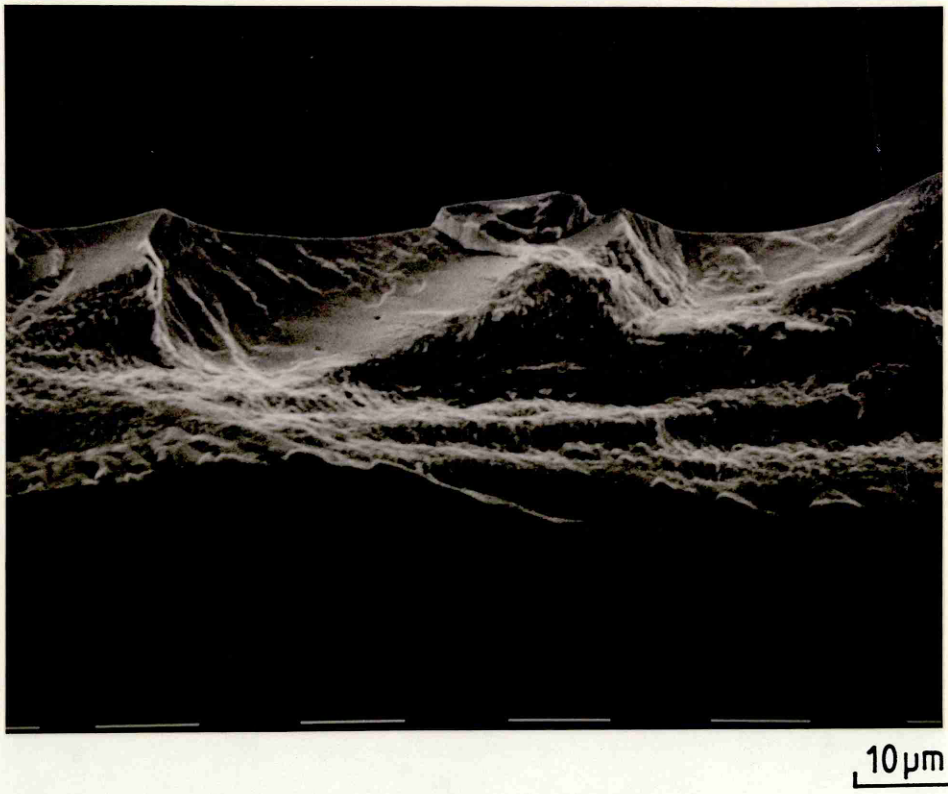

Figure 6.11 Fatigue fracture morphology at ΔK = 9 MPa$\sqrt{m}$, R = 0.1.

Figure 6.12 Fatigue fracture morphology at ΔK = 5 MPa$\sqrt{m}$, R = 0.1.

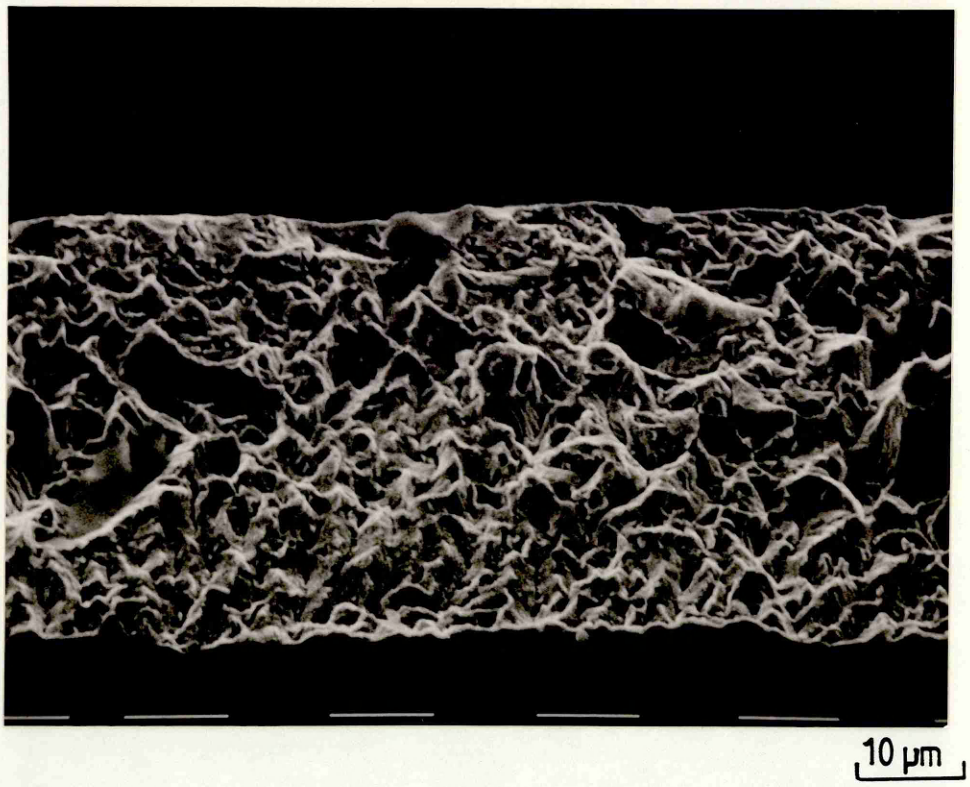

Figure 6.13 Fatigue fracture morphology at ΔK = 3 MPa$\sqrt{m}$, R = 0.1.

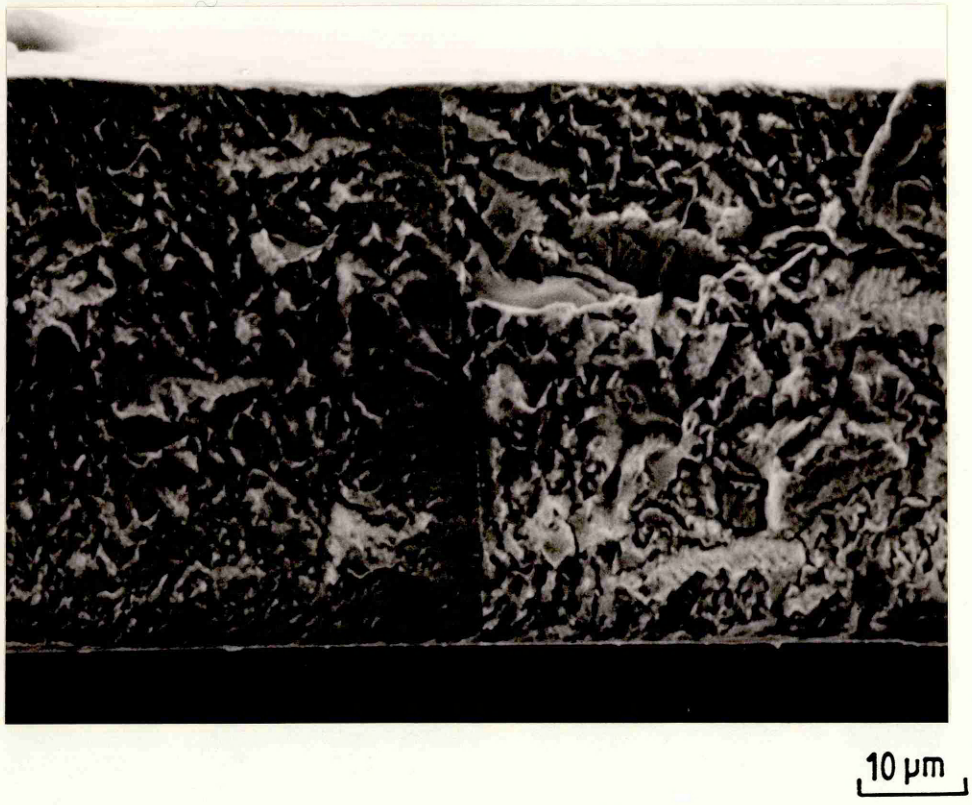

Figure 6.14 Fatigue fracture morphology at ΔK = 2.1 MPa$\sqrt{m}$ (area on the left) and ΔK = 1.65 MPa$\sqrt{m}$, R = 0.1.

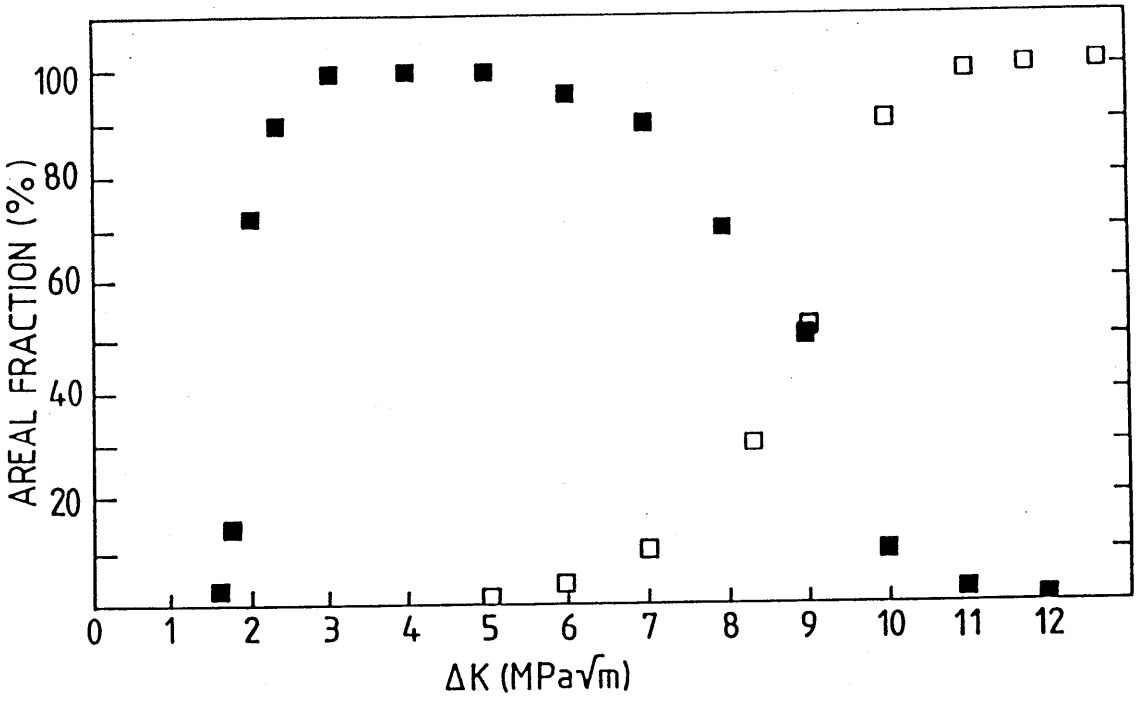

Figure 6.15 Areal fraction of the paraboloidal facets (■) and the periodic fracture markings (□) as a function of ΔK.

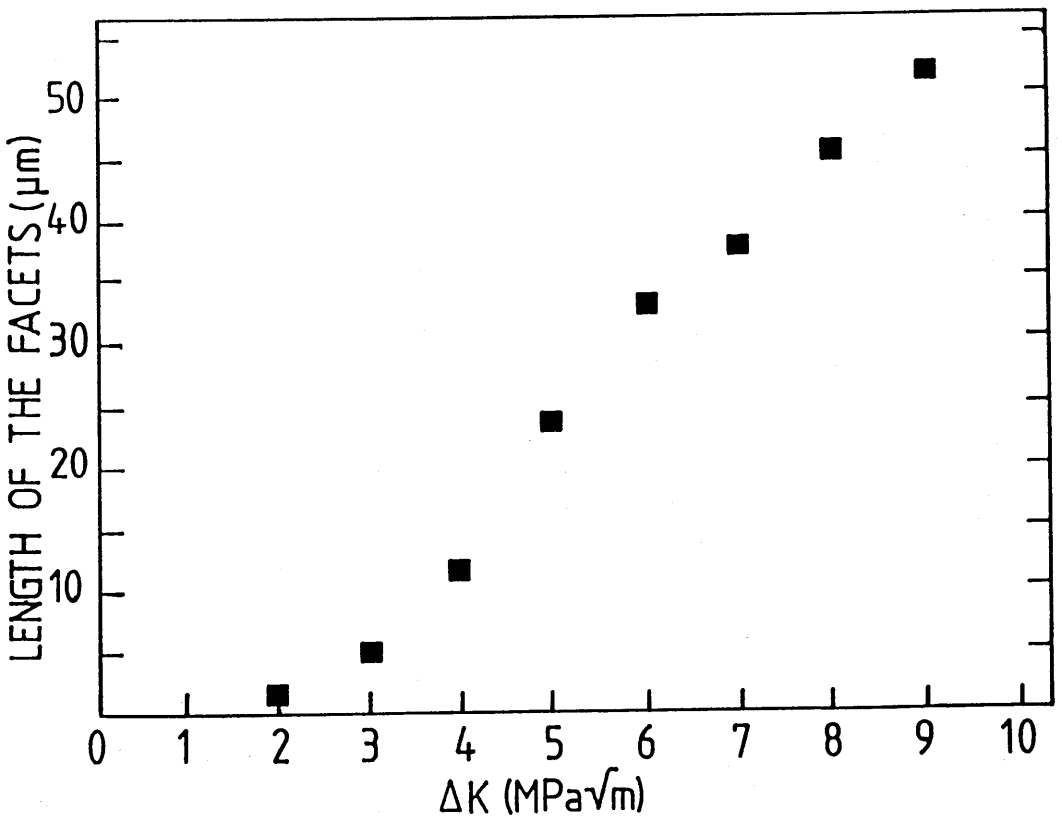

Figure 6.16 Dependence of the length of the parabolodial facets to ΔK (the length of the facets were measured in the crack growth direction).

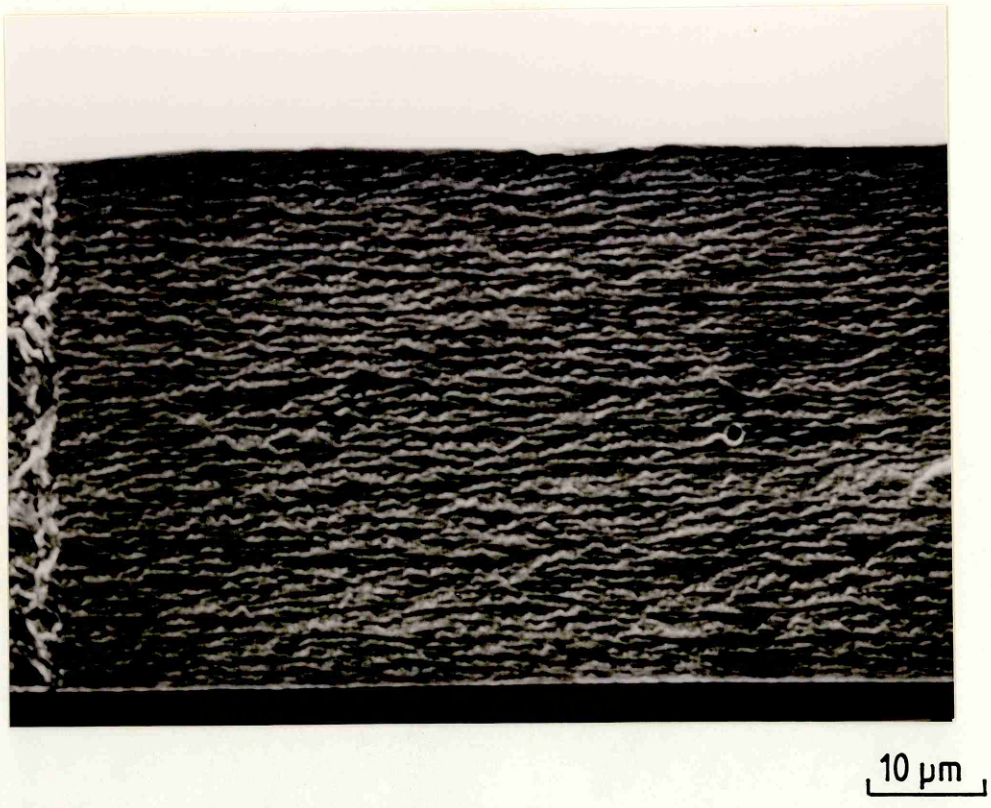

Figure 6.17 Fatigue fracture morphology at ΔK = 0.7 MPa$\sqrt{m}$, R = 0.1.

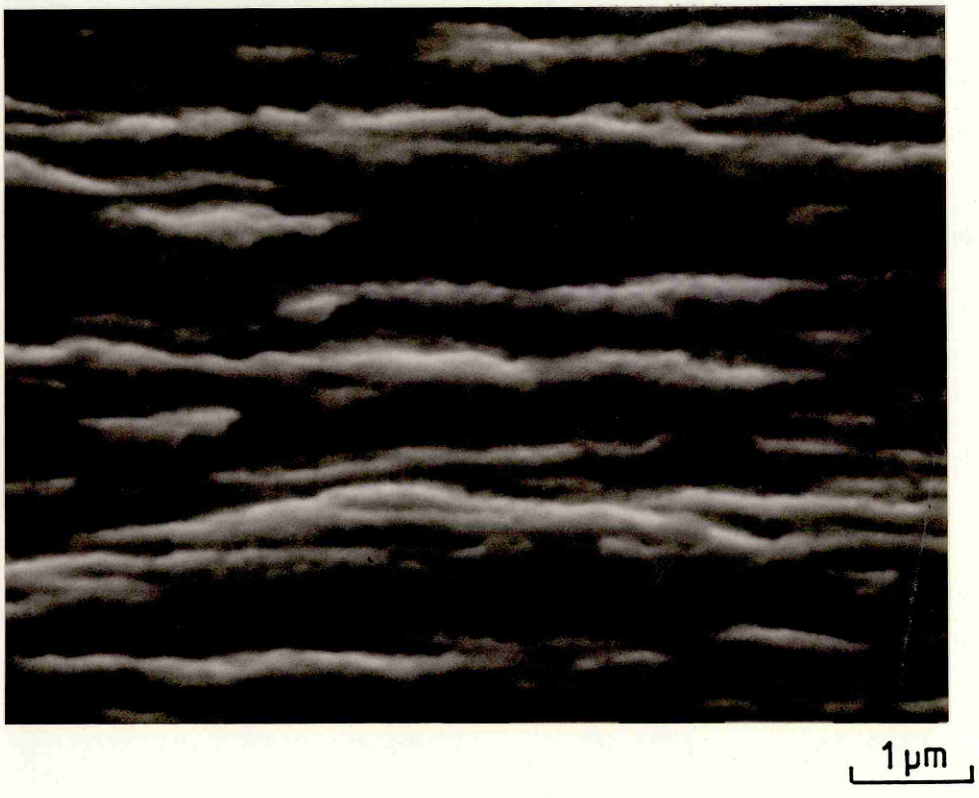

Figure 6.18 A high magnification detail from figure 6.17.

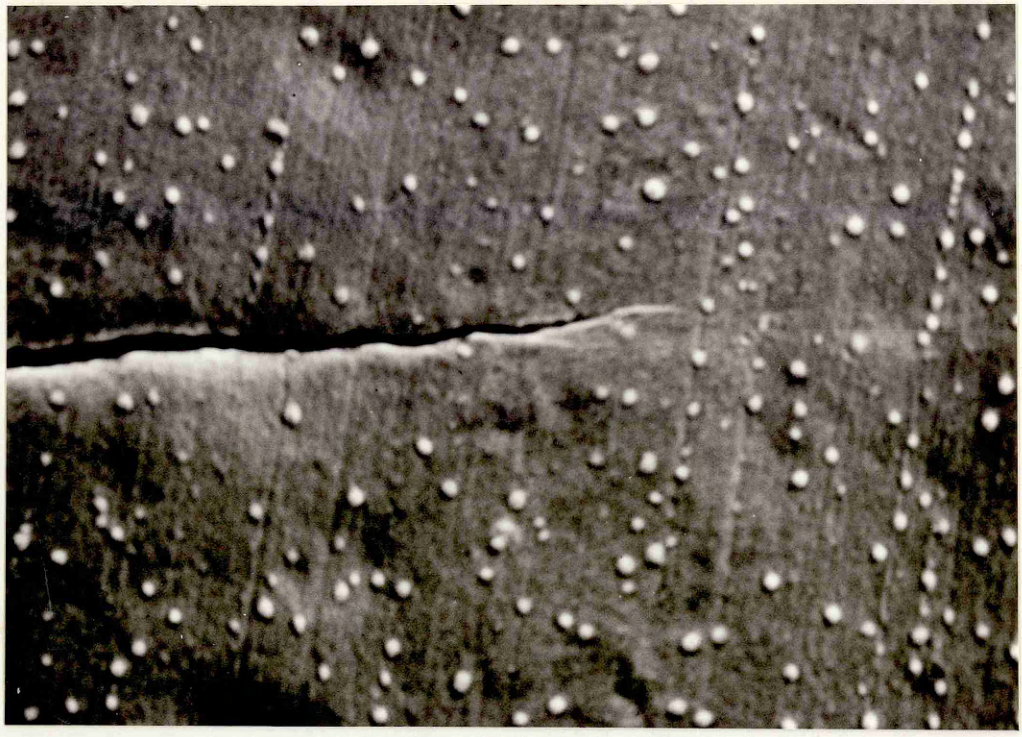

Figure 6.19 Fatigue crack tip morphology at ΔK = 0.7 MPa$\sqrt{m}$, R = 0.1.

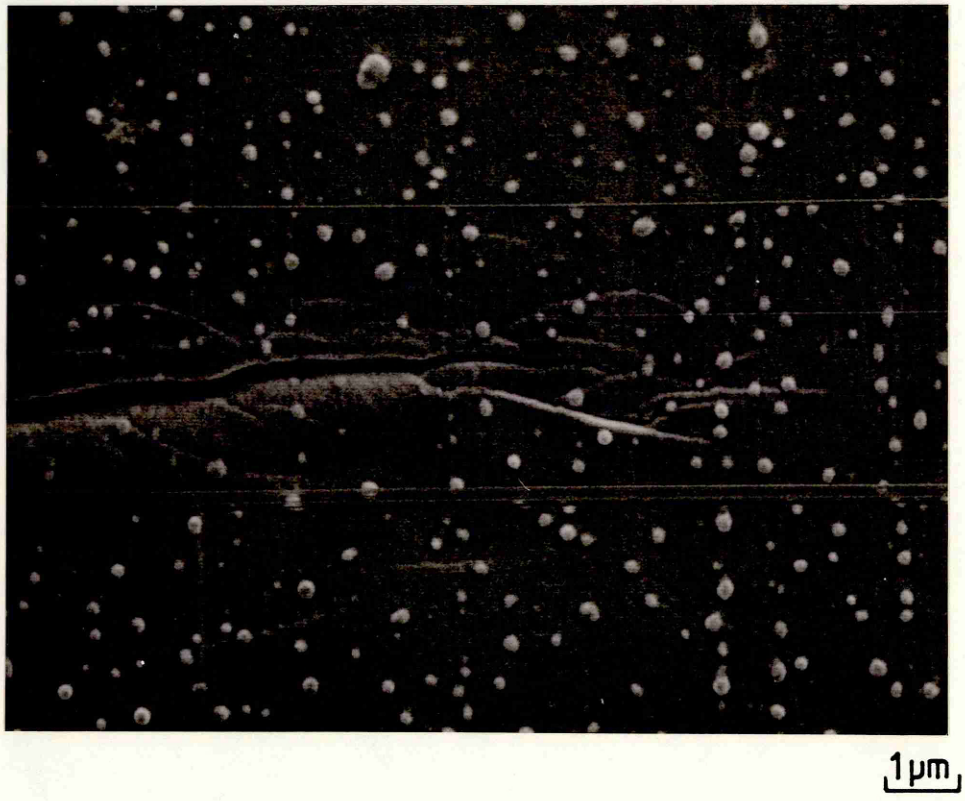

Figure 6.20 Fatigue crack tip morphology at ΔK = 3 MPa$\sqrt{m}$, R = 0.1.

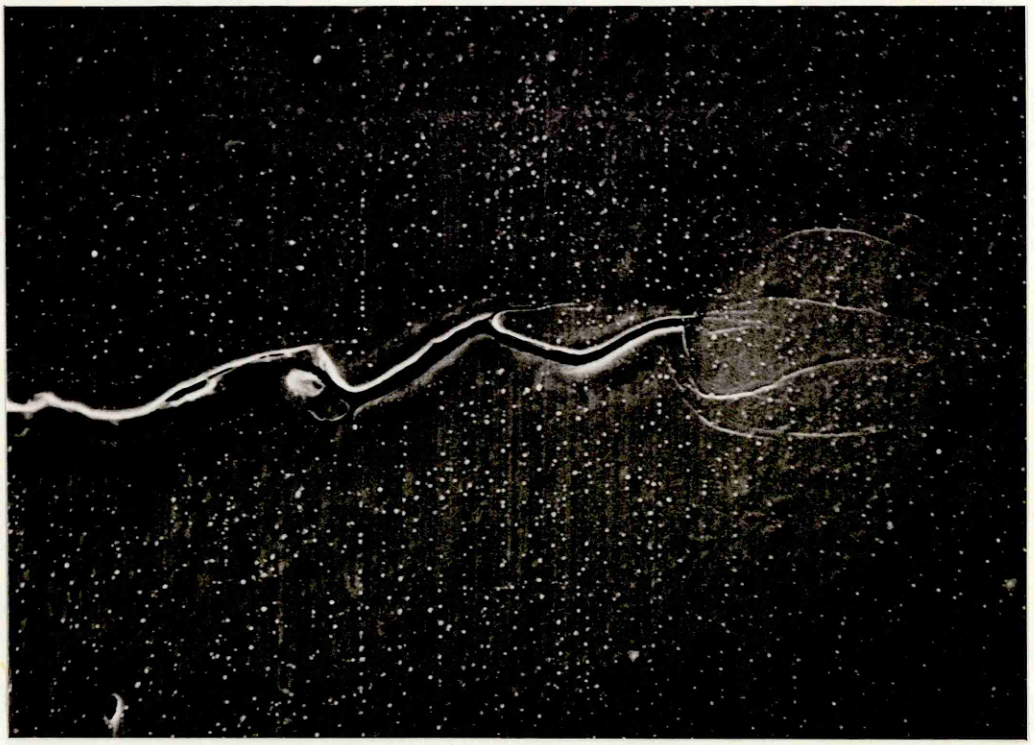

Figure 6.21 Fatigue crack tip morphology at ΔK = 5 MPa$\sqrt{m}$, R = 0.1.

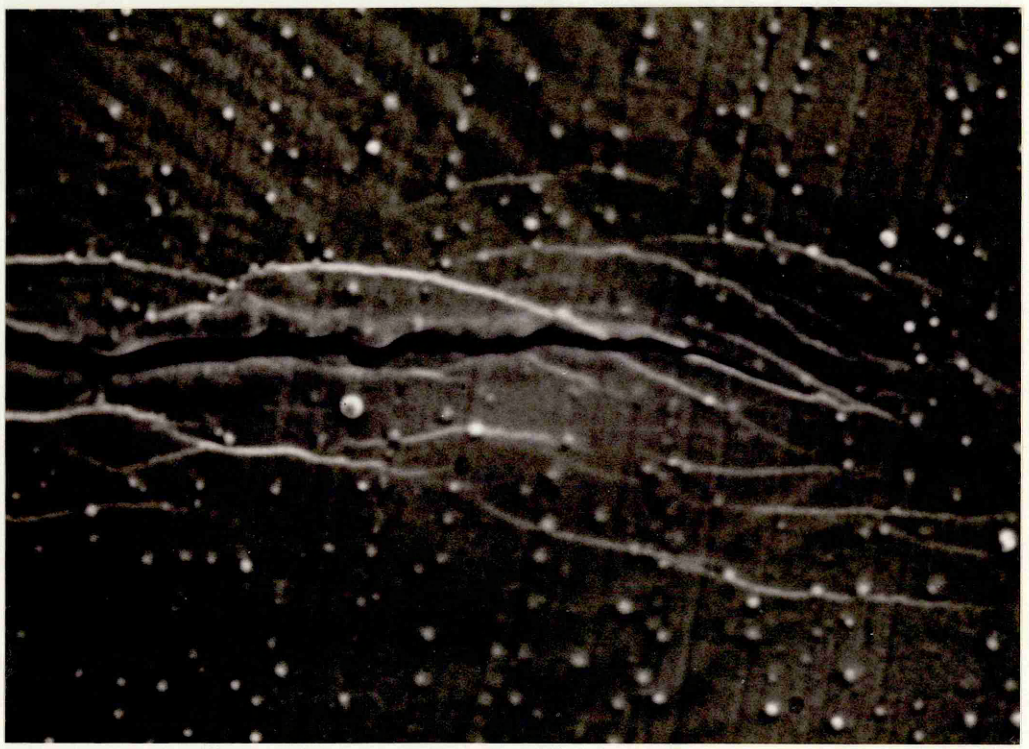

Figure 6.22 Fatigue crack tip morphology at ΔK = 16 MPa$\sqrt{m}$, R = 0.1.

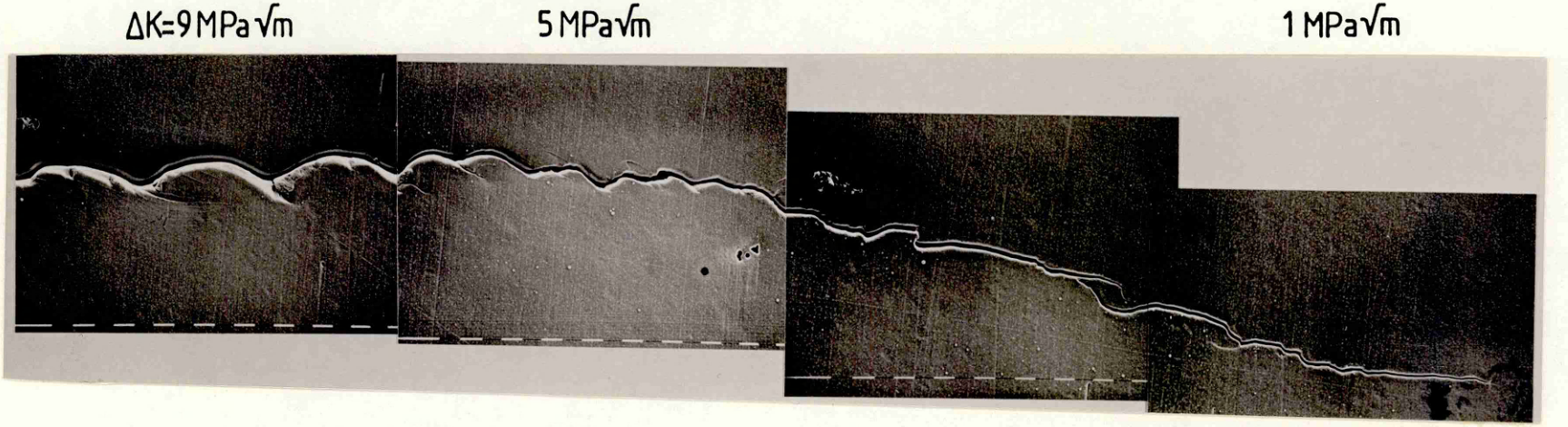

Figure 6.23 Sequential changes in the fatigue crack profile during a decreasing ΔK test.

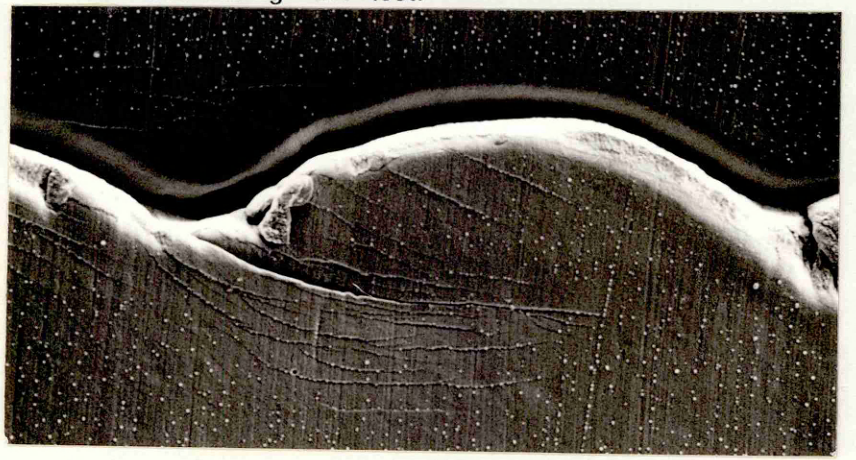

Figure 6.24 Fatigue crack profile at $\Delta K = 9$ MPa$\sqrt{m}$, $R = 0.1$.

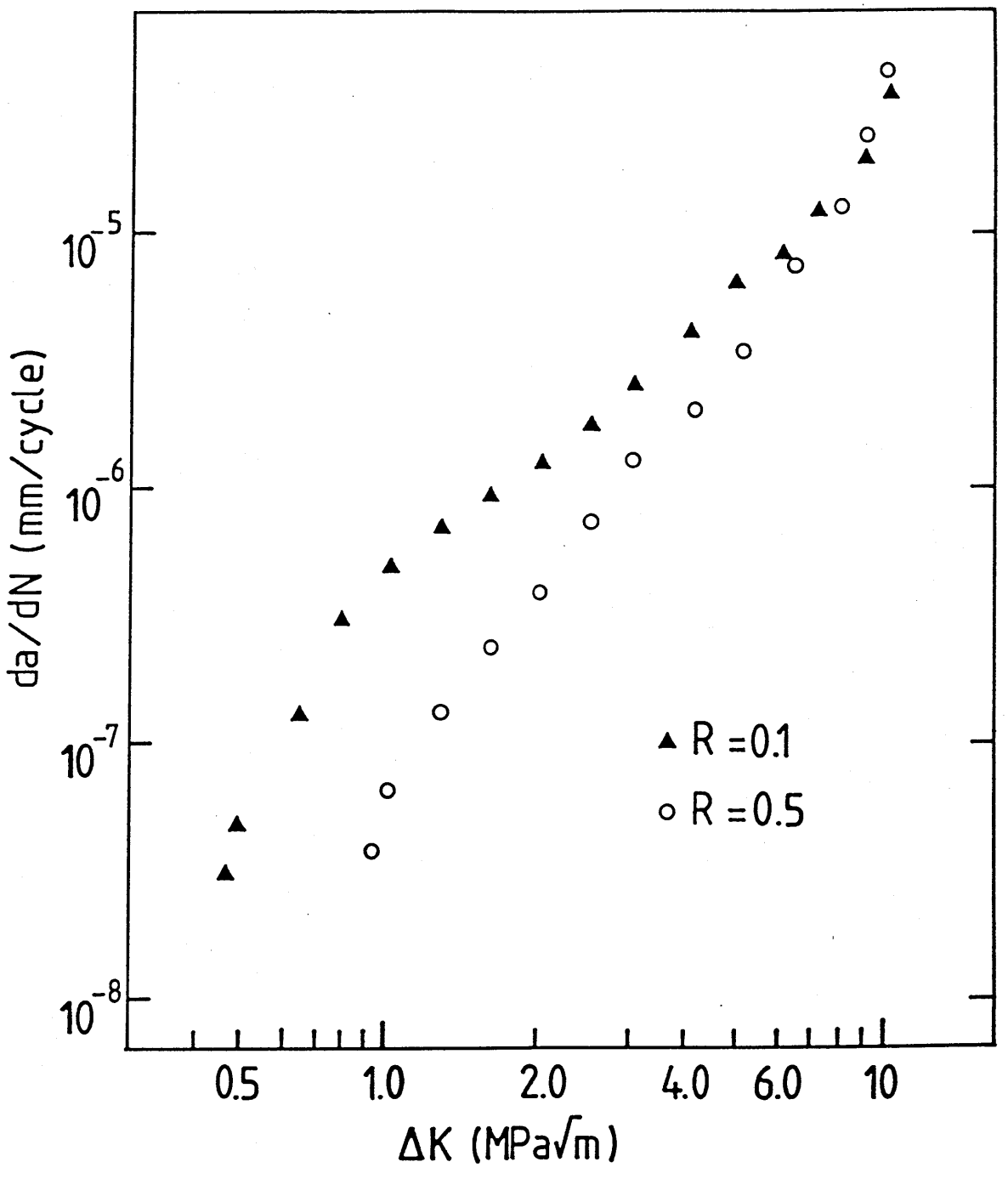

Figure 6.25 Effect of R-ratio on near-threshold and medium crack growth rates.

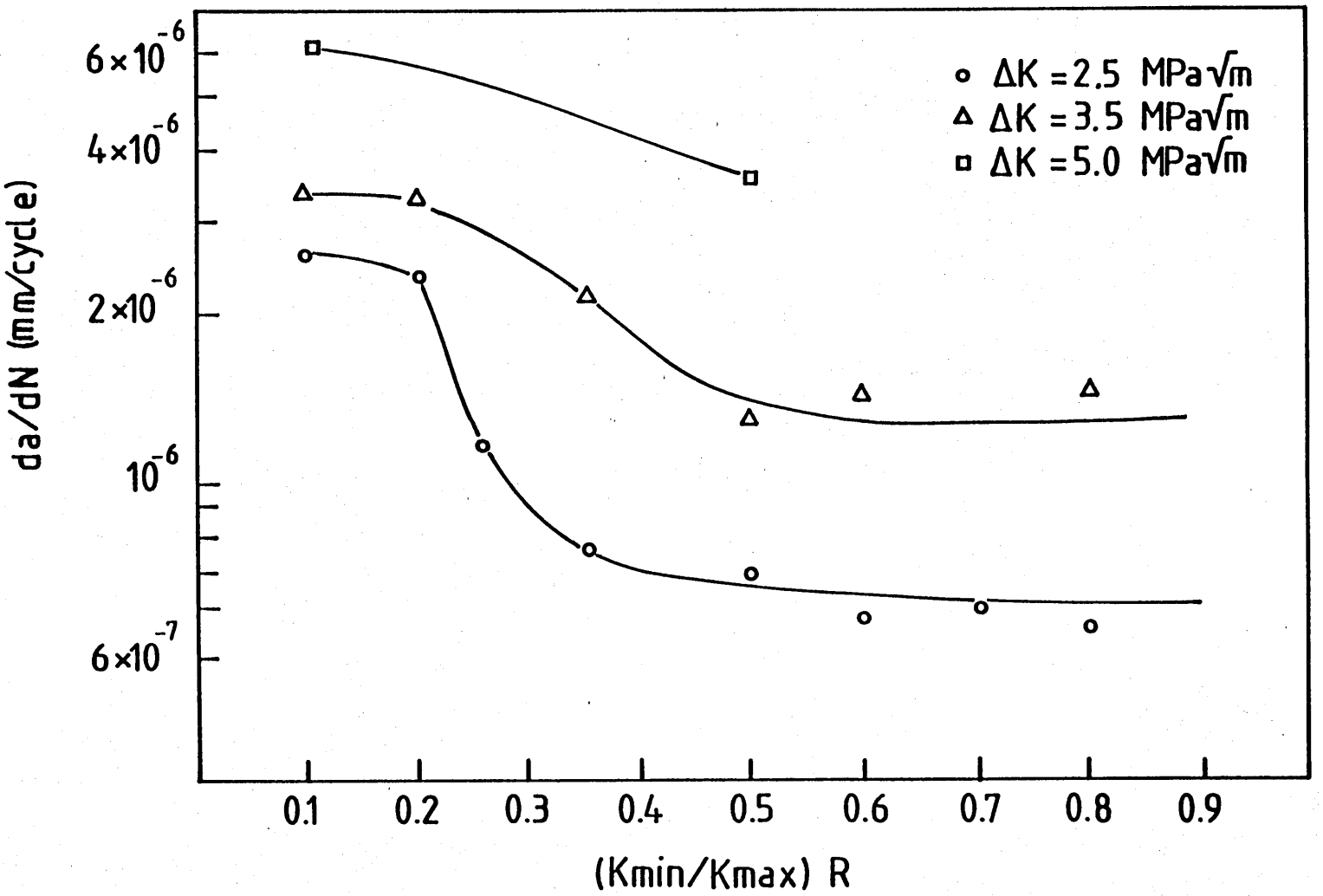

Figure 6.26 Variation of crack growth rates with R-ratio at constant ΔK.

Figure 6.27 Fatigue fracture morphologies produced at R = 0.1 and R = 0.5 at ΔK = 3 MPa$\sqrt{m}$.

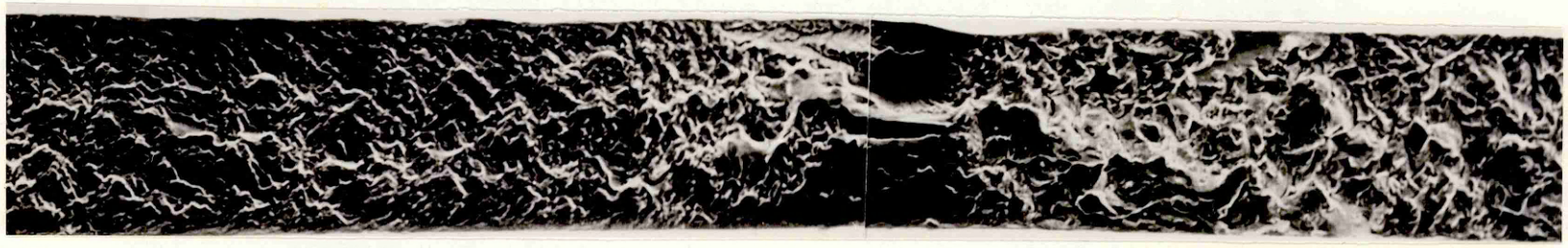

Figure 6.28 Fatigue fracture morphologies produced at R = 0.1 and R = 0.5 at ΔK = 2 MPa$\sqrt{m}$.

Figure 6.29 Fatigue fracture morphologies produced at R = 0.1 and R = 0.5 at ΔK = 5 MPa$\sqrt{m}$.

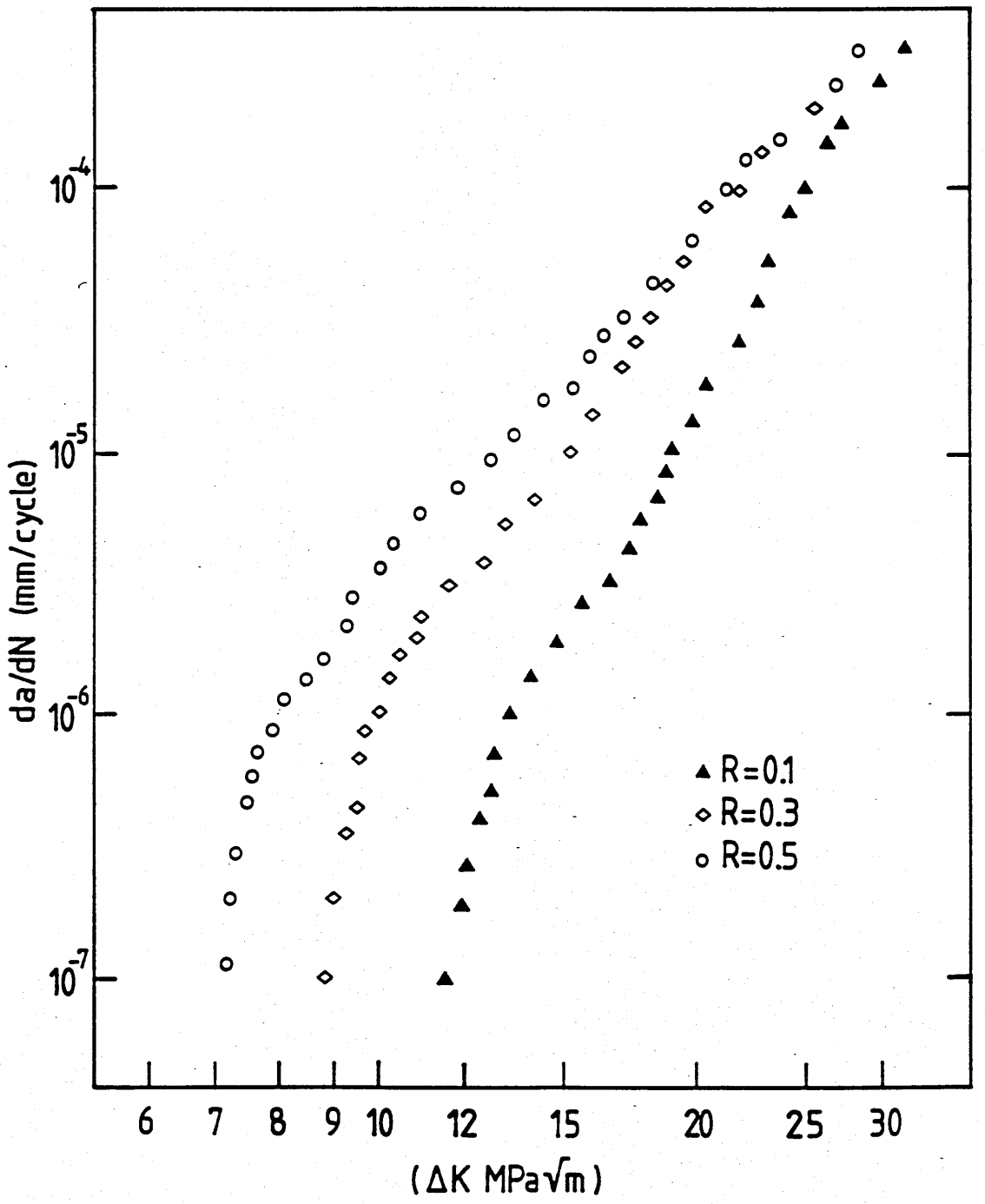

Figure 6.30 Effect of R-ratio on crack growth rates in a AISI 316 austenitic stainless steel (t = 50μm).

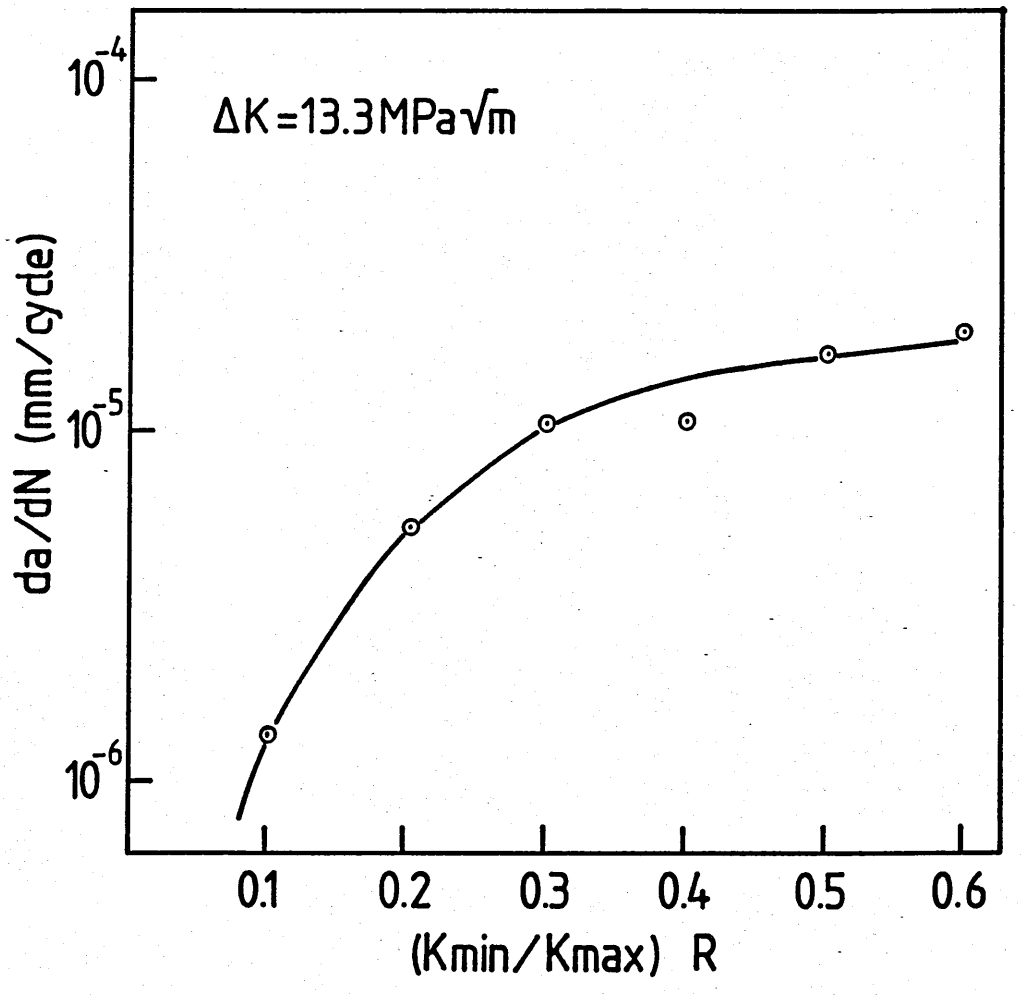

Figure 6.31 Variation of crack growth rates with R at a constant ΔK in a AISI 316 stainless steel.

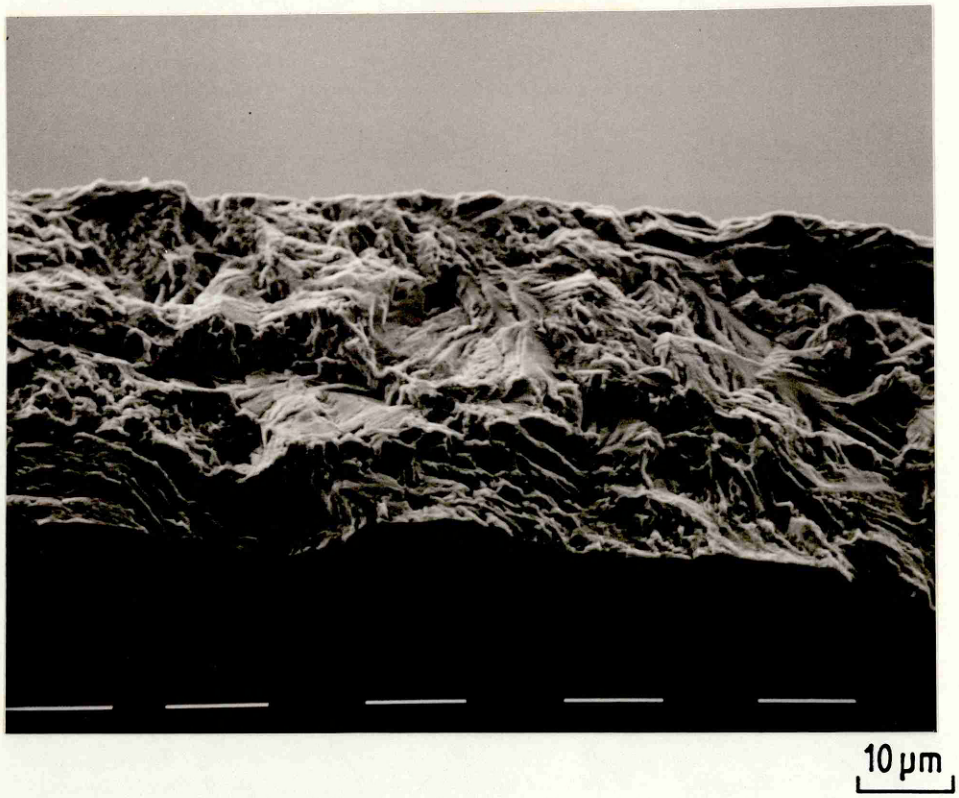

Figure 6.32a Fracture surface of a AISI 316 stainless steel at ΔK = 13.3 MPa$\sqrt{m}$, R = 0.5.

Figure 6.32b Fracture surface of a AISI 316 stainless steel at ΔK = 13.3 MPa$\sqrt{m}$, R = 0.1.

Figure 6.33a Fatigue crack tip morphology of a AISI 316 stainless steel at ΔK = 13 MPa$\sqrt{m}$, R = 0.5.

Figure 6.33b Fatigue crack tip morphology of a AISI 316 stainless steel at ΔK = 13 MPa$\sqrt{m}$, R = 0.1.

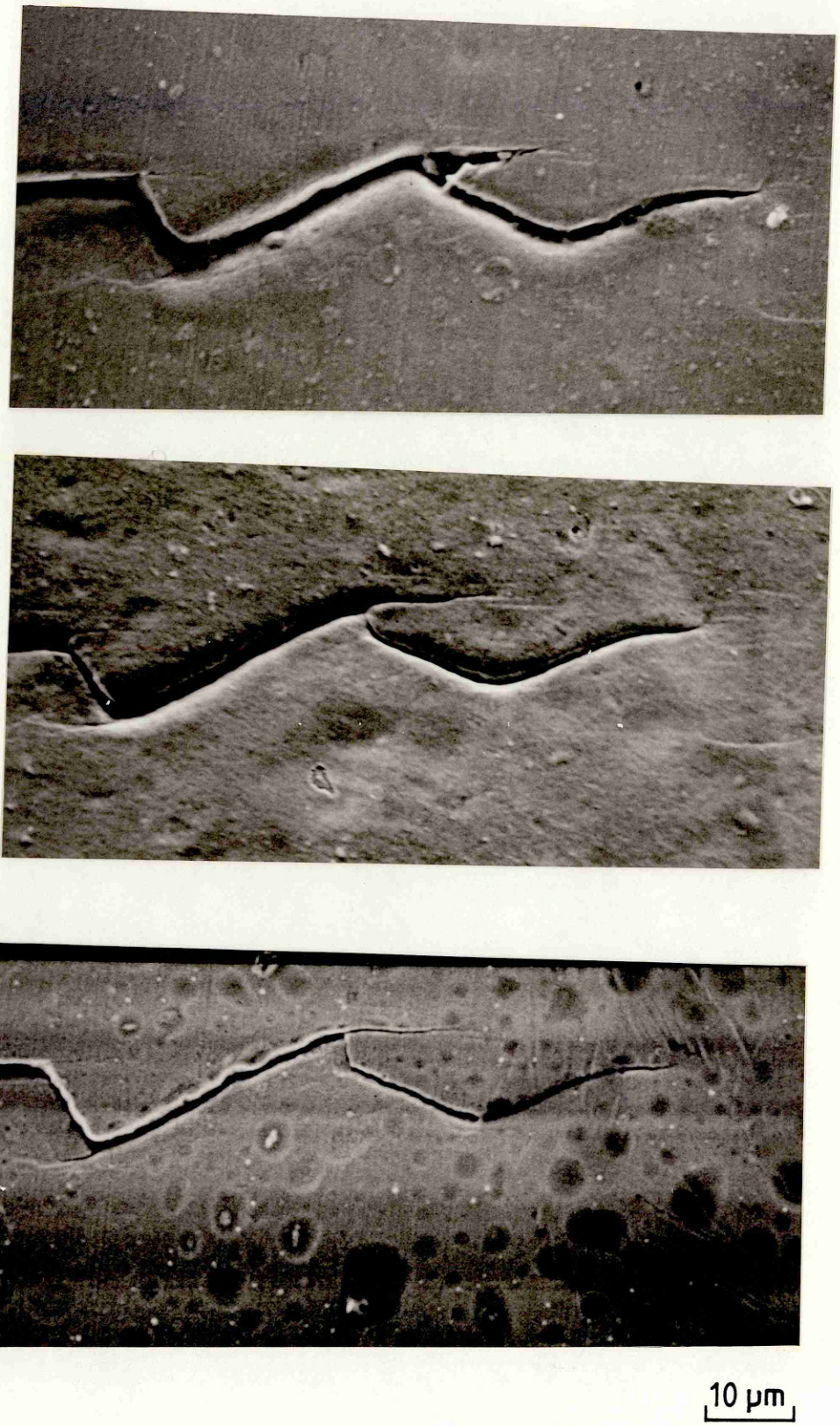

Figure 6.34 Photographs of the crack tip during unloading half of fatigue cycling at

a K_{max}

b K_{min} + 20 % ΔK

c K_{min} (ΔK = 5 MPa$\sqrt{m}$, R = 0.1)

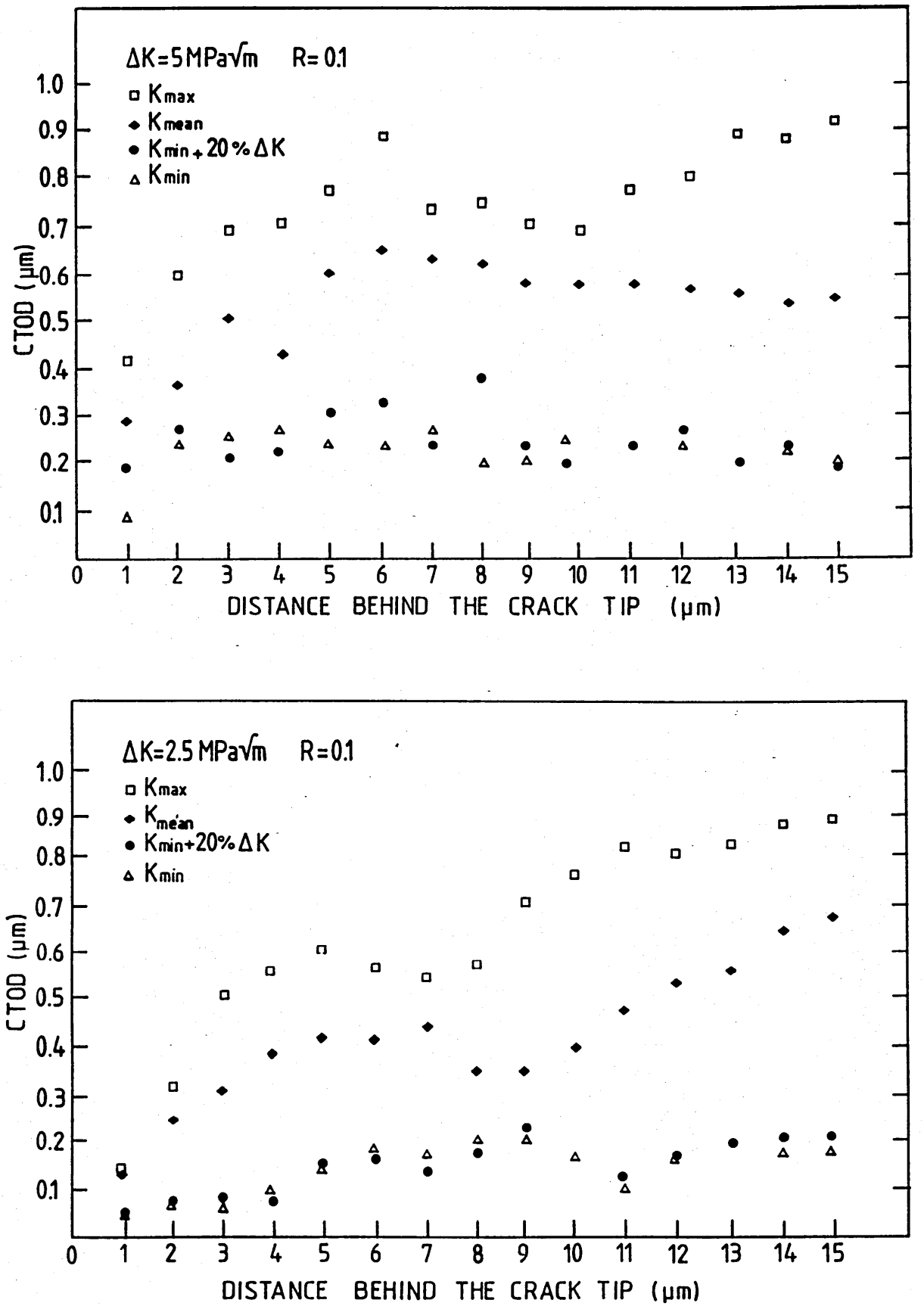

Figure 6.35 Fatigue crack tip opening displacement as a function of the distance behind the crack tip.

a $\Delta K = 5$ MPa$\sqrt{m}$, $R = 0.1$.

b $\Delta K = 2.5$ MPa$\sqrt{m}$, $R = 0.1$.

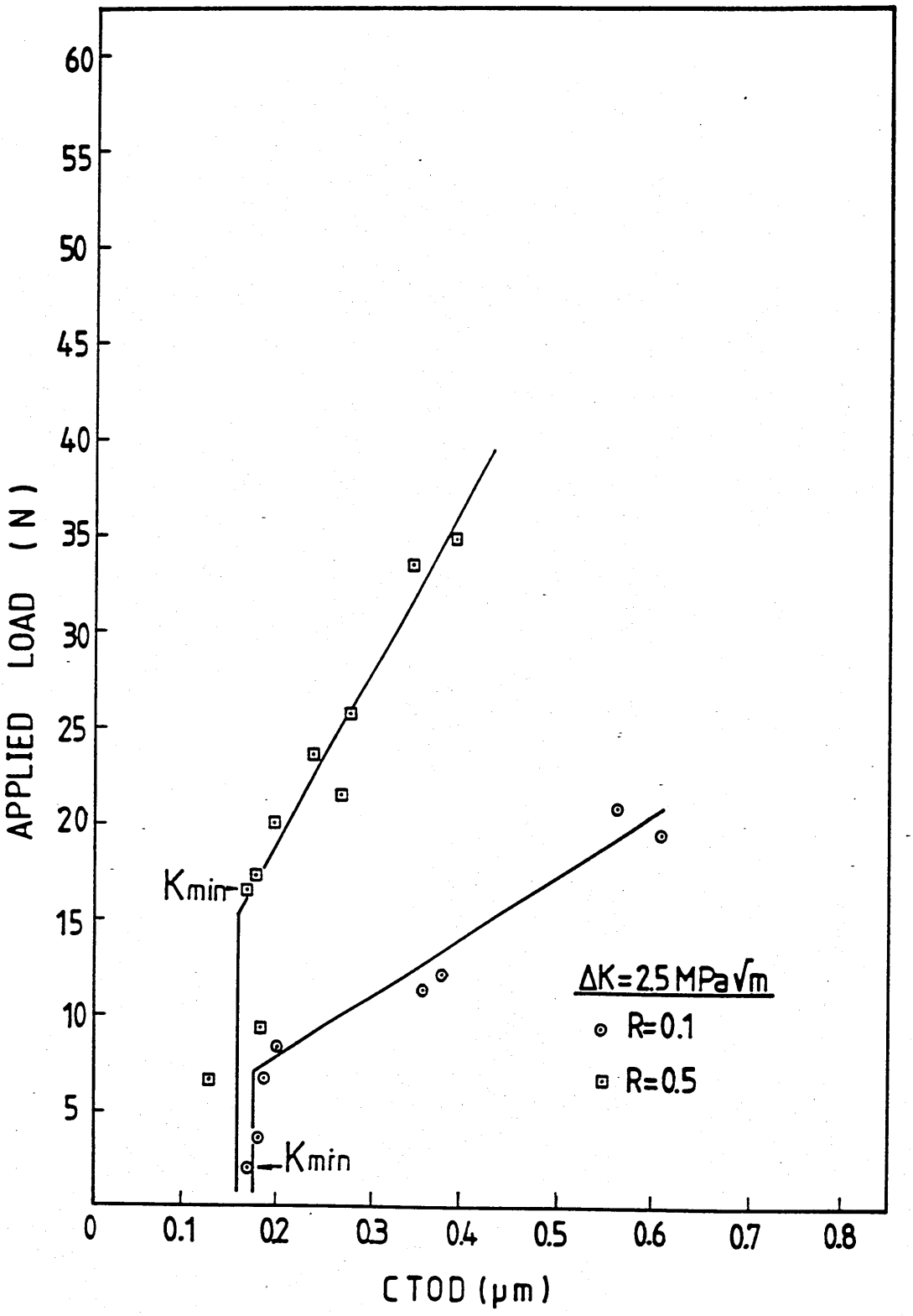

Figure 6.36 Load versus crack tip opening displacement curve at ΔK = 2.5 MPa$\sqrt{m}$ for R = 0.1 and R = 0.5.

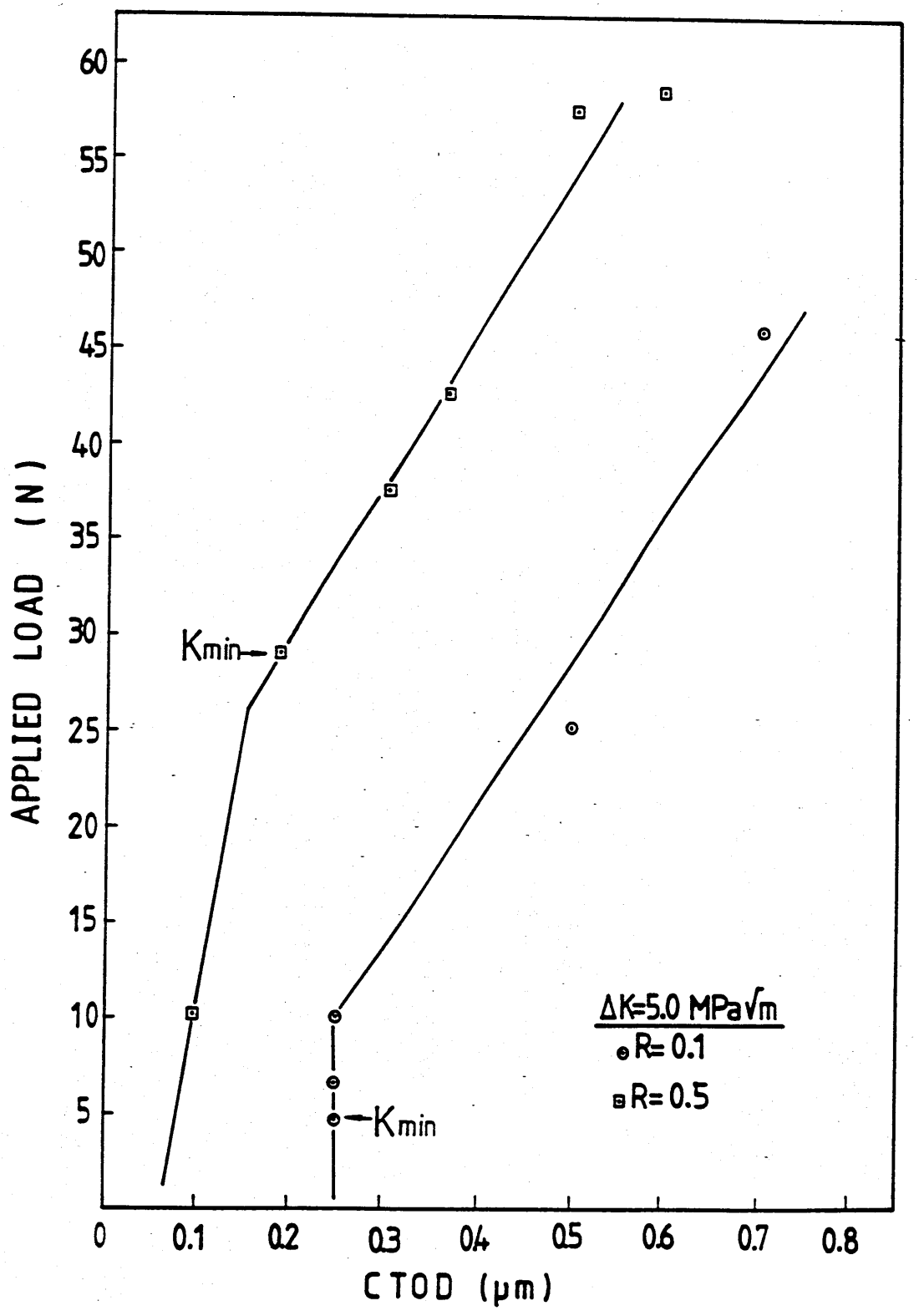

Figure 6.37 Load versus crack tip opening displacement curve at $\Delta K = 5$ MPa$\sqrt{m}$ for $R = 0.1$ and $R = 0.5$.

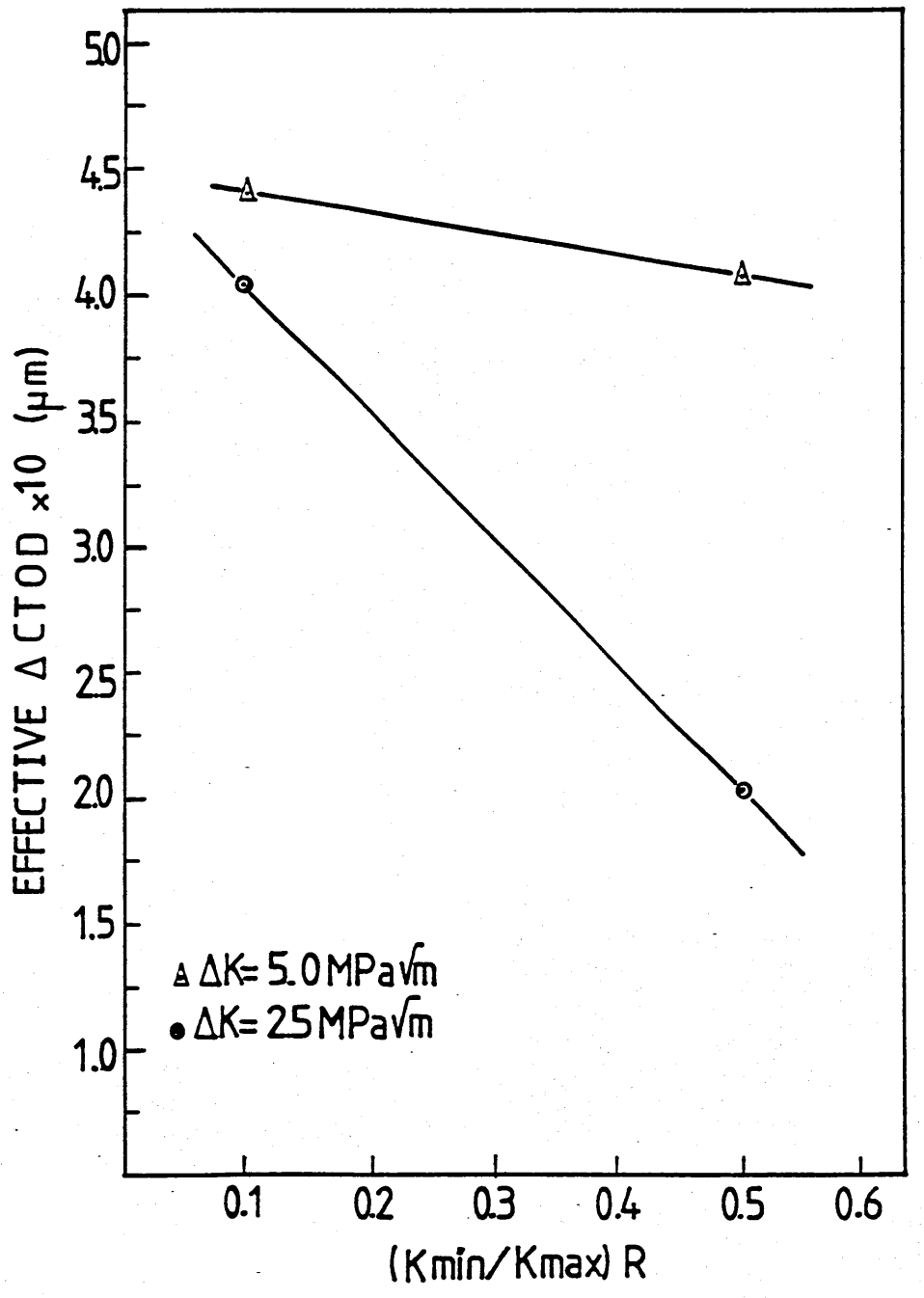

Figure 6.38 Variation of the effective crack tip opening displacement range with R at $\Delta K = 5$ MPa$\sqrt{m}$ and $\Delta K = 2.5$ MPa$\sqrt{m}$.

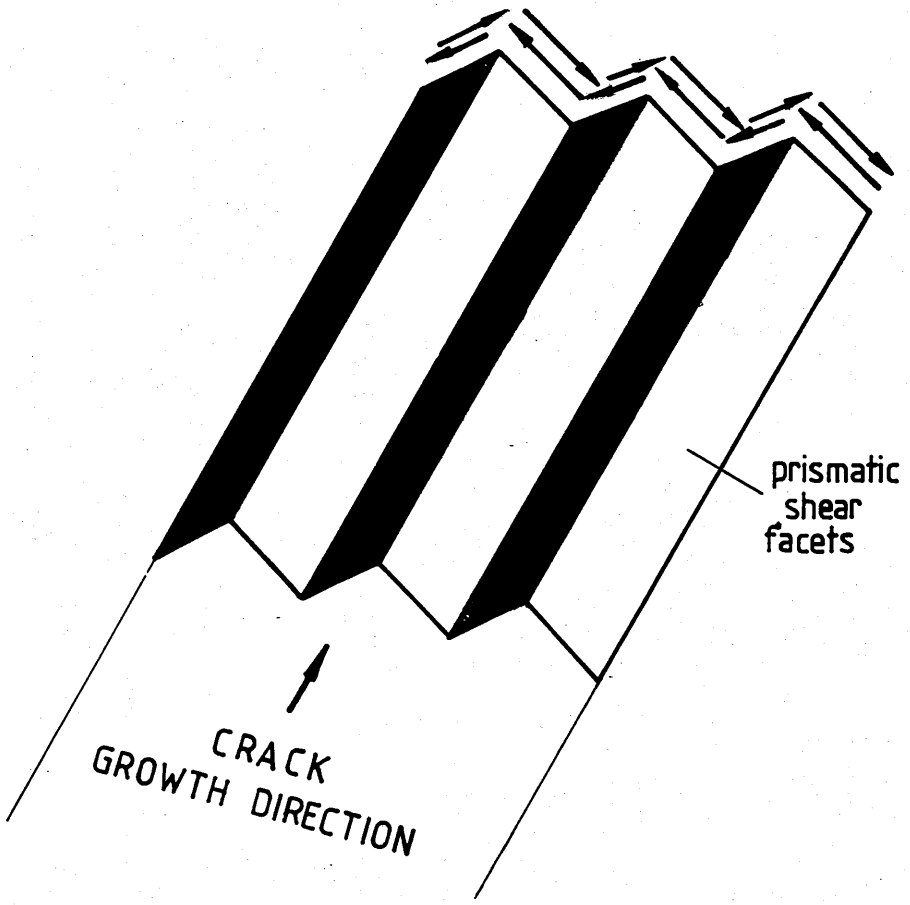

Figure 6.39 Schematic illustration of the threshold crack growth mechanism.

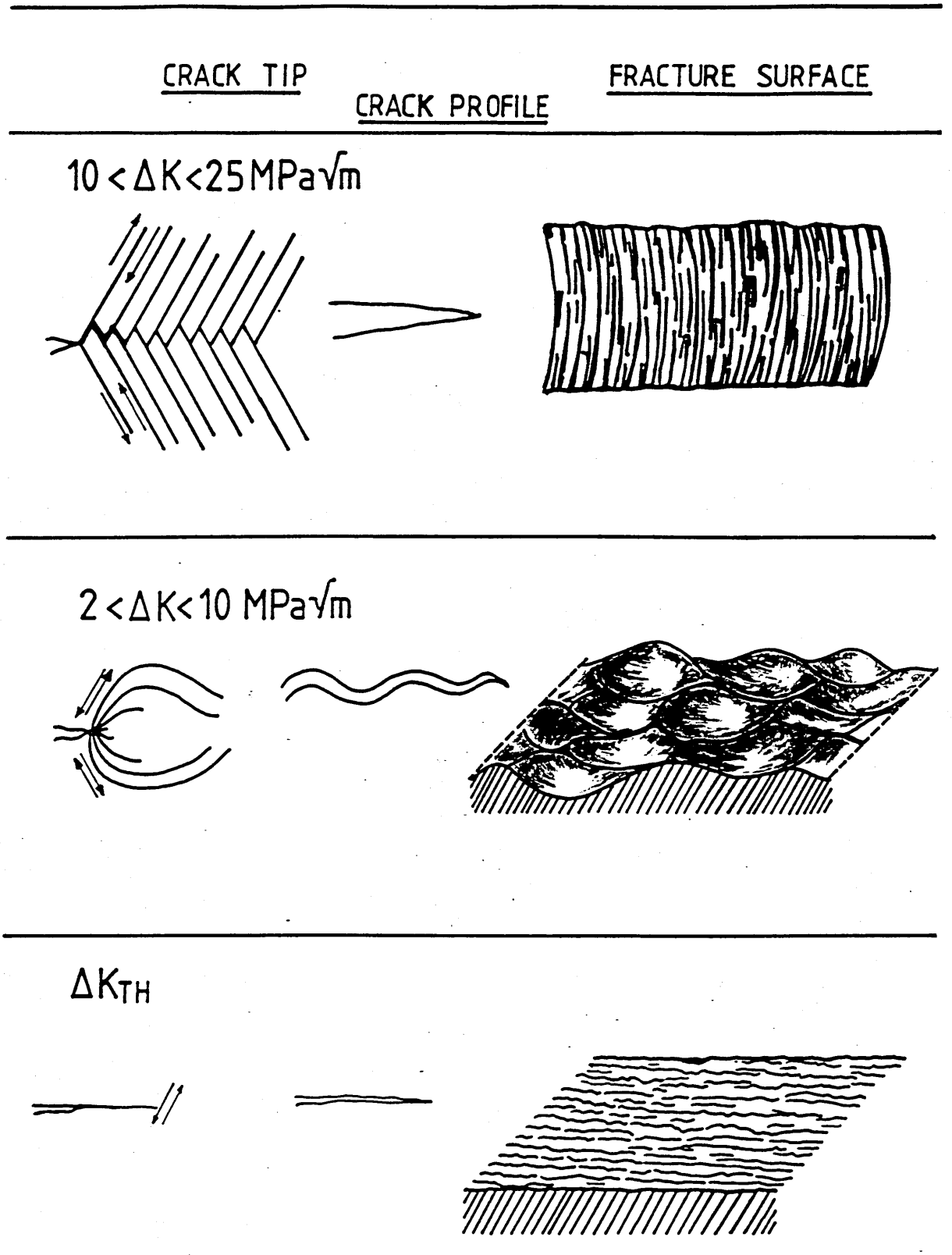

Figure 6.40 Summary of proposed fatigue crack propagation mechanisms and resulting fracture surfaces peculiar to amorphous $Ni_{78}Si_{10}B_{12}$ at medium and low ΔK levels.

CHAPTER SEVEN

SUMMARY AND SUGGESTIONS FOR FURTHER WORK

7.1 Summary

In this study, the fracture and fatigue in thin ribbons of a Ni-base metallic glass have been investigated. The alloy is distinguished by a very high tensile strength combined with a high toughness, but it differs from the other high strength metallic materials by the absence of a metallurgical microstructure. Yielding at room temperature proceeds by the development of a characteristic deformation microstructure consisting of localized shear bands. The mechanisms of crack extension in specimens under monotonic and cyclic loads are discussed in terms of the distribution, the density and the geometrical features of these bands. The main results can be summarized as follows:

1. On tensile loading, fracture of unnotched specimens occurs coincidentally with the formation of an intense shear band inclined at ~45 degrees to the loading axis. Rupture leaves behind a 'vein pattern' on the fracture surfaces.

2. The crack tips in notched and prefatigued specimens under monotonic tensile loads are attended by plastic zones dominated by shear bands elongated in the direction of crack extension. Dugdale's 'strip yield' model of cracks in elastic-rigid plastic materials offers a reasonable description of the zone size and the crack tip opening displacement in the alloy. Accordingly, failure occurs under plane stress conditions mainly by a mode III antiplane shear decohesion mechanism.

3. Trouser leg tear specimens loaded in mode III tension show plastic zones with recognisable components of deformation. Three types of shear bands are identified near the tip of a tear crack: one type is associated with the bending of the legs of the testpiece while the others provide evidence for types II and III shear

deformations. Based on the geometry of these bands, a model has been developed from which an accurate estimate of the tear energy has been obtained. Although the tear crack advanced by following a mode III type shear band, the model reveals that the contribution of this type of shear to the total energy expended is only 35 pct. The model also accounts for the observed linear dependence of the tear energy upon the specimen thickness in terms of the volume of the plastically deformed material.

4. The alloy has a fatigue limit of only 12 pct of the tensile fracture strength in agreement with those of other metallic glasses and crystalline alloys which display localized plastic deformation.

5. Fatigue crack growth versus ΔK curves exhibit a typical sigmoidal shape. For growth rates between 10^{-6} - 5×10^{-4} mm/cycle, the Paris Law with an exponent $m \approx 2$ is obeyed independent of R-ratio. Ductile striations could be observed only at high ΔK levels in this region. At lower crack growth rates, crack tip plastic zones are composed of 'parabolic' shear bands which define deformation patterns similar to the Prandtl slip line field for non-hardening materials under plane strain conditions. The path of crack advance follows one of these bands and leads to the formation of 'paraboidal' facets on fracture surfaces. As the number of shear bands increases with ΔK, the fatigue crack tends to propagate by the decohesion of the ligaments between these bands. Above the Paris region, the specimen develops shear lips under the control of K_{max} and finally fails by shear rupture.

6. Fatigue cracks in the alloy can continue to propagate at remarkably low ΔK levels, down to a threshold value $\Delta K_{TH} \approx 0.5$ MPa$\sqrt{m}$ at $R = 0.1$. The surface appearance of the plastic zone under near threshold conditions is that of a single, short band extending ahead of the crack tip. The low ΔK_{TH} is attributed to the ease of the nucleation of such a localized shear band which provides the large irreversible shear displacements necessary for fatigue crack growth.

7. At near threshold levels of ΔK, fatigue crack growth rates show an unusual dependence upon the R-ratio. As the R-ratio is raised, ΔK_{TH} increases and crack growth rates decrease. It is proposed that in this region, the driving force

for crack extension ΔK_{eff} increases with an increase in R-ratio. This is confirmed by establishing an experimental relationship between effective ΔCTOD and ΔK_{eff}. The R-ratio dependence of near threshold growth rates could not be explained purely in terms of the small thickness of the ribbons because stainless steel specimens of comparable thicknesses exhibited usual R-ratio dependence that is familiar in bulk specimens. This normal R-ratio dependence can be ascribed to the occurrence of crack closure. However, although crack closure was detected in the metallic glass, it has been shown that this does not account for the anomolous R-ratio dependence of crack growth rates.

7.2 Suggestions for Further Work

The mechanical behaviour of metallic glasses is a relatively new research area in materials science. The results reported in this study shed light on some previously unknown aspects of fracture and fatigue of these alloys: the determination of the components of plastic deformation during fracture toughness and tear tests, and fatigue crack propagation properties at low ΔK levels. However, observations made on $Ni_{78}Si_{10}B_{12}$ need to be extended to other metallic glasses, with different compositions, to establish whether these are general characteristics of metallic glasses. In particular, the unusual R-ratio dependence of near threshold fatigue crack growth rates requires further investigation. Binaries or ternaries of Pd-Si based metallic glasses which can be prepared in thicker sections might be suitable alloys for such studies. It may then be possible to determine unambigously the effect of specimen thickness in modifying the driving force for crack extension and to clarify the role of crack closure and local buckling on fatigue crack growth at low ΔK levels. On the other hand, the precise mechanisms leading to a very low ΔK_{TH} and to crack extension by non-crystallographic facet formation need to be studied in greater detail. The double stage replication technique used in this study proved to be a powerful tool for these investigations but it may be supported by cinematographic techniques to

determine specific details of shear band decohesion mechanisms. High-speed photography through a light microscope may provide a possibility of recording the nucleation/propagation sequences of shear bands during fatigue (as well as tensile or tear) tests.

In this thesis, only the results concerning the mechanical properties of the alloy in the amorphous state are reported. Some preliminary studies on the fracture and fatigue of annealed samples of the metallic glass have also been performed. It was observed that strain localization may be prevented by the crystallization of the specimens but, they then become entirely brittle. However, by selecting a suitable heat treatment procedure (e.g. 450° C, 7 min) it is possible to obtain the alloy in a semi-crystalline form which contains primary nickel crystallites of 50 nm diameter, finely dispersed in the amorphous matrix. This treatment results in an improvement in the fracture strength and hardness of the alloy without affecting its ductility detrimentally. This point is important regarding the potential use of the metallic glass ribbons as high strength reinforcing elements. Studies directed towards finding heat treatment procedures to optimise the mechanical properties of the metallic glasses may offer rewarding research prospects.

The study of the mechanical behaviour of metallic glasses characterized by the lack of a metallurgical microstructure but by the development of a deformation microstructure consisting of conspicuous shear bands may contribute to an improvement in the understanding of the properties of other materials. For example, in this study, the localized nature of shear bands in amorphous $Ni_{78}Si_{10}B_{12}$ has enabled the components of the plastic deformation at the tip of a tear crack to be identified. These components are thought to be a general feature of tearing and may help to interpret the tests performed on rubbers or on crystalline alloys for which the same geometry applies. Furthermore, metallic glasses may be advantageous in the study of the propagation behaviour of short fatigue cracks because they provide an opportunity to isolate the effect of applied mechanical factors from the effect of microstructure. These examples show that

scientific interest in the fracture and fatigue of metallic glasses extends beyond the discovery of the properties of a new class of materials.

List of References

Anderton, G.E. and Treloar L.R.G. (1971) J. Mat. Sci., 6, p562.

Argon, A.S. (1973) The Homogenity of Plastic Deformation, A. S. M. Metals Park, Ohio, p161.

Argon, A.S. (1979) Acta. Met., 27, p47.

Argon, A.S. (1980) Glass: Science and Technology, Vol. 5, Uhlmann, D.R. and Kriedl, N.J., Eds., Academic Press, New York, p79.

Argon, A.S. and Salama, M. (1976) Mat. Sci. Eng., 23, p219.

Argon, A.S. and Kuo, H.Y. (1978) Rapidly Quenched Metals III, Vol. 2, Cantor, B., Ed., Metals Society, London, p276.

Argon, A.S., Megusar, J, and Grant, N.J. (1985) Scripta Met., 19, p591.

Asaro, R.J., Hermann, L. and Baik J.M. (1981) Met. Trans., 12A, p1133.

Ashby, M.F. and Logan, J. (1973) Scripta Met., 7, p513.

Ast, D.G. and Krenitsky, D. (1976) Mat. Sci. Eng., 23, p241.

ASTM (1978) D 1938-67, Tear Propagation Resistance of Plastic Film and Thin Sheeting by a Single Tear Method.

ASTM (1981) E 399-81, Plane Strain Fracture Toughness of Metallic Materials.

ASTM (1981) E 561-81, R-Curve Determination.

ASTM (1981) E 647-81, Constant-Load Amplitude Fatigue Crack Growth Rates Above 10^{-8} m/cycle.

Bathias, C. and Pelloux, R.M. (1973) Met. Trans., 4A, p1265.

Beachem, C.D. and Yoder, G.R. (1973) Met. Trans., 4A, p1145.

Beevers, C.J. (1977) Metal Science, 11, p362.

Beevers, C.J. (1980) Metal Science, 14, p418.

Beevers, C.J., Cooke, R.J., Knott, J.F. and Ritchie, R.O. (1975) Metals Science, 9, p119.

Bilby, B.A., Cottrell, A.H. and Swinden, K.H. (1963) Proc. Roy. Soc., A272, p304.

Blarenblatt, G.I. (1962) Advances in Appl. Mech., 7, p55.

Blind, A.B. (1982) D. Phil Thesis, Oxford University.

Blom, A.F. (1984) Fatigue Crack Growth Threshold Concepts, Davidson D.L. and Suresh, S., eds., Metallurgical Society of AIME, New York, p263.

Bretz, P.E., Petit, J.I. and Vasudevan, A.K. (1983) Fatigue Crack Growth Threshold Concepts, Davidson, D.L. and Suresh, S., eds., Metallurgical Society of AIME, New York, p163.

Broek, D. (1974) Elementary Engineering Fracture Mechanics, Noordhoff International Publishing, The Netherlands.

Brown, L.M. (1977) Metal Science, 11, p315.

British Standard (1977) 5447, Plane Strain Fracture Toughness of Metallic Materials.

Burdekin, F.M. and Stone, D.E.W. (1966) J. Strain Analysis, 1, p145.

Byrne, J. and Duggan, T.V. (1982) Fatigue Thresholds, Vol. 2, Backlund, J., Bloom, A.F. and Beevers, C.J., Eds., EMAS, p759.

Cantor, B., ed. (1978) Rapidly Quenched Metals III, The Metals Society, London.

Chaki, T.K. and Li, J.C.M. (1984) Scripta Met., 18, p703.

Chan, R.W., Patten, N.A., Scott, M.G., Sinning, H,R. and Leonardson, L. (1983) Rapidly Quenched Metastable Materials, Mat. Research Soc., Boston, p173.

Chen, H.S. (1976) Appl. Phys. Lett., 29, p328.

Chen, H.S., Leamy, H.J. and O'Brien, M.J. (1973) Scripta Met., 7, p415.

Chiu, D.S., Gent, A.N. and White, J.R. (1984) J. Mat. Sci., p2622.

Clayton, J.Q. and Knott, J.F. (1976) Metal Science, 10, p63.

Cohen, M.H. and Tunbull, D. (1959) J. Chem. Phys., 31, p1164.

Cooke, R.J., Irving, P.E., Booth, G.S. and Beever, C.J. (1975) Eng. Fract. Mech., 7, p69.

Cottrell, A.H. and Bilby, B.A. (1949) Proc. Phys. Soc., 62A, p49.

Cummings, H.N., Stulen, F.B. and Schultze, W.C. (1957) Trans., ASM 49, p482.

Davidson, D.L. (1981) Fat. Eng. Mat. Struct., 3, p229.

Davidson, D.L. (1984) Acta Met., 32, p707.

Davidson, D.L. and Suresh S., eds., (1984) Fatigue Crack Growth Threshold Concepts, AIME, New York.

Davis, L.A. (1975a) Scripta Met., 9, p339.

Davis, L.A. (1975b) J. Mat. Sci., 10, p1557.

Davis, L.A. (1976) J. Mat. Sci., 11, p711.

Davis, L.A. (1978) Metallic Glasses, (ASM Seminar, 1976, Niagara Falls), American Society for Metals, Ohio, p190.

Davis, L.A. (1979) Met. Trans., 10A, p235.

Davis, L.A. and Kavesh, S. (1975) J. Mat. Sci., 10, p453.

Davis, L.A. and Hasegawa, R. (1981) Treatises in Metallurgy, Tien, J.K. and Elliott, J., Eds., New York, p301.

Deng, D. and Lu, B. (1983) Scripta Met., 17, p515.

Devaux, J.C. (1980) Rapport Framatome, TMIC DC179.024.

Donahue, R.J., Clark, H.M., Atanno, P. and Mc Evily, A.J. (1972) Inter J. Fract. Mech., 8, p209.

Donovan, P.E. and Stobbs, W.M. (1981) Acta Met., 29, p1419.

Dugdale, D.S. (1960) J. Mech. Phys. Sol., 8, p100.

Duffy, A.R. et. al. (1969) Fracture I, Liebowitz, ed., Academic Press, p159.

Duwez, P., Willens, R.H. and Klement, W. (1960) J. Appl. Phys., 31, p1137.

Edwards, L. (1981) D. Phil. Thesis, Oxford University.

Elber, W. (1970) Eng. Fract. Mech., 2, p37.

Elber, W. (1971) ASTM STP 486, p230.

Ewalds, H.L., Wanhill, R.J.H. (1985) Fracture Mechanics, Edward Arnold, Ed., London.

Ewing, J.A. and Humphrey, J.C. (1903) Phil. Trans. A200, p241.

Fine, M.E. and Ritchie, R.O. (1979) Fatigue and Microstructure, American Society For Metals, Ohio, p245.

Finney, J.M. and Laird, C. (1975) Phil. Mag., 31, p339.

Fleck, N.A. (1982) The use of complience and electrical resistance techniques to characterize fatigue crack closure, Cambridge University Eng. Dept. Internal Report No CUED/C/MATS/TR.89.

Fleck, N.A. (1984) An investigation of fatigue crack closure, Cambridge University Eng. Dept. Internal Report No CUED/C/MATS/TR.104.

Forsyth, P.J.E.. (1961) Proc. Crack Propagation Symp., Vol.I, Cranfield College of Aeronautics, p76.

Forsyth, P.J.E. and Stubbington, C.A. (1957-58) J. Inst. Met. 86, p90.

Forsyth, P.J.E. and Ryder, D.A. (1961) Metallurgia, 63, p117.

Forsyth, P.J.E. (1969) The Physical Basis of Metal Fatigue, American Elsevier Pub. Co., New York.

Frommeyer, G. and Seifert, K. (1981) Z. Metallkde., 72, p391.

Frost, N.E., Marsh, K.J. and Pook, L.P. (1974) Metal Fatigue, Clarendon Press, Oxford.

Garret, G.G. and Knott, J.F. (1975) Met. Trans., 6A, p1663.

Gerberich, W., Wright, A. and Lei, M.J. (1984) Advances in Fracture Research (ICF6), Valluri, S.R., ed., Pergamon Press, p2153.

Giessen, B.C., Madhava, M. and Polk, D.E. (1976) Mat. Sci. Eng., 23, p145.

Gilman, J.J. (1975) J. Appl. Phys., 46, p1625.

Graf, M. and Hornbogen, F. (1978) Scripta Met., 12, p41.

Grant, N.J., ed., (1984) Rapidly Solidified Metals, V, Springer - Verlag, Berlin.

Grant, N.J. and Giessen, B.C., eds. (1976a) Rapidly Quenched Metals, Section I, M.I.T. Press, Cambridge, Massachussetts.

Grant, N.J. and Giessen, B.C., eds. (1976b) Mat. Sci. Eng., 23, p83.

Green, G. and Knott, J.F. (1976) Trans. ASME H, 98, p37.

Greensmith, H.W. and Thomas A.G. (1955) J. Polymer Sci., 18, p189.

Griffith, A.A. (1920) Phil. Trans. Roy. Soc., A221, p163.

Griffiths, J.R., Mogford, I.L. and Richards, C.E. (1971) Metal Science, 5, p150.

Hahn, G.T. and Rosenfield, A.R. (1965) Acta Met., 13, p293.

Hahn, G.T. and Rosenfield A.R. (1968) ASTM STP 432, p5.

Hahn, G.T. and Rosenfield A.R. (1975) Met. Trans., 6A, p653.

Hahn, G.T., Sarrate, M. and Rosenfield, A.R. (1970a) Proc. USAF Conf. on Fat. and Fract., p1.

Hahn, G.T., Rosenfield, A.R. and Sarrate, M. (1970b) Inelastic Behaviour of Solids, Kanninen, M.F., ed., Mc Graw-Hill, Ohio, p673.

Hahn, G.T., Hoagland, R.G. and Rosenfield, A.R. (1972) Met. Trans., 3A, p1189.

Hall, E.O. (1970) Yield Point Phenomena in Metals, Plenum Publishing Co., New York.

Halliday, M.D. and Beevers, C.J. (1979) Int. J. Fract., 15, p27.

Hancock, J.W. and Cowling, M.J. (1980) Metal Science, 14, p293.

Head, A.K. (1953) Phil. Mag., 44, p925.

Heald, P.T., Lindley, T.C. and Richards, C.E. (1972) Mat. Sci. Eng., 10, p235.

Henning, W., Calvo, M. and Osterstock F. (1985) J. Mat. Sci., 20, p1889.

Hill, R. (1950) The Mathematical Theory of Plasticity, Oxford University Press.

Hillenbrand, H.G. (1983) Dipl.-Ing. Thesis, University of Bochum.

Hilsinger, H.R. (1984) Private communication.

Iino, Y. (1976) Metal Science, 10, p159.

Ikeda, S., Izumi, Y. and Fine, M.E. (1977) Eng. Fract. Mech., 9, p123.

Inglis, C.E. (1913) Trans. Inst. Nav. Archi., 60, p219.

Irwin, G.R. (1948) Fracturing of Metals, ASM Publication, p147.

Irwin, G.R. (1958) Encyclopedia of Physics, Vol. VI, Springer, Berlin.

Irwin, G.R. (1960) Proc. 7th Sagamore Conf., pIV-63.

Isherwood, D.P. and Williams, J.G. (1978) Eng. Fract. Mech., 10, p887.

Kambour, R.P. (1964) Polymer, p143.

Kanninen, M.F., Atkinson, C. and Mc Evily, A.J. (1977) Int. J. Fract., 13, p887.

Kim, Y.H., Mura, T. and Fine, M.E. (1978) Met. Trans., 9A, p1679.

Kimura, H. and Masumato, T. (1975) Scripta Met., 9, p211.

Kimura, H. and Masumato, T. (1981) Phil. Mag., 44A, p1005.

Kimura, H. and Masumato, T. (1983) Met. Trans., 14A, p709.

Klement, W., Willens, R.H. and Duwez P. (1960) Nature, 187, p869.

Knott, J.F. (1980) Metal Science, 14, p327.

Knott, J.F. (1973) Fundamentals of Fract. Mech., Butterworths, London.

Kobayashi, S., Maeda, K. and Takeuchi, S. (1980) Acta Met., 28, p1641.

Koster, U. and Hillenbrand, H.G. (1980) Metallic Glasses: Science and Technology. Hargiatai, C., Bakonyi, I. and Kemeny, T., eds., Institute For Physics, Budapest, p91.

Krafft, J.M., Sullivan, A.M. and Boyle, R.W. (1962) Proc. of the crack Propagation Symp., Cranfield, Vol. I, p8.

Krug, W., Rienitz, J. and Schulz, G. (1967) Contributions to Interference Microcopy, Chapter 4, Hilger and Watts, Berlin.

Laird, C. and Smith, G.C. (1962) Phil. Mag., 7, p847.

Lankford, J. and Barbee, J.G. (1974) J. Mat. Sci., 9, p1906.

Lankford, J. and Davidson, D.L. (1976a) J. of Eng. Mat. and Tech., 98, p17.

Lankford, J. and Davidson, D.L. (1976b) J. of Eng. Mat. and Tech., 98, p24.

Lankford, J., Davidson, D.L. and Cook, T.S. (1977) ASTM STP 637, p36.

Lankford, J. and Davidson, D.L. (1983) Acta Met., 31, p1273.

Lankford, J. and Kusenberger, F.N. (1972) Phil. Mag., 26, p1485.

Lardner, R.W. (1968) Phil. Mag., 17, p71.

Leamy, H.J., Chen, H.S. and Wang, T.T. (1972) Met. Trans., 3A, p699.

Levy, N., Marcal, P.V., Ostergren, W.J. and Rice, J.R. (1971) Int. J. of Fract. Mech., 7, p143.

Li, J.C.M. (1978) Metallic Glasses (ASM Seminar, 1976, Niagara Falls) American Soc. for Metals, Ohio, p224.

Li, J.C.M. (1981) Rapidly Quenched Metals IV, Masumato, T., ed., Japan Soc. of Metals, Sendai, p1335.

Li, J.C.M. (1982a) Treatise on Mat. Sci. and Tech., Vol.XX, Herman, H., ed., Academic Press, p325.

Li, J.C.M. (1982b) Rapidly Solidified Amorphous and Crystalline Alloys, Kear, B.H., Giessen, B.C. and Cohen, M., eds., Elsevier, p267.

Lindley, T.C. and Richards, C.E. (1974) Mat. Sci. Eng., 14, p281.

Lindley, T.C. and Richards, C.E. and Ritchie, R.O. (1976) Metallurgica and Metal Forming, 43, p268.

Liu, H.W. and Iino, N. (1969) Fracture 1969, Pratt, ed., Chapman and Hall, London, p812.

Louwaard, E.P. (1977) Delft Univ. of Tech., Dept. of Aero Eng., Report LR-243, Delft, The Netherlands.

Lu, M.C. and Weissmann, S. (1978) Mat. Sci. Eng., 32, p41.

Lukas, P., Klensil, M. and Krejci, J. (1968) Phy. Stat. Sol., 27, p545.

Maeda, K. and Takeuchi, S. (1977) Tech. Rep. ISPP Japan, No A828.

Marcal, P.V. and King, I.P. (1967) Int. J. of Mech. Sci., 9, p143.

Masumato, T. (1977) Sci. Rep. Research Inst. Tohoku Univ., 26A, p246.

Masumato, T., ed. (1981) Rapidly Quenched Metals IV, Japan Soc. of Metals, Sendai.

Masumato, T. and Maddin, T. (1971) Acta Met., 19, p725.

Masumato, T. and Maddin, R. (1975) Mat. Sci. Eng., 19, p1.

Mc Clintock, F.A. (1967) ASTM STP 415, p170.

Mc Clintock, F.A. (1971) Fracture, Liebowitz, ed., Academic Press, Vol. III, p47.

Mc Clintock, F.A. and Irwin, G.R. (1965) ASTM STP 381, p84.

Mc Evily, A.J. (1977) Metal Science, 11, p274.

Mc Meeking, R.M. (1977) J. Mech. Phys. Solids, 25, p357.

Megusar, J., Argon, A.S. and Grant, N.J. (1979) Mat. Sci. Eng., 38, p63.

Megusar, J., Argon, A.S. and Grant, N.J. (1982) Rapidly Solidified Amorphous and Crystalline Alloys, Kear, H.B., ed., Elsevier, New York, p283.

Minakawa, K. and Mc Evily, A.J. (1981) Scripta Met., p633.

Minakawa K. and Mc Evily, A.J. (1984) Fatigue 84, Beevers, J.C., ed., EMAS, Vol. I, p373.

Murata, T., Masumato, T. and Sakai, M. (1978) Rapidly Quenched Metals III, Cantor, B., ed., Vol. II, Metals Soc., London, p401.

Muskhelishvili, N.A. (1953) Some Basic Problems of Mathematical Theory of Elasticity, P. Noordhoff, London.

Neumann, P. (1974) Acta Met., 22, p1155.

Newman, J.C. (1976) ASTM STP 590, p281.

Nomarski, G. and Weill, A.R. (1955) Rev. Met., 52, p121.

Ogura, T., Fukushima, K. and Masumato, T. (1975) Scripta Met., 19, p979.

Ogura, T., Fukushima, K. and Masumato, T. (1976) Mat. Sci. Eng., 23, p231.

Ogura, T., Masumato, T. and Fukushima, K. (1975) Scripta Met., 8, p109.

Orowan, E. (1949) Rep. Progr. Phys., 12, p185.

Otsuka, A., Mori, K. and Miyata, T. (1975) Eng. Fract. Mech., 7, p429.

Pampillo, C.A. (1972) Scripta Met., 6, p915.

Pampillo, C.A. (1975) J. Mat. Sci., 10, p1194.

Pampillo, C.A. and Chen, H.S. (1974) Mat. Sci. Eng., 13, p181.

Pampillo, C.A. and Polk, D.E. (1974) Acta Met., 22, p741.

Pampillo, C.A. and Reimschuessel, A.C. (1974) J. Mat. Sci., 9, p718.

Paris, P.C. and Erdogan, F. (1963) J. Basic Eng., (Trans. ASME D), 85, p528.

Paris, P.C. and Sih, G.C. (1965) ASTM STP 381, p30.

Pelloux, R.M.N. (1969) ASM Trans. Quart., 62, p1.

Pelloux, R.M.N. (1970) Eng. Fract. Mech., 1, p697.

Pineau, A. (1981) 5th Int. Conf. on Fracture, Francois, D., ed., Pergamon Press, Vol. II, p553.

Pook, L.P. (1972) ASTM STP 513, p106.

Pook, L.P. (1983) The Role of Crack Growth in Metal Fatigue, The Metals Soc., London.

Pook, L.P. (1985) Private communication.

Polk, D.E. and Turnbull, D. (1972) Acta Met., 20, p493.

Priddle, E.K. and Walker, F.E. (1976) J. Mat. Sci., 11, p386.

Prince, K.C. (1977) D. PHil Thesis, Oxford University.

Purushothaman, S. and Tien, J.K. (1979) Strength of Metals and Alloys, ICSMA 5, Haasen, P., ed., Pergamon Press, New York, Vol. II, p1267.

Rawal, S.p. and Gurland, J. (1976) Proc. of 2nd Int. Conf. on Mech. Behaviour of Mat., Michigan, p1154.

Ray, R. and Kavesh, S. (1977) U.S.P., No4, 036, p638.

Ray, R. (1979) U.S.P., No4, 140, p525.

Rice, J.R. (1967) ASTM STP 415, p247.

Rice, J.R. and Johnson, M.A. (1970) Inelastic Behaviour of Solids, Kanninen, M.F., ed., Ohio, p641.

Rice, J.R. and Rosengren, G.F. (1968) J. Mech. Phys. Solids, 16, p1.

Rice, J.R. and Sorensen, E.P. (1978) J. Mech. Phys. Solids, 26, p163.

Rice, J.R. and Tracey, D.M. (1969) J. Mech. Phys. Solids, 17, p201.

Ritchie, R.O. (1977) Met. Trans., 8A, p1131.

Ritchie, R.O. and Knott, J.F. (1974) Mat. Sci. Eng., 14, p7.

Ritchie, R.O., Knott, J.F. and Rice, J.R. (1973) J. Mech. Phys. Solids, 21, p395.

Ritchie, R.O. and Suresh, S. (1980) J. Mat. Eng. Techn., Trans ASME H, 102, p293.

Ritchie, R.O. and Suresh, S. (1982) Met. Trans., 13A, p937.

Rivlin, R.S. and Thomas, A.G. (1953) J. Polymer Sci., 10, p291.

Rooke, D.P. and Cartwright, D.J. (1976) Compendium of Stress Intensity Factors, HM's Stationery Office, London.

Sawyers, K.N. and Rivlin, R.S. (1974) Eng. Fract. Mech., 6, p557.

Saxena, A. and Antolovich, S.D. (1975) Met. Trans., 6A, p1975.

Schijve, J. (1979) Eng. Fract. Mech., 11, p167.

Schmidt, R.A. and Paris, P.C. (1973) ASTM STP 536, p79.

Schwalbe, K.H. (1977) Eng. Fract. Mech., 9, p795.

Sehitoglu, H. (1985) ASTM STP 868, p361.

Sims, G.L.A. (1975) J. Mat. Sci., 10, p647.

Skelton, R.P. and Haigh, J.R. (1978) Mat. Sci. Eng., 36, p17.

Spaepen, F. (1974) Acta Met., 23, p615.

Spaepen, F. (1977) Acta Met., 25, p407.

Spaepen, F. (1978) J. Non-Crystalline Solids, 31, p207.

Spaepen, F. and Turnbull, D. (1974) Scripta Met., 8, p563.

Srolovitz, D. Vitek, V. and Egami, T. (1983) Acta Met., 34, p335.

Stewart, A.T. (1980) Eng. Fract. Mech., 13, p463.

Suresh, S. (1983) Met. Trans., 14A, p2375.

Suresh, S. and Ritchie, R.O. (1982) Met. Trans., 13A, p1627.

Suresh, S. and Ritchie, R.O. (1983) Scripta Met., 17, p575.

Suresh, S. and Ritchie, R.O. (1984) Fatigue Crack Growth Threshold Concepts, Suresh, S. and Ritchie, R.O., eds., AIME, New York, p227.

Suresh, S., Parks, D.M. and Ritchie, R.O. (1982) Proc. 1st Int. Symp. on Fatigue Thresholds, Backlaund, J., Blom, A.F. and Beevers, C.J., eds., EMAS Publ., Warley, p391.

Takayama, S. (1979) Mat. Sci. Eng., 38, p41.

Takayama, S. and Maddin, R. (1975a) Acta Met., 23, p943.

Takayama, S. and Maddin, R. (1975b) Met. Trans., 7A, p1065.

Takayama, S. and Maddin, R. (1976) Mat. Sci. Eng., 23, p261.

Taplin, D.M.R. and Wingrove, A.L. (1967) Acta Met., 15, p1231.

Taylor, G.I. (1950) Proc. R. Soc., 201A, p192.

Thomas, A.G. (1955) J. Polymer Sci., 18, p177.

Thompson, N., Wadsworth, N.J. and Luat, N. (1956) Phil. Mag., 1, p113.

Tomkins, B. (1975) Proc. of Conf. on the Mech. and Phys. of Fract., Churchill College, Cambridge, The Metals Society, p226.

Tomkins, B. (1980) Metal Science, 14, p408.

Tomkins, B. and Biggs, W.D. (1969) J. Mat. Sci., 4, p544.

Tracey, D.M. (1971) Eng. Fract. Mech., 3, p255.

Tracey, D.M. (1976) Trans. ASME 98, Series H, J. Eng. Mat. Tech., p146.

Trebules, V.W., Roberts, R. and Hertzberg, R.W. (1973) ASTM STP 536, p115.

Tu, L.K.L. and Seth, B.B. (1978) J. Test. Eval., 6, p66.

Tuba, I.S. (1966) J. Strain Analysis, 1, p115.

Turnbull, D. (1961) Trans. AIME, 221, p424.

Turnbull, D. and Cohen, M.H. (1970) J. Chem. Phys., 52, p3038.

Venables, R.A. Hicks, M.A. and King, J.E. (1983) Fatigue Crack Growth Threshold Concepts, Davidson. D.L., Suresh, S., eds., Met. Soc. of AIME, New York, p341.

Waku, Y. and Masumato, T. (1981) Rapidly Quenched Metals IV, Masumato, T., ed., Japan Soc. of Metals, Sendai, p1395.

Walker, N. and Beevers, C.J. (1979) Fat. Eng. Mat. Struct., 1, p135.

Walter, J.L., Legrand, D.G. and Luborsky, F.E. (1977) Mat. Sci. Eng., 29, p161.

Ward-Close, C.M. and Beevers, C.J. (1980) Met. Trans., 11A, p1007.

Waseda, Y., Aust, K.T. and Masumato, T. (1979) Scripta Met., 13, p187.

Waseda, Y. and Egami, T. (1979) J. Mat. Sci., 14, p1249.

Weertman, J. (1965) Proc. 1st Int. Conf. on Fract., Sendai, p157.

Weertman, J. (1979) Fatigue and Microstructure, American Soc. for Metals, p279.

Weiss, V. and Lal, D. (1974) Met. Trans., 5A, p1946.

Westergaard, H.M. (1939) J. Appl. Mech., 61, A49.

Yamamoto, R., Matsuoko, H. and Doyama, M. (1979) Physica Status Solidi (a), p.163.

Yokobori, Y., Konosu, S. and Yokobori, A.T. (1977) ICF4, Waterloo, Canada, 1, p665.

Zappfe, C.A. and Worden, C.D. (1949) Trans. ASM 41, p396.

Zielinski, P.G. and Ast, D.G. (1983) Phil. Mag., 48A, p811.